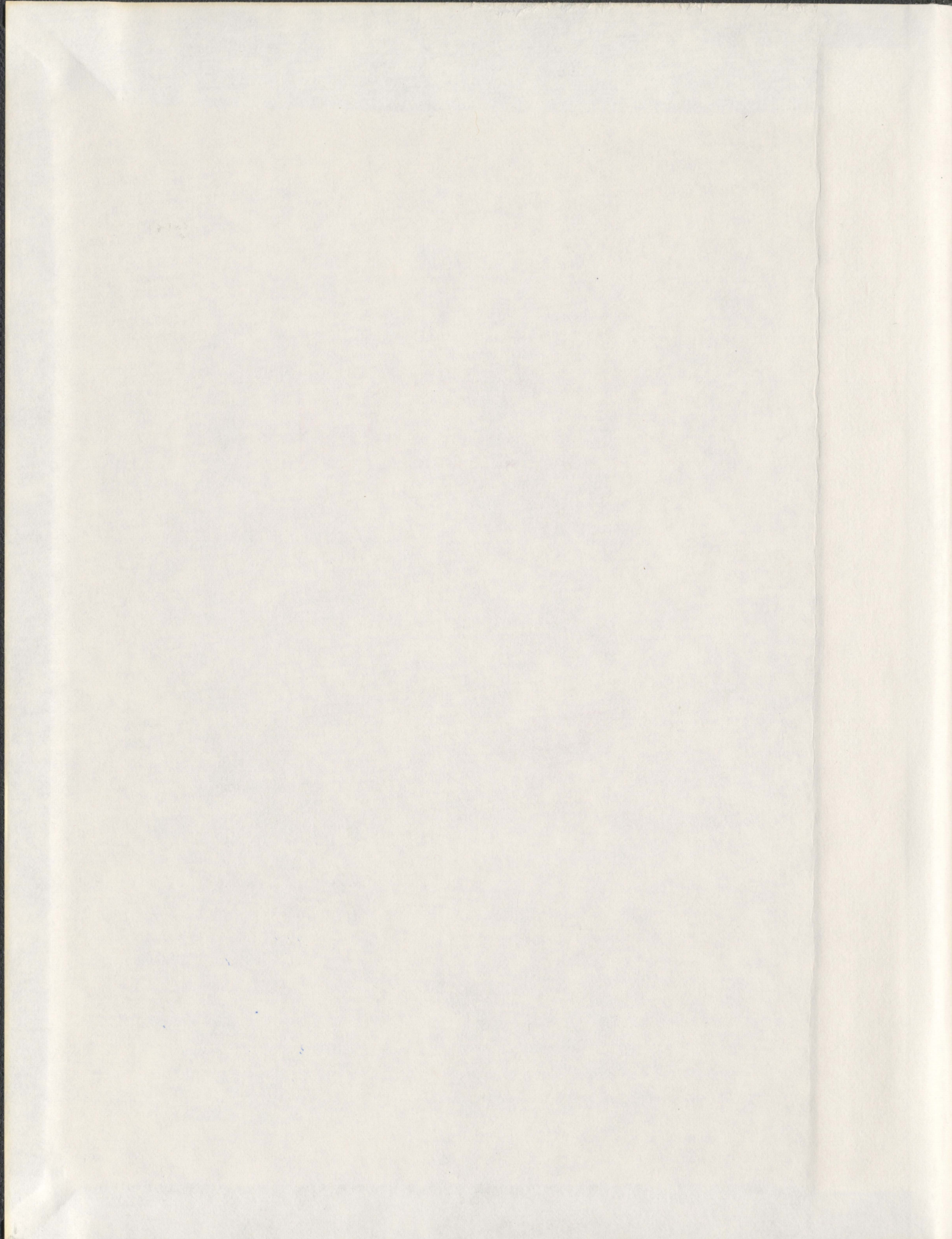


**SEISMIC LIQUEFACTION COUNTERMEASURES
FOR WATERFRONT SLOPES**

AHMAD JAFARI MEHRABADI



Seismic Liquefaction Countermeasures for Waterfront Slopes

By:

©Ahmad Jafari Mehrabadi, B.Sc., M.Sc.

A thesis submitted to the
School of Graduate Studies
in partial fulfillment of the requirements for the degree of

Doctor of Philosophy
in
Civil Engineering

**Faculty of Engineering & Applied Science
Memorial University of Newfoundland
St. John's, NL, Canada
November 2006**

To Humanity

To my Father

And

In Memory of my Lovely Mother

Abstract

A large number of the observed catastrophic effects during past earthquakes all over the globe including loss of human life, and drastic economic losses caused by severe damage to many structures are related to the occurrence of soil failure and large displacements caused by soil liquefaction.

The Fraser River Delta in British Columbia is highly prone to liquefaction hazards, and a large amount of money is spent annually to mitigate the detrimental consequences of soil liquefaction in this region. In this respect, NSERC sponsored a Liquefaction Remediation Initiative (LRI) to assess and optimize the required seismic liquefaction countermeasures in the Fraser River Delta using a series of centrifuge experiments and numerical simulations.

Optimization of liquefaction remediation techniques requires understanding their effectiveness at different levels of seismic intensity. This can be achieved if the seismic behavior of soil during an earthquake is accurately predicted. Numerical methods, accompanied by advanced constitutive models that have been validated in the past for liquefaction analysis, are able to achieve such a prediction.

The primary objective of this research is to study the seismic behavior of waterfront slopes consisting of liquefiable sands in the Fraser River Delta and to assess the performance and effectiveness of liquefaction countermeasures for such slopes within the framework of the LRI project, based on numerical simulations. The numerical model used in this study is the multi-yield plasticity soil constitutive model, implemented in the finite element code Dynaflo. Other objectives followed in this research along with the

main one include: 1) calibrating and validating the numerical model to be used for liquefaction analysis in the Fraser River Delta, 2) studying the boundary effects caused by a rigid centrifuge container used in LRI on the seismic behavior of waterfront slopes, and 3) studying the effects of incomplete saturation on the sand seismic behavior within the process of numerical model calibration.

The first step in this research is to calibrate the multi-yield plasticity soil constitutive model for Fraser River sand, and to validate the model based on the results of the LRI centrifuge test series. Therefore, this research presents in detail the procedures used for calibrating and validating the presented numerical model. Effects of incomplete saturation on the sand seismic behavior are also studied in this step.

The second step in achieving the main objective of this research is to use the validated numerical model and extend the scope of the LRI centrifuge experiments for mitigation studies. This is desirable since the cost of centrifuge modeling is remarkably higher than that of numerical simulations. As the rigid container used in the LRI centrifuge experiments can significantly influence the slope seismic behavior, considerations regarding the effects of centrifuge rigid boundaries are presented along with the study on the effectiveness of liquefaction countermeasures, to investigate the scope and applicability of the LRI centrifuge tests for practical purposes.

Finally, a summary of numerical studies on the performance and effectiveness of different seismic liquefaction countermeasures considered for a waterfront slope in the Fraser River Delta within the framework of the LRI project is presented in this research. The performance of several remediation techniques used in LRI is studied and discussed.

In addition, a feasible mitigation solution is proposed for waterfront slopes with a performance comparable to that of the measures studied in LRI. Furthermore, fragility curves are used to represent the effectiveness of different remediation techniques at different earthquake intensities. It is shown that the effectiveness of liquefaction countermeasures strongly depends upon the level of seismic intensity.

Acknowledgements

The author would like to express his sincere appreciation to his supervisor, Dr. Radu Popescu, for his patience, helpful comments, and guidance throughout the course of this research. The author is also indebted to the other members of his supervisory committee, Dr. Ryan Phillips and Dr. Majid Abedinzadegan Abdi, for their valuable comments, which undoubtedly boosted the quality of this research.

The financial support provided by Natural Sciences and Engineering Research Council of Canada (NSERC) as part of a Liquefaction Remediation Initiative (LRI) and Grant No. RG203795-02 is gratefully acknowledged. The Graduate Fellowship provided by the School of Graduate Studies, Memorial University, is also acknowledged.

The author is thankful to Professor Jean H. Prevost at Princeton University for providing the finite element code Dynaflow, to Professor P. M. Byrne for discussion and result analysis and to Professor Byrne's collaborators at the University of British Columbia for providing laboratory test results on Fraser River sand, and again to Dr. R. Phillips and his team at C-CORE for providing the results of centrifuge experiments.

My unbounded thanks go to my devoted parents who have taught me to attain my goals through patience, perseverance and diligence. I am pleased to acknowledge their support, encouragement, and kindness during the course of my life.

Finally, I thank God who loves all human beings and provides me with hope to seek a brighter future and serve humanity.

Table of Contents

Abstract	iii
Acknowledgements	vi
Table of Contents	vii
List of Tables	x
List of Figures	xi
List of Abbreviations	xvi
List of Symbols	xvii
Chapter 1- Introduction	1
1.1 Liquefaction Remediation Initiative (LRI).....	1
1.2 Research objectives.....	3
1.3 Thesis outline.....	5
Chapter 2 - Literature review	6
2.1 Introduction.....	6
2.2 Soil liquefaction and conventional method of analysis.....	6
2.3 Finite element analysis of soil liquefaction.....	10
2.3.1 General view.....	10
2.3.2 Considerations related to liquefaction analysis.....	13
2.4 Constitutive models for liquefiable soils.....	14
2.4.1 General considerations.....	14
2.4.2 Modeling soil liquefaction phenomenon.....	17
2.5 Calibration of numerical models.....	19
2.6 Validation of numerical models.....	26
2.7 Mitigation of liquefaction hazards.....	30
2.7.1 General considerations.....	30
2.7.2 Concept and various measures of liquefaction remediation.....	32
2.7.3 Performance of the improved ground.....	36
2.7.3.1 Practical assessment of the performance of remediation measures.....	36
2.7.3.2 Effects of size and location of remediation measures.....	37
2.7.3.3 Centrifuge study on the performance of different remediation measures.....	41
2.7.3.4 Numerical simulations of the centrifuge tests described by Adalier et al. (1998).....	47
2.8 Effects of impermeable (barrier) layers on liquefaction potential.....	49
2.9 Liquefaction potential of nearly saturated soils.....	52
2.9.1 Experimental observations.....	52
2.9.2 Theoretical studies.....	56
Chapter 3 - Numerical Model	59

3.1 Introduction	59
3.2 Coupled field equations implemented in Dynaflo	61
3.3 Multi-yield plasticity soil constitutive model	63
3.3.1 <i>Description and basic relations</i>	63
3.3.2 <i>Constitutive parameters of the multi-yield plasticity soil model</i>	67
3.4 A constitutive formulation for nearly saturated liquefiable sands	68
3.4.1 <i>Assumptions</i>	68
3.4.2 <i>Physical laws used in the proposed constitutive formulation</i>	69
3.4.3 <i>Compressibility of pore fluid</i>	72
3.4.4 <i>Conservation of mass</i>	73
3.4.5 <i>Transient air dissolution</i>	78
3.4.6 <i>Limit of air dissolution</i>	85
3.4.7 <i>Model constants and parameters</i>	86
3.4.8 <i>Model evaluation based on cyclic triaxial tests</i>	88
3.4.9 <i>Scope and limitations of the proposed formulation</i>	94
3.5 Concluding note	98
Chapter 4 - Calibration of the numerical model	100
4.1 Introduction	100
4.2 Numerical model calibration	105
4.2.1 <i>Constitutive parameters for Fraser River sand</i>	105
4.2.2 <i>Calibration of other soil materials used in centrifuge experiments</i>	117
4.3 Class A predictions for tests CT4 and CT6 to CT8	120
4.3.1 <i>Test CT4: Slope with a drainage dyke</i>	121
4.3.2 <i>Test CT6: Uniform loose sand slope without toe</i>	124
4.3.3 <i>Test CT7: Similar to test CT6 with an inclined silt layer</i>	127
4.3.4 <i>Test CT8: Similar to test CT7 but mitigated by three drainage dykes</i>	127
4.4 Discussions	132
4.4.1 <i>Effects of incomplete saturation on the predicted behavior of test CT2</i>	132
4.4.2 <i>Effects of sample preparation method</i>	140
4.4.3 <i>Evolution of pore water pressure after the earthquake</i>	142
4.4.4 <i>Boundary effects due to rigid box</i>	142
4.4.5 <i>Limitations of the numerical model</i>	147
4.5 Concluding note	148
Chapter 5 - Seismic behavior and mitigation of slopes	150
5.1 Introduction	150
5.2 Boundary effects in centrifuge modeling of waterfront slopes	151
5.2.1 <i>Case 1: Modeling deep loose sand</i>	153
5.2.2 <i>Case 2: Modeling deep dense sand underlying loose sand</i>	155
5.3 Study on waterfront slope liquefaction countermeasures	160
5.3.1 <i>Decision on the size of the FE domain for mitigation studies</i>	160
5.3.2 <i>Performance of the improved slope</i>	167
5.4 Effectiveness of different mitigation measures	174

5.5 Concluding remarks	183
Chapter 6 - Conclusions	186
6.1 Summary and concluding remarks	186
6.2 Original contributions	188
6.3 Suggestions for future studies	189
References	191
Appendix A- FE meshes and boundary conditions	207
Appendix B- CD ROM including numerical predictions	210

List of Tables

Table 2.1 Correlations for low-strain shear modulus and Young's Modulus.....	22
Table 2.2 Correlations for Poisson's ratio.	23
Table 2.3 Correlations for power exponent.	23
Table 2.4 Correlations for hydraulic conductivity.....	24
Table 2.5 Correlations for phase transformation angle (dilation angle).	25
Table 2.6 Correlations for angle of internal friction.	25
Table 2.7 Correlations for coefficient of lateral earth pressure at rest.....	26
Table 2.8 Scaling factors in centrifuge modeling.	30
Table 2.9 Various liquefaction countermeasures (after Ferritto et al., 1999).	34
Table 2.10 Specifications of Ottawa sand samples used for cyclic triaxial tests (curtailed and modified from Grozic et al., 2000).....	54
Table 3.1 Parameters of the multi-yield plasticity soil constitutive model.....	68
Table 3.2 Assumed set of soil constitutive parameters for Toyoura sand at $D_r = 40\%$	91
Table 3.3 Quantitative comparisons between the numerical and experimental results. ...	94
Table 4.1 Specifications of the LRI centrifuge experiments.	103
Table 4.2 Constitutive parameters of different soil materials.....	106
Table 5.1 Quantitative comparison of the performance of different mitigation measures (C_v , C_h , and W_h are the computed maximum values corresponding to the crest settlement, crest horizontal displacement and horizontal displacement of the soil wedge relative to the soil below the silt layer.)	170

List of Figures

Figure 2.1 Comparison of settlements in two different sites after 1995-Hyogooken-Nanbu Earthquake (Redrawn based on the information from Bardet et al., 1997).	37
Figure 2.2 Geometry and material specifications in the study by Riemer et al. (1996) (modified from Cooke, 2000).	38
Figure 2.3 Effects of the size of soil improvement in the study by Riemer et al. (1996) (modified from Cooke, 2000).	39
Figure 2.4 Effects of the location of the treated zone in the study by Riemer et al. (1996) (modified from Cooke, 2000).	39
Figure 2.5 Shaking table tests studied by Yanagihara et al. (1991) (modified from Cooke, 2000).	41
Figure 2.6 Different mitigation configurations studied by Adalier et al. (1998) (modified from Adalier et al., 1998: Not to scale).	43
Figure 2.7 Displacements of models 1, 2, and 3 (after Adalier et al., 1998: Not to scale).	45
Figure 2.8 Displacements of models 4 and 5 (after Adalier et al., 1998: Not to scale). ...	46
Figure 2.9 Shaking table tests performed by Kokusho (modified from Kokusho, 1999).	51
Figure 2.10 Deformed shaped of the models studied by Kokusho (1999) during shaking (left) and after shaking (right): Case a) with silt arc; Case b) without silt arc (modified from Kokusho, 1999).	51
Figure 2.11 Triaxial cyclic resistance ratio, CRR, versus number of cycles to liquefaction for unsaturated samples of Ottawa sand. (after Grozic, 2003).	54
Figure 2.12 Cyclic resistance ratios versus number of cycles to liquefaction corresponding to different unsaturated sand samples provided by a) Sherif et al. (1977), b) Yoshimi et al. (1989), c) Xia and Hu (1991), and d) Ishihara et al. (2001). (Figure modified from Yang et al., 2004).	55
Figure 2.13 Initial and final pressure and volume conditions assumed by Hilf in his analysis (after Grozic et al., 2005).	58
Figure 3.1 Main features of the multi-yield plasticity soil constitutive model. The Drucker-Prager type surfaces are shown in this figure (after Popescu, 1995).	66
Figure 3.2 Schematic presentation of a typical round cornered Mohr-Coulomb type yield surface.	67

Figure 3.3 Variation of pore fluid bulk modulus ratio, B_v/B_w , due to changes in the soil degree of saturation for two different absolute pore pressures.	73
Figure 3.4 Variation of saturation pressure versus initial soil degree of saturation for different initial absolute pore pressures at a temperature of 20° C.	77
Figure 3.5 Single air bubble model used to compute the transient mass fraction of the dissolved air in water.	79
Figure 3.6 The finite element mesh used in this study for simulating the cyclic triaxial tests conducted by Tsukamoto et al. (2002).	92
Figure 3.7 Calibration and validation of the proposed constitutive model for nearly saturated Toyoura sand at 40% relative density based on the numerical simulations of the cyclic triaxial tests performed by Tsukamoto et al. (2002).	93
Figure 3.8 Upper and lower bounds as well as model predictions of the excess pore pressure ratios at $B = 0.2$ (i.e., for a $CRS = 0.2$ and an initial degree of saturation equal to 98.54%).	95
Figure 3.9 Predicted excess pore pressure ratios at different degrees of saturation and different cyclic stress ratios based on the laboratory experiments by Tsukamoto et al. (2002).	95
Figure 3.10 Effects of frequency of cyclic loading on the liquefaction strength of 40% relative density Toyoura sand at $S_0 = 98\%$ and $CSR = 0.2$	98
Figure 4.1 Layouts of the LRI centrifuge experiments: a) slope geometry and instrumentation layout in tests CT1 to CT4 (from EIDMSL, 2003), b) slope geometry in tests CT5 to CT8, c) instrumentation layout in tests CT5 and CT8, and d) instrumentation layout in tests CT6 and CT7. All dimensions are in meters.	102
Figure 4.2 a) Original (unfiltered) seismic acceleration time history, b) filtered acceleration time history used as the target base input motion in the LRI centrifuge experiments. Filtered motion A2475 was used in experiments CT1 to CT4. Filtered and amplified motion 2 x A2475, shown here, was used in experiments CT5 to CT8, c) Fourier transforms of the acceleration time histories shown in Figures 4.2a and 4.2b. .	104
Figure 4.3 Liquefaction strength analysis: a) Experimental and numerical liquefaction strength curves for Fraser River sand b) recorded and predicted effective vertical stress vs. number of cycles for set 1 of soil parameters, and c) experimental and numerical stress paths corresponding to Figure 4.3b.	111
Figure 4.4 Predicted contours of maximum shear strain and deformed shapes at the end of analysis in test CT2 using (a) set 1 of soil parameters, and (b) set 2 of soil parameters.	116
Figure 4.5 Test CT2: Recorded vs. predicted (sets 1 and 2) time histories at locations a) LVDT2, b) EPP2, and c) EPP7 (IEVS = initial effective vertical stress at EPP transducer location).	118

Figure 4.6 Test CT2: Recorded vs. predicted acceleration time histories at location ACC7 (sets 1 and 2 of soil parameters).	119
Figure 4.7 Test CT4: a), b), and c): Recorded vs. predicted (class A and class C) time histories at locations LVDT2, EPP2, EPP7, respectively, and d) predicted maximum shear strain contours at the end of analysis. (IEVS = initial effective vertical stress at EPP transducer location).....	123
Figure 4.8 Recorded vs. predicted acceleration time histories in test CT4 at location ACC7.	124
Figure 4.9 Test CT6: a), b), and c): Recorded vs. predicted (class A and class C) time histories at locations LVDT3, EPP5, EPP7, respectively, and d) predicted maximum shear strain contours at the end of analysis. (IEVS = initial effective vertical stress at EPP transducer location).....	125
Figure 4.10 Recorded vs. predicted acceleration time histories in test CT6 at location ACC7.	126
Figure 4.11 Test CT7: a) Recorded vs. predicted (class A and class C) time histories at location LVDT3, b) predicted time histories at location EPP5 (no record available), c) recorded vs. predicted time histories at location EPP7, and d) predicted maximum shear strain contours at the end of analysis.(IEVS = initial effective vertical stress at EPP transducer location).....	128
Figure 4.12 Recorded vs. predicted acceleration time histories in CT7 at location ACC7.	129
Figure 4.13 Test CT8: a), b), and c) Recorded vs. predicted (class A and class C) time histories at locations LVDT3, EPP5, EPP7, respectively, and d) Predicted maximum shear strain contours at the end of analysis. (IEVS = initial effective vertical stress at EPP transducer location).....	131
Figure 4.14 Recorded vs. predicted acceleration time histories in test CT8 at location ACC7.	132
Figure 4.15 Predicted contours of excess pore water pressure ratios during and after the end of earthquake in tests CT7 and CT8.....	134
Figure 4.16 Predicted excess pore pressure ratio time histories at location EPP2 for different degrees of saturation.	135
Figure 4.17 Predicted excess pore water pressure ratio contours at $t = 12s$ after the beginning of the earthquake for different degrees of saturation.	137
Figure 4.18 Predicted Maximum shear strain contours and deformed shape of the slope at the end of shaking for different degrees of saturation. Deformation magnification factor = 1.....	138
Figure 4.19 Predicted vertical displacement time histories at locations LVDT1, LVDT2, and LVDT4 for different initial degrees of saturation.	139

Figure 4.20 Recorded excess pore water pressure ratio time histories in test CT7 at locations a) EPP4, and b) EPP7. (IEVS = initial effective vertical stress at EPP transducer location).	144
Figure 4.21 Test CT7: Comparisons of the predicted excess pore water pressure ratio time histories using the original FE mesh and FE mesh extensions #1 and #2 at locations a) EPP4, b) EPP5 and c) EPP7, respectively. Mesh extensions 1 and 2 correspond to 25 m and 50 m extension of the original FE mesh analysis domain from both sides. (IEVS = initial effective vertical stress at EPP transducer location).....	145
Figure 4.22 Comparison of the recorded and predicted crest settlement time histories in test CT7 for the original FE mesh and extensions # 1 and # 2.	147
Figure 4.23 Predicted contours of the maximum shear strains at the end of analysis in test CT7 using, a) the original FE mesh, b) extension # 1, and c) extension # 2.	147
Figure 5.1 Layout of the waterfront slope analyzed in this study a) In the LRI centrifuge experiment CT7 performed using a rigid container (dimensions at the prototype scale), b) In FE analyses with extended domains in downward (denoted by Z), and lateral (denoted by L) directions.	152
Figure 5.2 Submerged slope underlain by loose sand to great depth: Contours of maximum shear strains and deformed shapes at the end of analyses ($t = 42.6s$) for different FE mesh extensions in depth corresponding to $L = 75$ m (see Figure 5.1b); a) $Z = 0$, b) $Z = 8m$, c) $Z = 16m$, and d) $Z = 24m$. In this figure the deformed shape magnification factor is 3.	154
Figure 5.3 Submerged slope underlain by loose sand to great depth: Computed displacements at different locations at the end of each analysis ($t = 42.6s$) for a range of FE mesh extensions (denoted by L and Z in Figure 5.1b) a) crest settlement, b) crest horizontal displacement.	156
Figure 5.4 Submerged slope underlain by dense sand to great depth: Contours of maximum shear strains and deformed shapes at the end of each analysis ($t = 42.6s$) for different FE mesh extensions in depth corresponding to $L = 75$ m (see Figure 5.1b) a) $Z = 0$, b) $Z = 8m$, c) $Z = 16m$, and d) $Z = 24m$. In this figure the deformed shape magnification factor is 1.	159
Figure 5.5 Submerged slope underlain by dense sand to great depth: Computed displacements at different locations at the end of each analysis ($t = 42.6$ s) for a range of FE mesh extensions (denoted by L and Z in Figure 5.1b) a) crest settlement, b) crest horizontal displacement.	161
Figure 5.6 Computed displacements at the end of each analysis ($t = 42.6s$) at key points in the slope as a function of mesh extension in depth with dense sand, Z, using a set of base input accelerations obtained from scaling the event 2 x A2475 by different factors that result in similar Arias intensities at point A shown in Figure 5.1a. The results correspond to a lateral FE analysis domain extension represented by $L = 75m$ (see Figure 5.1b).	166

Figure 5.7 Computed displacements at key points of the slope at the end of each analysis (t = 42.6s) versus parameter L in case of Z = 0 (i.e., only lateral extension of the FE analysis domain). Event 2 x A2475 was used as the base input acceleration.....	167
Figure 5.8 Layouts of different mitigation configurations studied a) drainage or dense dykes similar to the measures used in the LRI centrifuge experiments, and b) a 6-m deep sheet pile (sheet pile section from TXI Chaparral Steel, 2003 with modifications).....	169
Figure 5.9 Computed contours of the maximum shear strains and deformed shapes (deformation magnification factor = 3) at the end of each analysis (t = 42.6s) corresponding to the mitigation measures listed in Table 5.1.	171
Figure 5.10 Computed contours of the excess pore water pressure ratio at the end of each analysis (t = 42.6s) corresponding to the mitigation measures listed in Table 5.1.....	172
Figure 5.11 Computed maximum displacements for a range of Arias intensities and corresponding to different mitigation measures: a) crest settlement, b) crest horizontal displacement. The horizontal lines on figures represent displacement thresholds used for constructing fragility curves.	176
Figure 5.12 An illustrative example regarding the construction of a fragility curve. The data shown in the figure correspond to the relative horizontal displacement of the soil wedge in case of mitigation measure M4, i.e., 6-m deep sheet pile. a) depending upon whether or not the computed displacement exceeds the assumed threshold (0.5m), the corresponding probability level is assigned 1 (in case of exceedance) or 0 (in case of non-exceedance) as shown in the figure, b) fitting a shifted log-normal probability distribution function for the points shown in Figure 5.12a.	180
Figure 5.13 Fragility curves illustrating the effectiveness of different mitigation measures expressed at different Arias intensities: a) crest settlement b) crest horizontal displacement).	181
Figure A.1 The finite element mesh used in numerical class A and class C predictions of the LRI centrifuge tests CT1 to CT4.....	208
Figure A.2 The finite element mesh used in numerical class A and class C predictions of the LRI centrifuge tests CT5 to CT8.....	208

List of Abbreviations

ACC: Accelerometer
AP: Air pluviation
BEM: Boundary element method
BPT: Becker penetration test
BVP: Boundary value problem
CPT: Cone penetration test
EIDMSL: Earthquake Induced Damage Mitigation from Soil Liquefaction
ESB: Equivalent shear beam
FDM: Finite difference method
FEM: Finite element method
FRD: Fraser River Delta
FRS: Fraser River sand
LRI: Liquefaction Remediation Initiative
LVDT: Linear variable differential transformer
MUN: Memorial University of Newfoundland
NCEER: National Center for Earthquake Engineering Research
NSERC: Natural Sciences and Engineering Research Council of Canada
NSF: National Science Foundation
ODE: Ordinary differential equation
PDE: Partial differential equation
SPT: Standard penetration test
UBC: University of British Columbia
USBR: US Bureau of Reclamation
USACE: US Army Corps of Engineers
VELACS: Verification of Liquefaction Analysis by Centrifuge Studies
WP: Water pluviation

List of Symbols

English Symbols

- a : Radius of the representative air bubble
- a_0 : Initial radius of the representative air bubble
- a_c : Coordinate of the yield surface center in the deviatoric stress space
- a_F : Radius of the representative air bubble at the end of each time interval
- a_g : Ground acceleration
- a_I : Radius of the representative air bubble at the beginning of each time interval
- a_{max} : Peak horizontal acceleration
- a^s : Solid acceleration
- a_t : Attraction ($c/tg\phi$)
- A : Interface area between air and water phases
- A_b : Surface of the representative air bubble (interface area)
- b : Assumed external boundary of water surrounding the representative air bubble
- b_f : Body force
- B : Skempton's pore pressure coefficient (B-value)
- B_s : Bulk modulus of the soil skeleton
- B_{s0} : Low-strain bulk modulus of the soil skeleton at a reference confining stress p_0
- B_v : Equivalent bulk modulus of pore fluid
- B_w : Bulk modulus of water
- c : Cohesion
- C : Concentration of the dissolved air in water
- C_b : Concentration at $r = b$
- C_h : Maximum crest horizontal displacement
- C_I : Concentration at the beginning of each time interval
- C_s : Concentration at the interface between air and water
- C_u : Uniformity coefficient
- C_v : Maximum crest settlement
- CSR : Cyclic stress ratio
- CRR : Cyclic resistance ratio
- $CRR_{7.5}$: Cyclic resistance ratio corresponding to an earthquake with a magnitude of 7.5
- D : Coefficient of diffusion
- D_{10} : Effective grain size
- D_{20} : The particle size corresponding to 20% finer (by weight) obtained from grain size distribution
- D_{50} : Mean particle size
- D_r : Sand relative density
- e : Void ratio
- e_{max}, e_{min} : Maximum and minimum void ratios
- E : Integration constant

E_0 : Modulus of elasticity
 f : Frequency
 f_y : Yield function
 f_z : Scaling factor for the base input motion at depth Z beneath the centrifuge box base
 FS : Factor of safety
 g : Acceleration of gravity
 $g(\theta)$: A function determining the cross section of the yield surface on deviatoric plane
 G : Low-strain shear modulus
 G_0 : Low-strain shear modulus at a reference confining stress p_0
 G_{max} : Initial sand shear modulus
 h : Volumetric coefficient of solubility of gas into water
 H : Henry's constant
 I : Arias intensity
 I_z : Arias intensity at a specific point within the soil medium obtained from applying the base input motion at depth Z beneath the centrifuge box base
 \bar{J}_2 : Second invariant of the stress tensor, \bar{s}
 \bar{J}_3 : Third invariant of the stress tensor, \bar{s}
 k : Hydraulic conductivity
 k_0 : Coefficient of lateral earth pressure at rest
 k_s : Size of the yield surface
 K_α : Correction factor for the effect of static shear stress on liquefaction susceptibility
 K_σ : Correction factor for the effect of overburden pressure on liquefaction susceptibility
 L : A parameter representing finite element mesh extensions in lateral directions
 m_a : Molecular mass of air
 m_d^* : Transient dissolved air mass fraction with respect to M_{max}
 m_i^* : Transient dissolved air mass fraction with respect to the initial mass of free air
 m_{id}^* : Transient dissolved air mass fraction at the beginning of each time interval
 m_{if}^* : Transient dissolved air mass fraction at the end of each time interval
 m_w : Molecular mass of water
 M_{b0} : Initial mass of the representative air bubble
 M_{bt} : Transient mass of the representative air bubble dissolving in water
 M_{da} : Mass of air dissolved in water at equilibrium condition
 M_{fa} : Mass of free air in the air-water mixture
 M_k : Material parameter determining the shape of failure surface
 M_{max} : Maximum mass of free air that can be dissolved in water due to a pressure change
 M_t : Transient mass of air dissolving in water
 M_w : Mass of water
 MSF : Magnitude scaling factor

n : Number of moles
 n_p : Power exponent
 n^w : Porosity
 n_0^w : Initial porosity
 N : Number of cycles to liquefaction
 N_{SPT} : Standard penetration resistance
 p : Effective mean normal stress
 \bar{p} : Difference between the mean stress and attraction ($\bar{p} = (p - a_c)$)
 p_0 : Reference confining stress
 p_a : Atmospheric pressure
 p^w : Pore fluid pressure (gauge pressure)
 \mathbf{P} : Symmetric second order tensor representing the direction of plastic deformations
 q_c : CPT cone tip resistance
 Q : An auxiliary variable containing the proposed model parameters
 r : Radial position
 r_d : Stress reduction factor
 R : Universal gas constant
 RU : Excess pore water pressure ratio
 s : Deviatoric stress tensor
 \bar{s} : Transformed deviatoric stress tensor ($\bar{s} = s - \bar{p} a_c$)
 S : Degree of saturation
 S_0 : Initial degree of saturation
 S_{low} : Lower bound of the soil degree of saturation
 S_{up} : Upper bound of the soil degree of saturation
 t : Time
 T : Absolute temperature
 T_e : Total earthquake duration
 U : Absolute pore pressure
 U_0 : Initial absolute pore pressure
 U_a : Absolute pressure of the air phase
 U_F : Absolute pore pressure at the end of each time interval
 U_{g0} : Initial absolute gas pressure
 U_I : Absolute pore pressure at the beginning of each time interval
 U_{sat} : Saturation pressure
 U_w : Absolute pressure of the water phase
 v^s (v^w): Solid (fluid) velocity
 V : Volume
 V_a : Volume of the air phase
 V_{a0} : Initial volume of the air phase in soil
 V_b : Volume of the representative air bubble

V_{b0} : Initial volume of the representative air bubble
 V_w : Volume of water
 W_h : Maximum relative horizontal displacement of the soil wedge above the silt layer
 x : Mole fraction of the dissolved air in water at equilibrium condition
 X_{pp} : Dilation parameter
 z : A change of variable as a function of time(t) and position(r)
 Z : A parameter representing finite element mesh extensions in downward direction

Greek Symbols

α, β : Auxiliary variables
 γ_w : Unit weight of fluid
 δ : Kronecker delta tensor
 Δn^w : Change in porosity
 Δt : Time interval
 ΔU_g : Change in absolute gas pressure
 ε_{dev}^{max} : Maximum deviatoric strain
 η : Mobilized stress ratio
 $\bar{\eta}$: Normalized stress ratio
 η_ψ : Mobilized stress ratio corresponding to the phase transformation angle, ψ .
 λ : A proportionality coefficient related to the radius of the representative air bubble
 ν : Poisson's ratio
 ρ_s : Solid mass density
 ρ_w : Mass density of water
 τ_h : Cyclic shear stress amplitude
 $\frac{\tau_h}{\sigma_v}$: CSR in cyclic simple shear tests
 σ_c : Initial confining stress
 σ_d : Cyclic deviatoric stress
 $\frac{\sigma_d}{2\sigma_c}$: CSR in cyclic triaxial tests
 σ'^s : Solid (effective) stress
 σ_v : Initial effective vertical stress
 σ_{v0} : Total vertical stress
 σ'_{v0} : Effective vertical stress
 ϕ : Friction angle
 ψ : Dilation angle (phase transformation angle)
 Ω : Transient solubility parameter

Chapter 1- Introduction

1.1 Liquefaction Remediation Initiative (LRI)

During past earthquakes liquefaction has caused a large number of disastrous effects including severe damage to many structures resulting in loss of human life and drastic economic losses all over the globe (e.g., Bardet et al., 1997; EIDMSL, 2003; Ferritto, 1997; and Seed et al., 2003). Various soil improvement techniques are employed to reduce the risk of soil failure caused by liquefaction. Optimization of such remediation methods may lead to great savings in investments without loss of effectiveness.

The Fraser River Delta in British Columbia, Canada, is highly prone to liquefaction hazards, and millions of dollars are spent annually to reduce the detrimental consequences of soil liquefaction in this region (EIDMSL, 2003). In this respect, Natural Sciences and Engineering Research Council of Canada (NSERC) sponsored a Liquefaction Remediation Initiative (LRI), to study and optimize a series of liquefaction remediation measures for the Fraser River Delta by means of centrifuge experiments and numerical modeling.

The NSERC sponsored Liquefaction Remediation Initiative (LRI) included laboratory soil tests for estimating the geomechanical properties of Fraser River sand, eight centrifuge experiments (tests CT1 to CT8) conducted on waterfront slopes made of Fraser River sand with different configurations to assess the performance of various soil liquefaction countermeasures, and numerical modeling for calibrating numerical procedures used for liquefaction analysis. The primary goal of the LRI project was to

optimize soil improvement methods for liquefaction hazards. Short term benefits of this study include great savings in the amount and extent of the soil treatment methods, and in the long run it is expected to result in the saving of lives as well as minimizing damages to structures in the event of a major earthquake (EIDMSL, 2003).

The LRI laboratory soil tests were performed at the University of British Columbia (UBC). The centrifuge experiments were conducted at C-CORE using a rigid box and a centrifugal acceleration of 70g. A Ph.D. student conducted research at C-CORE to perform the LRI centrifuge experiments and to study the effects of mitigation measures on waterfront slopes (EIDMSL, 2003; and Tu, 2003). There has been a close collaboration between the present research and the research performed at C-CORE on dynamic centrifuge experiments.

Two different methods were used for the LRI numerical modeling: one at UBC based on the finite difference code FLAC (Itasca Consulting Group Inc., 2000), and other at Memorial University of Newfoundland (MUN) based on the finite element code Dynaflo (Prevost, 2002). The numerical predictions were class A predictions, i.e., they were performed and submitted prior to conducting the relevant centrifuge experiments (EIDMSL, 2003). Non-academic partners such as consulting firms joined this initiative to comment on the soil conditions and suggest mitigation solutions.

1.2 Research objectives

The present research focuses on numerical modeling of liquefaction countermeasures for waterfront slopes in the Fraser River Delta within the framework of the LRI project. The numerical model used in this study is the multi-yield plasticity soil constitutive model (Prevost, 1985a) implemented in the finite element code Dynaflow (Prevost, 2002) that has been repeatedly validated in past for liquefaction analysis (e.g., Popescu and Prevost, 1993). The main objective of this study follows the primary goal of the LRI project to optimize remediation techniques for waterfront slopes in the Fraser River Delta. Optimization of waterfront slope liquefaction countermeasures requires assessment of their effectiveness at different levels of seismic intensity. Consequently, the main objective of this research is to study the effectiveness and performance of different liquefaction remediation techniques for waterfront slopes in the Fraser River Delta.

The first step in attaining the main objective of this research is to calibrate and validate the numerical model used in this study. Therefore, this research presents in detail the numerical model calibration procedure based on the results of laboratory soil tests, information from the literature and results of the first three LRI centrifuge experiments. The numerical model validation is also presented in this research based on comparing the numerical predictions of the LRI centrifuge experiments with their experimental counterparts (GEOSIM, 2001). Effects of incomplete sand saturation were also studied in this thesis within the process of model calibration since these effects could be quite important both in field and in centrifuge models and could cause discrepancies between the numerical and experimental results.

As mentioned in Section 1.1, a rigid container was used in the LRI centrifuge experiments. This can significantly influence the slope seismic behavior, particularly in the vicinity of lateral boundaries. Therefore, the boundary effects caused by the rigid container used in LRI are also studied along with the study on liquefaction countermeasures to investigate the scope and applicability of the LRI centrifuge tests for practical purposes.

To achieve the main objective of this research, the performance of different mitigation measures considered in LRI for waterfront slopes is studied and presented in this research. In addition, a feasible mitigation solution is suggested for waterfront slopes with a performance comparable to that of soil improvement methods used in the LRI centrifuge experiments. The research also includes the results of a comparative study on the effectiveness of different liquefaction remediation techniques at different earthquake intensities. Fragility curves are used to represent the effectiveness of different liquefaction countermeasures at different levels of seismic intensity.

The objectives of the present research include:

- Calibrating and validating a state of the art numerical model based on the results of centrifuge experiments, and use it to extend the scope of the LRI centrifuge experiments.
- Studying the effectiveness of different liquefaction remediation techniques at various seismic intensities based on an extensive numerical study.

- Studying the performance of various liquefaction countermeasures within the framework of LRI and suggesting a feasible mitigation solution for waterfront slopes in the Fraser River Delta.
- Investigating the applicability of the LRI centrifuge experiments for practical purposes due to centrifuge boundary effects caused by a rigid container used in the LRI centrifuge experiments.
- Studying the effects of incomplete saturation on the sand seismic behavior within the process of model calibration.

1.3 Thesis outline

This thesis contains six chapters. Objectives of the research have been presented in this chapter. The literature pertinent to this study is reviewed in Chapter 2. Chapter 3 includes the numerical model used in this study and an original constitutive formulation suggested for liquefaction susceptibility of nearly saturated sands. The procedures used for calibrating and validating the numerical model along with the numerical predictions of the LRI centrifuge experiments are presented in Chapter 4. In Chapter 5, seismic behavior and mitigation of waterfront slopes are studied. Concluding remarks, original contributions and suggested future work are presented in Chapter 6.

Chapter 2 - Literature review

2.1 Introduction

In this chapter, the literature corresponding to the fundamental topics and phenomena discussed in this thesis is reviewed. These topics include soil liquefaction, nonlinear finite element analysis of earth structures under seismic loads, constitutive models for liquefiable soils, calibration and centrifuge-based validation of numerical models for soil liquefaction, remediation measures against liquefaction and study of their performance, effects of low-permeability soil layers on the seismic behavior of saturated soil slopes, as well as liquefaction susceptibility of nearly saturated soils. It is not intended in this chapter to discuss all these topics in detail; however, a concise review of each topic is provided to cover the background and references required for pursuing specific phenomena studied in this thesis.

2.2 Soil liquefaction and conventional method of analysis

According to Marcuson (1978), liquefaction is the transformation of a granular material from a solid state to a liquefied state as a consequence of increased pore water pressure and reduced effective stress. In particular, tendency of soils consisting of saturated loose granular materials to compact under shear may result in development of sufficient excess pore water pressure and cause liquefaction (e.g., Seed and Idriss 1982). Soil liquefaction is primarily related to medium to fine grained saturated cohesionless

soils (Das, 1983). However, since liquefaction can be seen in other types of soils (e.g., silt as mentioned by Kramer, 1996), this phenomenon is not limited only to granular materials. Pore pressure buildup may be induced either by static or cyclic loads (Seed, 1976). In this research, soil liquefaction caused by cyclic loads is studied.

During earthquakes loose to medium dense saturated sands may lose their strength. Due to shaking during earthquakes, solid particles of these sands tend to achieve a denser configuration accompanied by reducing the volume of voids. For saturated sands subjected to shaking, if rapid drainage of the pore water is impossible, instead of changing the volume of voids, pore water pressure increases; consequently, the effective stresses between solid particles are reduced. When due to excess pore water pressure buildup the effective stresses between solid particles in the soil skeleton vanish, soil loses its shear strength and behaves like a viscous liquid. In fact, increase in pore water pressure is due to the tendency of granular materials to compact under shear. Loose to moderately dense granular materials with poor drainage conditions such as silty sands or sands containing seams of impermeable sediment subjected to cyclic loads exhibit high potential to liquefaction (Youd et al., 2001). Due to softening of soil during liquefaction, large cyclic deformations can occur. For a loose soil deposit this is accompanied by loss of the soil shear strength that may result in flow failure under moderate to high shear stresses; however, in the case of denser materials, tendency to dilate prevents significant loss of shear strength and condition of cyclic mobility may develop (Youd et al., 2001).

The phenomenon of soil liquefaction has been studied both numerically and experimentally by a large number of researchers all over the globe (e.g., Amini and Duan,

2002; Ishihara, 1984 and 1993; Kammerer et al., 2001; Popescu and Prevost, 1993; and Vaid and Sivathayalan, 1996 and 2000).

Since the occurrence of catastrophic earthquakes in Alaska and in Niigata, Japan in 1964, where most reported damages were related to soil liquefaction in those places, researchers have been trying to introduce a method for evaluating liquefaction susceptibility of soils. Among these attempts, a simple empirical method proposed by Seed and Idriss (1971) has been recognized as the most popular approach for this purpose. This procedure has been developed and modified during the past three decades by the original authors as well as by many other researchers throughout the world. Some of the most recent modifications corresponding to the proposed method can be found in a paper by Youd et al. (2001) as a summary report from the 1996 NCEER and 1998 NCEER/NSF workshops on evaluation of liquefaction resistance of soils.

The simplified procedure initially proposed by Seed and Idriss (1971) is valid for sites with gently sloping or flat ground and for shallow depths. In this method two variables are compared with each other to evaluate the factor of safety against liquefaction. These variables are (1) cyclic stress ratio, CSR , caused by external forces due to earthquake, which directly depends on the magnitude of shaking, and (2) cyclic resistance ratio, $CRR_{7.5}$, which accounts for the liquefaction resistance of soil against an earthquake with magnitude of 7.5. This latter ratio depends on soil specifications, and it can be correlated to the results of different field tests like standard penetration test, SPT (e.g., Seed et al., 1985), cone penetration test, CPT (e.g., Robertson and Wride, 1998) shear wave velocity, (e.g., Andrus and Stokoe, 2000) or Becker penetration test, BPT

(e.g., Sy and Campanella, 1994; and Sy et al., 1995). According to the 1998 NCEER/NSF workshop conclusions, CPT is able to provide the most detailed descriptions of soil strata, which should also be confirmed by sampling (Robertson and Wride, 1998). However, based on the soil type and availability of test facilities, other field tests maybe used to evaluate liquefaction susceptibility of soils. A discussion on the advantages, disadvantages and limitations of all these field tests for assessment of liquefaction susceptibility of soils can be found in the paper by Youd et al. (2001).

The factor of safety, FS , against liquefaction is calculated using the following relationship:

$$FS = (CRR_{7.5}/CSR) \cdot MSF \cdot K_{\alpha} \cdot K_{\sigma} \quad (2-1)$$

In this equation, MSF is a correction factor for earthquakes with magnitudes other than 7.5, called magnitude scaling factor. This factor is selected based on the magnitude of earthquake; however, there are some differences among the values of MSF suggested by different investigators (Youd et al., 2001). Factors K_{α} and K_{σ} are applied to consider the effects of initial static shear stress and overburden pressure, respectively. The suggested values for these factors, initially provided by Seed and Harder (1990), seem to be conservative especially for loose sand (Vaid et al., 2001). Boulanger (2002), Vaid et al. (2001), and Harder and Boulanger (1997) provided detailed discussions in this regard. The value of CSR is computed from the equation suggested by Seed and Idriss (1971).

$$CSR = 0.65(a_{max}/g)(\sigma_{v0}/\sigma'_{v0})r_d \quad (2-2)$$

In Equation (2-2), a_{max} is the peak horizontal acceleration, obtained from the earthquake acceleration time history, σ_{v0} and σ'_{v0} are the total and effective vertical stresses, respectively, g is the acceleration of gravity, and r_d is a stress reduction factor, accounting for the deformability of the soil profile as a function of depth (Youd et al., 2001).

2.3 Finite element analysis of soil liquefaction

2.3.1 General view

Two basic categories of methods to analyze boundary value problems (BVP) include analytical and numerical methods. Analytical methods give the exact solutions of boundary value problems, and they are more preferable than numerical approaches. However, using analytical methods is limited only to problems with simple geometries, simple boundary conditions and simple constitutive relationships. Therefore, in case of problems with complicated geometries, boundary conditions, and constitutive behaviors, analytical solutions may not exist, and numerical methods should be applied.

Applying any numerical method to a soil medium requires understanding of three basic parts: (1) the governing differential equation, related to a particular physical phenomenon within the medium, (2) boundary conditions, which force the medium to have a set of certain responses at certain locations, and (3) a constitutive relation, describing the behavior of a certain material under certain conditions. This latter aspect is very important. In fact, in order to reasonably capture the behavior of a material by

means of numerical simulations, introducing a suitable constitutive law is one of the most fundamental steps. This will be discussed later in more detail for soil liquefaction analysis. Major numerical approaches for solving geotechnical problems are the finite element method (FEM), the finite difference method (FDM), and the boundary element method (BEM).

In the finite element method, the solution domain of a problem is idealized by a finite number of smaller solution domains called finite elements. For each finite element, the governing differential equation is approximated within the element using trial functions (or shape functions that define the variation of primary unknowns within the element). The total solution of the problem can be found from solving a global matrix equation, obtained from the assembly of the effects of all finite elements into a global matrix along with imposing boundary conditions. The method has extensively been described in many references (e.g., Bathe, 1982; Cook et al., 1989; Gallagher, 1975; Segerlind, 1976; and Zienkiewicz and Taylor, 1991 and 1989). FEM can be applied to most kinds of boundary value problems with different geometries and boundary conditions.

The finite difference method solves a BVP using approximate mathematical definitions of derivatives for the governing differential equation at different points within the solution domain. This, accompanied by imposing boundary conditions, leads to a system of equations that gives the values of the desired unknowns within the domain. The method is very powerful; however, using FDM for problems with irregular geometries is not easy. In addition, due to the usage of non-central finite difference formulas, approximation errors at the boundaries of the problem are usually higher than those

inside the solution domain. This method has also widely been discussed in many references like Kleiber and Borkowski (1998) or online references such as Weisstein (2006).

Another major numerical method, used in geotechnical engineering, is the boundary element method (BEM). In this approach, the exact solution of a problem should be known at its boundaries. By approximating the boundary of the problem into a number of boundary elements (discretization of the boundary), the solution of the problem at any point inside the domain can be achieved from the assembly of the solutions obtained from each boundary element at that point. This method is also powerful. Due to the ability of the boundary element method to deal with infinite boundaries, the method is widely used in the analysis of underground openings. The difficulty in this method stems from the fact that the fundamental solution for the problem at boundaries should be known in advance; however, this solution is not applicable for highly nonlinear and non-homogenous materials. Detailed description of the method can be found in a number of references such as Crouch and Starfield (1983) and Gao and Davies (2002).

In this research FEM has been used for soil liquefaction analysis. Due to the rapid advances of computer technology in the recent decades, the method has been developed very quickly, and it has found its place as a robust tool for analysis in different areas of science and technology. Like the other numerical methods FEM is a numerical approach to provide approximate solutions for differential equations; however, the fundamental difference between the finite element method and the other numerical solutions such as the finite difference approach can be found in its way of approximation. Unlike finite

difference in which mathematical approximations are used to define the governing differential equation, in finite element analysis the general physics of the problem is approximated in terms of shape functions. In other words, FEM applies physical approximations to the problem, while in FDM mathematical approximations are considered in analysis.

Application of the finite element method in geotechnical engineering began in 1966, when Clough and Woodward used this method for analysis of embankments, and Reyes and Deer showed its application in underground openings (USACE, 1995). Later on, the method has successfully been used for various geotechnical problems (e.g., Desai and Siriwardane, 1984; Naylor et al., 1981; Owen and Hinton, 1980; and Smith, 1982). In recent years, finite element method has been widely used for analysis of soil liquefaction (e.g., Elgamal et al., 2002a and 2002b; Ming and Li, 2003; Peng et al., 2004; Popescu and Prevost, 1993 and 1995; and Yang et al., 2003).

2.3.2 Considerations related to liquefaction analysis

Liquefaction occurs in a medium including a solid phase and a liquid phase; moreover, there is a relation between the soil skeleton strains and the pore fluid pressure (e.g., Popescu et al., in press; and Prevost, 1989). Therefore, single phase equations like diffusion equation for analysis of flow through porous media, or solid phase dynamic equilibrium equation for stress-strain analysis of dry soil deposits, separately, are not able to correctly capture the behavior of the medium (Prevost, 1989). Biot introduced a theory for mechanics of deformation of an elastic porous medium (e.g., Biot, 1962). This theory has been extended into the nonlinear regime (Prevost, 1989). In fact, due to dependence

of the soil skeleton strains and pore fluid pressure on each other, a coupled field analysis should be used for liquefaction problems in which a set of dependent dynamic equilibrium equations (one equation for each phase, which depends upon the dynamic equilibrium equation of the other phase through coupling terms) are solved in a step-by-step manner to accurately capture the soil behavior. Detailed discussion in this regard is provided in Chapter 3 of this thesis.

2.4 Constitutive models for liquefiable soils

2.4.1 General considerations

A constitutive law is a mathematical relationship describing the response of a certain material under certain conditions (Desai and Siriwardane, 1984). Experiments have shown that there is no universal constitutive equation for geotechnical problems. Depending on the nature of the material and loading types, a large number of constitutive equations have been applied to different geologic materials and different boundary value problems. Detailed discussions on different constitutive models in geomechanics can be found in references such as Prevost (1990), Desai and Siriwardane (1984), and Naylor et al. (1981). A summary of this subject and a relatively complete list of references in this regard are given by Prevost and Popescu (1996). They believe the necessary characteristics of a feasible material model are as follows:

- “The model should be complete, i.e., able to make statements about the material behavior for all stress and strain paths, and not merely restricted to a single class of paths (e.g., triaxial or pure shear).
- It should be possible to identify the model parameters by means of a small number of standard or simple material tests.
- The model should be founded on some physical interpretation of the ways in which the material is responding to changes in applied stress or strain (e.g., the material should not be modeled as elastic if permanent deformations are observed upon unloading)”.

The yielding phenomenon and occurrence of permanent strains in soil deposits can be investigated in many situations; therefore, almost all soil constitutive models have been formulated based on the theory of plasticity (e.g., Bathe, 1982; Naylor et al., 1981; and Prevost, 1977 and 1978). In this theory, three fundamental questions should be answered to attain the behavior of the material.

Question 1: Under what conditions does a material begin to yield?

The answer of this question forms a yield criterion for the material. In fact, a yield criterion is a mathematical relationship, called yield function, defining the commencement of plastic straining in the material.

Question 2: Is there any change in the threshold of yielding during the plastic flow of the material? If yes, how does it change with plastic strains?

A law answering this question is called hardening law. If for a material it is assumed that there is no change in the threshold of yielding during plastic flow, the material is called perfectly plastic material.

Question 3: Given a stress state of the material, in what directions do plastic strains take place?

A mathematical rule, which at every state of stress during yielding determines the directions of plastic strains, is called flow rule.

It is prevalent to define the yield function in the principal stress space as a surface called the yield surface. Stress states outside of the yield surface are impossible and those inside are in the elastic range.

Hardening law can be considered as: (1) isotropic hardening, when the yield surface contracts or expands in the stress space, (2) kinematic hardening, when position or orientation of the yield surface changes in the stress space, and (3) local hardening, if any local change occurs in the yield surface. Also, combinations of all these types may occur in some situations.

Flow rule is one of the most challenging concepts in plasticity. In this regard, a function is introduced as the plastic potential function of the material. This function defines a surface in the stress space, called the potential surface, such that any tensor of plastic strain increments is normal to this surface. If potential and yield surfaces are identical, this tensor is also normal to the yield surface. In the latter case it is stated that normality condition is satisfied (Naylor et al., 1981). This type of flow rule, where the vector of the plastic strain increments is associated with the yield surface based on the

normality condition, is called associative flow rule. In general, yield and plastic potential surfaces do not coincide, and the flow rule is non-associative.

2.4.2 Modeling soil liquefaction phenomenon

Recent outcomes obtained from experiments, i.e., centrifuge modeling, shaking tables and undrained cyclic laboratory tests, have significantly developed our understanding of soil liquefaction (e.g., Yang and Elgamal, 2001). In fact, a variety of soil behavioral features like material non-linearity, stress history dependence, shear-induced plastic dilation/compaction, shear stress-induced anisotropy, and hysteretic behavior due to loading, unloading and reloading, should be considered for simulating the behavior of a soil deposit under cyclic loads. Thus, a constitutive model for liquefaction analysis should properly address the above features. Improvements of some of these features have recently been formulated and implemented in constitutive models. For example, implementing the concept of state dependent dilatancy in sand constitutive model (Li and Dafalias, 2000; and Manzari and Dafalias, 1997) enables one to capture different soil response characteristics, i.e., contraction, dilation, cyclic mobility and flow liquefaction within a unified plasticity framework (Yang et al., 2003). Here, two major categories of constitutive models, widely used for liquefaction analysis by researchers in North America, are mentioned.

The first is a constitutive model based on the concept of a ‘field of work hardening moduli’, which was first introduced simultaneously by Mroz (1967) and Iwan (1967). They showed the complex behavior of a material during plastic flow can be simulated by approximating its nonlinear stress-strain curve to a number of linear segments with

constant hardening moduli. This results in defining a series of nested yield surfaces in the stress space. Adopting this concept, Prevost (1985a) developed and introduced his multi-yield plasticity soil model. Use of the multi-yield plasticity concept in soil liquefaction analysis is widely accepted (e.g., Elgamal et al., 2002a; and Popescu and Prevost, 1993). The numerical model used in the present research for liquefaction analysis is the multi-yield plasticity soil constitutive model, implemented in the finite element program, Dynaflow (Prevost, 2002). This model is presented in detail in Chapter 3.

Another prevalent constitutive model for soil liquefaction analysis is called the bounding surface model. According to this model, all the possible stress states of a material are bounded by a surface in the stress space called the bounding surface. Any yielding and plastic flow inside this surface is formulated based on mapping the stress point onto its image on the bounding surface. In fact, within the framework of this model, occurrence of plastic deformation is possible for the stress states inside the bounding surface. At any time, the plastic modulus of the material depends upon the distance from its present stress state to the image of the stress point on the bounding surface. The concept was first introduced by Dafalias and Popov (1975) and later developed by others (e.g., Bardet, 1986). This model has been widely used for soil liquefaction analysis. Detailed discussions on the bounding surface plasticity can be found in a number of references such as Dafalias and Herrman (1980) and Bardet (1986).

Both bounding surface and multi-yield plasticity theories have their own disadvantages including storage limitations for the multi-yield surface theory, and

selection of the evolution law and arbitrariness in the mapping rule for the bounding surface theory (Prevost, 1982a).

2.5 Calibration of numerical models

Calibration of a numerical model is to determine the values of constitutive parameters required for analysis. As mentioned in the previous section, one of the characteristics of a feasible constitutive model is to find its parameters based on the results of conventional laboratory soil tests (Prevost and Popescu, 1996). However, uncertainties due to lack of sufficient information, sampling and testing errors as well as spatial variability of soil parameters, often cause engineers to use the available correlation formulas along with their judgments to reasonably estimate the required soil parameters. In this regard, Kulhawy and Mayne (1990) have collected a large number of correlation formulas and charts for soil parameters. More correlation charts and equations may be found in other references such as US Army Corps of Engineers (USACE, 1992); Popescu (1995); and Prevost and Popescu (1996).

Every constitutive model has its own parameters. However, some of these parameters are common among most models. The following list includes common parameters required to simulate the behavior of sand due to cyclic loads.

- Low-strain elastic shear modulus, G_0 , or Young's modulus, E_0 , at a reference effective mean normal stress, p_0 .
- Poisson's ratio, ν .

- Power exponent, n_p .
- Hydraulic conductivity, k .
- Mass density, ρ_s .
- Porosity, n^w , or void ratio, e .
- Friction angle at failure, ϕ .
- Coefficient of lateral earth pressure at rest, k_0 .
- Phase transformation angle, ψ .

The power exponent, n_p , is used to simulate the dependence of the low-strain shear and bulk moduli, G and B_s , on the effective mean normal stress, p , using the following expressions (e.g., Cubrinovski, and Ishihara, 1998; and Prevost, 1989).

$$G = G_0 \left(\frac{p}{p_0} \right)^{n_p} \quad ; \quad B_s = B_{s0} \left(\frac{p}{p_0} \right)^{n_p} \quad (2-3)$$

where p_0 is the reference effective confining stress and G_0 and B_{s0} are the values corresponding to p_0 . The commonly accepted value of n_p for sands is $n_p = 0.5$ (e.g., Richart et al., 1970).

Also, each constitutive model possesses specific parameters. This will be discussed later in the next chapter for the multi-yield plasticity soil model.

Tables 2.1 to 2.7 include some useful correlation formulas, charts, tables, comments and their corresponding references for the constitutive parameters mentioned above excluding mass density and porosity, which can be obtained in laboratory for a particular soil.

At this point, it is worth mentioning that all constitutive models dealing with soil liquefaction have one or more soil parameters for scaling plastic dilation. In this respect, liquefaction strength curve can be used to calibrate these parameters (dilation parameters). The liquefaction strength curve is a plot of the cyclic stress ratio as a function of the number of cycles necessary to induce initial liquefaction in an undrained cyclic soil test, e.g., cyclic simple shear test or cyclic triaxial test. Dilation parameter can be estimated by back-fitting the liquefaction strength curve using element tests (i.e., liquefaction strength analysis described by Prevost and Popescu, 1996). This is discussed in detail in Chapter 4 for calibrating dilation parameters of the multi-yield plasticity soil constitutive model (Prevost, 1985a) for Fraser River sand.

Table 2.1 Correlations for low-strain shear modulus and Young's Modulus.

Basic relation	Comments	Reference
1. Table: $\frac{E_0}{p_a} = f(\text{state of sand})$	Typical values for all sands	Kulhawy and Mayne (1990)
2. Chart: $G_0 = f(e, \frac{\sigma_3}{p_a})$	Dry sands	Richart et al. (1970)
3. $G_0 = 700 \frac{(2.17 - e)^2}{1 + e} (p_0)^{0.5}$ (kgf/cm ²)	Round Ottawa sand at shear strain level = 10 ⁻⁴ , and for $e < 0.80$	Hardin and Richart (1963)
4. $G_0 = 326 \frac{(2.97 - e)^2}{1 + e} (p_0)^{0.5}$ (kgf/cm ²)	Angular Ottawa sand at a shear strain level = 10 ⁻⁴ (Sharp grains and clay)	Hardin and Richart (1963)
5. $G_0 = 850 \frac{(2.17 - e)^2}{1 + e} (p_0)^{0.44}$ (kgf/cm ²)	Japanese code at a shear strain level = 10 ⁻⁵	Iwasaki and Tatsuoka (1977)
6. $G_0 = 900 \frac{(2.17 - e)^2}{1 + e} (p_0)^{0.4}$ (kgf/cm ²)	Japanese code at shear strain level = 10 ⁻⁶	Iwasaki and Tatsuoka (1977)
7. $G_{max} = 400 p_a \cdot \exp\{1.39 D_r\} (\frac{p_0}{p_a})^{0.43}$	Ticino sand (fine)	Bellotti et al. (1986)

Table 2.2 Correlations for Poisson's ratio.

Basic relation	Comments	Reference
1. $v = 0.1 + 0.3 \frac{(\phi - 25)}{20}$	Cohesionless soils	Kulhawy and Mayne (1990)
2. $v = 0.3$ to 0.4	Dense sand	Kulhawy and Mayne (1990)
$v = 0.1$ to 0.3	Loose sand	

Table 2.3 Correlations for power exponent.

Basic relation	Comments	Reference
1. $n_p = 0.5$	Commonly assumed value	Kardestuncer and Norrie (1987)
2. $n_p = 0.7$	Nevada sand	Popescu and Prevost (1993)
3. $n_p = 0.65$ to 0.75	Ticino sand	Belloti et al. (1986)
4. $n_p = 0.91$ to 0.93 $n_p = 0.74$ to 0.78	Dense sand ($D_r = 77.4\%$) Loose sand ($D_r = 34.4\%$)	Cubrinovski and Ishihara (1998)

Table 2.4 Correlations for hydraulic conductivity.

Basic relation	Comments	Reference
1. Chart: $k = f(\text{soil type})$	Typical values for all soils	Terzaghi and Peck (1967)
2. Chart: $k = f(e, D_{10})$	Sands and gravel mixtures, with comments on gradation	USACE (1994)
3. $k = 1.2C_u^{0.735} D_{10}^{0.89} \frac{e^3}{1+e}$ $D_{10}(\text{mm}), k(\text{cm/s})$	Medium and fine sands	Shahabi et al. (1984)
4. $k = (100-150) D_{10}^2$ $D_{10}(\text{cm}), k(\text{cm/s})$	Sandy soils	Hazen (1930)
5. Table: $k = f(\text{soil type}, D_{20})$	All soils	Creager et al. (1945)

Table 2.5 Correlations for phase transformation angle (dilation angle).

Basic relation	Comments	Reference
1. $\psi = f(D_r, \text{particles shape}, D_{10}, C_u, \text{grain size, types of minerals})$	Single mineral soils	Koerner (1970)
2. $\psi = 30^\circ - 32^\circ$	Different sands. Also, values out of this range exist.	Been and Jefferies (1985)
3. $\psi = 34^\circ$	Fraser River sand	Vaid et al. (2001)

Table 2.6 Correlations for angle of internal friction.

Basic relation	Comments	Reference
1. $\phi = \sqrt{12N_{\text{SPT}}} + 15$	Sands with round grains (uniform size)	Dunhum (1954)
$\phi = \sqrt{12N_{\text{SPT}}} + 20$	Sands with round grains (well graded)	
$\phi = \sqrt{12N_{\text{SPT}}} + 20$	Sands with sharp grains (uniform size)	
$\phi = \sqrt{12N_{\text{SPT}}} + 25$	Sands with sharp grains (well graded)	
2. Chart: $\phi = f\left(D_r, \frac{q_c}{p_a}, \frac{\sigma'_{v0}}{p_a}\right)$	Quartz sands	Robertson and Campanella (1983)
3. Chart: $\phi = f\left(N_{\text{SPT}}, \frac{\sigma'_{v0}}{p_a}\right)$	Cohesionless soils	Schmertmann (1975)
4. Table: $\phi = f(D_r, \text{size, gradation})$	Different sands	USACE (1992)

Table 2.7 Correlations for coefficient of lateral earth pressure at rest.

Basic relation	Comments	Reference
1. $k_0 = 1 - \sin \phi$	NC sands	Jaky (1948)
2. $k_0 = \frac{\sqrt{\left(\frac{\pi}{2}\right)^2 + \tan^2 \phi} - \tan \phi}{\sqrt{\left(\frac{\pi}{2}\right)^2 + \tan^2 \phi} + \tan \phi}$		Ochiai (1977)
3. $k_0 = \frac{\nu}{1 - \nu}$	Inferred from theory of Elasticity	(e.g., Wang, 1953)

2.6 Validation of numerical models

Any numerical model needs to be validated before its extensive usage in real projects. Assessment of a numerical model ensures its ability to predict the behavior of a geologic medium without having knowledge of the results of in-situ or physical model tests. In this respect, comparison of the predicted behavior with in-situ observations provides a basis to judge the performance of a numerical model. For the most parts, due to lack of full-scale observations, it is prevalent to use the results of physical models for comparing with numerical simulations. In geotechnical engineering, centrifuge modeling provides such a base for this comparison.

The behavior of a geomaterial is highly dependent upon its stress history. Consequently, it is desirable to perform experimental investigations on the physical models with similar gravity-induced stresses as in the prototype. To reach such a stress level in a physical model with dimensions N times smaller than those of the corresponding prototype, the model should be subjected to an acceleration with a magnitude N times larger than the acceleration of gravity. This is achieved using centrifuge technology.

According to the Committee of Modeling Techniques in Geomechanics (1999), centrifuge modeling is a technique for simulating the mechanical response of full-scaled geotechnical structures in reduced-scale physical models. The history of centrifuge modeling in geotechnical engineering dates back to the work by Bucky in 1930 (Japanese Geotechnical Society, 1998). Centrifuge technology has been significantly developed and applied for different engineering projects. Detailed discussions related to the concept and applications of centrifuge technology in geotechnical engineering have been provided by Taylor (1995). Some important aspects of the centrifuge modeling and contributions of centrifuge and numerical simulations to each other are discussed here (Zeng, 2001).

There are two obvious differences between a centrifuge model and its corresponding prototype. The first is related to the variations of centrifugal acceleration within the model both in magnitude and in direction. This is due to changes in the radius of a centrifuge within the model and radial nature of the centrifugal force. On the contrary, in the prototype, acceleration of gravity can be considered constant. According to the 1D analysis performed by Schofield (1980), if the depth of a model is one-tenth of the radius

of a centrifuge, the magnitude of the error in vertical stresses is lower than 2%. The second difference between a centrifuge model and the corresponding prototype is related to the effects of artificial boundary walls used in centrifuge modeling, mostly rigid boundaries, that influence the stress distribution in the model and cause discrepancies between the model and prototype responses (Zeng, 2001). Other problems like grain size and conflict in the time scaling for diffusion and dynamic phenomena (see Table 2.8) have also been discussed by many researchers (e.g., Taylor, 1995).

Centrifuge technology is also used for simulating earthquake events and liquefaction phenomenon (e.g., Adalier and Sharp, 2004; Coulter and Phillips, 2003; and Phillips et al., 2004). In recent years, due to development of new actuators and new containers mimicking the dynamic stiffness of the soil being modeled, significant improvements have been made in the area of centrifuge simulation of liquefaction phenomena (Sharp et al., 2000).

One of the major contributions of centrifuge modeling to numerical simulations is validation of numerical models (e.g., Byrne et al., 2004a and 2004b; Elgamal et al., 2002a; and Popescu and Prevost, 1993 and 1995). VELACS (VERification of Liquefaction Analysis by Centrifuge Studies) is an example of such a study aimed at better understanding the mechanisms of soil liquefaction and at collecting data for the verification of different numerical procedures used for analysis of soil liquefaction (e.g., Arulanandan and Scott, 1993 and 1994).

The second contribution of centrifuge modeling to numerical simulations, due to new developments in centrifuge technology and its instrumentations, is reducing uncertainties

in estimating the constitutive parameters for numerical models. In fact, the results of numerical analyses are highly affected by uncertainties in the values of constitutive parameters such as low-strain shear modulus and coefficient of earth pressure at rest. For instance, recent developments in instrumentation techniques, studied at Case Western Reserve University, allow accurate measurements of these parameters, and as a result enhance the ability of numerical models to predict the seismic soil behavior (Zeng, 2001).

Moreover, centrifuge modeling provides a base for calibrating numerical models by means of class C predictions, i.e., analysis of the soil behavior when the results of centrifuge tests are available. This helps reduce the errors in estimating the soil constitutive parameters (e.g., GEOSIM, 2001).

In order to interpret the results of a centrifuge test dynamic similitude considerations and scaling laws are very important. Table 2.8 includes basic scaling factors used in centrifuge modeling (see Taylor, 1995; and Kramer, 1996). As it can be seen in Table 2.8, there is a potential conflict in the time scaling factor for dynamic (pore pressure generation) and diffusion (pore pressure dissipation) events. Usually, this problem is solved using a pore fluid with viscosity N times larger than the viscosity of water in dynamic centrifuge tests.

Table 2.8 Scaling factors in centrifuge modeling.

Quantity	Scaling factors	
	$N = \frac{\text{Prototype Dimension}}{\text{Model Dimension}}$	
	Prototype	Model
Length	1	1/N
Displacement	1	1/N
Stress	1	1
Strain	1	1
Mass	1	1/N ³
Density	1	1
Force	1	1/N ²
Gravity	1	N
Time (diffusion)	1	1/N ²
Time (dynamic)	1	1/N
Frequency	1	N
Acceleration	1	N
Energy	1	1/N ³

2.7 Mitigation of liquefaction hazards

2.7.1 General considerations

Many catastrophic events during the past earthquakes such as loss of human life and severe damage to a large number of structures are related to the soil failure and occurrence of large displacements caused by soil liquefaction (e.g., Bardet et al., 1997; EIDMSL, 2003; Ferritto, 1997; and Seed et al., 2003). Therefore, in order to reduce the detrimental consequences of this phenomenon, liquefaction countermeasures should be taken into account.

In general, it is not recommended to build a structure or a facility in a region highly vulnerable to liquefaction; however, sometimes due to limitations in site selection, structures are built in sites with potentially liquefiable soils.

Regardless of avoiding potentially liquefiable sites, the following measures can be applied to reduce liquefaction hazards (e.g., Ferritto et al., 1999; and Ferritto, 1997):

- Considering liquefaction resistant structural elements in the design and construction of structures.
- Using deep foundations
- Designing containment or encapsulation structures
- Modifying geometry of structures
- Replacing the liquefiable soil deposits with more resistant materials
- Providing drainage systems
- Improving the soil strength characteristics (densification)

The present research focuses on numerical study of the last two options. Unlike other aspects in geotechnical engineering, most of our knowledge of remediation techniques comes from experiences and innovations of different contractors who battle with difficulties encountered in construction projects (Kramer, 1996). In fact, mitigation measures and soil treatment engineering is a vast science including a combination of theory and experience, and it is not possible to discuss it in detail here. Detailed discussion on this subject can be found in a number of references (e.g., Bell, 1993; Bell, 2000; Hausmann, 1990; Kumar, 2001; and Lee et al., 2001); however, a succinct discussion regarding mitigation of soil liquefaction hazards seems to be useful.

2.7.2 Concept and various measures of liquefaction remediation

The concept of mitigation methods against liquefaction can directly be understood from the key phrase in definition of the phenomenon, i.e., increase in excess pore water pressure due to tendency of the soil materials to compact under shear. Therefore, liquefaction hazards can be reduced either by promoting drainage of the soil deposit to prevent excess pore water pressure buildup or by diminishing the tendency of the soil deposit to contract by means of soil densification.

In the densification technique, applying compaction energy, absorbed by ground, results in permanent volume changes in a soil deposit; consequently, the tendency of soil to contract is remarkably reduced. Prevalent densification methods include dynamic compaction, blasting, vibro-techniques including vibro-floatation and vibro-rod systems, and compaction grouting (see Kramer, 1996 and Hausmann, 1990).

In drainage techniques, excess pore water generation is reduced using a drainage system within the soil deposit. Mostly, this can be done by means of constructing vertical wells full of highly permeable gravels at various locations of site. Drainage techniques require careful considerations and use of appropriate filters to enhance the efficiency of the drainage system. Detailed discussion on various drainage methods can be found in almost all soil treatment reference books and relevant publications (e.g., Hausmann, 1990; Bell, 1993).

Also, it is possible to consider both drainage and densification techniques together to improve the soil conditions against liquefaction. For example, in vibro-techniques a vibrator penetrates ground and densifies the surrounding soil, and the resulting vertical

hollow space is filled with suitable gravels (stone column). If this operation is fulfilled at various locations of a site, e.g., at predetermined points with a grid pattern, the total resistance of the site against liquefaction will increase. There are three reasons for this increase in the soil resistance: densification of soil, increasing the site drainage capability (stone columns are highly permeable), and enhancing overall stiffness of the site due to the performance of stone columns as structural elements within the soil medium.

A summary of remediation techniques against liquefaction hazards including the relevant useful information in this respect is collected in Table 2.9 (Feritto et. al., 1999). More specific details related to different liquefaction countermeasures can be found in the papers by Brennan and Madabhushi (2002), Miller and Roycroft (2004), Martin et al. (2004), and many others.

At this point, it should be mentioned that suitable remediation techniques differ from site to site depending directly on:

- Soil type.
- The availability of remedial materials and technical facilities including expert labor force and construction equipment.
- Cost of remediation.
- Functions of structures or their neighboring constructions (e.g., in order to strengthen the soil conditions without interrupting the functions of structures, non-destructive measures like compaction grouting maybe considered.)

Table 2.9 Various liquefaction countermeasures (after Ferritto et al., 1999).

Method	Principle	Most Suitable Soil Conditions or Types	Maximum Effective Treatment Depth	Relative Costs
1) Vibratory probe a) Terraprobe b) Vibrorods c) Vibrowing	Densification by vibration; liquefaction-induced settlement and settlement in dry soil under overburden a higher density.	Saturated or dry clean sand; sand.	20 m routinely (Ineffective above 3-4 m depth); > 30 m sometimes; vibrowing, 40 m	Moderate
2) Vibrocompaction a) Vibrofloat b) Vibro-Composer system	Densification by vibration and compaction of backfill material of sand or gravel.	Cohesionless soils with less than 20% fines.	> 20 m	Low to moderate
3) Compaction Piles	Densification by displacement of pile volume and by vibration during driving, increase in lateral effective earth pressure.	Loose sandy soil; Partly saturated Clayey soil; loess.	> 20 m	Moderate to high
4) Heavy tamping (Dynamic compaction)	Repeated application of high intensity impacts at surface.	Cohesionless soils best, other types can also be improved.	30 m (possibly deeper)	Low
5) Displacement (Compaction grout)	Highly viscous grout acts as radial hydraulic jack when pumped in under high pressure.	All soils.	Unlimited	Low to moderate
6) Surcharge/buttress	The weight of a surcharge/buttress increases the liquefaction resistance by increasing the effective confining pressures in the foundation.	Can be placed on any soil surface.	Dependent on size of surcharge/buttress	Moderate if vertical drains are used
7) Drains Gravel Sand Wick Wells (For permanent dewatering)	Relief of excess pore water pressure to prevent liquefaction. (Wick drains have comparable permeability to sand drains). Primarily gravel drains; sand /wick may supplement gravel drain or relieve existing excess pore water pressure. Permanent dewatering with pumps.	Sand, silt, clay.	Gravel and sand > 30 m; depth limited by vibratory equipment; wick, > 45 m	Moderate to high

Table 2.9 (Cont.) Various liquefaction countermeasures (after Ferritto et al., 1999).

Method	Principle	Most Suitable Soil Conditions or Types	Maximum Effective Treatment Depth	Relative Costs
8) Particulate grouting	Penetration grouting-fill soil pores with soil, cement, and /or clay.	Medium to coarse sand and gravel.	Unlimited	Lowest of grout methods
9) Chemical grouting	Solutions of two or more chemical react in soil pores to form a gel or a solid precipitate.	Medium silts and coarser.	Unlimited	High
10) Pressure injected lime	Penetration grouting-fill soil pores with lime.	Medium to coarse sand and gravel.	Unlimited	Low
11) Electrokinetic Injection	Stabilizing chemical moved into and fills soil pores by electro-osmosis or colloids in to pores by electrophoresis.	Saturated sands, silts, silty clays.	Unknown	Expensive
12) Jet grouting	High-speed jets at depth excavate, inject, and mix a stabilizer with soil to form columns or panels.	Sands, silts, clays.	Unknown	High
13) Mix-in place piles and walls	Lime, cement or asphalt introduced through rotating auger or special in-place mixer.	Sands, silts, clays, all soft or loose inorganic soils.	> 20 m (60 m obtained in Japan)	High
14) Vibro-replacement Stone and sand Columns grouted Not grouted	Hole jetted into fine-grained soil and backfilled with densely compacted gravel or sand hole formed in cohesionless soils by vibro-techniques and compaction of backfilled gravel or sand. For grouted columns, voids filled with a grout.	Sands, silts, clays.	> 30 m (limited by vibratory equipment)	Moderate
15) Root piles, soil nailing	Small-diameter inclusions used to carry tension, shear, compression	All soils.	Unknown	Moderate to high
16) Blasting	Shock waves an vibrations cause limited liquefaction, displacement, remolding, and settlement to higher density	Saturated clean sand; partly saturated sands and silts after flooding.	> 40 m	Low

2.7.3 Performance of the improved ground

2.7.3.1 Practical assessment of the performance of remediation measures

Comparison of the results of in-situ and laboratory tests both before and after soil improvement operations provides a base for evaluating the performance of the applied remediation techniques. Basically, the best way to assess the performance of a mitigation method for a particular site subjected to an earthquake with certain intensity is to compare the observed seismic-induced effects (e.g., settlements, pore water pressure buildup, etc.) in the mitigated and unmitigated zones of the site. Figure 2.1 shows the observed settlements in two different sites due to the 1995-Hyogoken-Nanbu earthquake for various remediation configurations (Bardet et al., 1997). As it can be seen in this figure, the possibility of settlement occurring is significantly reduced using mitigation measures. For instance, the observed settlements in the unmitigated zones of both sites is higher than 40 cm, while practically no settlement was measured in the sites mitigated by sand compaction piles (Rokko Island) and vibro-rod compaction method (Port Island).

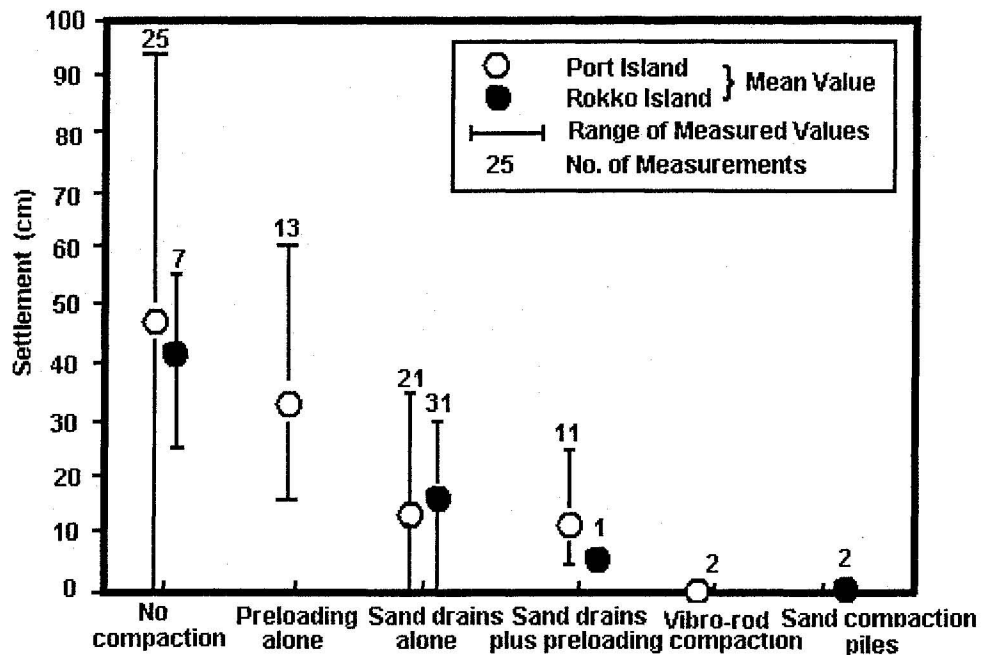


Figure 2.1 Comparison of settlements in two different sites after 1995-Hyogoken-Nanbu Earthquake (Redrawn based on the information from Bardet et al., 1997).

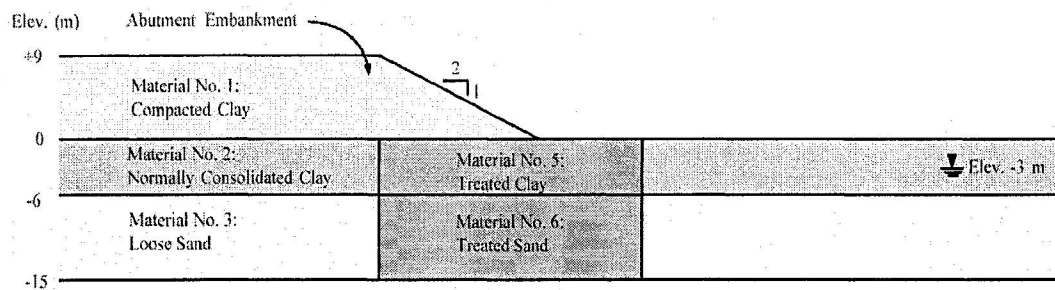
2.7.3.2 Effects of size and location of remediation measures

Effects of size and location of the improved ground on reducing liquefaction hazards have been studied by Riemer et al. (1996). They studied the performance of a section of the highway 1-57 Mississippi River bridge abutment under seismic acceleration time histories of 1989 Loma Prieta and 1988 Saguenay earthquakes using the 2D FLAC software (Itasca Consulting Group Inc., 2000).

Figures 2.2 to 2.4 (Cooke, 2000) show geometry and material specifications, effects of the size of soil improvement, and effects of the location of soil improvement, respectively, in the study conducted by Riemer et al. (1996). From these studies it was concluded that: (see also Riemer et al., 1996; and Cooke, 2000.)

- Increasing the size of the treated zone had a significant effect in decreasing the predicted lateral displacements, but with a descending rate.
- The most effective option for the location of the treated zone was option A (Figure 2.4), where the treated zone is exactly under the sloping portion of the embankment.

Despite the fact that the soil model used by Riemer et al. (1996) was not verified by laboratory tests or field case histories (Cooke, 2000), the results give a qualitative indication regarding the influences of the size and location of the improved zone on liquefaction-induced displacements.



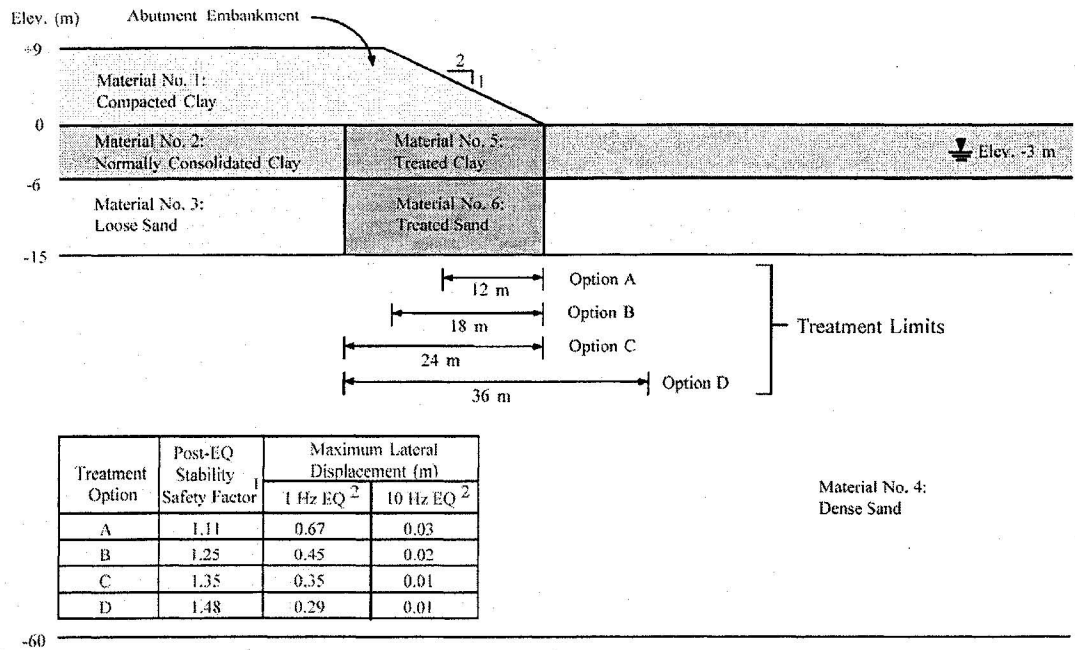
Material No.	SPT (N_{60})	Unit Weight (kN/m^3)	K_2	Friction Angle (degrees)	s_{ur} (kPa)
1	20	19.6	60	0	47.9
2	5	18.8	20	0	23.9
3	15	19.6	49	25	19.2
4	30	20.4	62	40	191.5
5	20	19.6	54	0	47.9
6	30	20.4	62	35	134.1

Material No. 4:
Dense Sand

-60

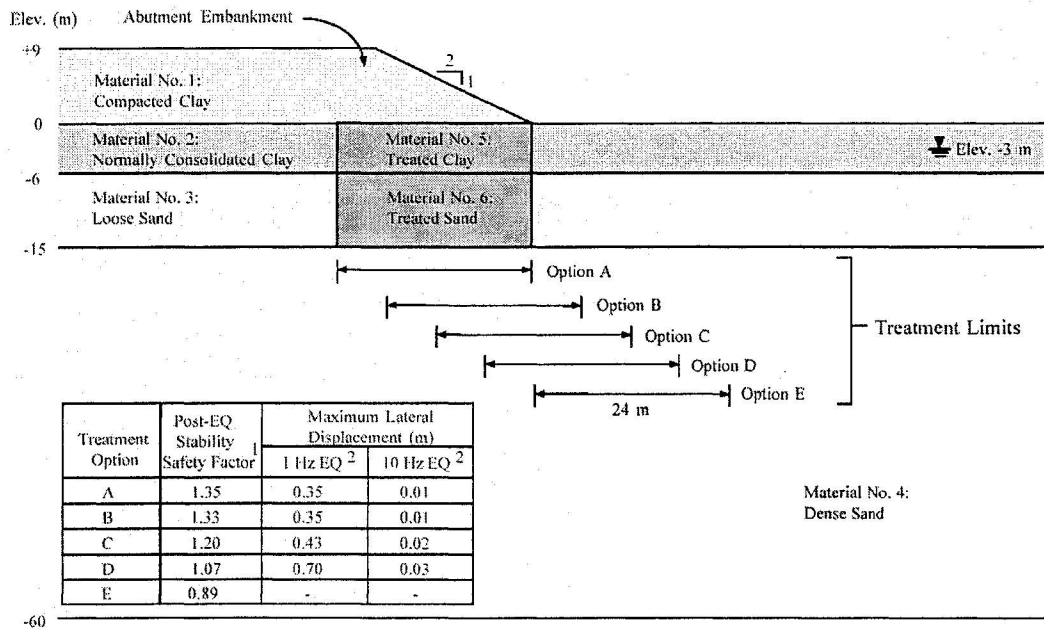
Notes: 1. K_2 is factor used for calculating maximum shear modulus
2. s_{ur} is the post-seismic shear strength.

Figure 2.2 Geometry and material specifications in the study by Riemer et al. (1996) (modified from Cooke, 2000).



Notes: 1. For no ground treatment the calculated post-earthquake factor of safety for stability was 0.71.
 2. Input motions had durations of 8 to 10 seconds and peak amplitude scaled to 0.22g.

Figure 2.3 Effects of the size of soil improvement in the study by Riemer et al. (1996) (modified from Cooke, 2000).



Notes: 1. For no ground treatment the calculated post-earthquake factor of safety for stability was 0.71.
 2. Input motions had durations of 8 to 10 seconds and peak amplitude scaled to 0.22g.

Figure 2.4 Effects of the location of the treated zone in the study by Riemer et al. (1996) (modified from Cooke, 2000).

Shaking table tests performed by Yanagihara et al. (1991) confirmed the second outcome of the study by Riemer et al. (1996) regarding the location of the treated zone (Cooke, 2000). They concluded that the treated zone is effective if sufficient embankment surcharge exists over the liquefiable soils behind the treated zone to battle against pore pressure buildup in the untreated zones. Figure 2.5 shows the cases studied by Yanagihara et al. (1991). The base input motion in the study by Yanagihara et al. (1991) was a sinusoidal acceleration having an amplitude of 2m/s^2 and a frequency of 2Hz.

In case 1, i.e., model with no remediation, high pore pressure buildups were observed in the free field and extended under the embankment causing large lateral displacements and settlements of foundation and embankment (Cooke, 2000). In case 3, in spite of small displacement of the treated zone, large settlements occurred in the embankment (80 to 125 mm), and due to high pore water pressure buildup the embankment cracked at a location near its toe causing the liquefied materials to be expelled out (Cooke, 2000). On the other hand, in case 2, excess pore water pressures were lower both in the densified zone and under the embankment. Also, the settlement of embankment was limited to 22 mm in this case.

Results of the study by Yanagihara et al. (1991) and the numerical studies by Riemer et al. (1996) have shown the significance of the effects of locations of improved zones on the behavior of mitigated geotechnical structures under cyclic loads. Detailed discussion in this respect can be found in Cooke (2000).

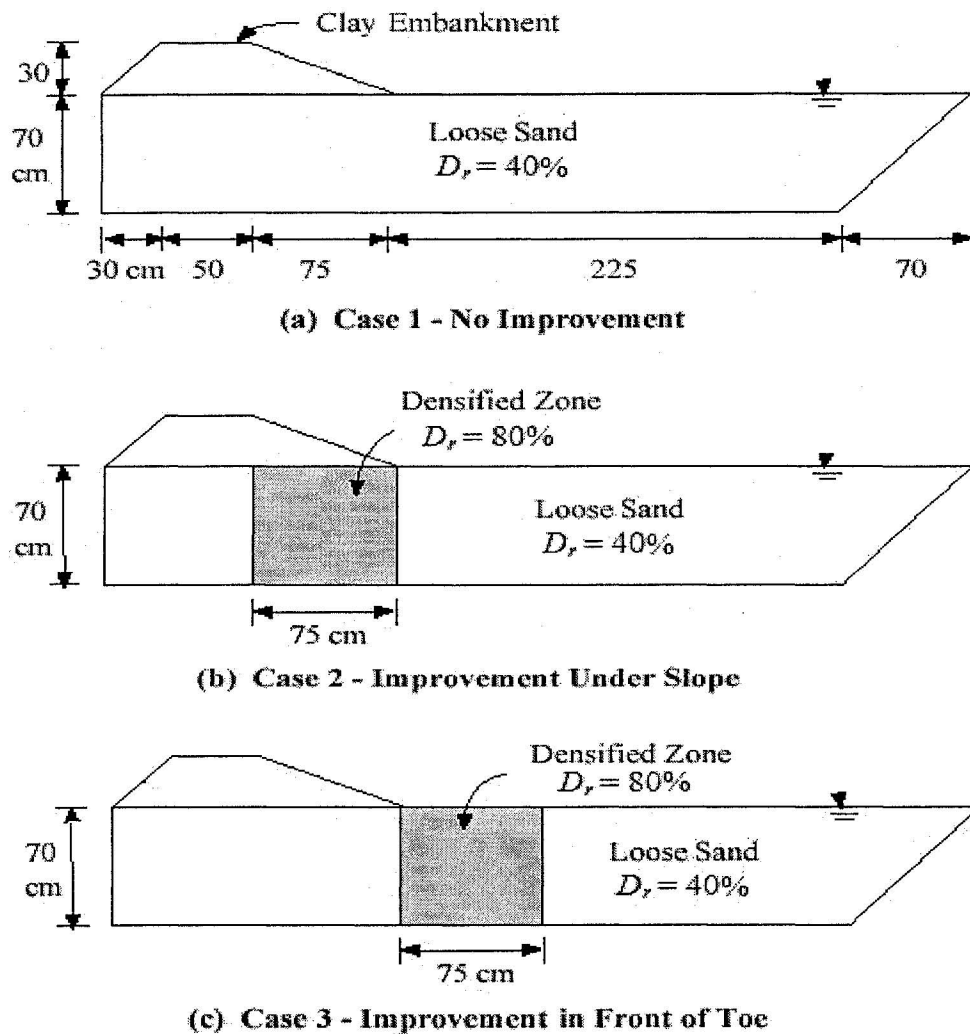


Figure 2.5 Shaking table tests studied by Yanagihara et al. (1991) (modified from Cooke, 2000).

2.7.3.3 Centrifuge study on the performance of different remediation measures

Effects of various remediation measures on the seismic response of an embankment structure were studied by Adalier et al. (1998) based on centrifuge modeling with a centrifugal acceleration of 75g. Figure 2.6 shows different mitigation configurations studied by Adalier et al. (1998). These model configurations include:

- Model 1: Base model with no soil improvement, i.e., a clayey sand embankment underlain by a loose sand layer with a relative density of $D_r = 40\%$.
- Model 2: Similar to model 1 but improved by two 6-m-wide densified zones beneath the toes of the embankment with $D_r = 90\%$ instead of the loose sand at those locations (Compaction).
- Model 3: Similar to model 1 but improved by two 6-m-wide solidified blocks with Portland cement beneath the toes of the embankment instead of the loose sand at those locations (Solidification).
- Model 4: Similar to model 1 but improved by additional two 3-m wide gravel berms at both sides of the embankment (Gravel berm).
- Model 5: Similar to model 1 but improved by steel sheet piles with tie rods under the embankment (Sheet Pile Enclosure).

All models were shaken with three successive sinusoidal base input accelerations with magnitudes of 0.09g, 0.18g, and 0.30g, respectively (10 cycles for each magnitude with a prototype frequency of 1.6 Hz).

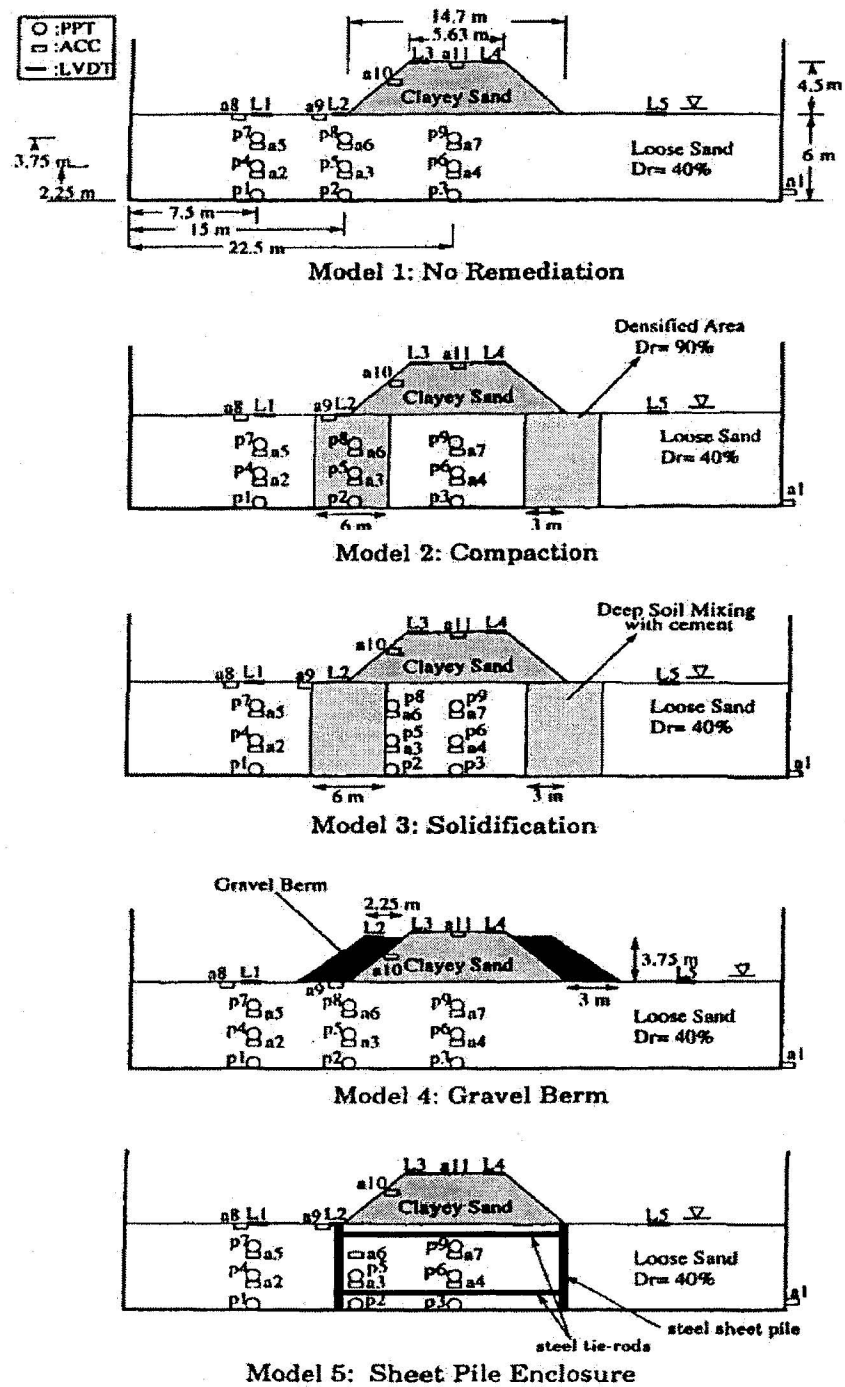
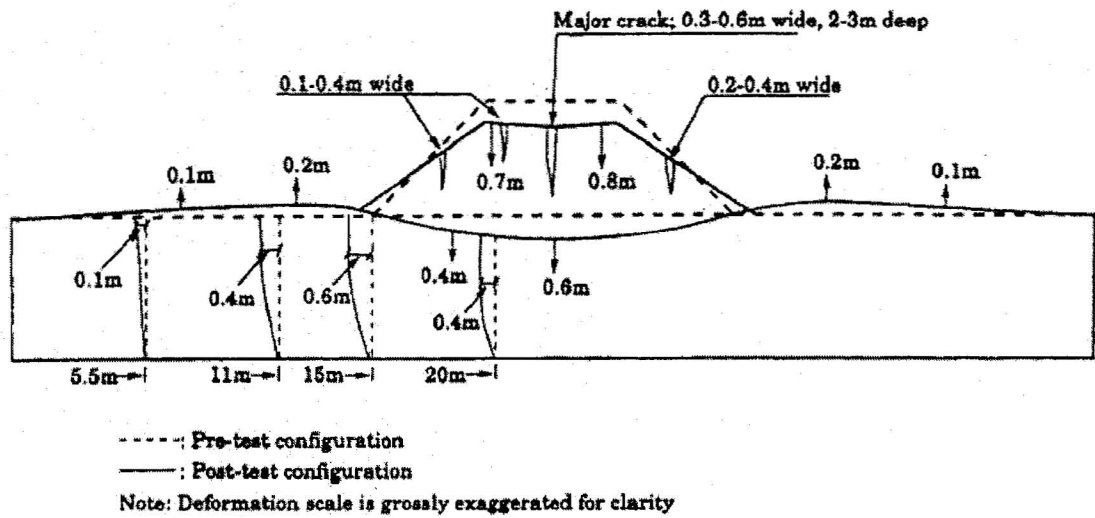


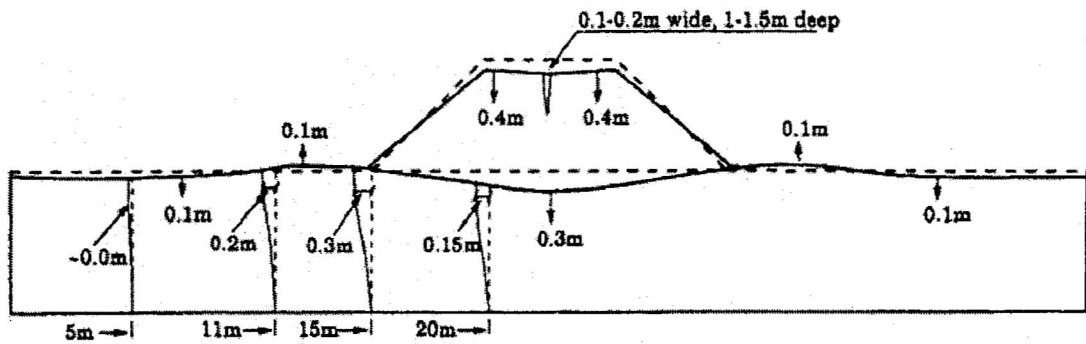
Figure 2.6 Different mitigation configurations studied by Adalier et al. (1998) (modified from Adalier et al., 1998: Not to scale).

Figures 2.7 and 2.8 show the lateral and vertical displacements for the models studied by Adalier et al. (1998) after the end of shaking. Based on the observed results, it can be concluded that: (see also Adalier et al., 1998 and Cooke, 2000)

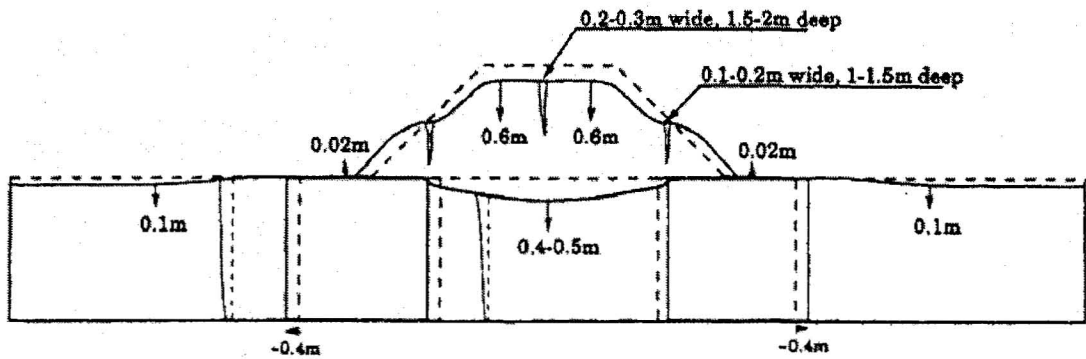
- Sheet piling with tie rods caused the smallest cracking and slumping of embankment, and it was the most effective method in reducing the lateral displacements of the embankment. The performances of densification (model 2) and gravel berms (model 4) were approximately similar. However, solidification using Portland cement (model 3) had no remarkable effect in this respect.
- Soil remediation by means of densification was the most effective measure in decreasing vertical settlement of the embankment and avoiding high pore water pressure buildup under the embankment; however, this resulted in increase in measured peak acceleration at the embankment crest about 1.3 times the base input motion.
- Gravel berms provided lateral support for the embankment and reduced its lateral displacement; however, the observed settlement under the embankment was higher than that obtained from using densification method. This may be due to the weight of the berms.



Model 1: Benchmark



Model 2: Densification



Model 3: Solidification

Figure 2.7 Displacements of models 1, 2, and 3 (after Adalier et al., 1998: Not to scale).

Moreover, based on the observations from the centrifuge tests (Adalier et al., 1998), it was concluded that (1) a limit may exist for reducing displacements and settlements, and (2) a particular method, which improves one kind of response (e.g., displacement, settlement, or pore water pressure), may not be very effective in improving other kinds of responses. For instance, densification (model 2) caused the lowest vertical settlement under the embankment, but the observed lateral displacement was significantly higher than that corresponding to model 5 (sheet pile enclosure).

2.7.3.4 Numerical simulations of the centrifuge tests described by Adalier et al. (1998)

Adalier et al. (1998) provided valuable understanding of the behavior of mitigation measures based on centrifuge test results. At this point, since the present research focuses on numerical studies of liquefaction countermeasures, it is useful to briefly discuss the results of numerical studies for the centrifuge tests performed by Adalier et al. (1998). In this respect, two different numerical studies are mentioned here:

First, Elgamal et al. (2002a) performed numerical studies for models 1 (no remediation), 2 (densification), and 5 (sheet pile enclosure). They used a multi-yield plasticity model along with a fully coupled finite element formulation. For all cases, the predicted accelerations were in good agreement with the recorded ones, and the predicted lateral displacements were also realistic both in pattern and in amplitude. However, significant differences were observed between the predicted and the recorded pore water pressures beneath the embankment as well as vertical settlements. They concluded that

these differences are related to the limitations of the model to accurately simulate the shear-induced plastic volumetric strains (Elgamal et al., 2002a).

Aydingun and Adalier (2003) and, Adalier and Aydingun (2003), performed numerical studies of the centrifuge models (except model 3) described by Adalier et al. (1998). They used the program DIANA-SWANDYNE II, a 2-D fully coupled finite element program (see Chan, 1993) with bounding surface plasticity model for sand. The predicted acceleration and excess pore pressure time histories as well as liquefaction-induced deformations were in reasonable agreement with the results of the corresponding centrifuge simulations. However, significant discrepancies were observed between the predicted and the recorded pore pressures and vertical deformations at zones beneath the embankment centerline. It was believed that these differences are related to inability of the computer code to cope with occurrence of large strains (Aydingun and Adalier, 2003).

In both numerical studies mentioned above, it was concluded that there is a need for more research both experimentally and numerically to achieve better experimental insights as well as computational abilities particularly for simulation of large shear-induced plastic strains.

2.8 Effects of impermeable (barrier) layers on liquefaction potential

Due to existence of impervious silty or clayey layers in many natural liquefiable sand deposits, during shaking water may be trapped beneath a stratum with a relatively low permeability. This traps water under the impervious layer causing reduction of shear strength of soil along the seam. Since drainage is hindered for a long time after earthquake, delayed flow failure and large displacements may take place after the end of shaking. Failure of Mochikoshi tailing dam in 1978 after 1978 Izu-Oh shima, Japan, earthquake is an example of this type of failure in practice (Yang, and Elgamal, 2001).

Shaking table tests performed by Kokusho (1999) confirmed the concerns regarding the effects of impermeable layer due to formation of water films. He performed both 1D and 2D shaking table tests on saturated sand samples (Figure 2.9). First, a silt layer was sandwiched in a 1D saturated sand layer of 2m thickness. In this case the sand layer was liquefied by instant shock, and a very thin water film (about a few millimeters) was formed under the silt layer after liquefaction of loose sand. Thickness of such a water film is inversely proportional to the relative density of sand. In 2D tests conducted by Kokusho (1999) the direction of shaking was normal to the direction of slope to exclude the effect of the inertia forces from lateral spread deformation. 2D shaking table tests with and without the silt layer showed that the presence of silt layers caused formation of water films beneath the silt seams during shaking. Lack of shear resistance along the water films causes the soil mass above them to move towards the slope toe both during and after shaking (see Case a in Figure 2.10 with a silt arc). On the other hand, in 2D models without silt seams water films were not formed. In this case, soil deformed

continuously mostly during shaking, and stopped afterward (see Case b in Figure 2.10 without silt arc)

Model tests and failure cases in practice show the significant influence of barrier layers on liquefaction susceptibility of soils, and this has been studied in the LRI centrifuge experiments (see Chapter 4).

A numerical study on the effects of low-permeability layers on the stability of slopes was performed by Chakraborty et al. (2004). The numerical model used in this study was the multi-yield plasticity soil constitutive model (Prevost, 1985a) implemented in the finite element code Dynaflo (see Chapter 3). The phenomenon was first analyzed at small scale by numerically simulating a series of laboratory cyclic undrained tests performed on uniform and layered soil samples. It was concluded that migration of water from more deformable layers into sand layers may significantly reduce liquefaction resistance. Also, fully coupled, effective stress non-linear dynamic analyses of saturated slopes, both with and without low-permeability layers were carried out. The results showed significant influence of those layers on the seismic behavior of such slopes.

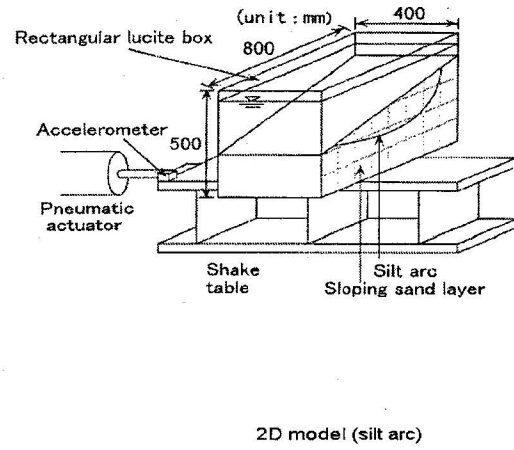
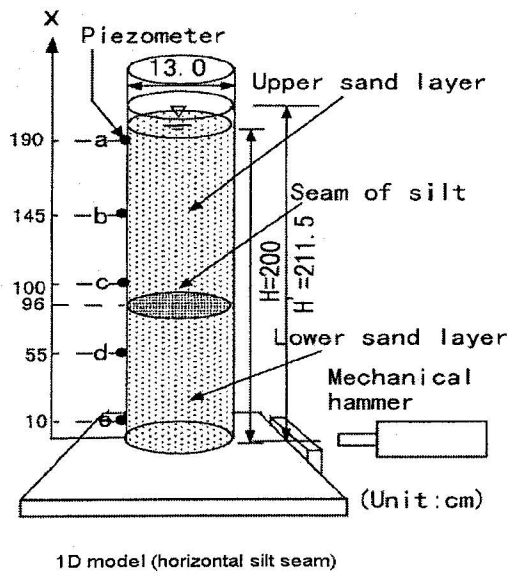


Figure 2.9 Shaking table tests performed by Kokusho (modified from Kokusho, 1999).

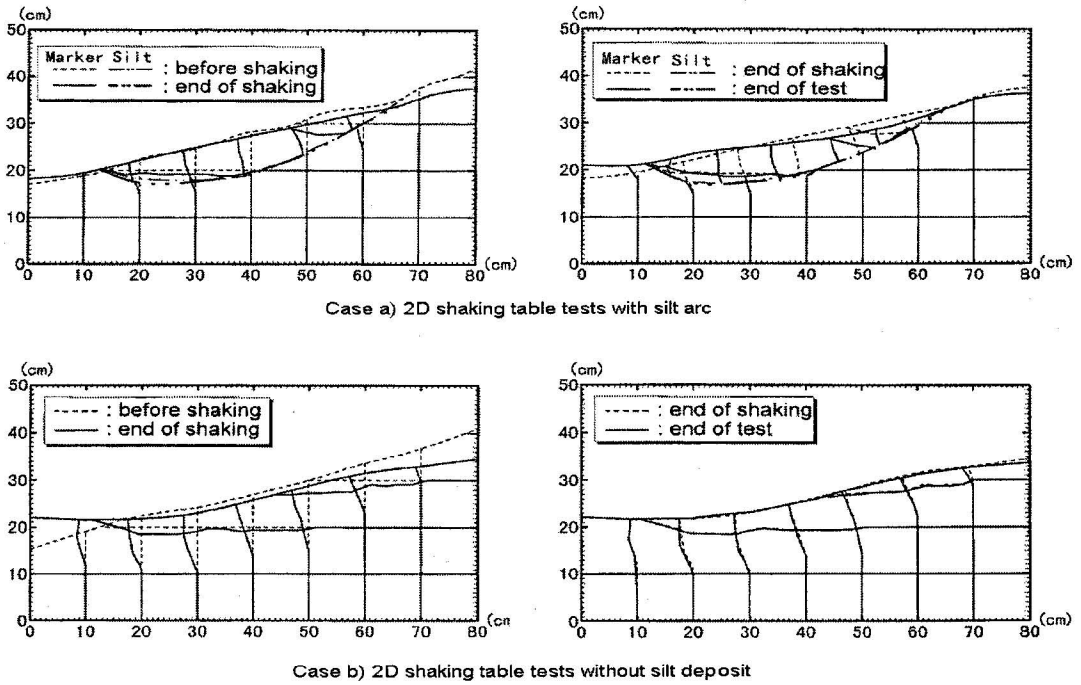


Figure 2.10 Deformed shaped of the models studied by Kokusho (1999) during shaking (left) and after shaking (right): Case a) with silt arc; Case b) without silt arc (modified from Kokusho, 1999).

2.9 Liquefaction potential of nearly saturated soils

2.9.1 Experimental observations

Almost all deltaic sands such as Fraser River sand often contain free or dissolved gas (Grozic, 2003). Many experimental studies have been performed to investigate the effects of the presence of gas in soils subjected to both monotonic and cyclic loads (e.g., Grozic et al., 1999 and 2000; Ishihara et al., 2001; Okamura et al., 2004; and Yang et al., 2004).

All the experimental studies have indicated that the existence of gas in partially saturated soils can remarkably modify the strength and liquefaction susceptibility of soils. In fact, free gas in nearly saturated soils significantly increases the compressibility of the pore fluid and as a result increases the strength and liquefaction resistance of these soils.

For instance, cyclic triaxial tests conducted on Ottawa sand samples (Grozic, 2003; and Grozic et al., 2000) confirmed that the presence of gas in partially saturated soils could enhance the liquefaction resistance of the soil samples expressed in terms of cyclic resistance ratio (CRR) by 200% to 300% (Figure 2.11). As discussed hereafter and illustrated in Figure 3.3 in Chapter 3, degree of saturation strongly affects the bulk modulus of the soil pore fluid (air-water mixture). In fact, the liquefaction resistance of soils increases considerably with decreasing the bulk modulus of the air-water mixture.

The specifications of sand samples used in the cyclic triaxial tests conducted by Grozic et al. (2000) are listed in Table 2.10. Other researchers have obtained similar results for increasing resistance against liquefaction due to incomplete saturation (e.g., Sherif et al., 1977; Yoshimi et al., 1989; Xia and Hu, 1991; Ishihara et al., 2001; and

Yang, 2002). A good review of experimental studies on liquefaction susceptibility of nearly saturated soils conducted by different researchers is presented by Yang et al. (2004) (Figure 2.12).

As shown in Figure 2.12, the Skempton B-value pore pressure coefficient (Skempton, 1954) has been considered as an indicator of the soil initial degree of saturation. Yang et al. (2004) mentioned the following expression for the pore pressure coefficient, B-value, in terms of the soil degree of saturation.

$$B = \frac{1}{1 + n^w \frac{B_s}{B_w} + n^w \frac{B_s}{U} (1 - S_0)} \quad (2-4)$$

In Equation (2-4), n^w is the sand porosity, B_s is the bulk modulus of the soil skeleton, B_w is the bulk modulus of pore water, U is the absolute pore fluid pressure (i.e., including the atmospheric pressure), and S_0 is the soil initial degree of saturation. As shown in Figure 2.12, the sand samples with lower B-values (i.e., lower initial degrees of saturation) exhibit higher resistance to liquefaction.

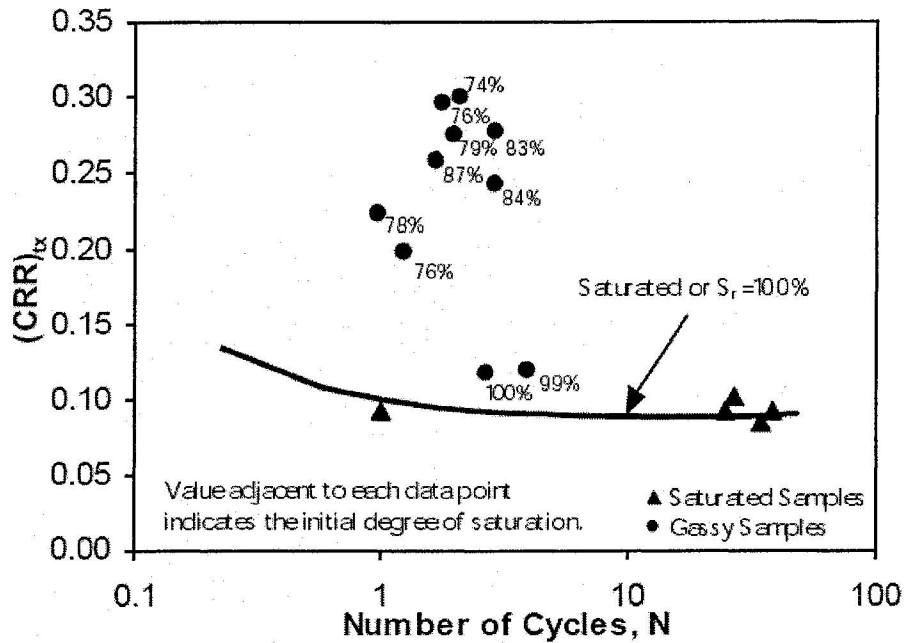


Figure 2.11 Triaxial cyclic resistance ratio, CRR, versus number of cycles to liquefaction for unsaturated samples of Ottawa sand. (after Grozic, 2003).

Table 2.10 Specifications of Ottawa sand samples used for cyclic triaxial tests (curtailed and modified from Grozic et al., 2000).

Sample No.	Type	Applied effective stress, σ_d' (kPa)	Initial mean normal effective stress, p' (kPa)*	Period (s)	Void ratio, e		Relative density, D_r (%)		Degree of saturation, S_r (%)
					Initial	Final	Initial	Final	Initial
16	Saturated	55	301	12	0.74	0.74	26	26	100
18	Saturated	55	298	12	0.72	0.72	33	33	100
19	Saturated	55	296	12	0.71	0.71	33	33	100
20	Saturated	50	294	12	0.71	0.71	35	35	100
25	Saturated	60	296	14	0.71	0.71	36	36	100
28	Gassy	70	297	15	0.71	0.70	34	38	100
32	Gassy	70	294	15	0.72	0.71	30	35	99
33	Gassy	140	272	30	0.75	0.70	21	37	87
36	Gassy	130	292	26	0.78	0.69	14	41	78
37	Gassy	115	291	24	0.80	0.71	8	34	76
38	Gassy	148	270	30	0.73	0.70	28	38	83
39	Gassy	155	213	31	0.79	0.69	10	39	74
40	Gassy	125	284	24	0.75	0.70	21	38	84
41	Gassy	158	271	31	0.67	0.61	46	66	75
42	Gassy	140	212	27	0.71	0.66	33	51	79

Sand Properties and Test Description

Material	D_{50} (mm)	C_u	e_{max}	e_{min}	D_r	Liquefaction criteria	Test type	Reference
Ottawa sand	0.40	2.1	0.76	0.50	—	EPP= σ'_c	Torsional shear	Sherif et al. (1977)
Toyoura sand	0.175	1.52	0.976	0.605	60%	DA=5%	Torsional shear	Yoshimi et al. (1989)
Tongjiashan sand	0.1	3.7	—	—	60%	EPP= σ'_c	Triaxial	Xia and Hu (1991)
Niigata sand	0.325	1.47	—	—	62%	DA=5%	Triaxial	Ishihara et al. (2001)

Note: DA=double amplitude of strain; EPP=excess pore pressure; and σ'_c =initial confining pressure.

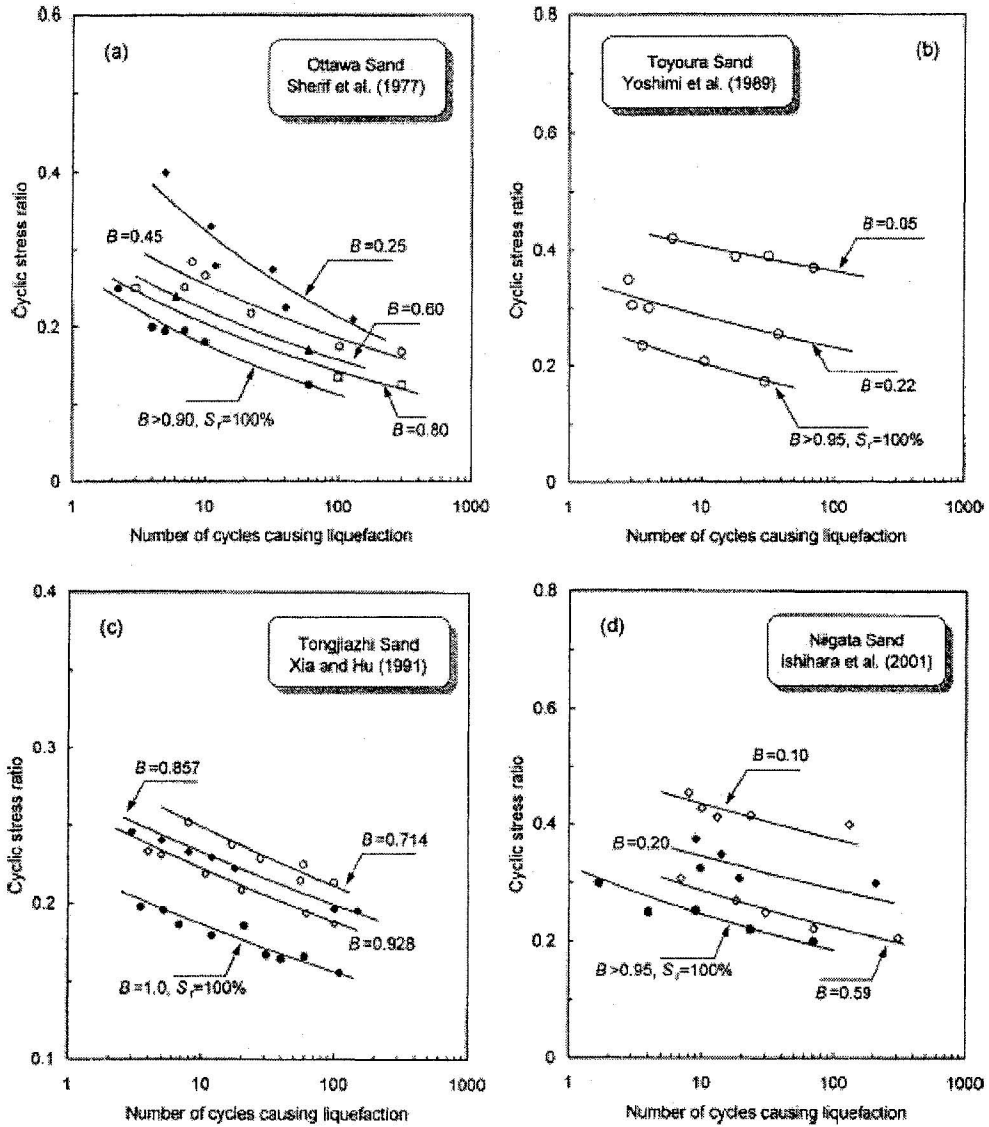


Figure 2.12 Cyclic resistance ratios versus number of cycles to liquefaction corresponding to different unsaturated sand samples provided by a) Sherif et al. (1977), b) Yoshimi et al. (1989), c) Xia and Hu (1991), and d) Ishihara et al. (2001). (Figure modified from Yang et al., 2004).

2.9.2 Theoretical studies

Soils below the ground water table in earthquake prone sites may not be fully saturated but in a state of near saturation (e.g., Tsukamoto et al., 2002; and Yang et al., 2004). So far not many theoretical studies have been performed for liquefaction susceptibility of partially saturated soils. Most of the proposed constitutive models such as the one presented by Pietruszczak and Pande (1991 and 1996) for partially saturated soils at high degrees of saturation are based on considering an equivalent bulk modulus for the mixture of gas and water (see also Schuurman, 1966; and Tamura et al., 2002). Pietruszczak et al. (2003) used the proposed model by Pietruszczak and Pande (1991 and 1996) to perform numerical studies on partially saturated sand layers under seismic excitations. This model is based on the assumption that each void space within the soil medium has a single spherical air bubble. The effects of transient air dissolution are neglected in this model. Tamura et al. (2002) showed that the effects of solubility and size of air bubbles on B-value and P-wave velocity of a partially saturated sand can not be disregarded. Iveson (2003) stated that the exact size and distribution of the air bubbles in a partially saturated soil is unknown.

Byrne et al. (2004a) assumed the same absolute pore pressures for water and air phases (neglecting the effects of surface tension) in soils and used the Boyle's law to estimate the value of pore fluid bulk modulus due to evolution of pore fluid pressure for partially saturated sands subjected to seismic loads. They neglected the effects of solubility of air in water in their computations.

Recently, Grozic et al. (2005) presented a constitutive model for gassy sand behavior using the Hilf's equation (Hilf, 1948) to account for the effects of air dissolution in water on the soil behavior. In deriving his equation, Hilf (1948) assumed that the effects of soil suction (corresponding to the effects of surface tension) are negligible. Grozic et al. (2005) mentioned that for a partially saturated sand at high degrees of saturation the Hilf's assumption is acceptable. Grozic et al. (2005) used their constitutive model for predicting the effect of gas on the undrained static behavior of loose Ottawa sand.

The Hilf's equation is based on the results of a one-dimensional oedometer test on a compacted soil, Boyle's law for ideal gas and Henry's law for solubility of gas into water (Fredlund and Rahardjo, 1993). This equation calculates changes in the pore fluid pressure due to changes in total stress. Initial and final conditions in the Hilf's equation are shown in Figure 2.13.

Hilf's equation is:

$$\Delta U_g = \left[\frac{\Delta n^w}{\{(1 - S_0)n_0^w + hn_0^w S_0 - \Delta n^w\}} \right] U_{g0} \quad (2-5)$$

Where:

ΔU_g = Change in absolute gas pressure

Δn^w = Change in porosity

S_0 = Initial degree of saturation

h = Volumetric coefficient of solubility of gas into water

n_0^w = Initial porosity

U_{g0} = Initial absolute gas pressure

The Hilf's equation has been widely used by USBR (US Bureau of Reclamation) to estimate pore pressures in compacted fills, and investigations have shown it has adequate accuracy for practical purposes (Fredlund and Rahardjo, 1993).

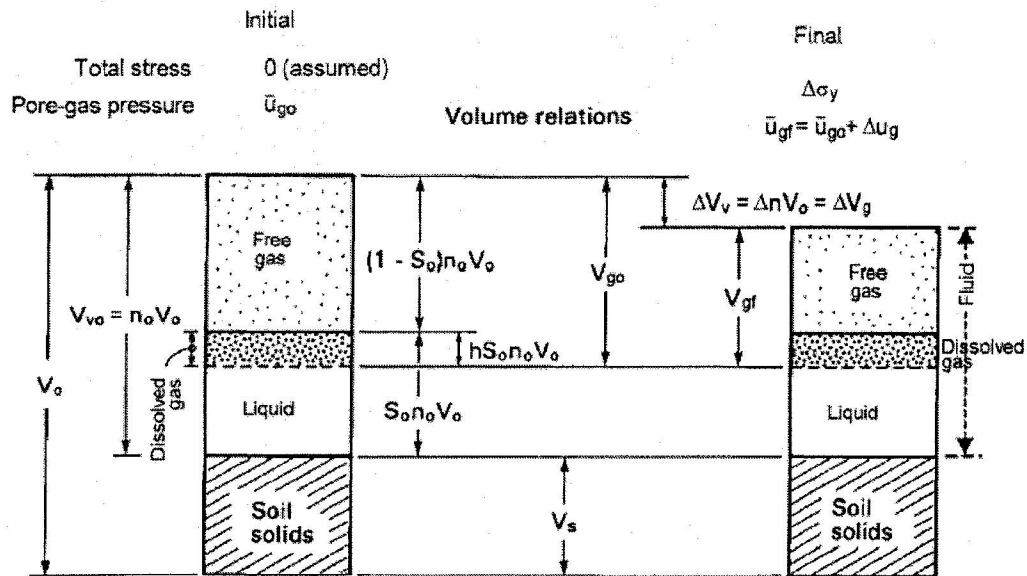


Figure 2.13 Initial and final pressure and volume conditions assumed by Hilf in his analysis (after Grozic et al., 2005).

Regardless of the increase in liquefaction resistance due to incomplete saturation, Atigh and Byrne (2003) identified a problem related to the effects of gas on the behavior of submarine slopes during tidal variations. Based on a numerical study they noted that unequal pore pressure generation with depth caused by volumetric strains due to gas compressibility during low tides may lead to a reduction in effective stresses on tidal drawdown. This may trigger instability in gassy submarine slopes.

Chapter 3 - Numerical Model

3.1 Introduction

A constitutive model used for liquefaction analysis should be able to address properly a number of different soil behavioral features including material nonlinearity, stress history dependence, shear-induced volumetric dilation/compaction, effects of stress anisotropy, and hysteretic behavior due to loading, unloading and reloading.

These features can be considered in constitutive models implemented in advanced numerical codes. Besides, due to dependence of the soil skeleton strains and pore fluid pressure on each other, a mathematical model appropriate for liquefaction analysis of saturated soils should perform a coupled field analysis in which a set of dependent dynamic equilibrium equations (one equation for each phase, which is dependent on the other phases through coupling terms) are solved in a step-by-step dynamic analysis to capture accurately the inertial and dissipative coupling terms (Popescu et al., in press). Dynaflo (Prevost, 2002), a finite element code introduced in this chapter, includes all the aforementioned aspects.

Dynaflo (Prevost, 2002) contains various constitutive models, solution algorithms, element types, and special features enabling users to model a large number of problems encountered in geotechnical engineering. A multi-yield plasticity soil constitutive model (Prevost, 1985a) is implemented in this code (Dynaflo) for liquefaction analysis. This model possesses a well-established calibration procedure based on the results of standard laboratory or in-situ soil tests. In addition, Dynaflo has a capability for solving coupled

field equations for multiphase media based on an extension of the Biot's formulation (e.g., Biot, 1962) for nonlinear porous media (Prevost, 1989). The multi-yield plasticity soil constitutive model described in this chapter has been validated several times in the past for analysis of liquefaction susceptibility of fully saturated soils based on results of centrifuge experiments (e.g., Popescu and Prevost, 1993 and 1995) and field tests (e.g., Keanne and Prevost, 1989).

In this chapter, the fundamental features of the multi-yield plasticity soil constitutive model, descriptions of the model parameters, and a summary of the coupled field equations (required for liquefaction analysis of fully saturated soils) and their implementation in the finite element code Dynaflow are briefly presented.

The chapter also includes an original constitutive formulation suggested for analysis of liquefaction susceptibility of nearly saturated sands. Incomplete saturation can significantly affect the liquefaction susceptibility of sands. In fact, free gas in a nearly saturated soil increases the pore fluid compressibility. Due to high compressibility of the pore fluid, the amount of seismically induced excess pore water pressure in a nearly saturated soil can be significantly lower than that induced in the same soil at full saturation. The formulation proposed in this chapter is based on the Henry's law for dissolution of gas in water, the ideal or perfect gas law and the mass balance law. Moreover, to account for the effects of transient air dissolution in water on the compressibility of pore fluid an analytical approach is provided for a moving boundary diffusion equation under a general loading condition. The formulation is able to predict the transient changes in the soil degree of saturation and pore fluid bulk modulus due to

changes in the pore fluid pressure. At constant temperature the proposed model requires only one constitutive parameter, in addition to the soil initial degree of saturation and parameters required by the constitutive model describing the stress-strain behavior. A suggested procedure for calibrating the proposed model is also provided in this chapter based on numerical simulations of isotropically consolidated cyclic triaxial tests conducted on nearly saturated samples of Toyoura sand (Tsukamoto et al., 2002).

3.2 Coupled field equations implemented in Dynaflow

This section includes the basic equations implemented in the finite element code Dynaflow based on extension of the Biot formulation (e.g., Biot, 1962) into the nonlinear regime (Prevost, 1989) that are essential for liquefaction analysis of fully saturated soils. It is assumed that soil consists of a solid skeleton interacting with pore fluid (Prevost, 1989).

The balance of linear momentum equations for solid and liquid phases can be expressed by Equation (3-1) and (3-2) (Prevost, 1980). In these equations the motion of the solid phase is used as the reference motion.

$$\rho^s a^s = \nabla \cdot \sigma'^s - (1 - n^w) \cdot \nabla p^w - \xi \cdot (v^s - v^w) + \rho^s b_f \quad (3-1)$$

$$\rho^w \frac{dv^w}{dt} = \rho^w (v^s - v^w) \cdot \nabla v^w - n^w \nabla p^w + \xi \cdot (v^s - v^w) + \rho^w b_f \quad (3-2)$$

In Equations (3-1) and (3-2), σ'^s = solid (effective) stress, a^s = solid acceleration, v^s (v^w) solid (fluid) velocity, b_f = body force (per unit mass), p^w = pore fluid pressure, $\rho^s = (1-n^w)\rho_s$ and $\rho^w = n^w\rho_w$ with ρ_s = solid mass density, ρ_w = fluid mass density and n^w = porosity; $\xi = n^{w^2}\gamma_w k^{-1}$, with k = hydraulic conductivity and $\gamma_w = \rho_w g$ = fluid unit weight, $g = \|b_f\|$ acceleration of gravity (see also Prevost, 1989). The primary unknowns in Equations (3-1) and (3-2) are solid displacements and the fluid velocities (Prevost, 2002).

When the compressibility of pore fluid is accounted for, the pore pressure is determined from the resulting solid and fluid velocities through time integration of the following equation: (Prevost, 1985b)

$$\frac{dp^w}{dt} = -(B_v/n^w) \left[\nabla \cdot (1-n^w)v^s + \nabla \cdot (n^w v^w) \right] \quad (3-3)$$

where B_v is the fluid bulk modulus.

If the pore fluid is assumed to be incompressible, the pore fluid pressure is determined from the computed velocities through the following equation:

$$p^w = -(B_v/n^w) \left[\nabla \cdot (1-n^w)v^s + \nabla \cdot (n^w v^w) \right] \quad (3-4)$$

where, B_v = a penalty parameter enforcing the incompressibility constraint as described by Prevost (1982b and 1985b).

The standard Galerkin approach (e.g., Bathe and Wilson, 1976; and Zienkiewicz 1989 and 1991) along with weak formulation is applied to initial boundary value problems resulting in a global matrix equation for finite element analysis. The solution domain of a

problem is discretized into non-overlapping finite elements. Low order isoparametric finite elements (i.e., four-node plane and eight-node brick) are used to discretize the solution domain (the same shape functions are considered for both the solid and the fluid phases). The detailed finite element formulation implemented in Dynaflo is presented by Prevost (1985b).

A finite difference time stepping algorithm is used for integrating the finite element equations implemented in Dynaflo (Prevost, 1985b). Both implicit and explicit (e.g., Hughes and Liu, 1978a and 1978b) integration options are available in Dynaflo (Prevost, 2002). The resulting nonlinear algebraic equations are solved using Newton-Raphson type iterations at each step (Prevost, 2002).

3.3 Multi-yield plasticity soil constitutive model

3.3.1 Description and basic relations

The multi-yield plasticity soil constitutive model implemented in Dynaflo (Prevost, 2002) is a kinematic hardening model based on a relatively simple plasticity theory (Prevost, 1985a), and is applicable to both cohesive and cohesionless soils. The main features of this model are shown in Figure 3.1. The fundamental theory behind the model has originated from the concept of a “field of work-hardening moduli” (Mroz, 1967) based on approximating the nonlinear soil stress-strain curve by a number of linear segments with constant shear moduli. This results in defining a series of nested yield surfaces in the stress space (Figure 3.1a). Each yield surface corresponds to a region of a

constant shear modulus. The outermost surface is called failure surface. Both Drucker-Prager (Figure 3.1a) and Mohr-Coulomb (Figure 3.2) type surfaces can be employed in the model for frictional materials (Prevost, 2002). The plastic flow rule is associative in its deviatoric component. A non-associative flow rule is used for the dilatational (volumetric) component to account for the dependence of soil dilatational behavior on the mobilized effective stress ratio (Figure 3.1b). The soil hysteretic behavior and shear stress-induced anisotropic effects are simulated by a purely deviatoric kinematic hardening rule (Prevost, 1989). As shown in Figure 3.1c, upon contact, the yield surfaces are translated in the stress space by the stress point. A stress relaxation approach is used for integrating the constitutive equations as illustrated in Figure 3.1d. In this respect, the return mapping algorithm proposed by Simo and Ortiz (1985) has been modified for the multi-yield plasticity soil model and implemented in Dynaflow (Prevost, 1989).

The basic equations of the model presented in the Dynaflow manual (Prevost, 2002) are given in this section. The yield function for pressure sensitive materials (e.g., Drucker-Prager or Mohr-Coulomb type yield surface) is expressed as (Prevost, 2002):

$$f_y = \{3/2 \operatorname{tr}(s - \bar{p}a_c)^2\}^{1/2} + k_s \bar{p}g(\theta) = 0 \quad (3-5)$$

In this equation, s is the deviatoric stress tensor (i.e., $s = \sigma - p\delta$, where σ is the effective stress tensor, $p = 1/3 \operatorname{tr}\sigma$, and δ is the Kronecker Delta tensor), a_c is the tensor representing the coordinate of the yield surface center in the deviatoric stress space, k_s is the size of the yield surface, and $\bar{p} = (p - a_t)$ with $a_t = \text{attraction} = c/\operatorname{tg}\phi$ ($\phi = \text{friction}$

angle and c = cohesion). The function $g(\theta)$ determines the shape of the cross-section on the deviatoric plane as expressed by the following relationship:

$$g(\theta) = \frac{2M_k}{(1 + M_k) - (1 - M_k) \sin 3\theta} \quad (3-6)$$

in which

$$\sin 3\theta = -\sqrt{6} \bar{J}_3 / \bar{J}_2^{3/2} \quad (3-7)$$

$$\bar{J}_2 = \text{tr} \bar{s}^{-2} \quad (3-8)$$

$$\bar{J}_3 = \text{tr} \bar{s}^{-3} \quad (3-9)$$

$$\bar{s} = s - \bar{p} a_c \quad (3-10)$$

M_k in Equation (3-6) is the material parameter. For a Drucker-Prager circular cone: $M_k = 1.0$, whereas for a round-cornered Mohr-Coulomb cone used in this study:

$$M_k = \frac{3 - \sin\phi}{3 + \sin\phi} \quad (3-11)$$

It is mentioned that by using the Mohr-Coulomb model the friction angle in extension can be specified to be the same as the one in compression.

The plastic potential is defined by the following equation (Prevost 2002):

$$\text{tr} \mathbf{P} = X_{pp} (\bar{\eta}^{-2} - 1) / (\bar{\eta}^{-2} + 1) \quad (3-12)$$

where \mathbf{P} is the symmetric second order tensor representing the direction of plastic deformations, X_{pp} is the dilation parameter, and $\bar{\eta}$ is the normalized stress ratio as defined by:

$$\bar{\eta} = \eta / \eta_{\psi} \quad (3-13)$$

$$\eta = \left\{ \frac{3}{2} \text{tr } s^2 \right\}^{1/2} / \bar{p} \quad (3-14)$$

In Equations (3-13) and (3-14), η is the mobilized stress ratio and η_ψ corresponds to the stress ratio mobilized at the phase transformation angle, ψ . In this thesis, ψ is also called dilation angle (e.g., Prevost 1989), which in fact represents the mobilized friction angle at which dilation starts.

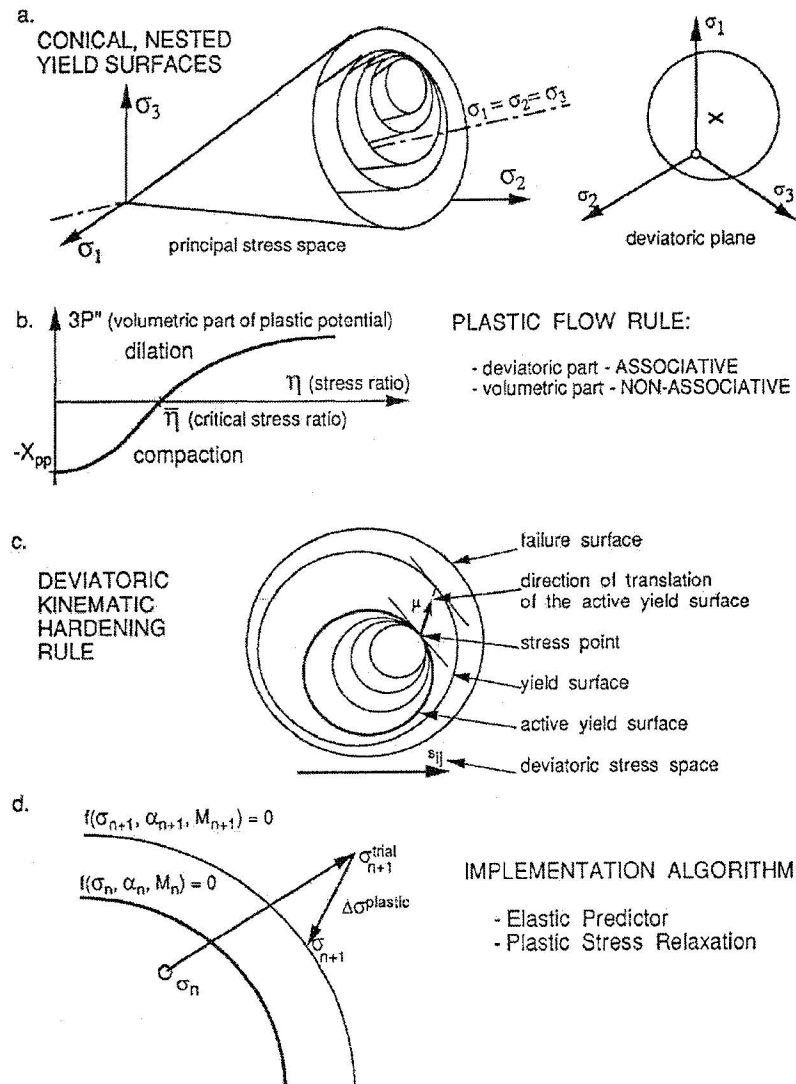


Figure 3.1 Main features of the multi-yield plasticity soil constitutive model. The Drucker-Prager type surfaces are shown in this figure (after Popescu, 1995).

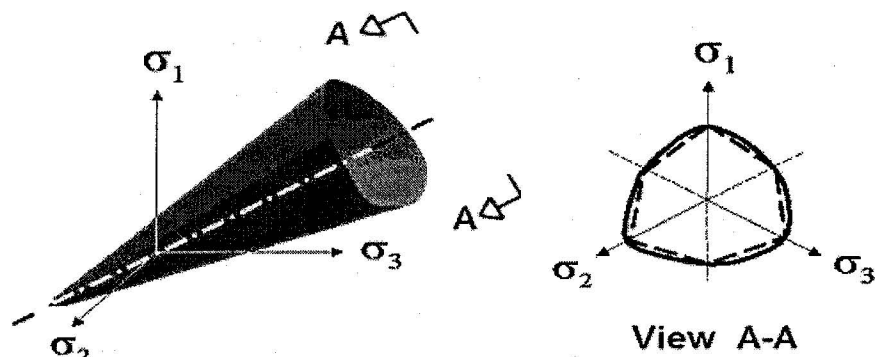


Figure 3.2 Schematic presentation of a typical round cornered Mohr-Coulomb type yield surface.

3.3.2 Constitutive parameters of the multi-yield plasticity soil model

The constitutive parameters of the multi-yield plasticity soil model are listed in Table 3.1. The model constitutive parameters can be generalized into state parameters (obtained from general laboratory soil tests), low-strain behavior parameters (describing elastic deformability parameters and their evolution with effective confining stress), yield and failure parameters (used for generating the nested yield surfaces), and dilation parameters (used to describe the plastic behavior). Yield parameters along with the low-strain shear modulus, G_0 , are used to obtain the initial position, size, and plastic modulus of each yield surface based on a modified hyperbolic function proposed by Prevost and Keane (1989) or Griffiths and Prevost (1990) covering a wide range of soil stress-strain relations. It should be noted that parameter k_0 is only used by the software for generating deviatoric stress-strain backbone curves (e.g., Griffiths and Prevost, 1990). Damping is accounted for by the software (Dynaflow) based on correctly simulating the hysteretic behavior of the soil (e.g., Prevost 1989). All the necessary parameters of the multi-yield

model except for the dilation parameter can be estimated from the results of conventional field or laboratory soil tests. The dilation parameter, X_{pp} , is obtained from liquefaction strength analysis (e.g., Popescu and Prevost, 1993) based on element tests (numerical simulations of undrained cyclic triaxial or simple shear tests). A detailed procedure for calibrating the multi-yield plasticity soil constitutive model for Fraser River sand is presented in Chapter 4.

Table 3.1 Parameters of the multi-yield plasticity soil constitutive model.

Type	Property	Symbol
State Parameters	Solid mass density	ρ_s
	Porosity	n^w
	Hydraulic conductivity	k
Low-strain parameters	Shear modulus	G_0
	Power exponent	n_p
	Poisson's ratio	ν
Yield and failure parameters	Friction angle at failure	ϕ
	Coefficient of earth pressure at rest	k_0
	Maximum deviatoric strain	ϵ_{dev}^{max}
Dilation parameters	Dilation angle (phase transformation angle)	ψ
	Dilation parameter	X_{pp}

3.4 *A constitutive formulation for nearly saturated liquefiable sands*

3.4.1 *Assumptions*

The formulation described here is based on the following main assumptions:

- Air is considered as an ideal gas. The ideal gas law is an acceptable approximation for the ranges of pressures and temperatures commonly encountered in geotechnical engineering (Fredlund and Rahardjo, 1993).

- The absolute pressures of the pore fluid constituents are considered to be identical. This corresponds to neglecting the effects of surface tension as suggested by other researchers (e.g., Byrne et al., 2004a; Grozic et al., 2005; and Hilf, 1948). A discussion related to the implications of this assumption is provided in the section on the scope and limitations of the proposed formulation at the end of the chapter.
- All the physical processes considered in the model are assumed to be isothermal. The assumption is reasonable since no significant change in temperature is expected in a real field situation due to pore pressure changes.
- Compressibility of pure water is assumed to be negligible as compared to the compressibility of pore water containing air bubbles.

3.4.2 Physical laws used in the proposed constitutive formulation

The physical laws used in the proposed constitutive formulation include ideal gas law, Henry's law and Fick's law (corresponding to transient air dissolution in water). These physical laws are expressed by Equations (3-15) to (3-17) (e.g., Fredlund and Rahardjo, 1993; and De Nevers, 2002). The subscript a used in these equations refers to air.

$$U_a V_a = nRT \quad \text{Ideal gas law} \quad (3-15)$$

$$U_a = Hx \quad \text{Henry's law} \quad (3-16)$$

$$\frac{dM_t}{dt} = -DA \frac{\partial C}{\partial r} \quad \text{Fick's law} \quad (3-17)$$

In the ideal gas law, U_a is the absolute pressure of air, V_a is the volume of air, T is the absolute air temperature, n is the number of gas (air) moles, and R is the universal gas constant. An ideal gas is a gas that obeys the ideal gas law. For an isothermal process (i.e., at constant temperature), the ideal gas law reduces to the Boyle's law ($U_a V_a = \text{CONSTANT}$).

In Equation (3-16), x is the mole fraction of the dissolved gas in a liquid at equilibrium condition (i.e., related to the maximum dissolvable mass of the gas phase estimated by the Henry's law at the corresponding absolute pressure), and H is Henry's constant, depending on temperature. This form of the Henry's law is the simplest form of this law since x is a dimensionless quantity and H has the dimension of pressure.

In Equation (3-17) $\frac{dM_t}{dt}$ is the mass rate of gas (air) flowing through the area A , D is the coefficient of diffusion, C is the concentration of air in water (mass of the dissolved air per unit volume of water), and $\frac{\partial C}{\partial r}$ represents concentration gradient in the r-direction.

In this chapter, M_t refers to the additional mass of air (in addition to the one already dissolved) that dissolved in water due to pore pressure changes (i.e., $M_t = 0$ at the beginning). The mass of free gas (air) in a mixture of air and water, M_{fa} , can be expressed by Equation (3-18) in which m_a is the molecular mass of air, or Equation (3-19) obtained from the ideal gas law.

$$M_{fa} = n m_a \quad (3-18)$$

$$M_{fa} = \frac{m_a U_a V_a}{RT} \quad (3-19)$$

Also, the volume of air as an ideal gas in Equation (3-15) can be written in terms of soil degree of saturation, S , and the volume of water, V_w (or mass of water, M_w , and its density, ρ_w) as expressed by Equation (3-20). Therefore, M_{fa} can be expressed by Equation (3-21).

$$V_a = \frac{1-S}{S} V_w = \frac{(1-S)M_w}{S\rho_w} \quad (3-20)$$

$$M_{fa} = \frac{m_a M_w U_a (1-S)}{\rho_w R T S} \quad (3-21)$$

Equation (3-21) indicates that the mass of free air is related to temperature. Thus, due to the isothermal assumption made in Section 3.4.1, temperature appears as a constant in the proposed formulation in this chapter. This is due to the fact that the model proposed here is based on the law of conservation of mass as presented later.

The mass of air dissolved in water at equilibrium conditions, M_{da} , is obtained from the Henry's law. The mole fraction x of air dissolved in water is expressed by:

$$x = \frac{\frac{M_{da}}{m_a}}{\frac{M_{da}}{m_a} + \frac{M_w}{m_w}} \quad (3-22)$$

In Equation (3-22), m_w is the molecular mass of water and the other symbols have already been explained. If x is eliminated between Equations (3-16) and (3-22), an alternative form of the Henry's law is obtained as expressed by Equation (3-23).

$$M_{da} = \frac{M_w m_a U_a}{m_w (H - U_a)} \quad (3-23)$$

3.4.3 Compressibility of pore fluid

A simplified approach to account for the effects of partial saturation is to consider a value for the bulk modulus of the fluid phase as an equivalent bulk modulus of the air-water mixture. Based on the assumption that surface tension effects are neglected, i.e., assuming the same absolute pressures for the pore fluid constituents ($U_a = U_w = U$) Koning (1963) developed an expression for the equivalent bulk modulus of the air-water mixture.

$$\frac{1}{B_v} = \frac{1-S}{U} + \frac{S}{B_w} \quad (3-24)$$

Equation (3-24) shows the variation of the equivalent bulk modulus of the pore fluid, B_v , as a function of absolute pore fluid pressure, U , bulk modulus of water, B_w , and the soil degree of saturation, S . Figure 3.3 shows the variation of B_v/B_w (bulk modulus ratio) with the degree of saturation for two different absolute pore pressures based on Equation (3-24). The presence of air (even 1%, i.e., $S = 0.99$) decreases very significantly the value of the equivalent bulk modulus of the mixture, and consequently increases the compressibility of the air-water mixture. In fact, the bulk modulus of pore fluid is very sensitive to the presence of gas in soils and even a small amount of air should be accounted for.

As the phenomenon of dissolution of air in water and changes in the volume of the air phase are functions of the absolute pressure (see Equations (3-15) and (3-16)), the degree of saturation in Equation (3-24) is also a function of the absolute pore pressure. Consequently, in order to find a relationship between the pressure and the equivalent bulk

modulus of the pore fluid in a nearly saturated soil, it is required to find how the degree of saturation changes due to changes in absolute pressure. This question is answered by the new constitutive formulation discussed hereafter.

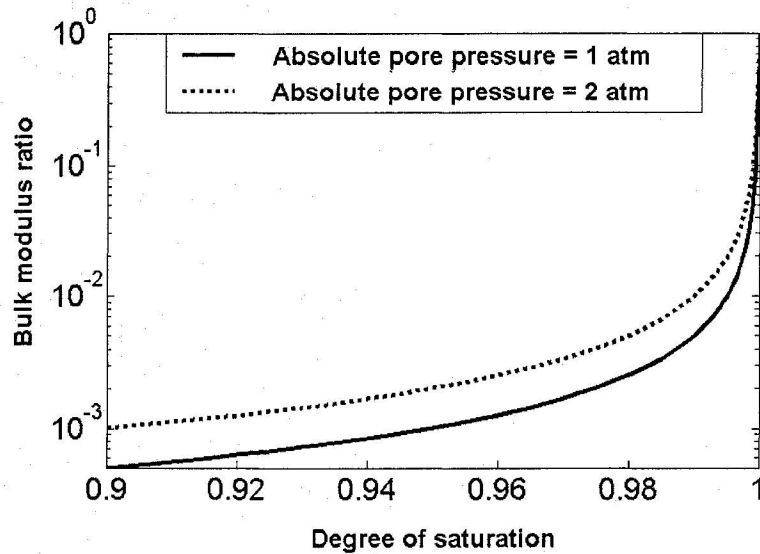


Figure 3.3 Variation of pore fluid bulk modulus ratio, B_v/B_w , due to changes in the soil degree of saturation for two different absolute pore pressures.

3.4.4 Conservation of mass

A constitutive formulation for partially saturated soils, which accounts for variation of the degree of saturation due to changes in the pore fluid pressure, should, in principle, comply with conservation of mass. In fact, the air in a partially saturated soil can exist either as free gas or dissolved in water. According to the law of conservation of mass, the total mass of the gas phase, i.e., the sum of the free and dissolved gas should remain constant and not depend upon the variation of the pore fluid pressure. It is very important to note that the Henry's law is valid only for an equilibrium condition in which under a constant pressure no further mass of gas is exchanged between the gas and water phases

in the mixture. This can be true for long term loading conditions such as static and slow monotonic loads, where there is sufficient time for the maximum amount of free gas denoted in Equation (3-22) by the mole fraction x to be dissolved in the water phase. However, during earthquakes and cyclic loads, any disturbance in the pore fluid pressure may trigger the process of gas (air) dissolution; this process then continues and the amount of gas (air) dissolved in water may consequently vary with time. Therefore, the dissolution of gas in water due to a variable pressure condition is a mass transfer problem and can be explained by the principle of gas diffusion.

For example, consider a soil element subjected to an absolute pore fluid pressure change from U_0 to $U > U_0$. The maximum amount of free air that can be dissolved in water in addition to the initial dissolved air due to this pressure change is equal to the difference between the mass of the dissolved air corresponding to equilibrium conditions at U_0 and U and is denoted by M_{max} . Therefore, according to Henry's law (Equation (3-23)), M_{max} can be expressed as:

$$M_{max} = \left(\frac{M_w m_a U}{m_w (H - U)} - \frac{M_w m_a U_0}{m_w (H - U_0)} \right) \quad (3-25)$$

The change in the absolute pore fluid pressure from U_0 to U results in a change in the soil degree of saturation from its initial value, i.e., S_0 to a final value, S . Conservation of mass implies that the difference in the mass of free gas between the initial and final states is equal to the mass of air dissolved in water during the transition between these states. The mass of air dissolved in water during the transition can be expressed as a

fraction of M_{max} , or alternatively, as a fraction of the initial mass of free gas, represented hereafter by mass fractions m_d^* (with respect to M_{max}) and m_t^* (with respect to the initial mass of free gas), respectively. Based on Equations (3-21) and (3-25), conservation of mass can be expressed as Equation (3-26) in terms of m_d^* , or alternatively, as Equation (3-27) in terms of m_t^* .

$$\frac{m_a M_w U_0 (1 - S_0)}{\rho_w R T S_0} - \frac{m_a M_w U (1 - S)}{\rho_w R T S} = m_d^* \left(\frac{M_w m_a U}{m_w (H - U)} - \frac{M_w m_a U_0}{m_w (H - U_0)} \right) \quad (3-26)$$

$$\frac{m_a M_w U_0 (1 - S_0)}{\rho_w R T S_0} - \frac{m_a M_w U (1 - S)}{\rho_w R T S} = m_t^* \frac{m_a M_w U_0 (1 - S_0)}{\rho_w R T S_0} \quad (3-27)$$

The left hand sides of Equations (3-26) and (3-27) represent the difference in the mass of the free gas at the initial and final states due to a pressure change from U_0 to U . Simplifying Equations (3-26) and (3-27) results in Equations (3-28) and (3-29), respectively, expressing changes in the soil degree of saturation as a function of absolute pressure.

$$S = \frac{U}{\left\{ \frac{1 - S_0}{S_0} U_0 + U - \frac{m_d^* \rho_w R T H (U - U_0)}{m_w (H - U) (H - U_0)} \right\}} \quad (3-28)$$

$$S = \frac{U}{\left\{ (1 - m_t^*) \frac{1 - S_0}{S_0} U_0 + U \right\}} \quad (3-29)$$

In Equation (3-28), the condition $m_d^* = 0$ refers to the case that no additional mass of air is dissolved in water compared to the initial condition, and the mass of free air remains constant. However, changes in the volume of free air due to changes in the

absolute pore pressure obey the Boyle's law. This case (i.e., $m_d^* = 0$) represents a lower bound for variation of the soil degree of saturation due to changes in the absolute pore pressure. In contrast, the condition $m_d^* = 1$ refers to the case where the maximum amount of free air that can be dissolved in water in addition to the initial dissolved air (i.e., M_{max} as expressed by Equation (3-25)) is actually dissolved in water. This case (i.e., $m_d^* = 1$) represents an upper bound for variation of the soil degree of saturation due to changes in the absolute pore pressure. The lower and upper bounds of the soil degree of saturation, i.e., S_{low} and S_{up} resulting from Equation (3-28), are expressed by Equations (3-30) and (3-31), respectively.

$$S_{low} = \frac{U}{\left\{ \frac{1-S_0}{S_0} U_0 + U \right\}} \quad (3-30)$$

$$S_{up} = \frac{U}{\left\{ \frac{1-S_0}{S_0} U_0 + U - \frac{\rho_w RTH(U-U_0)}{m_w(H-U)(H-U_0)} \right\}} \quad (3-31)$$

Under certain conditions, due to a pore fluid pressure change, the entire mass of gas can be dissolved in water. In this case, the soil becomes fully saturated. The absolute pore pressure at which the soil becomes saturated is called saturation pressure and is denoted by U_{sat} in the following. This pressure is obtained from Equation (3-31) by substituting $S_{up} = 1$. This results in the following expression:

$$U_{sat} = \frac{\left\{ \frac{1-S_0}{S_0} U_0 m_w H(H-U_0) + \rho_w RTH U_0 \right\}}{\left\{ \frac{1-S_0}{S_0} U_0 m_w (H-U_0) + \rho_w RTH \right\}} \quad (3-32)$$

It is readily noted from Equation (3-32) that for an initially saturated soil ($S_0 = 1$) U_{sat} is equal to U_0 . Figure 3.4 shows the variation of U_{sat} versus initial degree of saturation for different initial absolute pore pressures. This figure indicates that the higher the initial soil degree of saturation, the lower the saturation pressure. The values of constants used for plotting this figure are $R = 8314 \text{ J/kmol.K}$, $m_w = 18 \text{ kg/kmol}$, and $H = 6.64 \times 10^9 \text{ Pa}$ at a temperature of 20° C (e.g., Perry and Green, 1997).

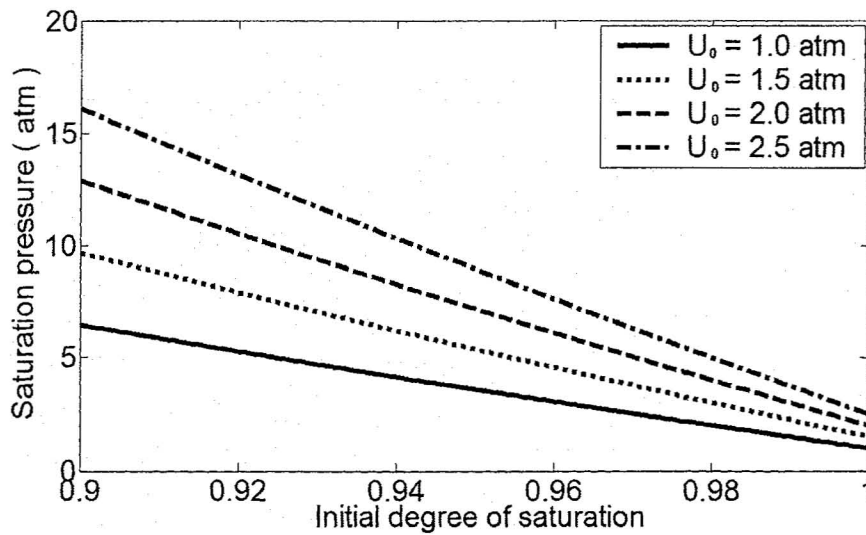


Figure 3.4 Variation of saturation pressure versus initial soil degree of saturation for different initial absolute pore pressures at a temperature of 20° C .

A relationship between m_d^* and m_t^* is important in order to set a limit for dissolution of air in water. The desired relationship can be obtained by comparing Equations (3-28) and (3-29) as expressed by Equation (3-33).

$$m_d^* = \frac{m_w U_0 (1 - S_0) (H - U) (H - U_0)}{S_0 \rho_w R T H (U - U_0)} m_t^* \quad (3-33)$$

3.4.5 Transient air dissolution

In Equation (3-29) (or Equation (3-28)), it is necessary to know the value of the transient mass fraction of the dissolved air, m_t^* (or m_d^*). This requires an assumption for the mechanism of air dissolution in water. Since in soils with high degrees of saturation the air phase exists as discrete bubbles (Fredlund and Rahardjo, 1993), the proposed model includes a single spherical air bubble (representative air bubble) and its surrounding water as shown in Figure 3.5 (during a time interval Δt). The assumed spherical domain considered in this model is such that at any time radii $a(t)$ and $b(t)$ are related to each other by the soil degree of saturation. Subscripts I and F in Figure 3.5 and hereafter in this chapter represent the initial (at the beginning of the time interval Δt) and the final (at the end of the time interval Δt) values of variables, respectively. Also, subscript 0 represents the initial value of a variable at the very beginning (e.g., a_0 represents the initial radius of the representative air bubble).

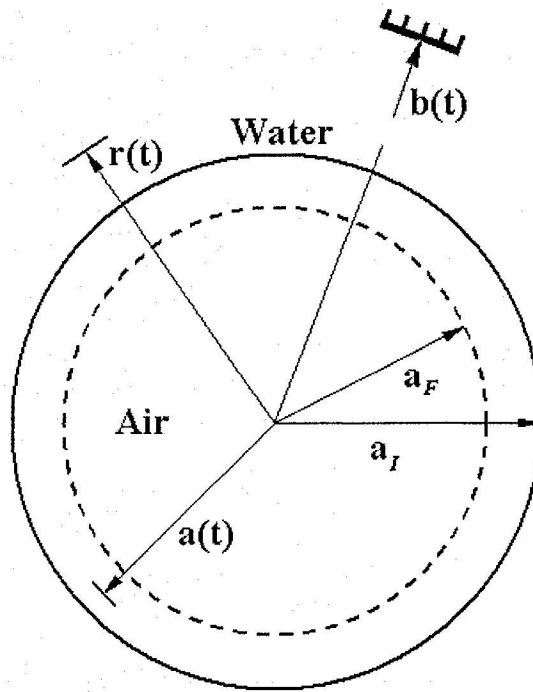


Figure 3.5 Single air bubble model used to compute the transient mass fraction of the dissolved air in water.

As stated in Section 3.4.4 the dissolution phenomenon is explained by the diffusion equation. However, since the radius of the air bubble varies with respect to time, the corresponding diffusion equation is a partial differential equation (PDE) with moving boundary conditions. Based on the Fick's diffusion law, the PDE related to the dissolution of air in water in spherical coordinates with radial symmetry is written in the form of Equation (3-34) (Crank, 1975). The boundary and initial conditions of Equation (3-34) considered within the time interval Δt are expressed by Equations (3-35) to (3-37). The function $C(r, t)$ represents transient concentration of the dissolved air in water, i.e., transient mass of the dissolved air per unit volume of water, and it has the dimension of specific mass. It is noted that this function is different from x (mole fraction) in the sense that x refers to dimensionless concentration of the air phase in water at equilibrium

condition expressed by the Henry's law (Equation (3-22)). The factor D in Equation (3-34) is the coefficient of diffusion. Also, $C_s(t)$ is the concentration at the interface between air and water at $r = a$ (i.e., only a function of time), and $C_I(r)$ is the concentration at the beginning of the time interval (i.e., only a function of position). The variables r and t are two independent variables representing position and time, respectively and $C(r, t)$ varies with both of them.

$$\frac{\partial C}{\partial t} = D \left(\frac{\partial^2 C}{\partial r^2} + \frac{2}{r} \frac{\partial C}{\partial r} \right) \quad 0 < t < \Delta t \quad (3-34)$$

$$C(a(t), t) = C_s(t) \quad t > 0 \quad (3-35)$$

$$C(b(t), t) = C_b(t) \quad t > 0 \quad (3-36)$$

$$C(r, 0) = C_I(r) \quad r \geq a_I \quad (3-37)$$

For this type of diffusion problems the following change of variable is considered (Crank, 1975):

$$z = \frac{r}{\sqrt{Dt}} \quad t > 0 \quad (3-38)$$

Using Equation (3-38) results in the following form for the diffusion equation (Crank, 1975):

$$\frac{\partial^2 C}{\partial z^2} = - \left(\frac{z}{2} + \frac{2}{z} \right) \frac{\partial C}{\partial z} \quad (3-39)$$

Equation (3-39) is a first order ordinary differential equation (ODE) in terms of $\frac{\partial C}{\partial z}$.

The solution of Equation (3-39) is: (Crank, 1975)

$$\frac{\partial C}{\partial z} = E z^{-2} \exp\left(-\frac{z^2}{4}\right) \quad (3-40)$$

The coefficient E in Equation (3-40) is the integration constant of the ODE and can be obtained from the boundary conditions. At the interface of air and water ($r = a$), the equilibrium condition is satisfied and the concentration of air in water is:

$$C_s = \frac{M_{da}}{V_w} \quad (3-41)$$

Substituting Equation (3-23) in Equation (3-41) results in:

$$C_s = \frac{\rho_w m_a U}{m_w (H - U)} \quad (3-42)$$

Also, from Equation (3-38):

$$\frac{\partial C}{\partial t} = \frac{\partial C}{\partial z} \frac{-z}{2t} \quad (3-43)$$

Substitution of Equations (3-38) and (3-42) in Equation (3-43) gives:

$$\frac{\partial C}{\partial t} = \frac{-E \sqrt{Dt}}{2rt} \exp\left(-\frac{r^2}{4Dt}\right) \quad (3-44)$$

At the interface of air and water, the following condition exists:

$$\left(\frac{\partial C}{\partial t}\right)_{r=a} = \frac{dC_s}{dt} \quad (3-45)$$

From Equation (3-42):

$$\frac{dC_s}{dt} = \frac{m_a \rho_w H}{m_w (H - U)^2} \frac{dU}{dt} \quad (3-46)$$

Therefore, from Equations (3-44), (3-45) and (3-46), the integration constant, E , is expressed in the following form:

$$E = \frac{Hm_a \rho_w (-2at)}{m_w (H-U)^2 \sqrt{Dt} \exp\left(-\frac{a^2}{4Dt}\right)} \frac{dU}{dt} \quad (3-47)$$

Using the Fick's law, the mass rate of the gas flowing through the interface area A_b is obtained by the following Equation: (Fredlund and Rahardjo, 1993; and Crank, 1975)

$$\frac{dM_{bt}}{dt} = -DA_b \left(\frac{\partial C}{\partial r} \right)_{r=a} \quad (3-48)$$

In Equation (3-48), $A_b = 4\pi a^2$ is the surface of the air bubble (interface area) and M_{bt} is the transient mass of air (in addition to the initially dissolved air) flowing through the interface area. Also, from Equation (3-38):

$$\left(\frac{\partial C}{\partial r} \right)_{r=a} = \left(\frac{\partial C}{\partial z} \frac{1}{\sqrt{Dt}} \right)_{r=a} \quad (3-49)$$

Expanding Equation (3-49) based on Equations (3-38), (3-40) and (3-47) and substituting the result in Equation (3-48) will give the following relationship for the transient mass rate of the dissolved air in water.

$$\frac{dM_{bt}}{dt} = \frac{8\pi D H m_a \rho_w t a}{m_w (H-U)^2} \frac{dU}{dt} \quad (3-50)$$

M_{bt} is a fraction of the initial mass of the representative air bubble (i.e., M_{b0}). The initial mass of the representative air bubble, M_{b0} , can be written in terms of the initial absolute pore fluid pressure, U_0 , and the initial volume of the air bubble, V_{b0} (see Equation (3-19)).

Therefore:

$$M_{bt} = m_t^* M_{b0} = m_t^* m_a \frac{U_0 V_{b0}}{RT} \quad (3-51)$$

$$V_{b0} = 4 \pi a_0^3 / 3 \quad (3-52)$$

$$\frac{dM_{bt}}{dt} = \frac{(4 \pi a_0^3 / 3) U_0 m_a}{RT} \frac{dm_t^*}{dt} \quad (3-53)$$

Moreover, at any time m_t^* can be written in the following form:

$$m_t^* = \frac{\frac{m_a U_0 V_{b0}}{RT} - \frac{m_a U V_b}{RT}}{\frac{m_a U_0 V_{b0}}{RT}} = 1 - \frac{U V_b}{U_0 V_{b0}} \quad (3-54)$$

Since $V_b = 4 \pi a^3 / 3$, m_t^* will be:

$$m_t^* = 1 - \frac{U a^3}{U_0 a_0^3} \quad (3-55)$$

From Equation (3-55) the radius of the air bubble is:

$$a = a_0 \sqrt[3]{\frac{(1 - m_t^*) U_0}{U}} \quad (3-56)$$

Assuming a linear function for changes in the absolute pore pressure during the time interval, Δt , (i.e., $U = \alpha t + U_I$ with: $\alpha = \frac{U_F - U_I}{\Delta t}$), substituting Equations (3-56) and

$t = \frac{U - U_I}{\alpha}$ in Equation (3-50) and comparing this equation with Equation (3-53) result in

the following separable ODE for m_t^* :

$$\frac{dm_t^*}{\sqrt[3]{1 - m_t^*}} = \frac{6 R T D H \rho_w}{a_0^2 U_0^{2/3} m_w \alpha} \frac{(U - U_I)}{\sqrt[3]{U} (H - U)^2} dU \quad (3-57)$$

The Henry's constant, H , is a very large number (Perry and Green, 1997) ($H = 664000$ atm at a temperature of 20° C), and it can be considered that $H - U \approx H$. Therefore, Equation (6-57) becomes:

$$\frac{dm_t^*}{\sqrt[3]{1-m_t^*}} = \frac{6RTD\rho_w}{\alpha_0^2 U_0^{2/3} m_w H \alpha} \frac{(U-U_I)}{\sqrt[3]{U}} dU \quad (3-58)$$

Integration of Equation (3-58) within the time interval Δt , i.e., from m_{II}^* to m_{IF}^* and from U_I to U_F on both sides of the equation, results in the following expression:

$$1 - m_{IF}^* = \left\{ (1 - m_{II}^*)^{2/3} - \frac{Q}{\alpha U_0^{2/3}} \left[\frac{(U_F^{5/3} - U_I^{5/3})}{5} - \frac{U_I (U_F^{2/3} - U_I^{2/3})}{2} \right] \right\}^{3/2} \quad (3-59)$$

Q in Equation (3-59) is:

$$Q = \frac{12RTD\rho_w}{H\alpha_0^2 m_w} \quad (3-60)$$

The transient dissolved air mass fraction obtained from Equation (3-59) can be used to calculate the values of degree of saturation and equivalent bulk modulus of the air-water mixture at any time using Equations (3-29) and (3-24), respectively. In fact, Equations (3-59), (3-29) and (3-24) are the governing equations of the proposed formulation.

3.4.6 Limit of air dissolution

For absolute pore pressures higher than the initial pressure, U_0 , the transient dissolved air mass fraction, m_d^* (the one corresponding to M_{max}), should be within the following limits:

$$0 \leq m_d^* \leq 1 \quad (3-61)$$

As stated earlier in Section 3.4.4, conditions $m_d^* = 0$ and $m_d^* = 1$ correspond to no additional air dissolution (lower bound) and full dissolvable air dissolution (upper bound), respectively. Based on Relationship (3-61) and Equation (3-33), i.e., the relationship between m_d^* and m_t^* , the transient dissolved gas mass fraction in terms of the initial gas mass, m_t^* , has the following limit:

$$m_t^* \leq \frac{S_0 \rho_w RTH(U - U_0)}{m_w U_0 (1 - S_0)(H - U)(H - U_0)} \quad (3-62)$$

The integral form of Equation (3-58) in terms of U is:

$$m_t^* = 1 - \left\{ \frac{Q}{\alpha U_0^{2/3}} \left(\frac{U^{2/3} U_1}{2} - \frac{U^{5/3}}{5} \right) + \beta \right\}^{3/2} \quad (3-63)$$

with:

$$\beta = (1 - m_d^*)^{2/3} - \frac{3Q}{10 \alpha U_0^{2/3}} U_1^{5/3} \quad (3-64)$$

From the Relationships (3-62) and (3-63), the following inequality is obtained:

$$1 - \left\{ \frac{Q}{\alpha U_0^{2/3}} \left(\frac{U^{2/3} U_1}{2} - \frac{U^{5/3}}{5} \right) + \beta \right\}^{3/2} \leq \frac{S_0 \rho_w RTH(U - U_0)}{m_w U_0 (1 - S_0)(H - U)(H - U_0)} \quad (3-65)$$

This inequality sets implicitly a limit for air dissolution based on U at any time. Beyond this limit the solution of the diffusion equation is not valid and the upper limit should be considered for the variation of the soil degree of saturation, i.e., Equation (3-31).

3.4.7 Model constants and parameters

As explained in this section, Factor Q expressed by Equation (3-60) includes all the model constants and parameters. The initial radius of the representative air bubble, a_0 , (included in the expression of Q) depending on many factors such as soil porosity, grain size distribution, grain shapes, types of minerals, soil fabric, initial degree of saturation, and surface tension (related to temperature) should be selected to represent the effects of the air dissolution phenomenon on the compressibility of the pore fluid. The smaller the initial radius of the representative air bubble, the higher the rate of air dissolution. This is due to the fact that for the same volume of air in soil, assuming smaller air bubbles radii results in a higher total interface surface between the air and water phases, and consequently a higher rate of air dissolution in water.

At constant temperature and for a given soil with a given grain size distribution and porosity it is assumed that the initial volume of air in soil, V_{a0} , is proportional to the initial volume of the representative air bubble (i.e., proportional to $V_{b0} = 4/3\pi a_0^3$, or simply a_0^3). Also, V_{a0} is related to the volume of water, V_w .

$$V_{a0} = \frac{1 - S_0}{S_0} V_w \quad (3-66)$$

The volume of water, V_w , is assumed to be constant; consequently, a_0^3 is proportional to $\frac{I - S_0}{S_0}$. This results in the following expression for the initial radius of the representative air bubble:

$$a_0 = \lambda \sqrt[3]{\frac{I - S_0}{S_0}} \quad (3-67)$$

Coefficient λ is the coefficient of proportionality in Equation (3-67). The greater values of λ (i.e., higher initial radius of the representative air bubble) result in a smaller total interface area between air and water phases and consequently, a lower dissolution rate. Combining Equations (3-60) and (3-67) results in:

$$Q = \Omega T \left(\frac{S_0}{I - S_0} \right)^{2/3} \quad (3-68)$$

with:

$$\Omega = \frac{12 R D \rho_w}{H m_w \lambda^2} \quad (3-69)$$

Equation (3-68) shows that the proposed constitutive model has three parameters; temperature (T), initial degree of saturation (S_0) and parameter Ω , which is named hereafter as “*Transient Solubility Parameter*”. Temperature and initial degree of saturation are measurable parameters. The Transient Solubility Parameter, Ω , depends upon temperature (D and H directly depend on temperature, e.g., see Perry and Green, 1997; and Barden and Sides, 1967) and initial radius of the representative air bubble (through coefficient λ). This parameter can be considered as an adjusting parameter of the model including the effects of many other factors that could not be considered in the

constitutive equations. In fact, Ω provides the model with a desired versatility to match with experimental data. The SI unit of Ω is 1/K.s in which K and s account for the Kelvin temperature scale and time, respectively.

3.4.8 Model evaluation based on cyclic triaxial tests

This section presents a procedure for evaluating the proposed constitutive model based on a set of available liquefaction strength data obtained from the results of cyclic triaxial tests performed on partially saturated samples of Toyoura sand at a relative density of $D_r = 40\%$ (Tsukamoto et al., 2002). It is noted that Dynaflo does not include the proposed formulation; however, using the variable bulk modulus feature recently implemented in this code, it is possible to calibrate and validate the proposed model at the element level test as described in this section based on numerical simulations of the cyclic triaxial tests performed on unsaturated samples of Toyoura sand. Toyoura sand is a poorly graded clean fine sand with a specific gravity equal to 2.65, a mean particle size $D_{50} = 0.19\text{mm}$ uniformity coefficient $C_u = 1.70$, and the maximum and minimum void ratios $e_{max} = 0.988$ and $e_{min} = 0.616$. The height and diameter of the triaxial sand samples in those tests were 120mm and 60mm. The initial confining pressure was $\sigma_c = 98\text{kPa}$, and the cyclic deviatoric stresses, σ_d , were applied with a frequency of 0.1Hz. The test results were plotted as Cyclic Stress Ratio, $CSR = \frac{\sigma_d}{2\sigma_c}$, versus number of cycles to liquefaction. Liquefaction was considered to occur at 5% double amplitude axial strain in the samples. The Skempton's B pore pressure coefficient (Skempton, 1954) was

considered to be an indicator of the soil initial degree of saturation. If the compressibility of soil grains is neglected, this coefficient is defined as (Skempton, 1954):

$$B = \frac{1}{1 + n^w \frac{B_s}{B_v}} \quad (3-70)$$

where, n^w is the soil porosity, B_s is the bulk modulus of the soil skeleton, and B_v is the bulk modulus of pore fluid, obtained from Equation (3-24) based on the initial degree of saturation. It is noted that the B-values mentioned in this section correspond to the initial B-values at the beginning of the cyclic triaxial tests conducted by Tsukamoto et al. (2002). The bulk modulus of the soil skeleton is expressed in terms of the low-strain shear modulus and Poisson's ratio (G_0 and ν) as:

$$B_s = \frac{2G_0(1+\nu)}{3(1-2\nu)} \quad (3-71)$$

In this study the multi-yield plasticity soil constitutive model implemented in the finite element code Dynaflo was used to describe the soil stress-strain behavior and simulate the cyclic triaxial tests conducted by Tsukamoto et al. (2002).

The soil constitutive parameters listed in Table 3.2 have been estimated based on engineering judgment and available information on Toyoura sand at $D_r = 40\%$ (Pradhan and Tatsuoka, 1989; Pradhan et al., 1989; and Tsukamoto et al., 2002). As the detailed experimental data on Toyoura sand are not available, this approach for estimating the multi-yield plasticity soil constitutive model parameters may not be flawless and is regarded as a limitation of the study presented in this section. It is mentioned however that the same calibration procedure was used in all cases studied in this section that

resulted in good agreement between the recorded and predicted behavior. The dilation parameter, X_{pp} , has been obtained from liquefaction strength analysis using the information from the tests on fully saturated soil. This initial calibration of the multi-yield plasticity soil model was aimed at reasonably reproducing the liquefaction strength of fully saturated soil obtained in the laboratory experiments by means of numerical simulations. The axisymmetric finite element model used in this study for performing the numerical simulations is shown in Figure 3.6. The initial confining stress, $\sigma_c = 98\text{kPa}$, was applied at all the external boundaries of the finite element model. The cyclic deviatoric stress, σ_d , was applied at the top of the finite element model. The base is fixed in vertical direction. All the external boundaries were assumed impervious.

The measured and predicted liquefaction strength curves (related to the tests performed on fully saturated samples) are shown in Figure 3.7 by a continuous and a dashed line, respectively. The proposed model for nearly saturated soils was calibrated based on the given liquefaction strength curve for a B-value of 0.2 (corresponding to an initial degree of saturation $S_0 = 98.54\%$ obtained from Equations (3-24), (3-70) and (3-71) and the assumed set of soil constitutive parameters listed in Table 3.2). For this purpose, the Variable Fluid Bulk Modulus option, recently implemented in Dynaflow, was used to perform the numerical simulations.

Table 3.2 Assumed set of soil constitutive parameters for Toyoura sand at $D_r = 40\%$.

Property	Symbol	Value
Grain mass density (kg/m^3)	ρ_s	2650
Porosity	n^w	0.4563
Hydraulic conductivity (cm/s)	k	0.04
Shear modulus (MPa)	G_0	20
Power exponent	n_p	0.5
Poisson's ratio	ν	0.35
Friction angle at failure	ϕ	34°
Coeff. of earth pressure at rest	k_0	1
Maximum deviatoric strain (both in compression and extension)	ε_{dev}^{max}	0.01
Dilation angle	ψ	28°
Dilation parameter	X_{pp}	0.6
Temperature (K)	T	293.16
Transient solubility parameter (1/K.s)	Ω	0.0264
Initial degree of saturation	S_0	see below

Note: Three initial degrees of saturation considered in the numerical analyses corresponding to calibration and validation of the proposed model are $S_0 = 96.72\%$, $S_0 = 98.54\%$, and $S_0 = 99.76\%$ corresponding to initial B-values of 0.1, 0.2, and 0.6, respectively.

The temperature was assumed to be constant at 20°C (equal to an absolute temperature of $T = 293.16\text{ K}$) as it was mentioned by Tsukamoto et al. (2002) for measuring the velocity of compression waves. The pore fluid bulk moduli at each spatial location (finite element centroid) were updated at the end of each loading cycle based on the calculated pore pressure. The updated fluid bulk moduli were used to calculate the pore fluid pressure at the end of the next loading cycle. Figure 3.7 shows the results of the numerical simulations related to calibration and validation of the proposed model in terms of CSR and number of cycles to liquefaction. Also, at $B = 0.2$ the liquefaction strengths corresponding to upper and lower bounds of the proposed model were obtained and

plotted in Figure 3.7. A value of $\Omega = 0.0264$ 1/K.s is required to match the numerical results with the experiments at $B = 0.2$.

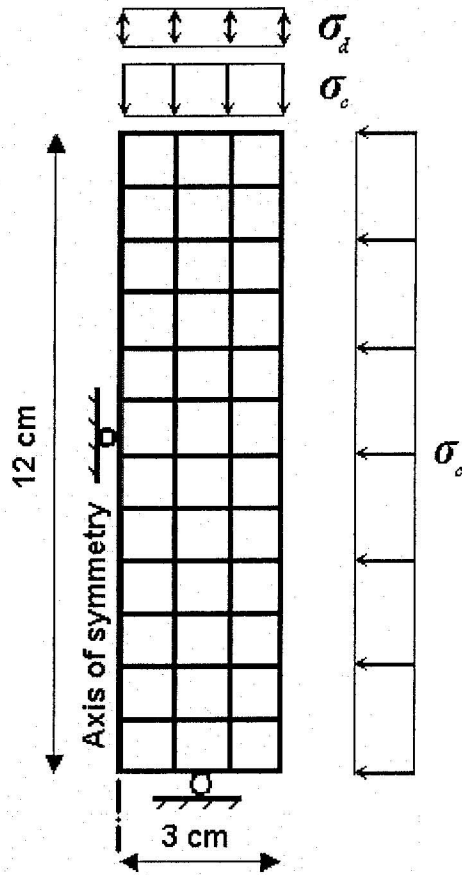


Figure 3.6 The finite element mesh used in this study for simulating the cyclic triaxial tests conducted by Tsukamoto et al. (2002).

The calibrated numerical model was then validated based on the numerical simulations of two other available experiments at $B = 0.1$ and $B = 0.6$ related to initial degrees of saturation equal to $S_0 = 96.72\%$ and $S_0 = 99.76\%$, respectively. Table 3.3 presents quantitative comparisons between the numerical and experimental results. As shown in Figure 3.7 and Table 3.3, the results of the numerical simulations are in very good agreement with their experimental counterparts. Figure 3.8 shows the predicted

excess pore pressure ratio vs. number of cycles corresponding to the numerical model ($\Omega = 0.0264 \text{ 1/K.s}$) and the upper and lower bounds analyses at $B = 0.2$. The predicted results by the numerical model and the lower bound are very close to each other at $B = 0.2$ (see Figure 3.8). The predicted excess pore pressure ratios vs. number of cycles at different degrees of saturation are shown in Figure 3.9. The results show that the liquefaction resistance is highly dependent upon the initial degree of saturation. For example, significantly more pore pressure build-up is predicted for the almost saturated soil ($B = 0.6$ and $S_0 = 99.76\%$) at a $CSR = 0.166$ than for a soil with lower degree of saturation ($S_0 = 96.72\%$) at a much larger CSR (i.e., $CSR = 0.229$). It is noted that numbers like 99.76% for the soil degree of saturation came from the fact that the experimental data were given based on B-values not the degree of saturation.

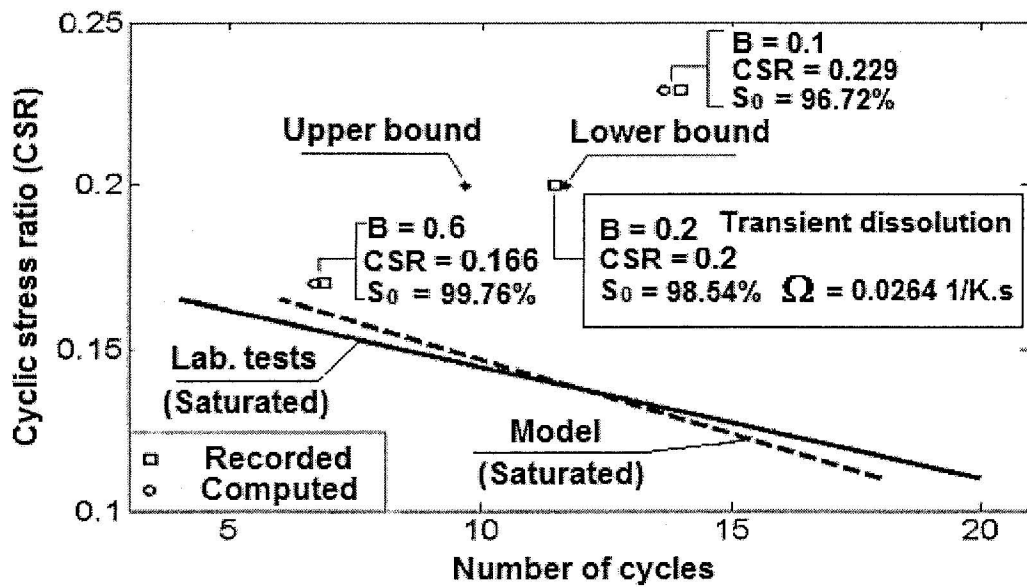


Figure 3.7 Calibration and validation of the proposed constitutive model for nearly saturated Toyoura sand at 40% relative density based on the numerical simulations of the cyclic triaxial tests performed by Tsukamoto et al. (2002).

Table 3.3 Quantitative comparisons between the numerical and experimental results.

Initial B-value	Initial degree of saturation (%)	CSR	Number of cycles	
			Experiment	Numerical Model
0.1	96.72	0.229	14	13.7
0.2	98.54	0.20	11.6	11.6
0.6	99.76	0.166	6.9	6.7

3.4.9 Scope and limitations of the proposed formulation

The constitutive formulation presented in this chapter is intended for analysis of liquefaction susceptibility of nearly saturated sands ($S_0 = 95\%$ and higher). In this section, some limitations of using the proposed constitutive model for liquefaction analysis are discussed.

Unlike undrained behavior of a fully saturated soil with practically incompressible pore fluid, nearly saturated soils have more compressible pore fluid and may experience changes in void ratio during undrained loading. These changes induce variations in relative density (and therefore in soil strength) and in hydraulic conductivity. For the degrees of saturation and stress levels analyzed in this study these variations are relatively small (e.g., Fredlund et al., 1997; Huang et al., 1998; and Yang et al., 2004) and have been neglected in the numerical simulations.

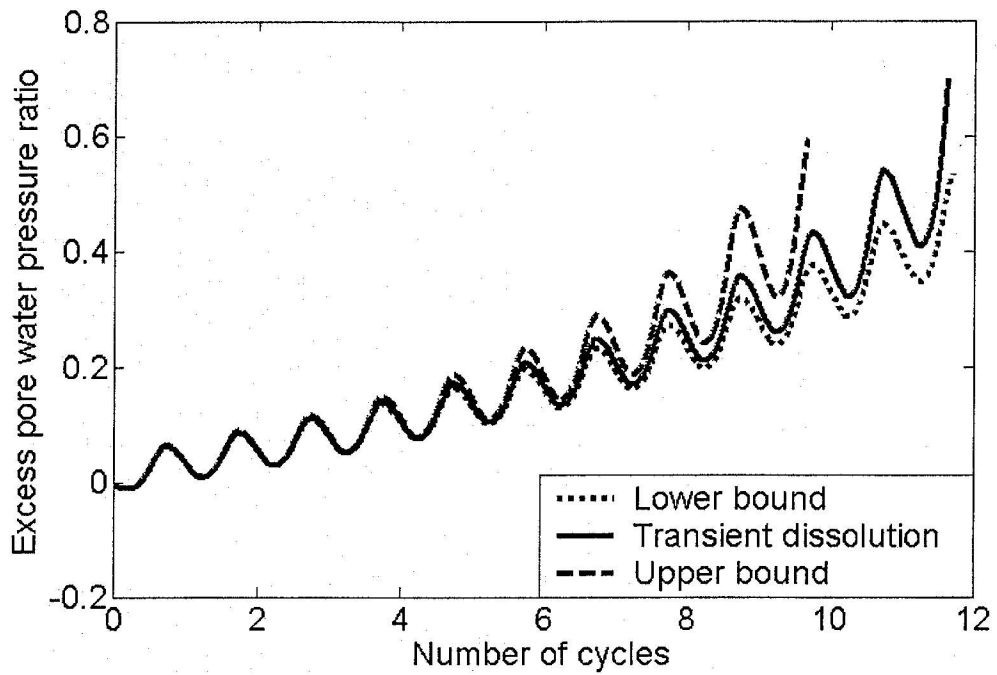


Figure 3.8 Upper and lower bounds as well as model predictions of the excess pore pressure ratios at $B = 0.2$ (i.e., for a $CSR = 0.2$ and an initial degree of saturation equal to 98.54%).

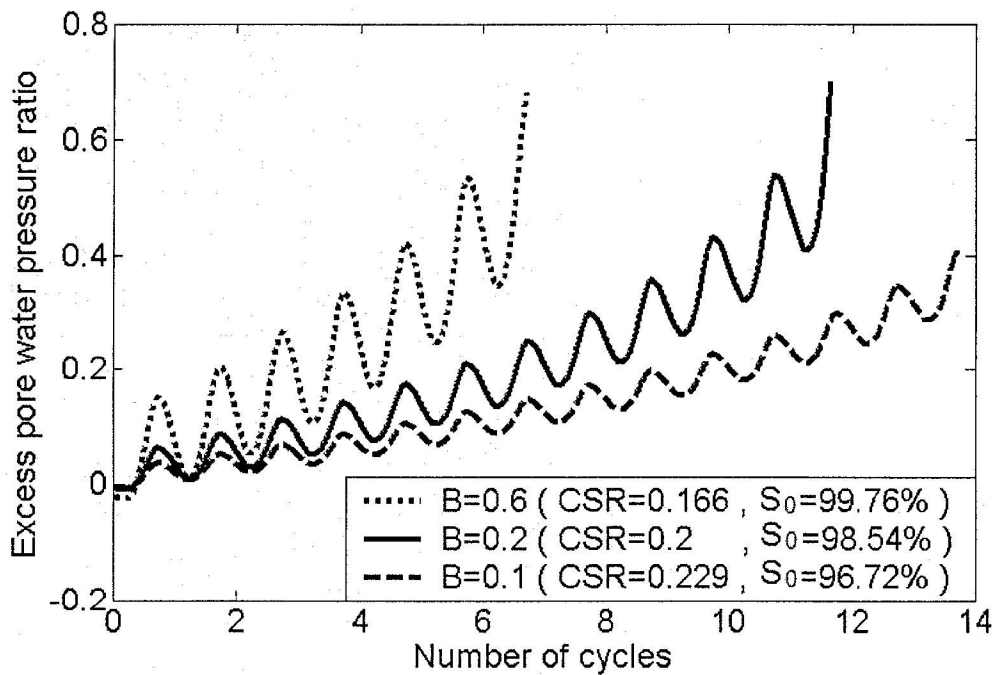


Figure 3.9 Predicted excess pore pressure ratios at different degrees of saturation and different cyclic stress ratios based on the laboratory experiments by Tsukamoto et al. (2002).

One of the assumptions made in the proposed constitutive formulation is related to neglecting the effects of surface tension as also assumed by other researchers (e.g., Byrne et al., 2004a; Grozic et al., 2005; and Hilf, 1948). The numerical predictions by the proposed formulation depend very much on the size of air bubbles. There is a relation between the radius of each bubble and its internal pressure based on surface tension. Surface tension directly affects the radius of each bubble, which subsequently changes the amount of air dissolution. The idea of using a representative air bubble scales the amount of the gas mass dissolved in water. In fact, by providing flexibility in selecting parameter Ω (that depends on the initial radius of the representative air bubble as discussed in Section 3.4.7) the overall effects of surface tension on the compressibility of the pore fluid are implicitly considered in the proposed formulation. Directly considering surface tension effects requires a number of assumptions that may not be realistic (e.g., Iveson, 2003). Moreover, as mentioned earlier in Section 3.4.7 there may be many factors affecting the initial size of the representative air bubble such as soil porosity, grain size distribution, grain shapes, types of minerals and their effects on the surface behavior at the interface between the soil, water and air, soil fabric, initial degree of saturation as well as the amount of contaminants in pore water (e.g., salts, etc.). By calibrating Ω based on experimental results obtained for the soil of interest all these factors are somehow included in the analysis.

As stated in Section 3.4.8, the frequency in the cyclic triaxial tests performed on nearly saturated sand samples of Toyoura sand was $f = 0.1\text{Hz}$ (Tsukamoto et al., 2002), which is about one order of magnitude less than that observed in most earthquakes.

Therefore, a numerical study was performed to investigate the effects of loading frequency on the seismic behavior of nearly saturated Toyoura sand. In this respect, using the calibrated numerical model and assuming an initial soil degree of saturation equal to $S_0 = 98\%$ and a cyclic stress ratio equal to $CSR = 0.2$, a number of numerical simulations were conducted for a range of frequencies between 0.1Hz to 2Hz. The study indicated that for a range of frequencies higher than 0.75Hz, the number of stress cycles required for liquefaction ($N = 15.6$ cycles) is equal to that of the lower bound analysis, i.e., no dissolution case (Figure 3.10). Based on the results of this study (i.e., for 40% relative density Toyoura sand at $S_0 = 98\%$ and $CSR = 0.2$), it can be concluded that in the case of rapid loads like seismic excitations during earthquakes the effects of dissolution of air in pore water is negligible and the lower bound approach (the Boyle's law) can be reasonably used to predict the seismic response of nearly saturated sands (see also the results shown in Figure 3.7 for $B = 0.2$, $S_0 = 98.54\%$, and $f = 0.1\text{Hz}$). Byrne et al. (2004a) assumed that the effects of air dissolution are negligible and used the same approximation in their calculations. It is mentioned however that the conclusions regarding the effects of loading frequency are obtained for a certain range of earthquake intensity (corresponding to a CSR of about 0.2) and for hydrostatic pressures in relatively shallow soil layers.

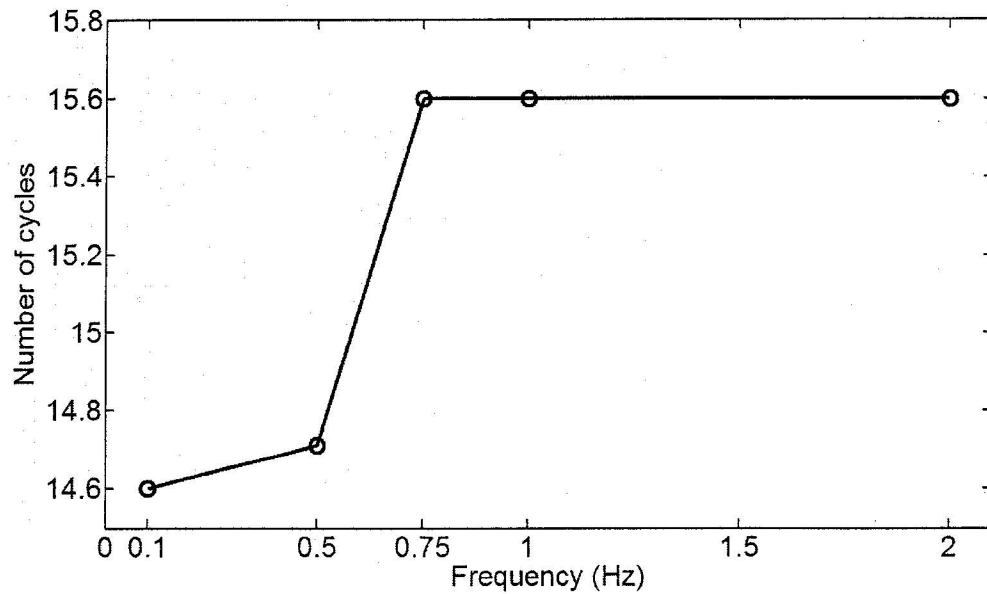


Figure 3.10 Effects of frequency of cyclic loading on the liquefaction strength of 40% relative density Toyoura sand at $S_0 = 98\%$ and $CSR = 0.2$.

As shown in this chapter, it is also noted that existence of gas (e.g., even 1% air in the voids) can significantly increase the compressibility of soil and increase the liquefaction resistance as it can significantly reduce the amount of seismically induced excess pore water pressure. However, this increase in liquefaction resistance due to presence of gas may vary based on soil types, soil fabric, shapes of the grains and many other factors and quantifying this issue requires a large number of experimental data (which presently are not available) and is beyond the scope of the thesis.

3.5 Concluding note

In this chapter, the fundamental features corresponding to the numerical model used in this thesis were briefly described. These included brief descriptions of the coupled

field equations (required for liquefaction analysis of fully saturated soils) and their implementation in the finite element code Dynaflo as well as the multi-yield plasticity soil constitutive model and its parameters.

The chapter also contained an original constitutive formulation suggested for liquefaction susceptibility of nearly saturated sands. Due to the presence of gas in nearly saturated soils compressibility of the pore fluid increases significantly. This enhances the liquefaction resistance of nearly saturated soils. A constitutive formulation was proposed to account for the effects of incomplete saturation on the liquefaction susceptibility of sands. The proposed formulation is based on the ideal gas law, the Henry's law, and the mass balance principle. Also, to account for the effects of transient air dissolution on the compressibility of pore fluid, an analytical approach for a moving boundary diffusion problem was provided. The proposed model introduces physically meaningful parameters that can be calibrated based on results of undrained cyclic laboratory soil tests on nearly saturated sands. A procedure for calibrating the proposed model was suggested, and it was shown that the model was able to predict reasonably the liquefaction strength of sands at different degrees of saturation. The scope and limitations of the proposed model were also discussed. It is concluded that the proposed constitutive model, if calibrated properly, can be used as a mathematical tool to investigate the liquefaction susceptibility of nearly saturated sands.

Chapter 4 - Calibration of the numerical model

4.1 Introduction

This chapter presents in detail the numerical model calibration procedure and class A and class C predictions (back-analyses) of the LRI centrifuge experiments performed at MUN using the multi-yield plasticity soil constitutive model (Prevost, 1985a) implemented in the finite element (FE) code Dynaflo (Prevost, 2002) as described in Chapter 3. The numerical model was calibrated based on the results of laboratory soil test, information from the literature and class C predictions of the first three LRI centrifuge experiments.

The layouts of the LRI centrifuge experiments CT1 to CT8 along with the locations of transducers are shown in Figure 4.1. In this figure, EPP (P), LVDT (L) and ACC (A) indicate pore water pressure transducer, linear variable differential transformer and accelerometer, respectively. Also, specifications of all the LRI centrifuge tests are summarized in Table 4.1.

Figure 4.2a shows the original (unfiltered) seismic acceleration time history selected as the base input acceleration time history in LRI. This motion corresponds to a probability of 2% in a 50-year period in Vancouver area (Seid-Karbasi, 2003). The motion was filtered and used as the target base input acceleration time history in the LRI centrifuge tests CT2 to CT4. In tests CT5 to CT8 the filtered motion was amplified with a magnification factor of 2, i.e., $2 \times A_{2475}$ as shown in Figure 4.2b. The Fourier transforms corresponding to the original (unfiltered) and the amplified filtered input

acceleration time histories are shown in Figure 4.2c. Both motions have a dominant frequency of about 0.65Hz; however, the filtered motion (Figure 4.2b) has a frequency range between 0.5Hz to 3Hz. The base input acceleration for test CT1 consisted of event A475 (with a level of seismic risk equal to 10% in a 50-year period as described by Seid-Karbasi, 2003) followed by event A2475 (Table 4.1). Test CT1 is not discussed in this chapter. Numerical class A and class C predictions of this test as well as their direct comparisons with the results of centrifuge modeling (CT1) are posted on the GEOSIM website (GEOSIM, 2001).

This chapter contains procedures for estimating different sets of soil constitutive parameters for the types of soils used in the LRI centrifuge experiments. Also, the numerical results are compared with the experimental measurements at a few selected transducers. These transducers are chosen at locations that are representative for the slope behavior to provide a basis for evaluating the performance of the numerical model in predicting seismic response. Comparisons of the numerical predictions for all of the LRI centrifuge experiments with their experimental counterparts at all transducer locations are available online on the GEOSIM website (GEOSIM, 2001) as well as Appendix B.

Some limitations of the numerical model are also discussed in this chapter.

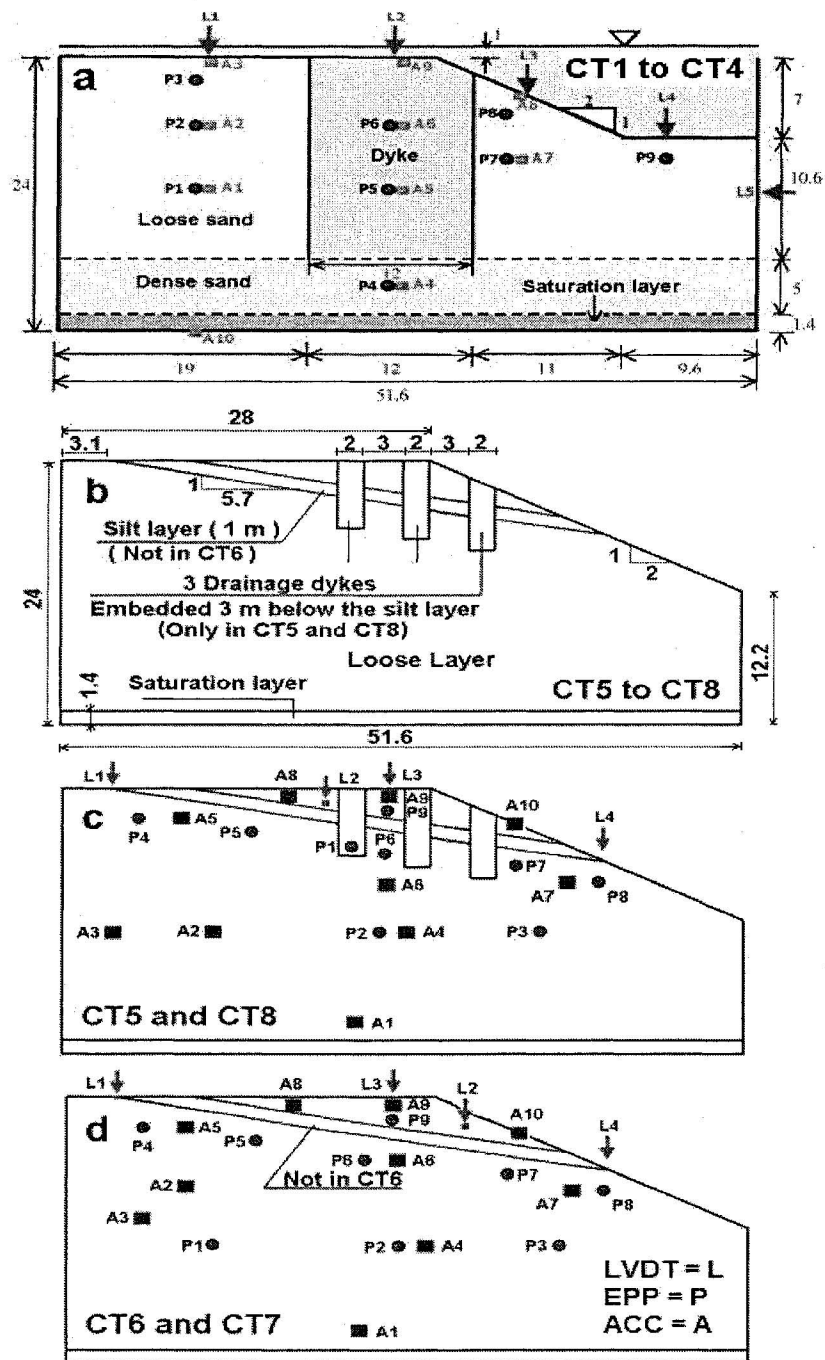


Figure 4.1 Layouts of the LRI centrifuge experiments: a) slope geometry and instrumentation layout in tests CT1 to CT4 (from EIDMSL, 2003), b) slope geometry in tests CT5 to CT8, c) instrumentation layout in tests CT5 and CT8, and d) instrumentation layout in tests CT6 and CT7. All dimensions are in meters.

The finite element meshes used in this study are shown in Appendix A as well as the reports submitted to UBC (class A predictions of the LRI centrifuge experiments), which are available online on the LRI website (EIDMSL, 2003) as well as GEOSIM (2001). The seismic motion was applied in horizontal direction at the base and lateral boundaries of the FE models to simulate the rigid box used in the centrifuge experiments. The base and the lateral boundaries were assumed impervious (see Appendix A for details related to boundary conditions).

Table 4.1 Specifications of the LRI centrifuge experiments.

Centrifuge experiments	Test configuration and mitigation strategy	Target Acceleration	Figure
CT1	Uniform loose sand No soil improvement	A475 followed by A2475	4.1a
CT2	Uniform loose sand No soil improvement	A2475	4.1a
CT3	Uniform loose sand Densification at dyke	A2475	4.1a
CT4	Uniform loose sand Drainage dyke	A2475	4.1a
CT5	Uniform loose sand with silt (barrier) layer; Drainage through 3 vertical dykes	$2 \times A2475$	4.1b and 4.1c
CT6	Uniform loose sand without silt (barrier) layer No soil improvement	$2 \times A2475$	4.1b and 4.1d
CT7	Uniform loose sand with silt (barrier) layer No soil improvement	$2 \times A2475$	4.1b and 4.1d
CT8	Uniform loose sand with silt (barrier) layer; Drainage through 3 vertical dykes	$2 \times A2475$	4.1b and 4.1c

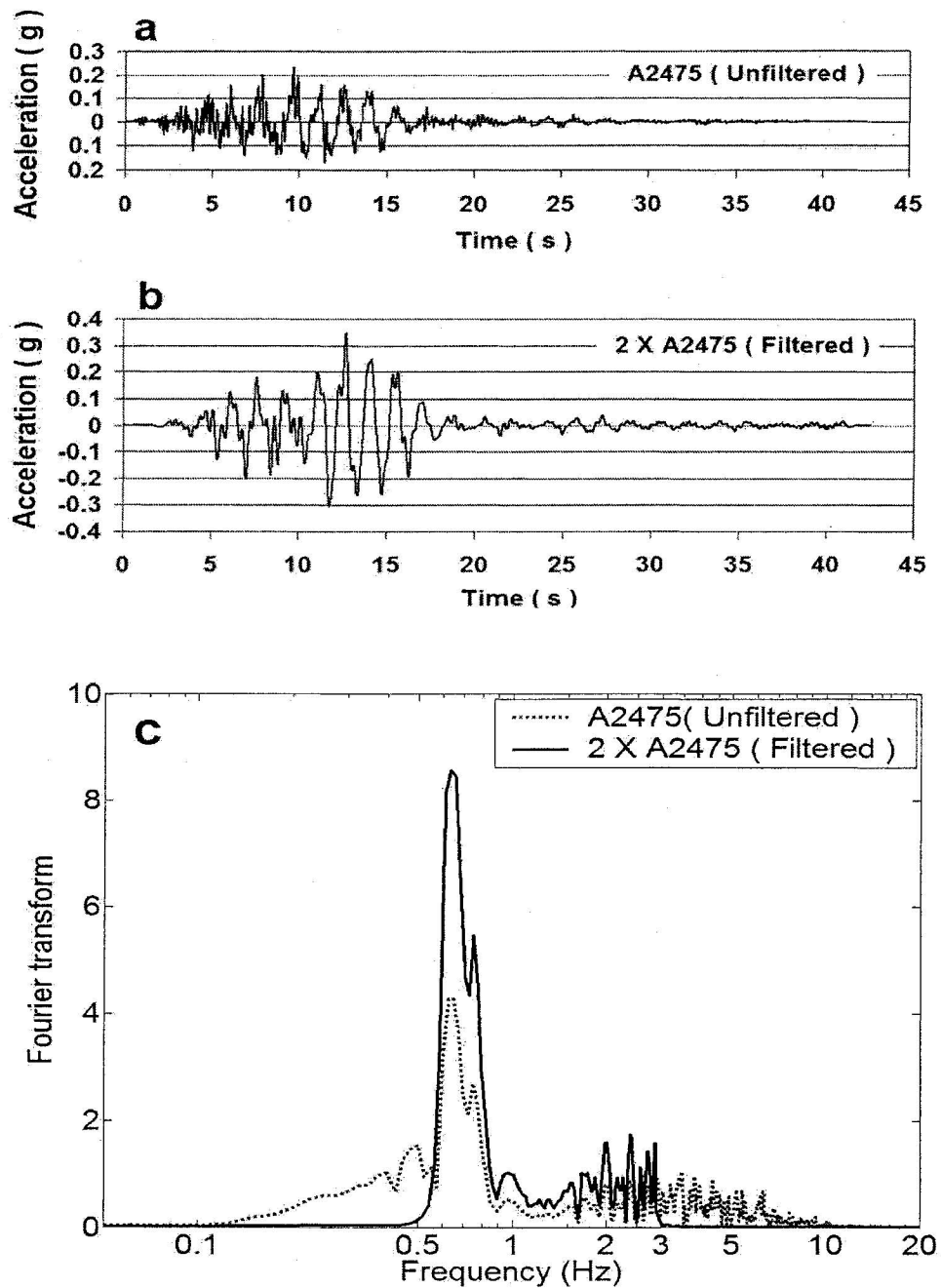


Figure 4.2 a) Original (unfiltered) seismic acceleration time history, b) filtered acceleration time history used as the target base input motion in the LRI centrifuge experiments. Filtered motion A2475 was used in experiments CT1 to CT4. Filtered and amplified motion 2 x A2475, shown here, was used in experiments CT5 to CT8, c) Fourier transforms of the acceleration time histories shown in Figures 4.2a and 4.2b.

4.2 Numerical model calibration

4.2.1 Constitutive parameters for Fraser River sand

The procedure for calibrating the multi-yield plasticity soil constitutive model, described in Chapter 3, for Fraser River sand based on the results of cyclic simple shear tests performed on air-pluviated Fraser River sand samples at UBC has been presented in detail by Jafari-Mehrabadi and Popescu (2004a). The corresponding constitutive parameters (for both loose and dense sands) are labeled hereafter as set 1 and listed in Table 4.2. This procedure for estimating the set 1 of soil parameters for loose Fraser River sand with a relative density of $D_r = 40\%$ is briefly presented in this section.

The state parameters obtained from the laboratory soil tests conducted at UBC (see EIDMSL, 2003) and the selected value for Poisson's ratio are shown in Table 4.2. The power exponent, n_p , used to simulate the dependence of the low-strain shear and bulk moduli, G and B , on the effective mean normal stress, p , (as expressed by Equations (2-3) in Chapter 2) was considered to be $n_p = 0.5$, which is the most commonly accepted value for sand (e.g., Richart et al., 1970).

The elastic range considered in this study for soil deformability (stress point inside the innermost yield surface) corresponds to a range of shear strains between 0 and 0.05%. Therefore, G_0 corresponds to the secant shear modulus at a shear strain equal to 0.05%.

Table 4.2 Constitutive parameters of different soil materials.

Constitutive parameters			Loose Sand		Dense sand		Drainage dykes	Silt	Very loose sand ⁽¹⁾
Type	Property	Symbol	Set 1	Set 2	Set 1	Set 2			
State Parameters	Mass density (kg/m ³)	ρ_s	2710	2710	2710	2710	2670	2670	2710
	Porosity	n^v	0.448	0.448	0.406	0.406	0.423	0.448	0.467
	Hydraulic conductivity (cm/s)	k	0.042	0.0084	0.031	0.0062	0.84	8.4×10^{-6}	0.0084
Low-strain parameters	Shear modulus (MPa) ⁽²⁾	G_0	30	45	52.31	78.3	45	5	15
	Power exponent	n_p	0.5	0.5	0.5	0.5	0.5	0.8	0.5
	Poisson's ratio	ν	0.3	0.3	0.3	0.3	0.3	0.4	0.3
Yield and failure parameters	Friction angle at failure	ϕ	36°	39°	42°	45°	41°	25°	35°
	Coeff. of earth pressure at rest	k_0	0.43	1	0.43	1	1	1	1
	Maximum deviatoric strain	ε_{dev}^{max}	0.08(C)	0.02(C)	0.01(C)	0.01(C)	0.02(C)	0.06(C)	0.02(C)
Dilation parameters	Dilation angle	ψ	34°	34°	34°	34°	34°	17°	34°
	Dilation parameter	X_{pp}	0.48	0.27	0.01	0.05	0.27	0.01	0.55

(1) Below the silt layer in tests CT7 and CT8

(2) At a mean effective confining stress $p_0 = 100\text{kPa}$

(C) Compression

(E) Extension

For a reference effective confining stress of $p_0 = 100$ KPa and at a shear strain of 0.05%, a value of about 30 MPa can be inferred for G_0 of Fraser River sand based the results of the isotropically consolidated drained triaxial test provided by Vaid and Eliadorani (2000). At 0.05% shear strain, from the first cycle of the stress-strain curve related to the cyclic simple tests performed on Fraser River sand at $D_r = 40\%$ (see EIDMSL, 2003) a value of about 14 MPa can be derived for G_0 . The correlation proposed by Belloti et al. (1986), as expressed by Equation (4-1), for very low shear strain levels (10^{-4}) results in a value of the initial sand shear modulus, G_{max} , of about 70MPa at $D_r = 40\%$.

$$G_{max} = 400p_a \cdot \exp\{1.39D_r\} \left(\frac{p_0}{p_a}\right)^{0.43} \quad (4-1)$$

In Equation (4-1), p_a is the atmospheric pressure equal to 100kPa. Estimation of the sand shear modulus at a shear strain level $\gamma = 0.05\%$ based on the modulus degradation curves given by Hardin and Drnevich (1972) and Ishibashi and Zhang (1993) results in values equal to 66% and 57% of G_{max} , i.e., 46.2MPa and 39.9MPa, respectively. Based on the information above, a reasonable range for G_0 is (30-45) MPa. A value of 30MPa was considered for G_0 of loose sand in set 1.

The values of friction angle are very scattered. For instance, the results of monotonic laboratory tests performed at UBC (EIDMSL, 2003) show unexpectedly low value for this parameter at 40% relative density (about 27°). The values of friction angle for Fraser River sand inferred from the results of monotonic undrained triaxial tests performed on very loose Fraser River sand at a relative density of about 20% (Vaid et al., 2001) are

about 35.5° and 39° in compression and extension, respectively. A reasonable range for this parameter is 36° - 39° (e.g., USACE, 1992). A value equal to 36° was considered for the friction angle of Fraser River sand at $D_r = 40\%$ both in compression and extension in set 1 (see also Azizian, 2004).

The coefficient of lateral earth pressure at rest, k_0 , was estimated from the theory of elasticity as $k_0 = \frac{\nu}{1 - \nu}$ for plane strain conditions.

A value of 8% was initially taken for the maximum deviatoric strain at failure based on previous experience with other types of sands (e.g., Popescu and Prevost, 1993).

The value of dilation angle (phase transformation angle) is independent of loading mode, type of deformation, and relative density (Vaid et al., 2001). A unique value of about 34° resulted for Fraser River sand from laboratory tests performed under different conditions (Vaid et al., 2001).

The dilation parameter, X_{pp} , was estimated by performing liquefaction strength analysis as described by Popescu and Prevost (1993). This analysis is based on back-fitting the experimental liquefaction strength curve using finite element simulations of cyclic undrained triaxial or simple shear tests (element tests). Cyclic undrained simple shear tests with and without initial static shear stress were performed at UBC on air-pluviated Fraser River sand samples (Wijewickreme et al., 2005). As shown by Byrne and Park (2003), liquefaction was considered to occur when excess pore water pressure ratio reached 95%. The tests without initial static shear were used to estimate the value of the dilation parameter in set 1. Figure 4.3a shows the liquefaction strength curve obtained from the laboratory soil tests and the back-fitting by numerical simulations. As shown in

Figure 4.3a, the numerical model (set 1) reasonably reproduces the experimental results in terms of liquefaction strength for $X_{pp} = 0.48$. Figures 4.3b and 4.3c show the evolution of effective vertical stress and the stress path, respectively, related to the middle point of the liquefaction strength curve. This point corresponds to a cyclic stress ratio, $CSR = 0.1$, and a number of cycles to liquefaction, $N = 6$. As shown in Figures 4.3b and 4.3c, the numerical model shows faster pore water buildup during the first few cycles than recorded in the test. The difference in the predicted and recorded stress paths may be related to the simplifying assumptions made in the constitutive model such as the fact that both loading and unloading are modeled by one single dilation parameter; however, the final number of cycles to liquefaction is the same and was used to perform liquefaction strength analysis. The dilation parameter has been obtained based on the final number of cycles required for liquefaction.

The constitutive parameters initially estimated for loose ($D_r = 40\%$) and dense ($D_r = 80\%$) states of Fraser River sand are shown in Table 4.2 and labeled as set 1. In case of dense sand, the state parameters were derived from laboratory tests conducted at UBC. The given range for the values of elastic shear modulus of loose sand (30-45 MPa) was modified for a relative density of 80% based on Equation (4-1) and modulus degradation curves discussed earlier. Based on the information from the literature (US Army Corps of Engineers, USACE, 1992) a reasonable range for the friction angle of the dense sand would be $42^\circ - 45^\circ$. The maximum deviatoric strain was estimated to be about 1% both in compression and extension based on the results of the monotonic undrained triaxial tests provided by Vaid et al. (2001). As discussed earlier, the dilation angle (phase

transformation angle) is independent of relative density and is equal to 34° . The obtained value for the dilation parameter of the dense Fraser River sand based on back-fitting of the cyclic simple shear tests performed on dense Fraser River sand samples at UBC (see EIDMSL, 2003) was $X_{pp} = 0.01$.

Numerical predictions of the first three LRI centrifuge experiments using set 1 of soil parameters, resulted in softer predicted behavior (higher displacements and larger pore water pressure build up) than measured in the centrifuge experiments (e.g., see Figure 4.5 for test CT2). Moreover, the numerical model predicted a deep rotational slope failure (Figure 4.4), while no slope failure was observed in the centrifuge experiments.

Two possible causes of the mismatch between the numerical predictions and the experimental results have been analyzed: (1) possible incomplete saturation of the soil in the centrifuge experiments, and (2) incorrect calibration of the soil constitutive model.

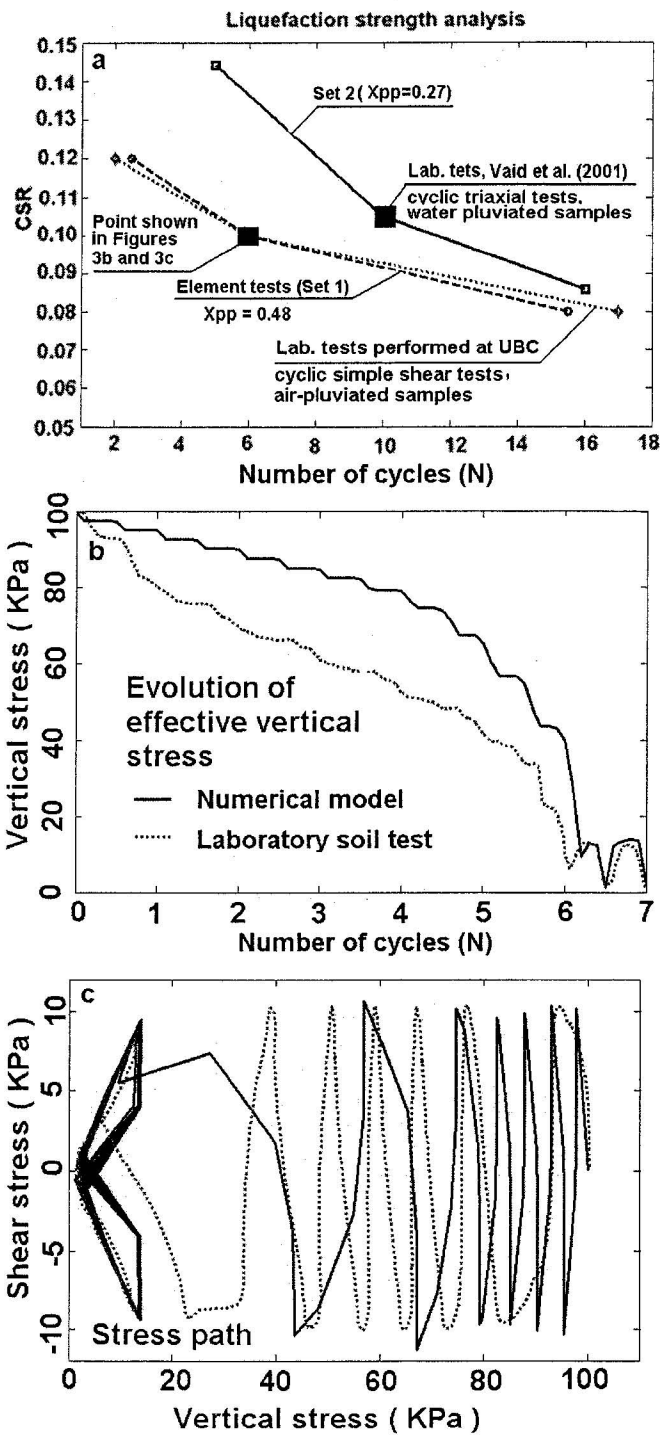


Figure 4.3 Liquefaction strength analysis: a) Experimental and numerical liquefaction strength curves for Fraser River sand b) recorded and predicted effective vertical stress vs. number of cycles for set 1 of soil parameters, and c) experimental and numerical stress paths corresponding to Figure 4.3b.

Partial saturation significantly increases the resistance of soils against liquefaction (e.g., Grozic, 2003 and Tsukamoto et al., 2002). Jafari-Mehrabadi and Popescu (2004b) investigated the effects of partial saturation on one of the LRI centrifuge tests (CT2). A summary of their study is presented in the discussion at the end of this chapter. Comparison between the numerical predictions for various initial degrees of saturation between 96% and 99% and the experimental results of test CT2 indicated that the numerical model, using the soil parameters labeled as set 1, was not able to reasonably capture the observed behavior when gradually lowering the initial degree of saturation. While the predicted displacements and excess pore water pressures decreased with the assumed soil initial degree of saturation, the numerical model continued to predict rotational slope failure, which was not observed in the centrifuge experiment. It was therefore decided to modify the values of soil parameters (both for loose and dense sand) within reasonable ranges found in the literature for low-strain shear modulus and friction angle. Also, the value of maximum deviatoric strain was modified according to the results of monotonic triaxial tests provided by Vaid et al. (2001). The sand hydraulic conductivity was also modified based on the pore water pressure dissipation rates recorded in the first three centrifuge experiments, to match the experimentally observed behavior. All those new values are listed in Table 4.2 under set 2. It is noted that the change in the value of sand hydraulic conductivity is not related to the ambient vibration during handling. This value was decided after performing back analyses (Class C predictions) of the first three LRI centrifuge tests. Parameter k_0 is only used by the software for generating deviatoric stress-strain backbone curves. The change from $k_0 =$

0.43 in set 1 to $k_0 = 1$ in set 2 corresponds to the values of k_0 in each type of cyclic undrained soil tests used to calibrate each of the parameter sets. As set 2 of soil constitutive parameters was calibrated based on isotropically consolidated cyclic triaxial tests; this parameter was taken as 1 for this set. The liquefaction strength data used for the dilation parameter in set 2 was selected based on the results of isotropically consolidated cyclic triaxial tests conducted on water-pluviated Fraser River sand samples (Vaid et al., 2001).

According to several studies, e.g., Amini and Chakravarty (2004); Vaid et al. (1999); Vaid and Negussey (1988); and Tatsuoka et al. (1986a and 1986b), the sample preparation method has significant influence on the cyclic resistance of soils. In general, specimens reconstituted by the water-pluviation method exhibit higher cyclic strengths compared to those prepared by air-pluviation technique. Wijewickreme et al. (2005) mentioned a similar trend for Fraser River sand. In fact, different sample preparation methods result in different sand fabric and different undrained behavior (Vaid and Sivathayalan, 2000; and Park et al., 2004). Air-pluviation method was used to prepare centrifuge models in the LRI project at a relative density (i.e., $D_r = 32\%$), lower than the target value to account for stress densification (Park and Byrne, 2004b) due to mechanical handling and centrifuge model swing up (C-CORE, 2004; and Park and Byrne, 2004a). During transportation of the centrifuge container with a lift truck the model was subjected to ambient vibrations for about 5-10 minutes (Tu, 2005). Those vibrations may have affected the very loose saturated sand in a similar manner as tapping or vibrating in water pluviated samples. It was therefore assumed that the soil fabric in

the centrifuge model is closer to that of water pluviated than air-pluviated samples. It is also noted that natural soil deposit formation resembles more to water-pluviation than to air-pluviation (e.g., Vaid, 1999), and therefore, set 2 of soil parameters may also be more appropriate for simulating the behavior of real soils. A closer look at the effects of sample preparation methods is included in the discussions at the end of this chapter.

The modified soil parameters (set 2 in Table 4.2), and the liquefaction strength data obtained from the results of cyclic triaxial tests conducted on water-pluviated Fraser River sand samples provided by Vaid et al. (2001) were used in a new liquefaction strength analysis for estimating X_{pp} . The new liquefaction strength curve for loose sand is shown in Figure 4.3a along with the results obtained for set 1.

The correlation proposed by Castro (1975), Equation (4-2), was used to obtain a unique cyclic stress ratio in both cyclic triaxial and simple shear tests:

$$\left[\frac{\tau_h}{\sigma_v} \right]_{Simple\ shear} = \frac{2}{3} \frac{(1 + 2k_0)}{\sqrt{3}} \left[\frac{\sigma_d}{2\sigma_c} \right]_{Triaxial} \quad (4-2)$$

In Equation (4-2), τ_h is the amplitude of cyclic shear stress, σ_v is the initial effective vertical stress, $\frac{\tau_h}{\sigma_v}$ is the *CSR* in cyclic simple shear tests, σ_d is the amplitude of cyclic deviatoric stress, σ_c is the initial effective stress, and $\frac{\sigma_d}{2\sigma_c}$ is the *CSR* in cyclic triaxial tests. For isotropically consolidated cyclic triaxial tests ($k_0 = 1$), Equation (4-2) results in:

$$[CSR]_{Simple\ shear} = \frac{2}{\sqrt{3}} [CSR]_{Triaxial} \quad (4-3)$$

The numerical model with the new set of the constitutive parameters (set 2 in Table 4.2) was checked based on class C prediction (back-analysis) of test CT2. Comparisons of the numerical results using constitutive parameters corresponding to sets 1 and 2 in Table 4.2 with the experimental results of test CT2 are provided in Figures 4.4 to 4.6. All results are shown at prototype scale.

Figures 4.4a and 4.4b show the predicted contours of maximum shear strains along with the deformed shape of the model at the end of analysis. As discussed before, set 1 of soil parameters resulted in large displacements and a rotational failure mechanism (Figure 4.4a), while when using set 2 of parameters, the numerical model predicted significantly lower displacements and no slope failure, similar to the experimental records. The predicted slope settlements (at LVDT2) shown in Figure 4.5a are much closer to the experimental records for set 2 than for set 1.

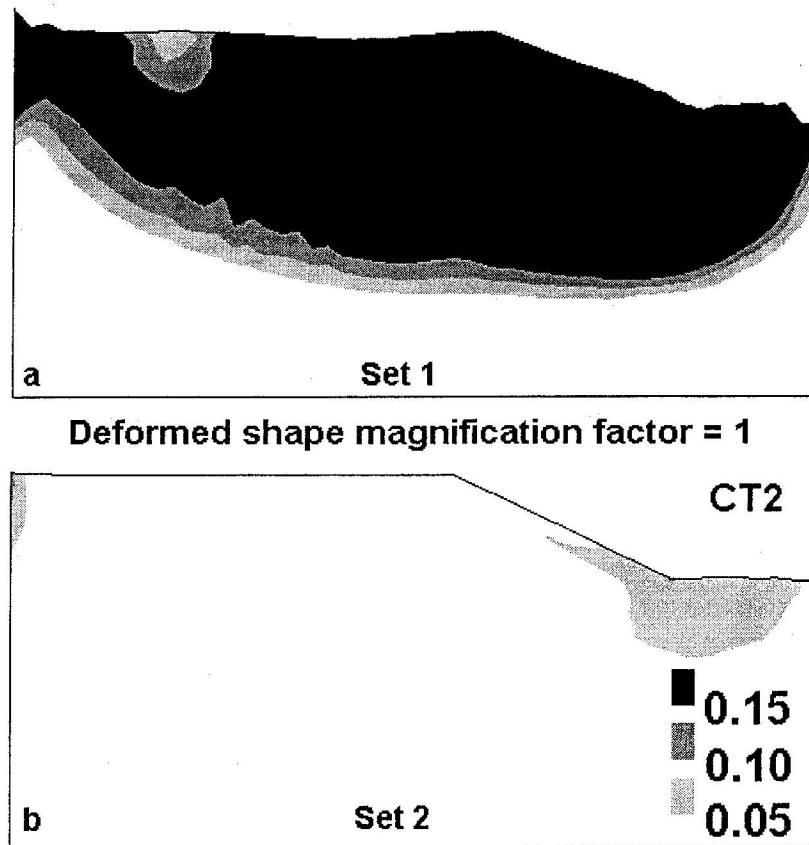


Figure 4.4 Predicted contours of maximum shear strain and deformed shapes at the end of analysis in test CT2 using (a) set 1 of soil parameters, and (b) set 2 of soil parameters.

Figures 4.5b and 4.5c show the predicted and measured excess pore water pressure ratios at EPP2 and EPP7, respectively. At EPP2, in the free field, both sets of parameters resulted in very good agreement with the results of the centrifuge experiment. At the location below the slope (EPP7 in Figure 4.5c), the numerical model with set 2 captured the residual excess pore water pressure much better than it did when using set 1.

Figure 4.6 shows the predicted (sets 1 and 2) and measured acceleration time histories at location ACC7 under the slope. The predicted acceleration time history corresponding to set 2 is in very good agreement with the experimental results both in trends and in

magnitudes. The superimposed acceleration responses are also available on the GEOSIM website (GEOSIM, 2001).

As discussed above, the numerical model with set 2 of constitutive parameters reasonably predicted the experimental response in test CT2. The numerical model with set 2 was also checked for test CT3 with reasonable performance (class C predictions available on the GEOSIM website, i.e., GEOSIM, 2001).

4.2.2 Calibration of other soil materials used in centrifuge experiments

As indicated in Figure 4.1 and Table 4.1, centrifuge experiments CT4, CT5 and CT8 included drainage dykes as a mitigation strategy. In tests CT7 and CT8 an inclined silt layer with a slope of 1:5.7 was also included.

Only general information was available for the material properties of drainage dykes. This included grain size distribution, values of maximum and minimum void ratios, hydraulic conductivity (about 100 times higher than that of the loose sand), and mass density of the solid grains (C-CORE, 2004). Therefore, all the other soil parameters related to low-strain behavior, yield and dilation have been assumed equal to those calibrated for loose sand except for the friction angle, which was assumed to be $\phi = 41^\circ$ (e.g., USACE, 1992).

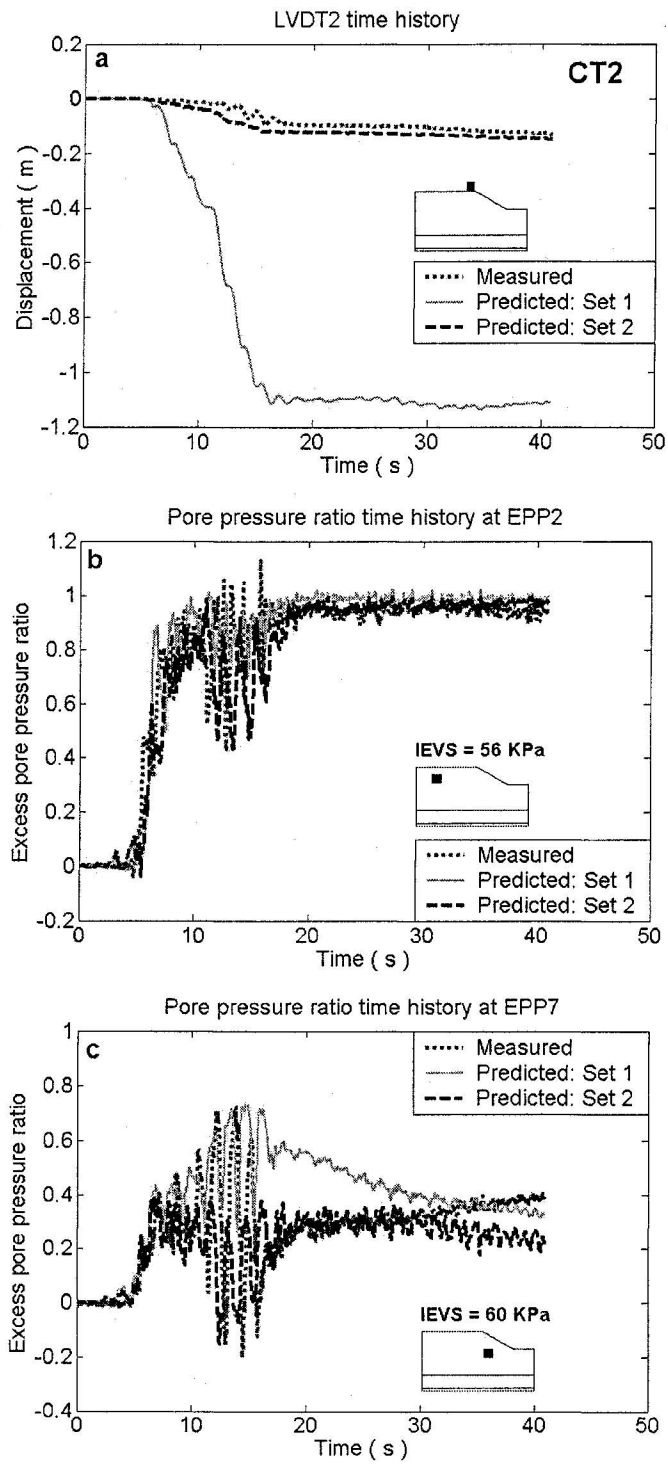


Figure 4.5 Test CT2: Recorded vs. predicted (sets 1 and 2) time histories at locations a) LVDT2, b) EPP2, and c) EPP7 (IEVS = initial effective vertical stress at EPP transducer location).

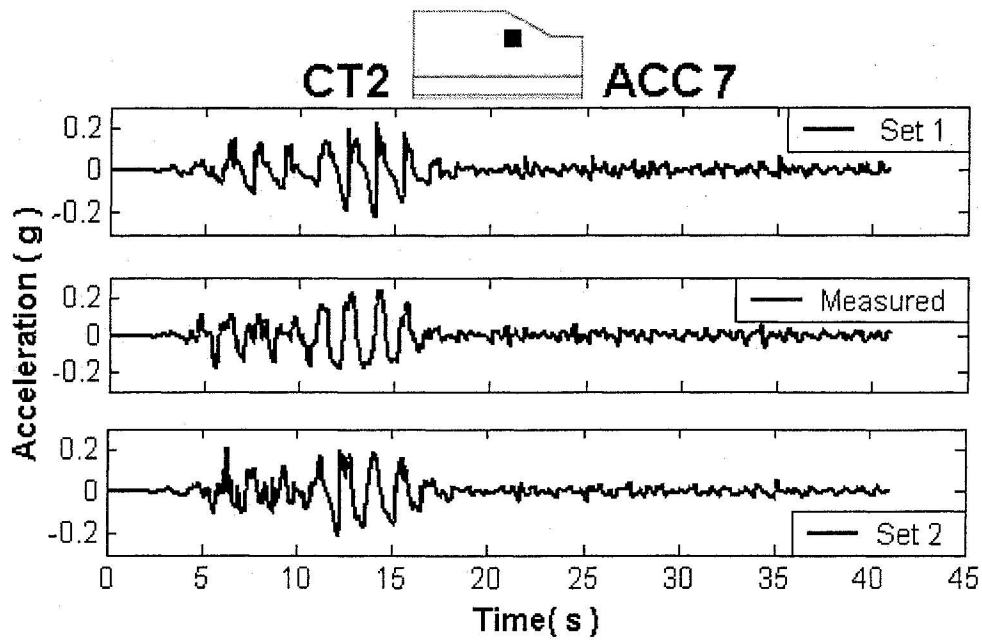


Figure 4.6 Test CT2: Recorded vs. predicted acceleration time histories at location ACC7 (sets 1 and 2 of soil parameters).

No information was available regarding the material properties of the silt layer. A trial set of parameters for this material (based solely on engineering judgment) was used in class A prediction of test CT5 (see GEOSIM, 2001; and EIDMSL, 2003). The silt parameters were subsequently corrected following comparisons between predictions and experimental records for test CT5 and also using the results of a centrifuge test (sand slope with a silt layer) performed for another project (namely COSTA-Canada, see Locat et al., 2001; and C-CORE, 2005). The corrected values of the silt parameters used in class A predictions of tests CT7 and CT8 are listed in Table 4.2.

It is noted that set 2 of soil parameters was calibrated based on isotropically consolidated cyclic triaxial tests (i.e., $k_0 = 1$); consequently, for consistency in selection of constitutive parameters for other soil materials (such as silt and drainage dyke),

parameter k_0 was selected to be equal to 1 and all the analyses and back analyses were performed based on this selection.

The sand slopes in centrifuge tests were shaped using a vacuum cleaner to provide the designed slope face. The final surface of the model in all tests and the sand below the silt layer in tests CT5, CT7, and CT8 were processed in this manner. It is believed that this procedure induced a thin layer of very loose sand at the slope surface. While presence of such a layer at the surface of the model may not influence the overall slope behavior, existence of a very loose sand layer immediately below the silt may have important effects on pore water pressure development. Therefore, it was decided to include a narrow layer of sand (about 1.5cm thick at the model scale) below the silt layer to simulate the effects of model preparation. The relative density of the sand in this layer was assumed to be 20%. A set of constitutive parameters was estimated for this narrow sand layer based on its assumed relative density and the dilation parameter was estimated based on the results of isotropically consolidated cyclic triaxial tests performed on water-pluviated Fraser River sand samples (Vaid et al., 2001). The constitutive parameters for the drainage dykes, silt layer and the narrow loose sand below the silt are also listed in Table 4.2.

4.3 Class A predictions for tests CT4 and CT6 to CT8

Test layout and geometry of test CT5 is similar to those of test CT8, and this test is not discussed in this chapter. Its class A prediction is available on the LRI project website

(EIDMSL, 2003). All the numerical predictions presented hereafter in the thesis correspond to set 2 of the soil parameters.

The predicted contours of the maximum shear strain along with the deformed shape of the model at the end of each analysis are shown for the tests discussed in this section. Also, similar to test CT2, the predicted displacement time histories at the crest of the slope, acceleration time histories at a location under the slope and pore pressure ratio time histories in free field upslope (EPP2 in test CT4 and EPP5 in tests CT6 to CT8) and under the slope area (EPP7), are directly compared with the corresponding experimental results. In tests CT6 to CT8, the predictions labeled here as “class C” were performed with the same soil parameters as used in the class A predictions. The only difference from class A predictions was using the recorded input accelerations instead of the target input accelerations.

4.3.1 Test CT4: Slope with a drainage dyke

The predicted and recorded displacement time histories at the slope crest (LVDT2) are shown in Figure 4.7a. One possible reason for the difference between the numerical and experimental results may be associated with the soil parameters assumed for the drainage dyke. However, it is noted that the recorded crest settlements in tests CT2 (using set 2 of the soil parameters) and CT4 (Figures 4.5a and 4.7a) show an unexpected trend; a larger crest settlement was recorded in the centrifuge for the improved sand slope (about 26cm in test CT4) than for the unimproved one (about 13cm in test CT2), while the numerical model predicted 15cm in test CT2 and 13cm in test CT4 after soil improvement. At

location EPP2 in the free field, the recorded and predicted excess pore water pressure ratio time histories are in very good agreement (Figure 4.7b). The numerical model predicted less pore water pressure than recorded at EEP7, located under the slope area with static shear stresses (Figure 4.7c). Figure 4.7d shows the predicted maximum shear strain contours at the end of analysis along with the deformed shape of the model. As it can be seen from this figure due to the presence of the drainage dyke, the predicted displacements and settlements are slightly smaller than those predicted for test CT2 with set 2 of soil parameters (Figure 4.5d), and the slope was predicted to be stable as observed in the centrifuge model. As shown in Figure 4.8, the predicted acceleration time history at ACC7 is in reasonable agreement with its recorded counterpart when the actual recorded input motion is used in numerical predictions (compare the class C predictions with the measured response in Figure 4.8).

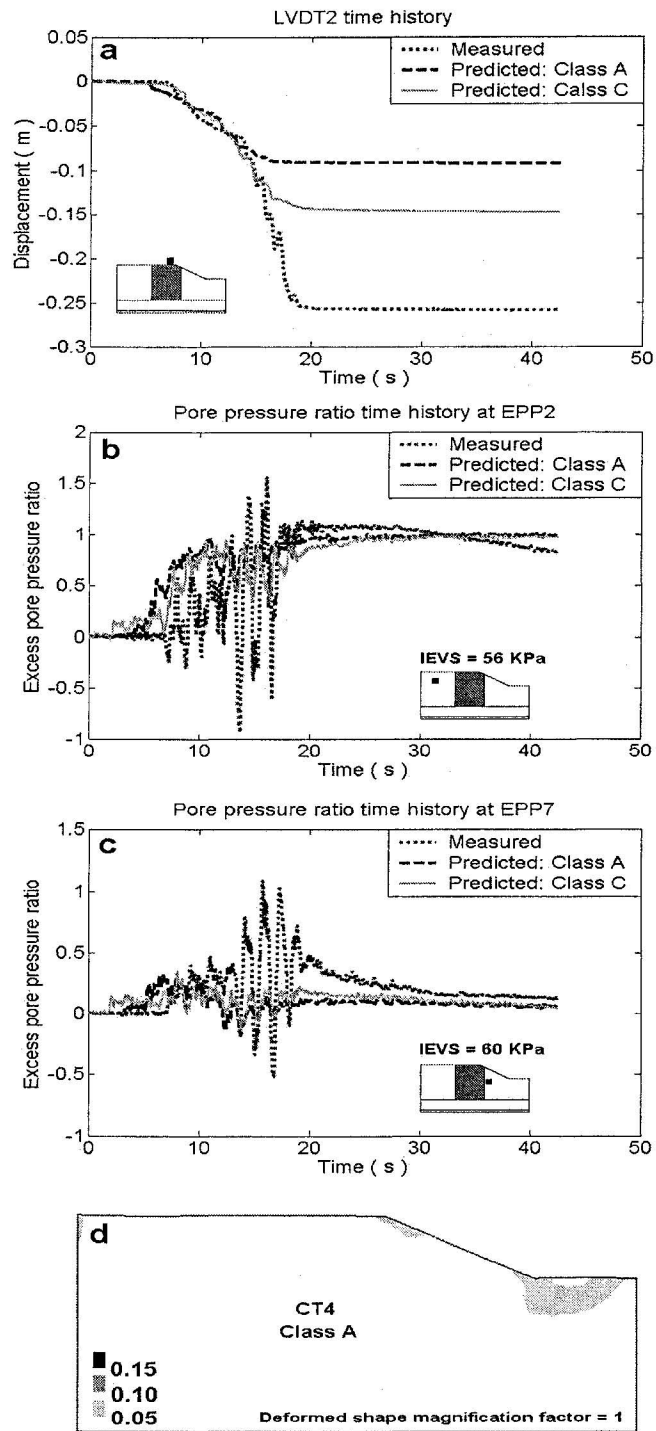


Figure 4.7 Test CT4: a), b), and c): Recorded vs. predicted (class A and class C) time histories at locations LVDT2, EPP2, EPP7, respectively, and d) predicted maximum shear strain contours at the end of analysis. (IEVS = initial effective vertical stress at EPP transducer location).

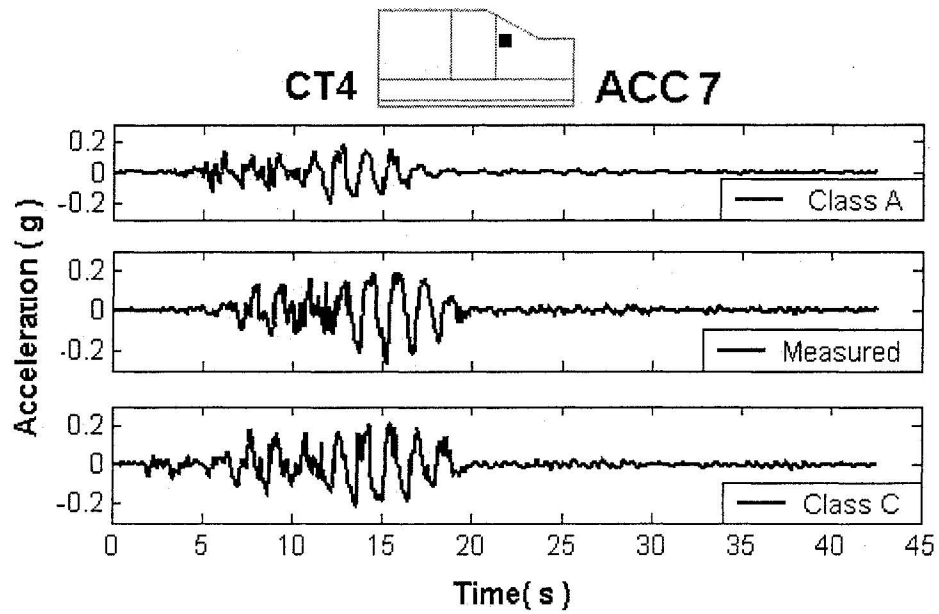


Figure 4.8 Recorded vs. predicted acceleration time histories in test CT4 at location ACC7.

4.3.2 Test CT6: Uniform loose sand slope without toe

For this test, the numerical model predicted limited slope failure (crest settlement higher than 30 cm with shear strains higher than 5% as shown in Figures 4.9a and 4.9d). The recorded behavior was somehow stiffer (smaller displacements). This may be due to the fact that in test CT6 the model was spun to 70g twice; first for measuring P-wave velocities and the second time for performing the actual test. This might have caused more sand densification (Tu, 2005) and stiffer soil behavior in the centrifuge model. The recorded and predicted excess pore water pressure ratio time histories in the free field (EPP5) are in reasonable agreement (Figure 4.9b). The numerical model predicted significantly less pore pressure build up at EEP7 (under the slope area) than recorded in the centrifuge experiment (Figure 4.9c).

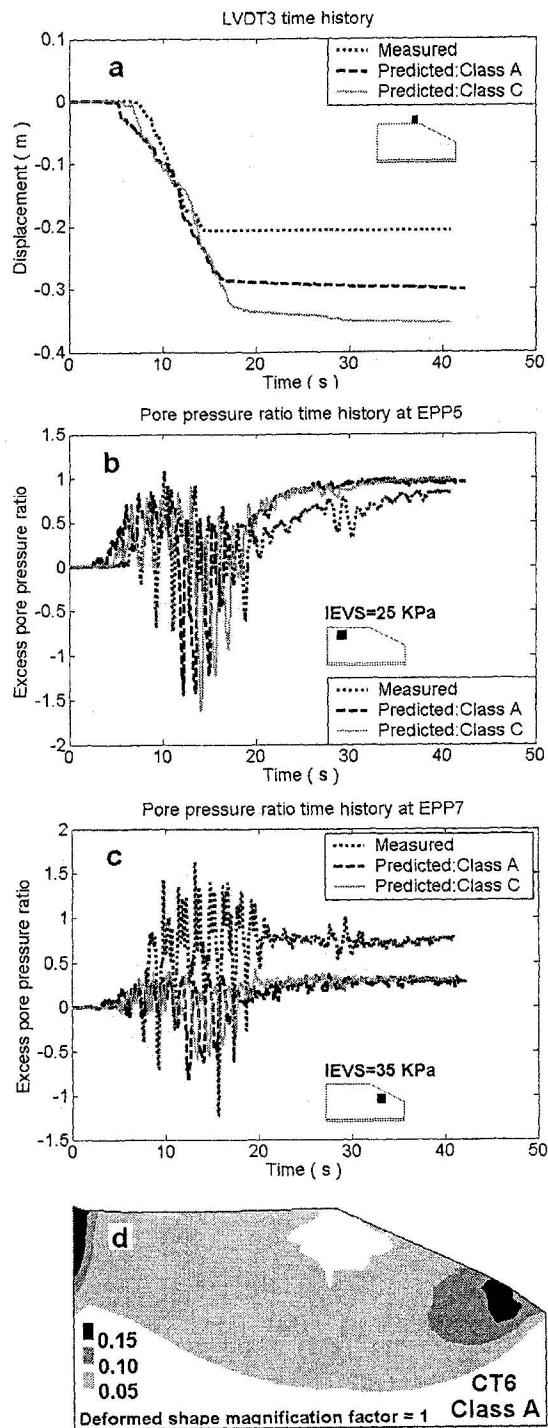


Figure 4.9 Test CT6: a), b), and c): Recorded vs. predicted (class A and class C) time histories at locations LVDT3, EPP5, EPP7, respectively, and d) predicted maximum shear strain contours at the end of analysis. (IEVS = initial effective vertical stress at EPP transducer location).

Figure 4.10 shows the comparison between the predicted and recorded acceleration time histories at ACC7. The numerical model could not capture the large negative spikes recorded in the centrifuge.

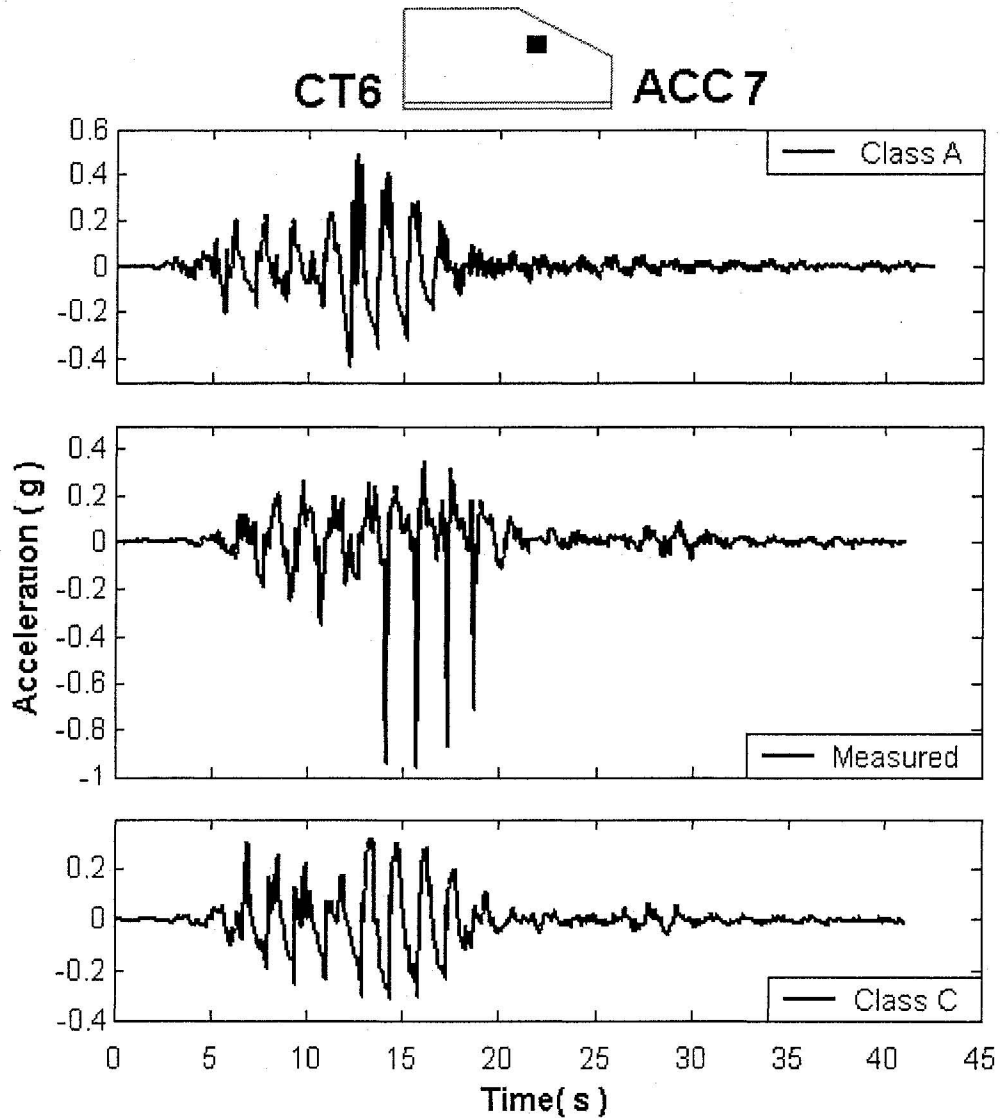


Figure 4.10 Recorded vs. predicted acceleration time histories in test CT6 at location ACC7.

4.3.3 Test CT7: Similar to test CT6 with an inclined silt layer

The predicted settlement time histories at LVDT3, shown in Figure 4.11a, are in very good agreement with the experimental records. The pore water pressure time history at EPP5 was not recorded (see Figure 4.11b). As shown in Figure 4.11c, at EPP7 reasonable agreement can be seen between the predicted and recorded excess pore water pressure ratio time histories. The predicted maximum shear strain contours of test CT7 at the end of analysis are shown in Figure 4.11d along with the deformed shape of the model. The silt layer and the soil above it had a rigid block down-slope movement as observed in the centrifuge model.

The predicted and recorded acceleration time histories at ACC7 are compared in Figure 4.12. The negative recorded acceleration peaks seem to indicate sudden stops of down-slope displacements followed by small upslope movements as recorded by LVDT3 (Figure 4.11a). The numerical model did not capture the negative high values, and the predicted acceleration time histories are more symmetrical.

4.3.4 Test CT8: Similar to test CT7 but mitigated by three drainage dykes

The comparison of the predicted and measured responses at the slope crest (LVDT3) is presented in Figure 4.13a. The predicted settlements are lower than those measured in the centrifuge. However, as discussed for tests CT2 and CT4, again the recorded final crest settlement in test CT7 (without mitigation about 45 cm) is smaller than that recorded in test CT8 (with mitigation about 65 cm). The predicted crest settlements

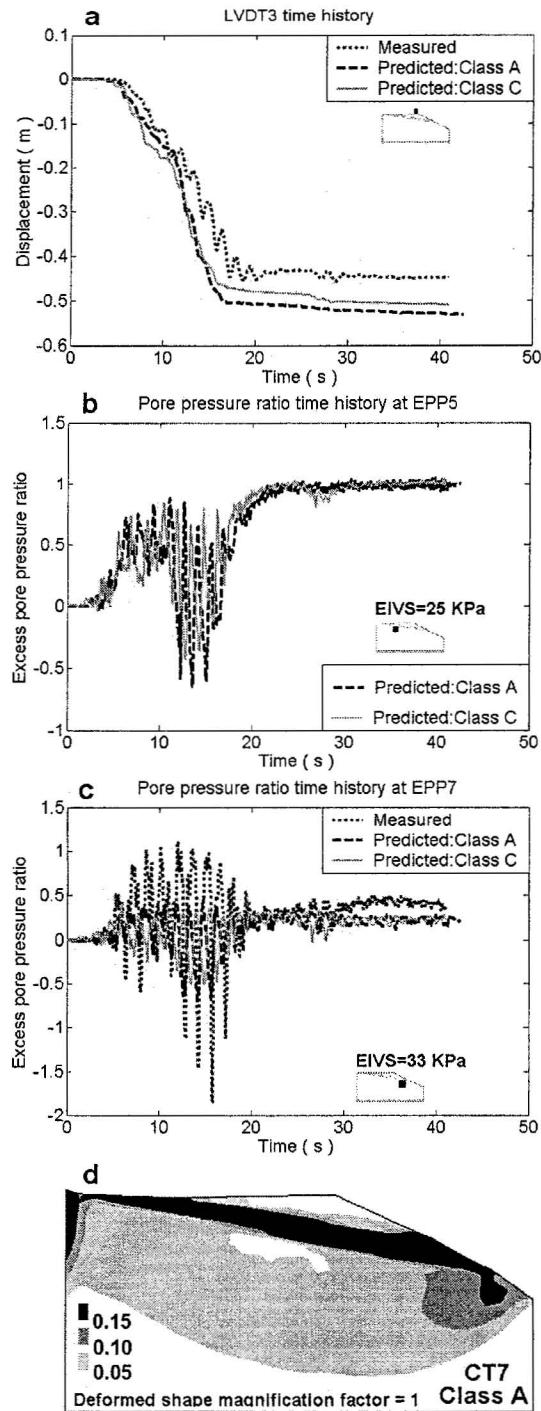


Figure 4.11 Test CT7: a) Recorded vs. predicted (class A and class C) time histories at location LVDT3, b) predicted time histories at location EPP5 (no record available), c) recorded vs. predicted time histories at location EPP7, and d) predicted maximum shear strain contours at the end of analysis.(IEVS = initial effective vertical stress at EPP transducer location).

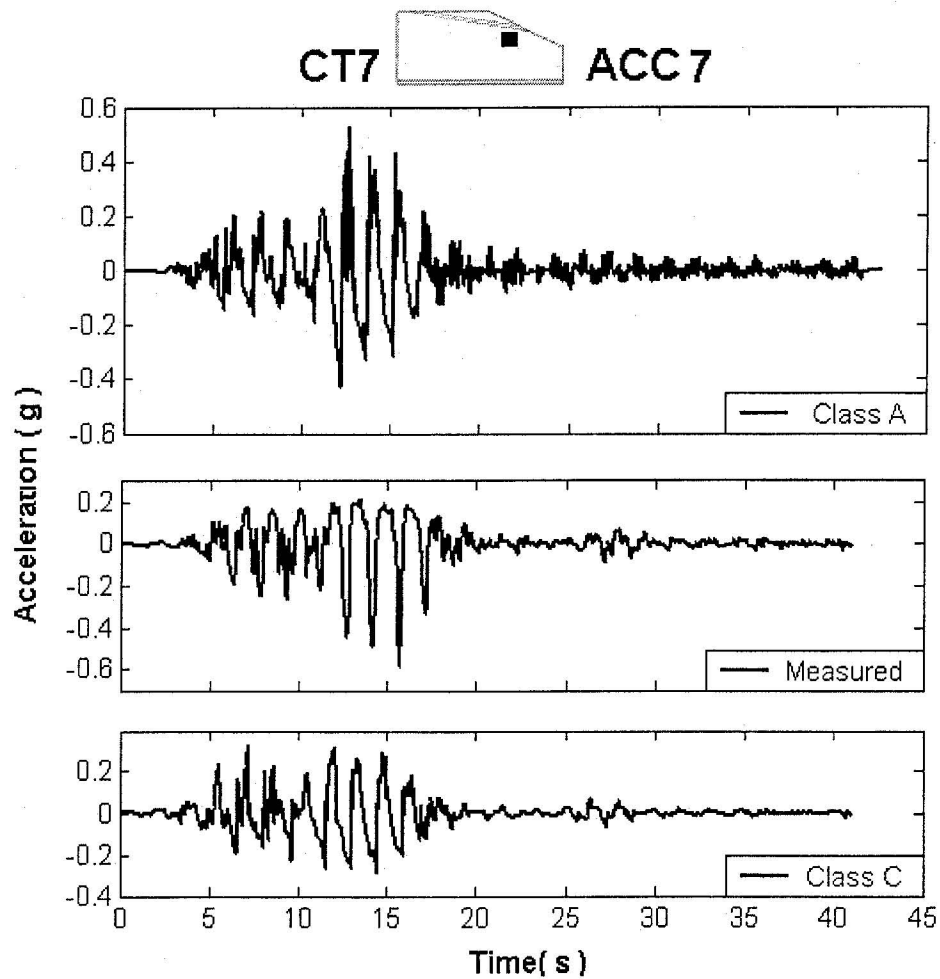


Figure 4.12 Recorded vs. predicted acceleration time histories in CT7 at location ACC7.

(lower in test CT8 compared to test CT7) show the expected pattern. At EPP5 (Figure 4.13b), during the last part of the earthquake, the numerical model predicted significant dilative response compared to the measurements; however, liquefaction was predicted to occur by the end of the earthquake. The recorded residual excess pore water pressure ratio at this location is higher than 1. This may be related to transducer sinking. Also, the numerical model predicted significantly more dilation at EPP7 compared to the centrifuge results as shown in Figure 4.13c. The predicted maximum shear strain

contours of test CT8 along with the deformed shape of the model at the end of analysis are shown in Figure 4.13d. Due to the presence of drainage dykes, the numerical model predicted lower maximum shear strains compared to test CT7 (compare with Figure 4.11d). Similar to test CT7, the predicted accelerations at location ACC7 are in the same range as the recorded ones, but the numerical model could not capture the large negative peaks recorded in the centrifuge experiment (Figure 4.14).

Figure 4.15 shows the predicted excess pore water pressure ratio contours at different instants in both tests CT7 and CT8. The numerical model predicted upward migration of the pore water after the end of the earthquake and its subsequent trapping below the silt layer. The same behavior was also observed in the centrifuge models (e.g., EPP5 in test CT8 shown in Figure 4.13b).

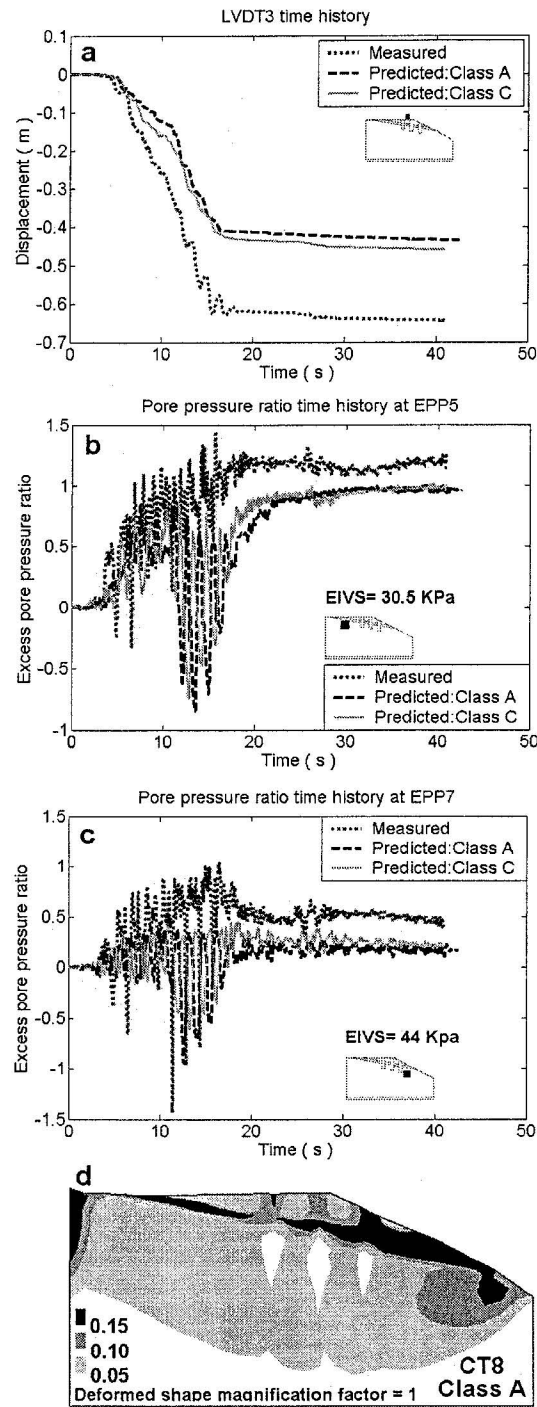


Figure 4.13 Test CT8: a), b), and c) Recorded vs. predicted (class A and class C) time histories at locations LVDT3, EPP5, EPP7, respectively, and d) Predicted maximum shear strain contours at the end of analysis. (IEVS = initial effective vertical stress at EPP transducer location).

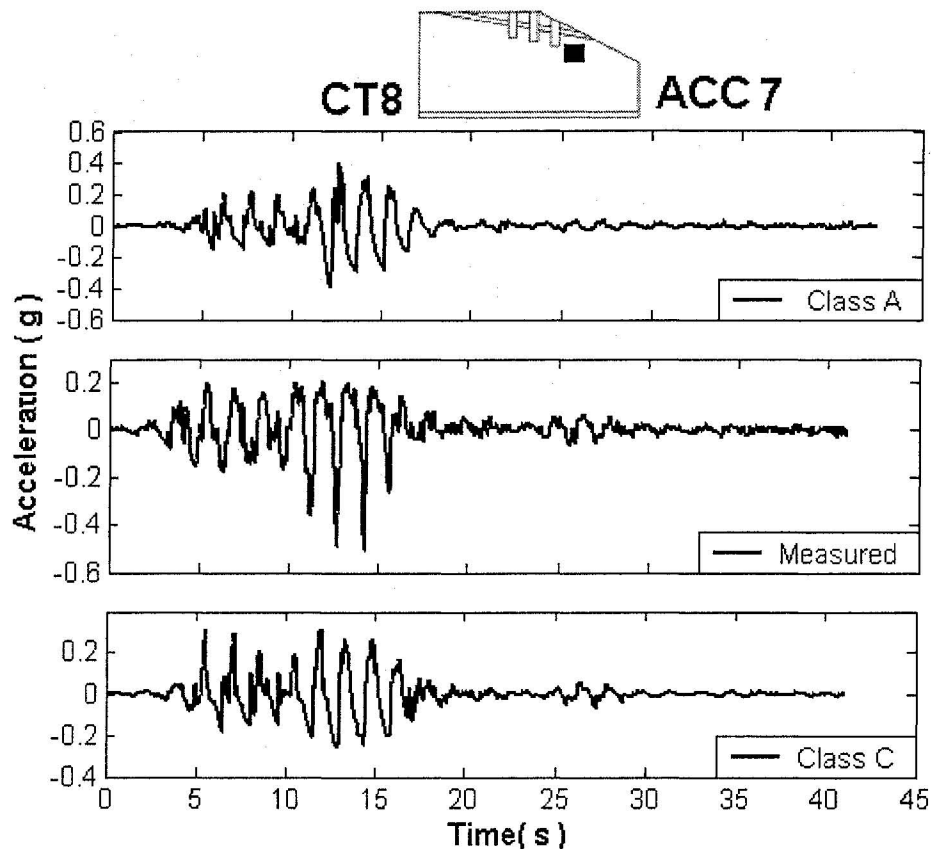


Figure 4.14 Recorded vs. predicted acceleration time histories in test CT8 at location ACC7.

4.4 Discussions

4.4.1 Effects of incomplete saturation on the predicted behavior of test CT2

Comparison between the results of numerical predictions of the first three LRI centrifuge experiments (using set 1 of the soil constitutive parameters) and their experimental counterparts revealed significant softer predicted behavior than that experimentally observed in the centrifuge tests. As mentioned in Section 4.2, it was initially believed that this discrepancy is related to the effects of incomplete saturation of

the centrifuge model. Using set 1 of the soil constitutive parameters for Fraser River sand as listed Table 4.2, in this section, the effects of incomplete saturation on the predicted behavior of the second LRI centrifuge experiment (test CT2) are presented. The numerical predictions presented here correspond to different initial soil degrees of saturation. Assuming an atmospheric pressure for U (i.e., the solid curve in Figure 3.3 of Chapter 3), in each case the bulk modulus of the air-water mixture is calculated from Equation (3-24) (see Chapter 3) based on the initial soil degree of saturation that was assumed to remain constant. These assumptions provide extreme overestimation of the effects of incomplete saturation on the predicted seismic behavior of test CT2 to investigate whether the poor numerical predictions using set 1 of the soil constitutive parameters (See Section 4.2) can be related to these effects or not.

A summary of the results of numerical predictions of test CT2 corresponding to initial degrees of saturation (S_0) equal to 100%, 99%, 98%, 96% is presented in this section. The slope geometry, transducers locations, input motion (event A2475), and test configuration of test CT2 are available in Figures 4.1 and 4.2 as well as Table 4.1.

Figure 4.16 shows the predicted excess pore water pressure ratio (RU) time histories at location EPP2 for different degrees of saturation.

Partial saturation affected the predicted excess pore water pressure ratio time histories. For instance, the predicted residual excess pore water pressure ratio reduces by 20% when the initial soil degree of saturation decreases from 100% to 96% (RU is about 1 for $S_0 = 100\%$ and about 0.8 for $S_0 = 96\%$ at $t > 20$ s). Moreover, it is predicted that liquefaction does not occur at this location for $S_0 < 98\%$.

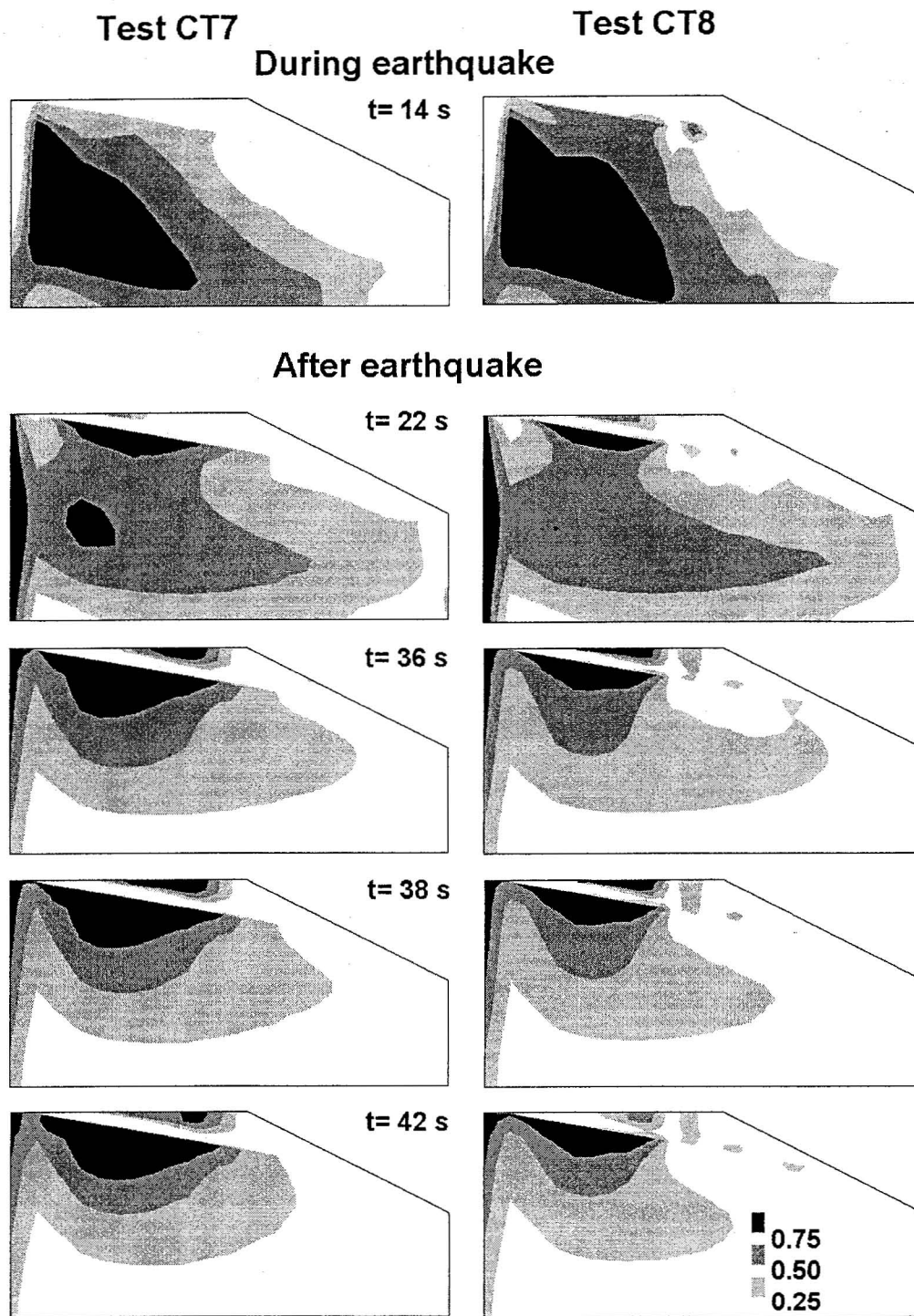


Figure 4.15 Predicted contours of excess pore water pressure ratios during and after the end of earthquake in tests CT7 and CT8.

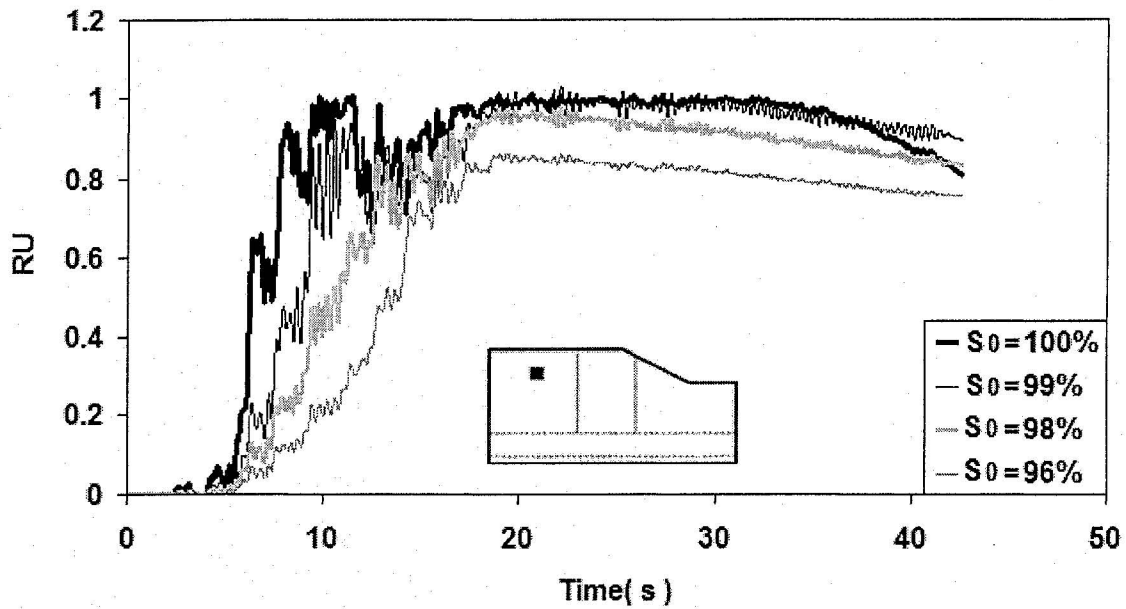


Figure 4.16 Predicted excess pore pressure ratio time histories at location EPP2 for different degrees of saturation.

It is also important to note the good agreement between the numerical results obtained assuming perfect saturation and their experimental counterparts (e.g., see Figure 4.5b). This supports the conclusion that the LRI centrifuge models were well saturated.

The predicted excess pore water pressure ratio contours at a certain instant during earthquake ($t = 12$ s) are shown in Figure 4.17. The lower the degree of saturation, the smaller the pore pressure build-up.

Figure 4.18 shows the predicted contours of maximum shear strains at the end of earthquake along with the deformed shapes of the slope for different degrees of saturation. The lower the soil degree of saturation, the smaller predicted strains. In the case of 100% saturation, the predicted failure mechanism extends over the entire analysis domain, while it affects smaller areas for lower degrees of saturation.

Figure 4.19 shows the predicted vertical displacement time histories at certain transducers, i.e., LVDT1 in the free field upslope, LVDT2 at the slope crest, and LVDT4 in front of the slope toe. It is predicted that the assumed degrees of saturation plays an important role in the value of vertical displacements predicted at these locations. In other words, incomplete saturation significantly decreases the liquefaction-induced displacements and settlements as illustrated in this figure. For instance, the predicted vertical settlement in the free field close to the slope crest (LVDT2) are significantly reduced due to decrease in the initial degree of saturation, i.e. from 0.9m for $S_0 = 100\%$ to 0.63m for $S_0 = 96\%$. Also, lowering the soil initial degree of saturation results in remarkable reduction of the predicted heave at the slope toe, i.e. from 1.1m for $S_0 = 100\%$ to 0.4 m for $S_0 = 96\%$.

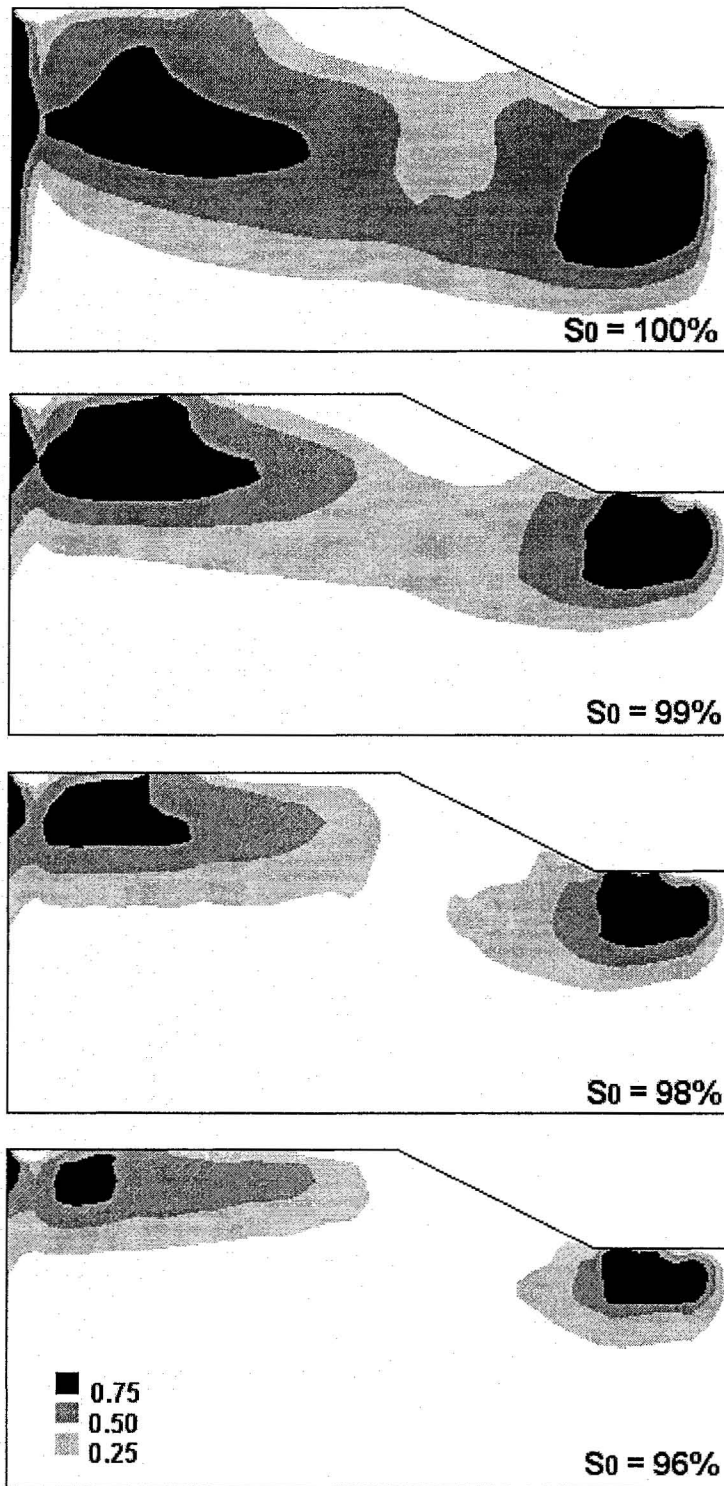


Figure 4.17 Predicted excess pore water pressure ratio contours at $t = 12$ s after the beginning of the earthquake for different degrees of saturation.

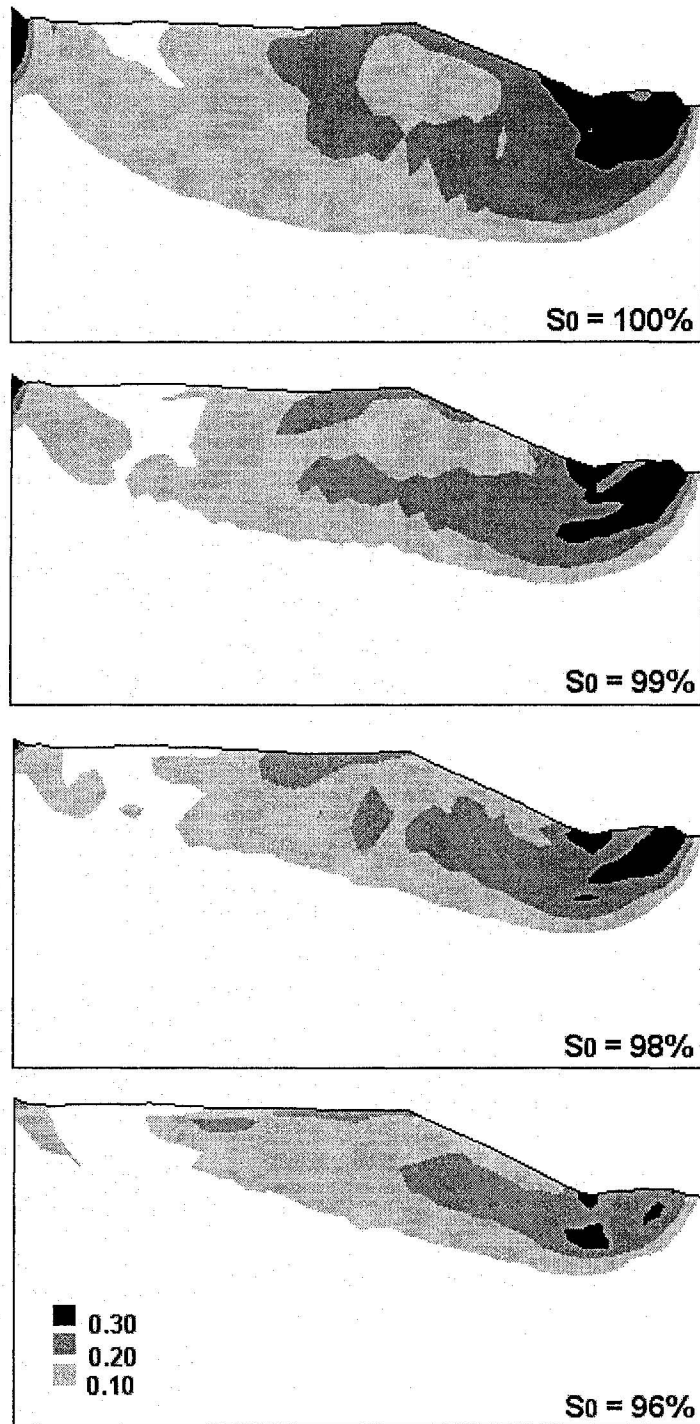


Figure 4.18 Predicted Maximum shear strain contours and deformed shape of the slope at the end of shaking for different degrees of saturation. Deformation magnification factor = 1.

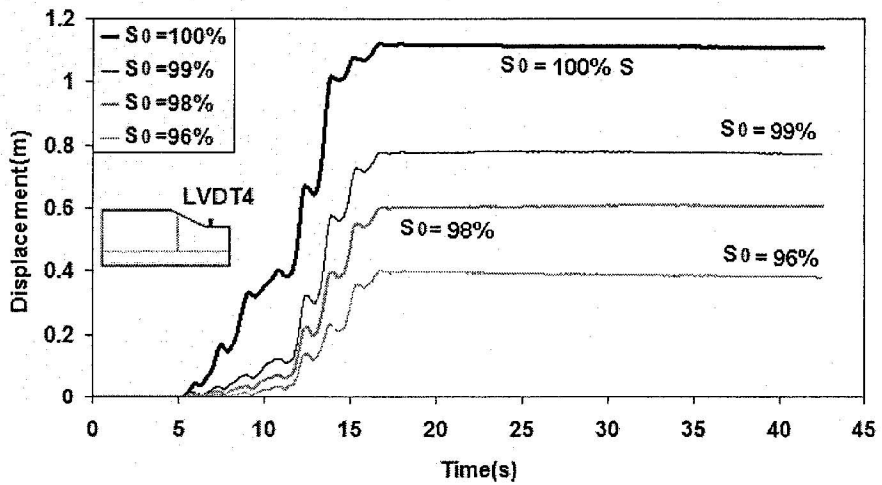
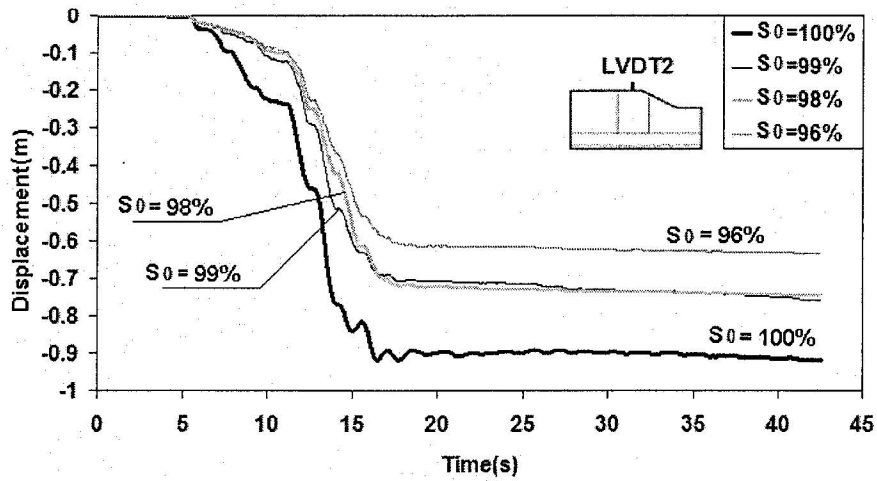
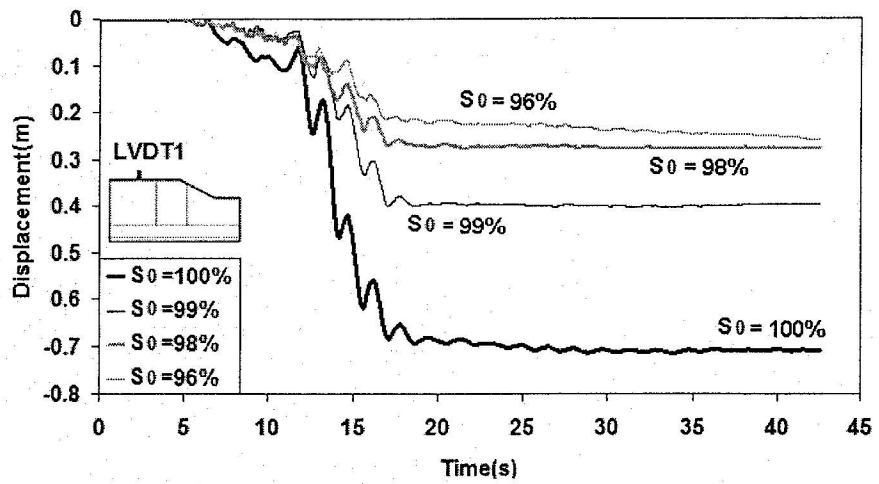


Figure 4.19 Predicted vertical displacement time histories at locations LVDT1, LVDT2, and LVDT4 for different initial degrees of saturation.

The predicted results summarized in Figures 4.16 to 4.19 for test CT2 (using set 1 of the soil constitutive parameters) indicate that the magnitude of predicted displacements are strongly influenced by the degree of saturation. However, the numerical model continued to predict rotational slope failure within the slope along with relatively large displacement, which was not observed in the centrifuge experiment. Therefore, it was decided to modify the values of constitutive parameters as described in detail in Section 4.2.

4.4.2 Effects of sample preparation method

Due to the importance of this issue a brief review of two common sample preparation methods is provided. In the air-pluviation (AP) method, the sample is constructed by pluviating air-dry sand. Vaid and Negussey (1988) postulated that the relative density obtained by this method is related to the kinetic energy of sand particles at the instant of impact at deposition. Based on this assumption, they showed that sample relative densities are dependent upon the rate of pouring and the drop height. Therefore, the desired relative densities are achieved by controlling the drop height and flow rate. In water pluviation (WP) technique, sand specimens are constructed by pluviating sand through water. Drop height in this method has no significant effect on the sample densities. Therefore, WP technique yields specimens of relatively loose densities. To achieve higher densities, if desired, vibration is applied. Based on a series of experimental results, Vaid et al. (1999) mentioned that pluviation in water resembles the

alluvial deposition process since the sand fabric obtained by water pluviation technique is very similar to that of the naturally deposited alluvial and hydraulic fill sands.

As mentioned earlier, when discussing the calibration of the numerical model, specimens reconstituted by water-pluviation method generally show higher resistance to liquefaction compared to air-pluviated samples. This trend is also valid for Fraser River sand (Wijewickreme et al., 2005). For set 1 of soil parameters used in this study for simulating the centrifuge experiments CT1 to CT3 and calibrated based on the liquefaction strength of air-pluviated Fraser River sand samples, the numerical model predicted smaller resistance to liquefaction than that observed in the experiments. It was therefore postulated that some densification of the centrifuge model sand caused by the ambient vibrations during handling at 1g may have had similar effects on the fabric of very loose saturated sand to that of tapping or vibrating water pluviated samples. Predictions performed using set 2 of constitutive parameters, calibrated based on the results from laboratory soil tests on water-pluviated samples, were much closer to the recorded behavior. Moreover, the change in soil behavior from AP to WP is believed to occur only for loose sand. In the case of dense sand the environmental factors mentioned before should not significantly affect the behavior. In order to have a consistent calibration procedure for set 2, the dense sand parameters were also estimated in this study based on the results of the available tests on water pluviated samples (e.g., Vaid et al., 2001). Based on a numerical study, it was found that the change in constitutive parameter values for dense sand from set 1 to set 2 did not significantly affect the slope behavior. The reasons are as follows: (1) the increase in the friction angle of dense sand

(from 42° in set 1 to 45° in set 2) may not have significant effect on the overall results as the mobilized friction angle is considerably lower than friction angle at failure and (2) the change in the dilation parameter of dense sand (from 0.01 in set 1 to 0.05 in set 2) may not have affected the excess pore pressure for the ranges of stress ratios considered here.

4.4.3 Evolution of pore water pressure after the earthquake

As shown earlier in the numerical predictions of tests CT7 and CT8 (Figure 4.15), the numerical model predicted excess pore water pressure build up under the silt layer after the end of earthquake. This phenomenon is believed to be similar to real soil deposit behavior. Due to existence of a low-permeability soil layer in a liquefiable sand deposit, after pore water pressure buildup during an earthquake, water may be trapped beneath a stratum with a relatively low permeability. This forms a water- rich seam under that layer causing reduction of the shear strength of soil along the seam. If drainage is hindered for a long time after the earthquake, delayed flow failure may take place (e.g., Kokusho, 1999).

4.4.4 Boundary effects due to rigid box

A rigid container was used in the LRI centrifuge experiments. This influenced the seismic soil response, especially in the proximity of the lateral boundaries. A numerical study was performed to investigate the effects of the rigid boundaries by extending laterally the original FE mesh used in the numerical predictions. The centrifuge

experiment CT7 was considered for this study. The input motion was the horizontal acceleration time history recorded in test CT7. The original FE mesh was extended from both sides in two stages. In extensions # 1 and # 2, the lengths of the extended FE mesh from each side were 25m, and 50m, respectively. The recorded excess pore water pressure ratio time histories at EPP4 and EPP7 are shown in Figure 4.20. Also, the predicted responses at EPP4, EPP5 and EPP7 corresponding to the original FE mesh and FE mesh extensions #1 and #2 are shown in Figure 4.21. As shown in Figure 4.21a, the significant dilative behavior recorded at EPP4 and predicted at this location using the original FE mesh disappeared completely by extending the FE mesh. Also, extending the FE mesh resulted in decreasing the dilative responses predicted at location EPP5 as shown in Figure 4.21b. The response predicted at location EPP7 (Figure 4.21c) did not significantly change by extending the analysis domain. This may be related to the fact that this transducer was far enough from the lateral walls of the rigid box to be unaffected by boundary conditions. The dilative behavior induced by the rigid lateral boundaries may have also affected the crest settlements at LVDT3. As it can be seen in Figure 4.22, the FE model with extended analysis domain predicted crest settlements about 20% larger than those predicted using the original FE mesh.

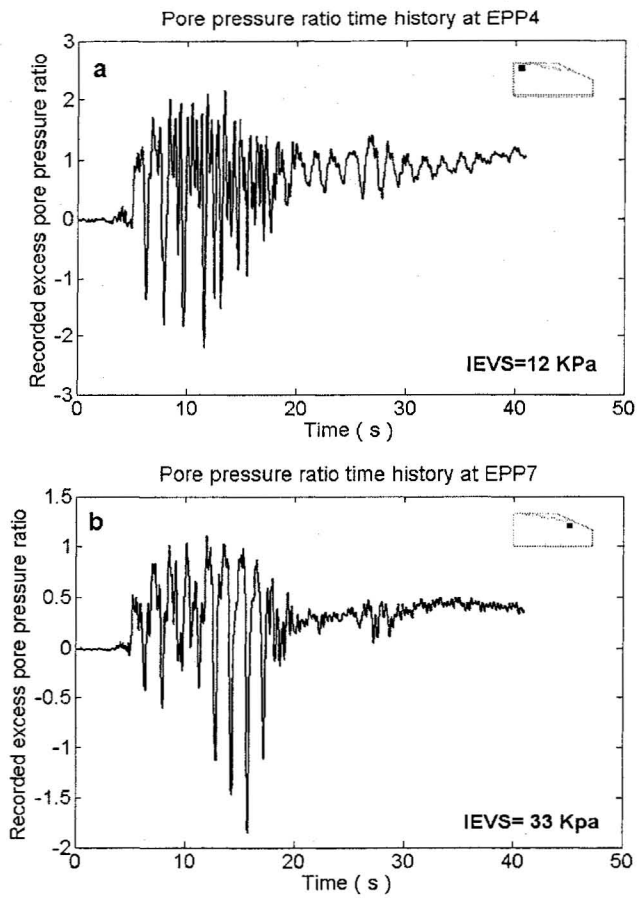


Figure 4.20 Recorded excess pore water pressure ratio time histories in test CT7 at locations a) EPP4, and b) EPP7. (IEVS = initial effective vertical stress at EPP transducer location).

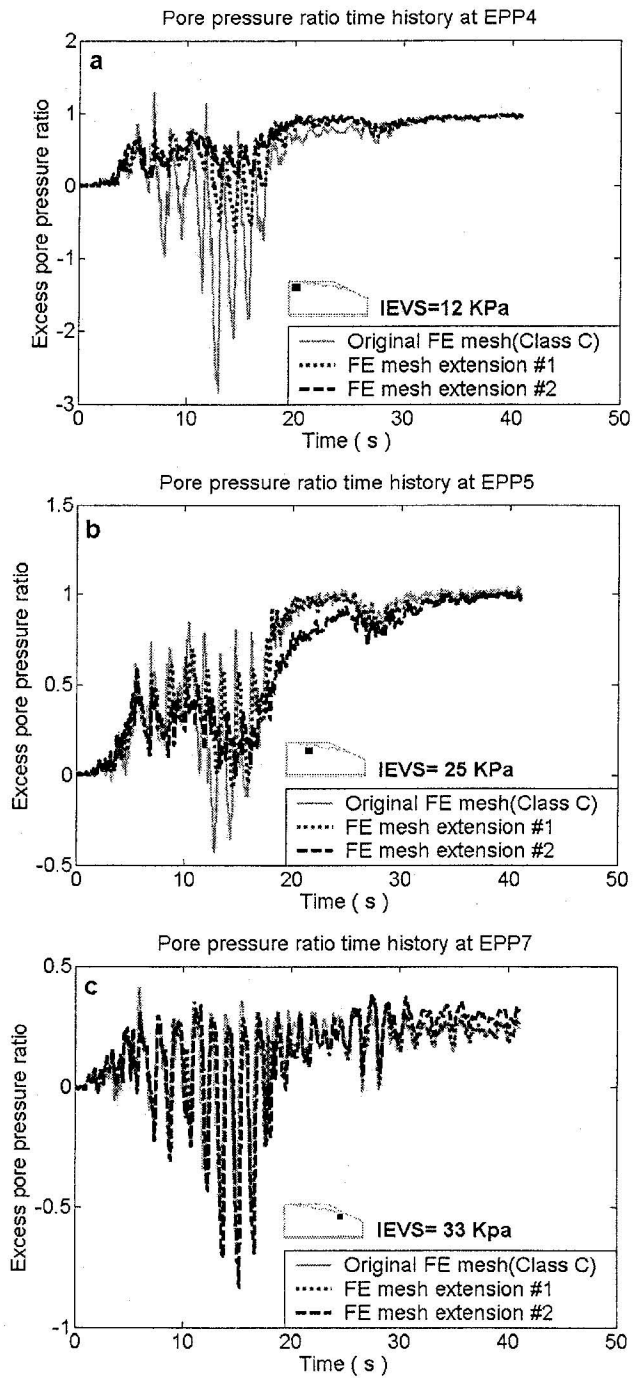


Figure 4.21 Test CT7: Comparisons of the predicted excess pore water pressure ratio time histories using the original FE mesh and FE mesh extensions #1 and #2 at locations a) EPP4, b) EPP5 and c) EPP7, respectively. Mesh extensions 1 and 2 correspond to 25 m and 50 m extension of the original FE mesh analysis domain from both sides. (IEVS = initial effective vertical stress at EPP transducer location).

The predicted contours of the maximum shear strains and the deformed shapes for the original FE mesh and extensions #1 and #2 are shown in Figure 4.23. Relatively large local shear strains close to the upslope boundaries are predicted when using the original mesh and extension #1 (Figures 4.23a and 4.23b). For extension #2 these effects are significantly attenuated (though still present). This may lead to the conclusion that high shear strains predicted close to the lateral boundaries are also related to the proximity of these boundaries to the slope.

Moreover, it is obvious that proximity of lateral rigid boundaries affects the failure mechanism. As the lateral boundaries are moved away from the slope, the failure surface extends both laterally and in depth. In this study the effects of the rigid bottom of the box were not assessed (it was assumed that this model simulated the presence of a rigid layer at a certain depth). It is obvious from the results in Figures 4.23b and 4.23c that the base rigid boundary also affects the failure mechanism. This is also reinforced by the predicted crest settlements shown in Figure 4.22, that are slightly lower for extension #2 (with failure mechanism more affected by the base boundary) than for extension #1.

More considerations regarding the effects of centrifuge container rigid boundaries on the seismic response of waterfront slopes made of Fraser River sand is provided in Chapter 5 of this thesis.

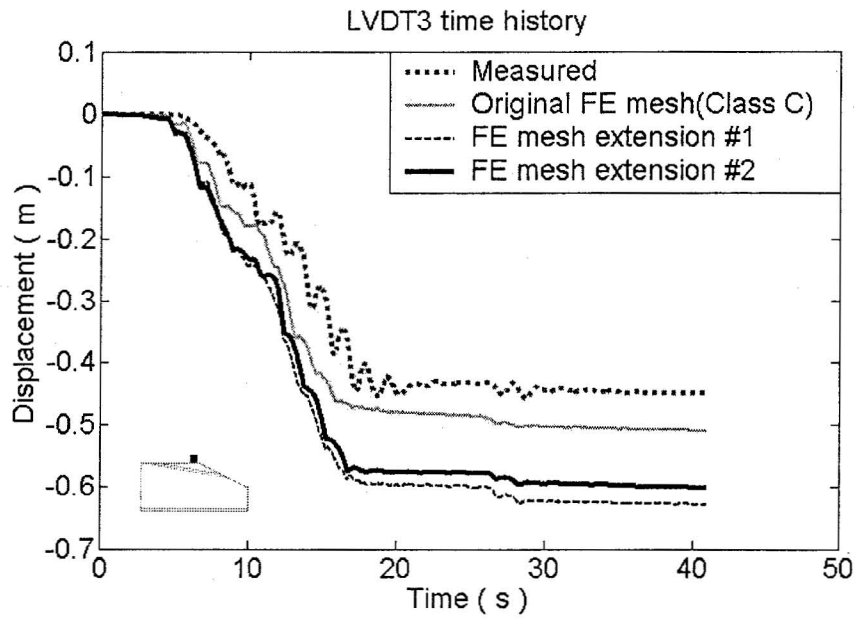


Figure 4.22 Comparison of the recorded and predicted crest settlement time histories in test CT7 for the original FE mesh and extensions # 1 and # 2.

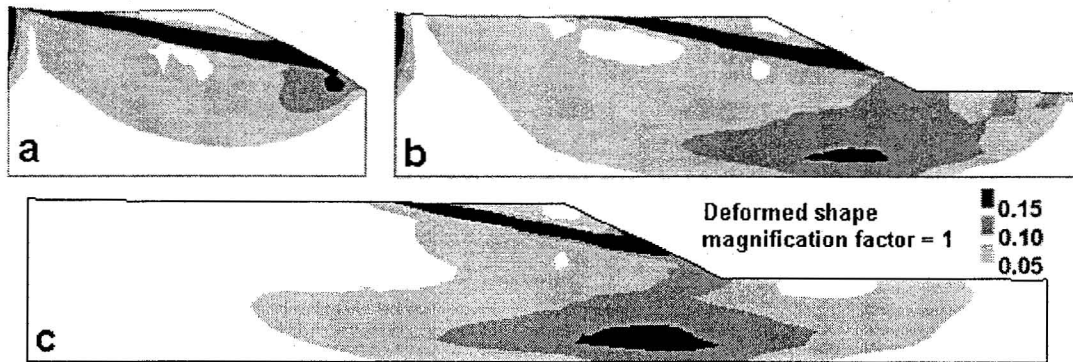


Figure 4.23 Predicted contours of the maximum shear strains at the end of analysis in test CT7 using, a) the original FE mesh, b) extension # 1, and c) extension # 2.

4.4.5 Limitations of the numerical model

More dilative behavior for the soil below the slope (regions with initial static shear stress) was consistently predicted by the numerical model than recorded in the centrifuge experiments (i.e., Figures 4.5c, 4.7c, 4.9c, and 4.13c). The same tendency was observed

during calibration of set 1, where a lower liquefaction resistance obtained in the laboratory for the undrained cyclic simple shear tests with static shear stress than for the ones without static shear stress could not be reproduced by the numerical model. While large liquefaction resistance (more dilative behavior) in the presence of static shear is a common characteristic of most sands, for sands in a very loose state static shear stress is known to lower the liquefaction resistance (e.g., Vaid et al., 2001 and Youd et al., 2001). Apparently, the latter feature is not correctly simulated by the numerical model. It is noted however that another version of the multi-yield plasticity model with a more advanced dilatancy formulation is already implemented in Dynaflow. This is a double plastic potential model based on the experimental work of Pradhan and Tatsuoka (1989) that leads to a more accurate simulation of plastic dilation under cyclic loading. This model, however, has two dilation parameters, instead of one, namely X_{pp} in the model used in this research. Calibration of two dilation parameters requires very detailed results of cyclic undrained tests that were not available for this research. Besides the model with double plastic potential has never been validated; consequently, it was decided to use the model with single plastic potential that could be reasonably calibrated from soil data available for this study.

4.5 Concluding note

In this chapter, a summary of class A predictions for the LRI centrifuge tests was presented using the multi-yield plasticity soil constitutive model implemented in the

finite element program Dynaflow (Chapter 3). The model was calibrated based on the laboratory soil data on Fraser River sand, information from the literature, and results of the first three centrifuge experiments. The results were presented in terms of time histories of accelerations, excess pore water pressures, and displacement and directly compared to the centrifuge records (see also GEOSIM, 2001). All the details corresponding to the numerical class A and class C predictions and description of boundary conditions and finite element meshes used in this study as well as comparisons of the numerical predictions with the centrifuge experimental data at all transducer locations are available on a CD ROM as Appendix B of this thesis and also posted on the GEOSIM website administered by MUN Engineering (GEOSIM, 2001). Since there are a large number of results, including them in the thesis would double its size; consequently, it was decided that all those results be made available online. It should be however mentioned that the most significant comparisons between the numerical predictions and their experimental counterparts have been included in this chapter. The boundary conditions for all FE analyses are also discussed in Appendix A.

Based on the comparisons between the numerical results and their experimental counterparts, it can be concluded that the numerical model calibrated in this chapter is able to reasonably predict the seismic behavior of Fraser River sand slopes, and it may be used for further studies as a tool to investigate mitigation procedures against soil liquefaction in the Fraser River Delta as presented in the next chapter.

Chapter 5 - Seismic behavior and mitigation of slopes

5.1 Introduction

This chapter is aimed at extending the scope of the LRI centrifuge experiments based on numerical studies. The numerical model validation was presented in Chapter 4. The research presented in this chapter extends the scope of the LRI centrifuge experimental results using the calibrated and validated numerical model as described in Chapter 4. The main objective followed in this chapter is to investigate and assess the performance and effectiveness of different liquefaction countermeasures within the framework of the LRI centrifuge experiments. Moreover, due to the importance of the effects of centrifuge rigid boundaries on the seismic behavior of waterfront slopes, practical considerations on boundary effects in centrifuge modeling of waterfront slopes are also discussed in this chapter. The soil constitutive parameters for various soil materials used in this chapter are listed in Table 4.2 (set 2 of soil parameters), obtained from back-analyses of the available laboratory soil tests and LRI centrifuge experiments as described in detail in Chapter 4.

Study on the centrifuge boundary effects is presented in the first part of this chapter. The performance of different mitigation measures proposed in the LRI project is discussed in the second part of the chapter. In addition, a feasible mitigation solution is suggested for the waterfront slopes, having a performance comparable to that of the mitigation solutions used in LRI.

Optimizing the liquefaction countermeasures requires understanding of their effectiveness at different levels of seismic intensity. Therefore, this chapter also includes

a comparative study on the effectiveness of different remediation techniques against liquefaction at different earthquake intensities using fragility curves. Arias intensity (Arias, 1970) is used as a measure of the earthquake intensity in this study.

5.2 Boundary effects in centrifuge modeling of waterfront slopes

As shown in Chapter 4, the rigid container used in the LRI centrifuge experiments significantly affected the soil seismic response, particularly in the vicinity of the lateral boundaries. In this section a summary of the results of a numerical study on the effects of the rigid container used in the LRI centrifuge experiments on the behavior of a waterfront slope made of Fraser River sand is presented. The LRI centrifuge test CT7 was selected as the base case in this respect. The slope geometry in test CT7 is shown in Figure 5.1a.

The centrifuge model consisted of a slope made of uniform loose Fraser River sand with an inclined silt layer. The study on the boundary effects is performed based on extending the original FE domain used for simulating the LRI centrifuge experiments CT5 to CT8. In this respect, the original FE domain is extended both laterally and in depth. Parameters L and Z in Figure 5.1b represent the lateral extension and the depth extension, respectively. The FE mesh extension in depth was performed for two cases including existence of either a very dense sand layer or a loose sand layer under the level of the centrifuge box base. Basically, the rigid base of the centrifuge container should represent the existence of a very stiff non-liquefiable layer to a great depth; however, due to size limitations a rigid box may be used to perform centrifuge experiments on

geotechnical structures underlain by a deep soft layer. As shown in the next subsections, there are significant differences between these two cases.

In the study on boundary effects, the target base input motion of test CT7, i.e. 2 x A2475, shown in Figure 4.2b (Chapter 4), is used as the base input acceleration for the finite element analyses.

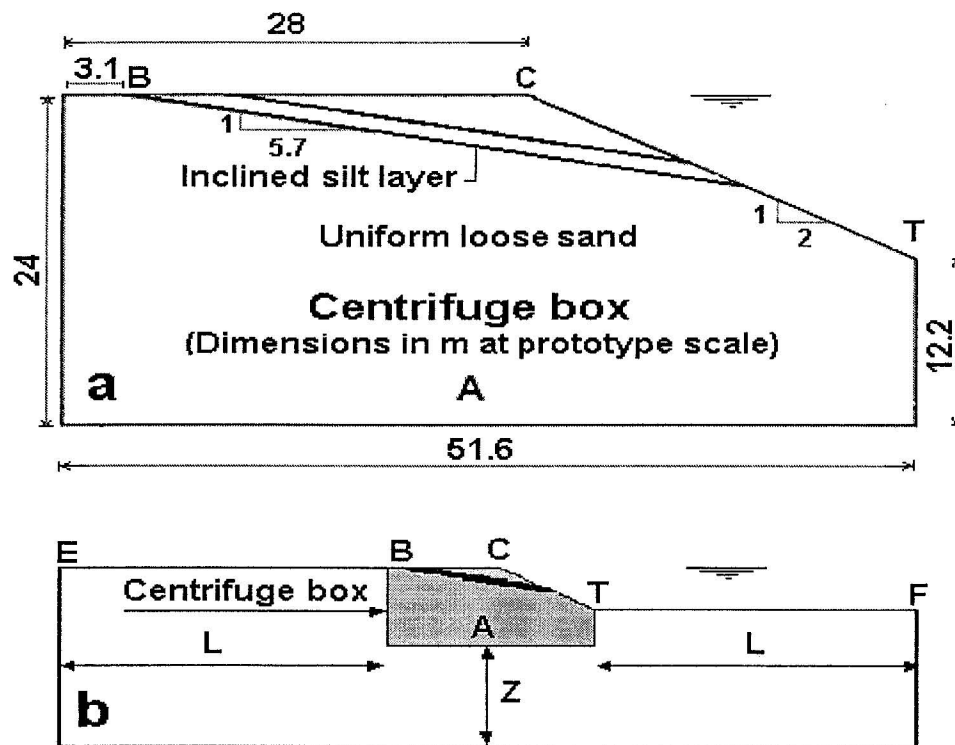


Figure 5.1 Layout of the waterfront slope analyzed in this study a) In the LRI centrifuge experiment CT7 performed using a rigid container (dimensions at the prototype scale), b) In FE analyses with extended domains in downward (denoted by Z), and lateral (denoted by L) directions.

5.2.1 Case 1: Modeling deep loose sand

Some results of numerical simulations corresponding to the FE mesh extensions in depth with a uniform loose sand layer (i.e., assuming $D_r = 40\%$ with no stress densification) are presented and discussed in this section. Figures 5.2 and 5.3 provide a summary of those results.

Maximum shear strain contours and deformed shapes computed at the end of analysis for a range of Z values and for a lateral FE mesh extension corresponding to $L = 75\text{m}$ are shown in Figure 5.2. Particularly for $Z \geq 16\text{m}$, two distinct failure mechanisms are formed in the slope by the end of analysis: a local failure along the silt layer, and a deep rotational failure causing settlement in the free field upslope and heave in front of the slope toe. The deep rotational slope failure predicted for $Z \geq 16\text{m}$ (Figures 5.2c and 5.2d) is restricted significantly by proximity of the base boundary for smaller Z (Figures 5.2a and 5.2b). The local failure along the silt layer was observed also in the centrifuge experiment, while the deep rotational failure did not take place in the experiments due to boundary effects.

The computed displacements at several locations at the end of each analysis for a range of FE domain extensions represented by parameters Z and L are shown in Figure 5.3. All the computed displacements increase as Z increases. This is probably due to the fact that for a certain value of L the rotational failure surface is deeper as Z increases (see also Figure 5.2).

As shown in Figures 5.3a to 5.3e, for a certain value of Z , as L increases all the computed displacements at several locations of the slope decrease. As mentioned in

Section 4.4.4 of Chapter 4 (i.e., for $Z = 0$), this is mainly caused by the vicinity of the rigid base that has higher restricting effects for full development of a circular failure mechanism within the slope for larger values of L . In fact, for higher values of L , ratio Z/L becomes smaller and the rotational failure mechanism is more restricted by the rigid base as explained in Section 4.4.4 (Chapter 4) in case of $Z = 0$.

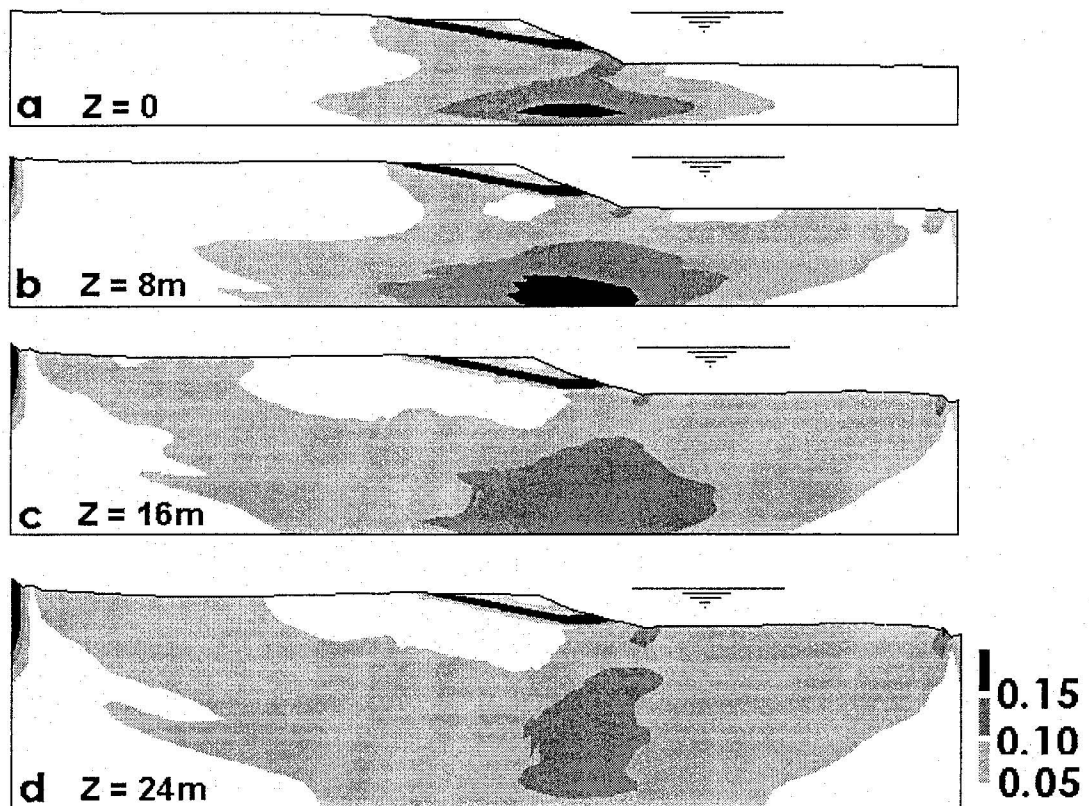


Figure 5.2 Submerged slope underlain by loose sand to great depth: Contours of maximum shear strains and deformed shapes at the end of analyses ($t = 42.6s$) for different FE mesh extensions in depth corresponding to $L = 75$ m (see Figure 5.1b); a) $Z = 0$, b) $Z = 8m$, c) $Z = 16m$, and d) $Z = 24m$. In this figure the deformed shape magnification factor is 3.

The results of numerical simulations of the waterfront slope underlain by a deep loose sand layer, summarized in Figures 5.2 and 5.3, indicate that the predicted seismic

behavior of a waterfront slope underlain by a deep loose sand layer (i.e., type of failure mechanism, and magnitude of the computed displacements) is significantly different from that of the same slope underlain by a rigid base (i.e., $Z = 0$). Consequently, centrifuge modeling of a waterfront slope underlain by a deep soft layer (loose sand in this study) with a rigid container provides under-conservative results, and it may not correctly represent the seismic behavior of such a slope.

5.2.2 Case 2: Modeling deep dense sand underlying loose sand

This section presents the results of the numerical simulations obtained based on extending the original FE domain in depth with a dense sand layer. Figure 5.4 shows contours of the maximum shear strain at the end of each analysis along with the deformed shapes of the slope for different values of Z and corresponding to a lateral FE mesh extension represented by $L = 75\text{m}$. The predicted contours of the maximum shear strain for different values of Z are very similar to each other and there is no significant discrepancy between the results as Z increases. Also, the tendency of loose sand to undergo a deep rotational failure is prevented by the presence of dense sand, and the local failure mechanism along the silt layer is prevailing.

Figure 5.5 shows the computed displacements at different locations in the slope at the end of each analysis for a range of FE domain extensions represented by parameters Z and L .

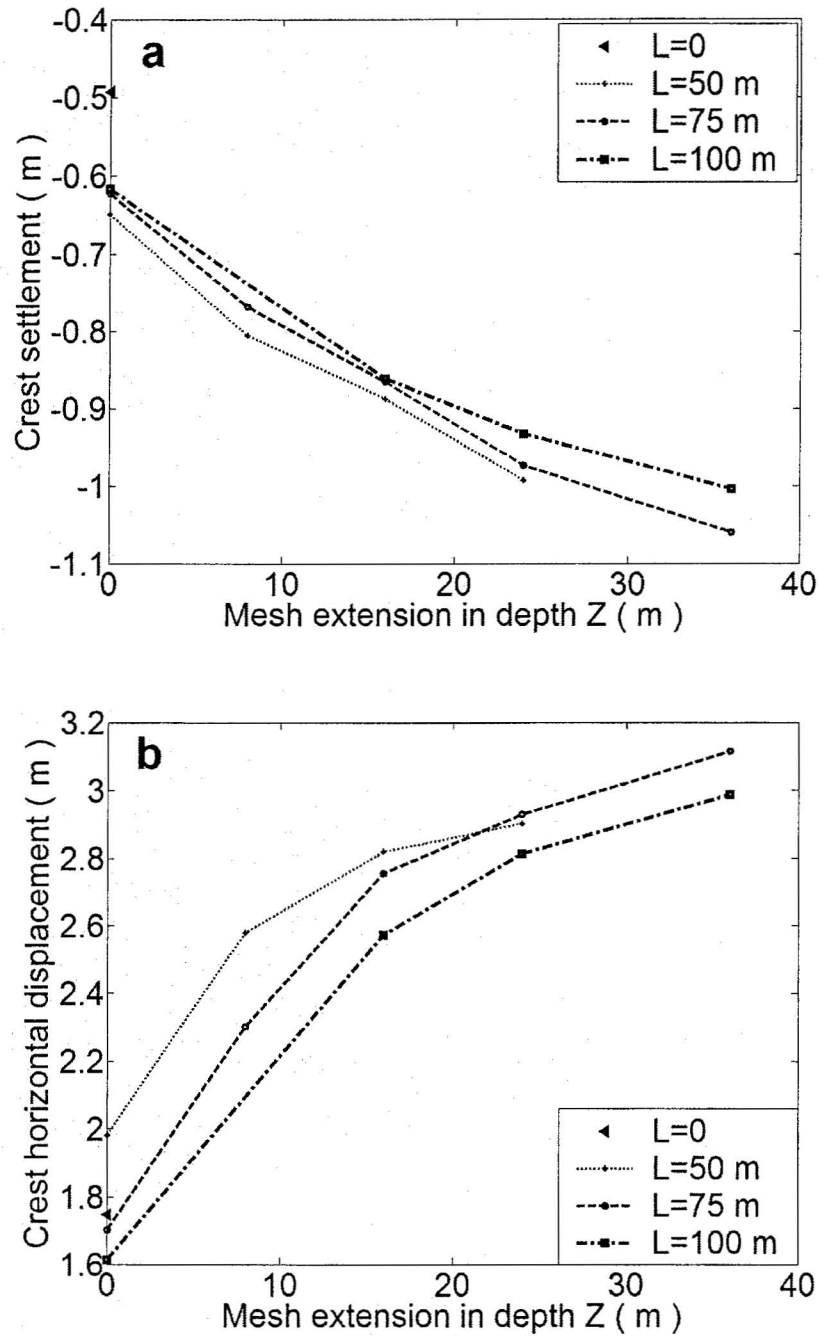


Figure 5.3 Submerged slope underlain by loose sand to great depth: Computed displacements at different locations at the end of each analysis ($t = 42.6s$) for a range of FE mesh extensions (denoted by L and Z in Figure 5.1b) a) crest settlement, b) crest horizontal displacement.

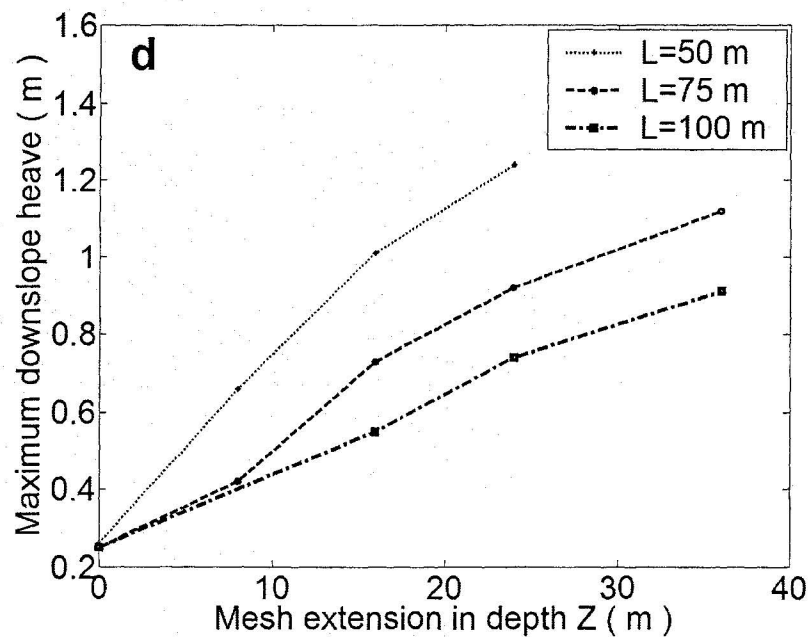
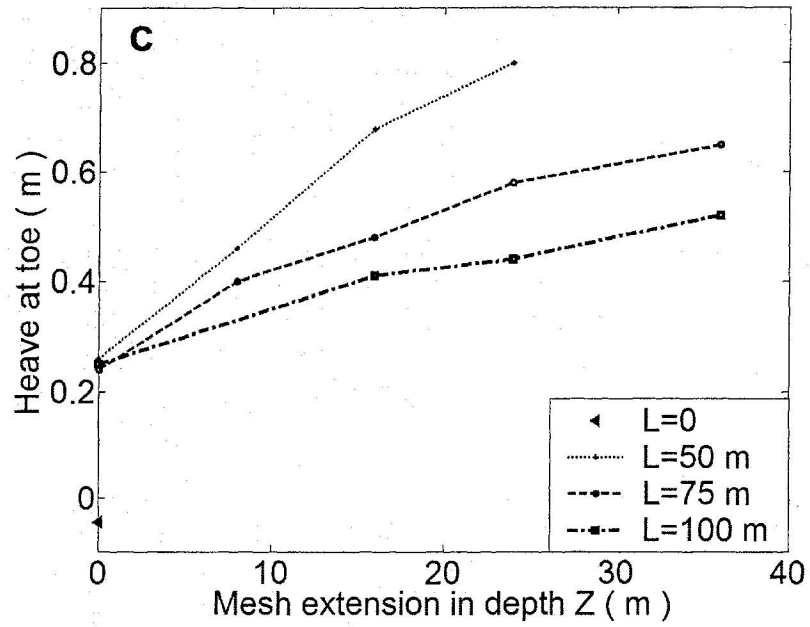


Figure 5.3 (Cont.) c) heave at the toe, d) maximum down-slope heave (anywhere on the line TF in Figure 5.1b).

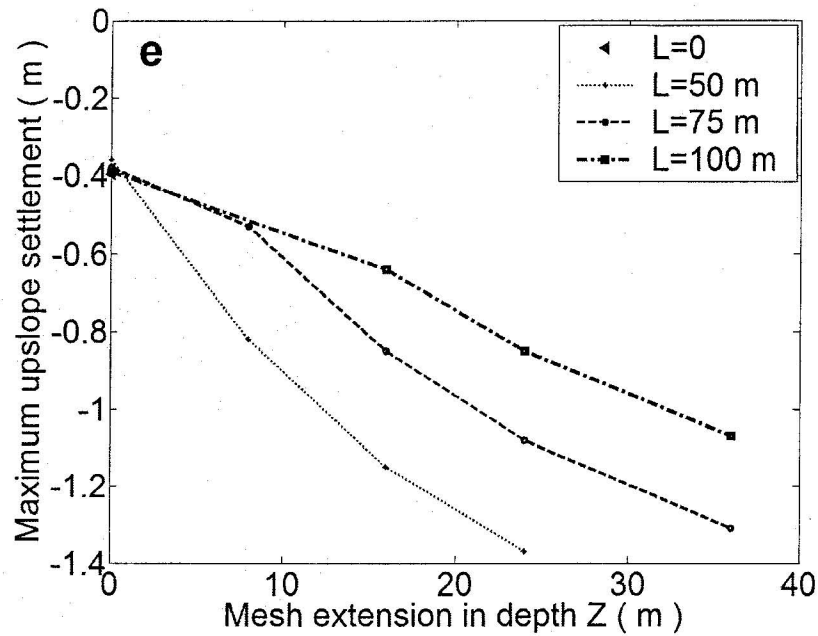


Figure 5.3 (Cont.) e) maximum upslope settlement (anywhere on the line BE in Figure 5.1b).

The significant difference between the seismic behavior of a waterfront slope underlain by a deep loose sand layer and that of the slope underlain by a deep dense sand layer is also confirmed by the magnitude of the computed displacements. In this regard, the computed maximum upslope settlement and maximum down-slope heave can be considered as a quantitative indicator for forming a rotational failure within the slope. For instance, the computed displacements corresponding to the FE mesh extension represented by $L = 75\text{m}$ and $Z = 24\text{m}$ in case of the slope underlain by a deep dense sand layer (Figures 5.5d and 5.5e) are 0.347m (maximum down-slope heave), and 0.52m (maximum upslope settlement); however in case of the slope underlain by a deep loose sand layer the computed displacements (corresponding to $L = 75\text{m}$ and $Z = 24\text{m}$) are significantly higher than those values (i.e., 0.92m for the maximum down-slope heave,

and 1.08m for the maximum upslope settlement as shown in Figures 5.3d and 5.3e). Comparison of these values also confirms that the tendency of the slope to undergo a deep rotational failure in case of a deep loose sand underlying the slope is significantly restricted if the slope is underlain by a deep dense sand layer.

For a certain value of L , all the computed displacements at several locations of the slope increase as Z increases (Figure 5.5a to 5.5e). This trend is mainly related to the ground motion amplification within the dense sand layer.

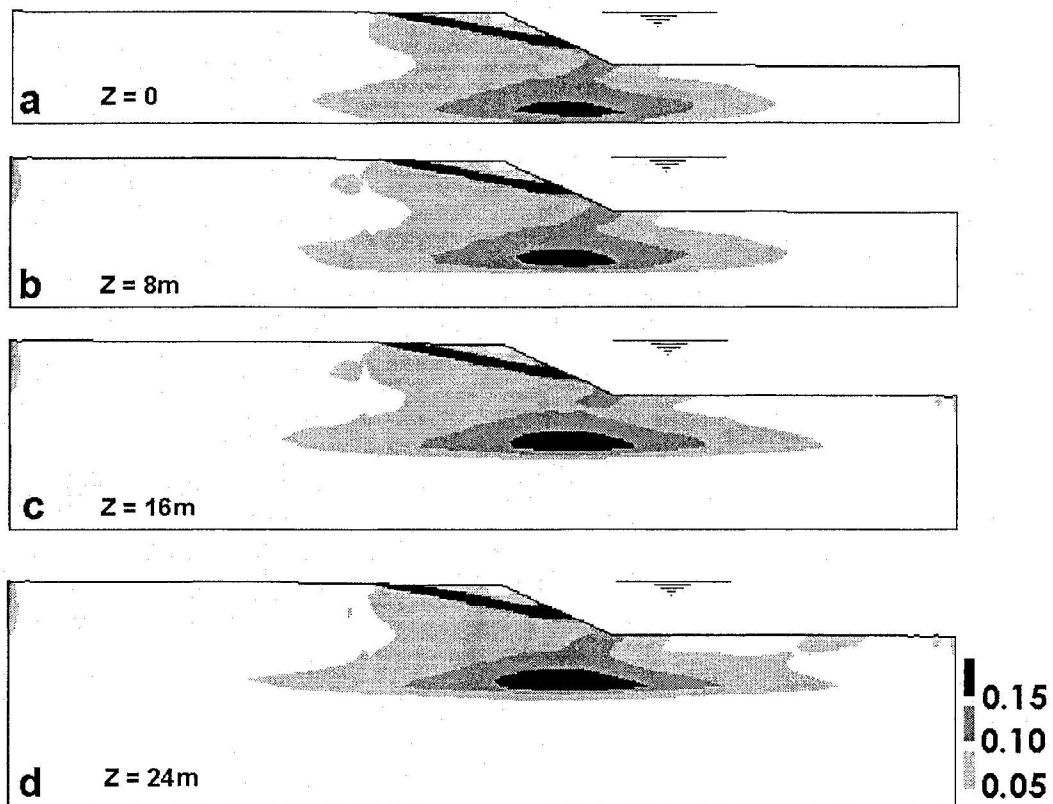


Figure 5.4 Submerged slope underlain by dense sand to great depth: Contours of maximum shear strains and deformed shapes at the end of each analysis ($t = 42.6\text{s}$) for different FE mesh extensions in depth corresponding to $L = 75\text{m}$ (see Figure 5.1b) a) $Z = 0$, b) $Z = 8\text{m}$, c) $Z = 16\text{m}$, and d) $Z = 24\text{m}$. In this figure the deformed shape magnification factor is 1.

The results obtained in this section indicate that if a waterfront slope is underlain by a strong non-liquefiable soil layer, the assumption of a rigid base at the depth of this layer ($Z = 0$) is reasonable, and it does not considerably affect the results. This assumption is also strengthened by a numerical study presented in the next section regarding the size of the FE domain decided for mitigation studies in this chapter (see Section 5.3.1).

5.3 Study on waterfront slope liquefaction countermeasures

5.3.1 Decision on the size of the FE domain for mitigation studies

Figures 5.5a to 5.5e indicate that in almost all cases as L increases the differences between the computed curves corresponding to two successive values of L diminish. In fact, for the values of L equal to $L = 75\text{m}$ and $L = 100\text{m}$ the results are very close to each other, and it can be concluded that, for the type and dimensions of the slope analyzed here, $L = 75\text{m}$ represents a reasonable value for extending the FE mesh in lateral directions.

To decide on the size of the FE domain extension in the downward direction Arias intensity (Arias, 1970) was employed as the indicator of earthquake intensity. This intensity (denoted by I hereafter) is a measure of the total energy delivered per unit weight of soil during an earthquake and is calculated as (Arias, 1970):

$$I = \frac{\pi}{2g} \int_0^{T_e} a_g^2(t) dt \quad (5-1)$$

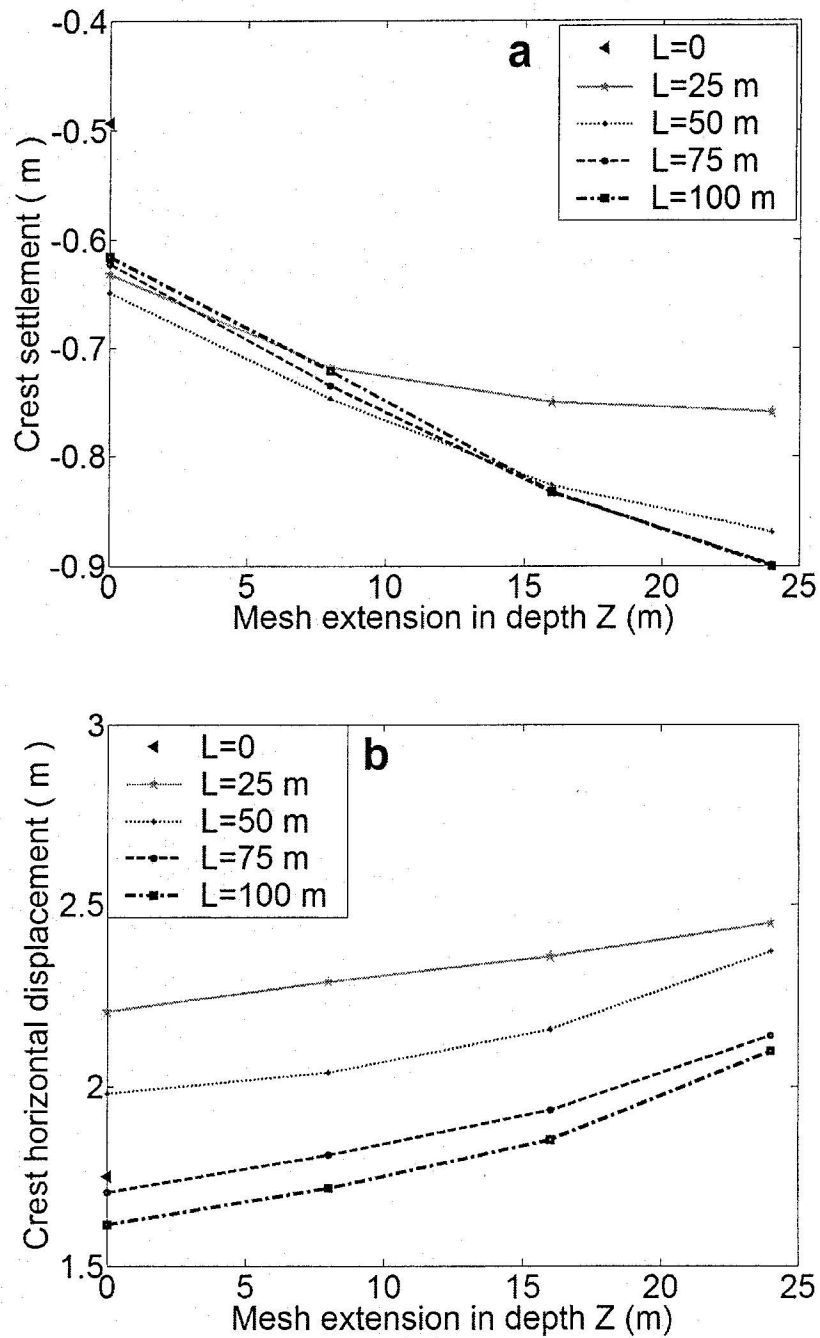


Figure 5.5 Submerged slope underlain by dense sand to great depth: Computed displacements at different locations at the end of each analysis ($t = 42.6$ s) for a range of FE mesh extensions (denoted by L and Z in Figure 5.1b) a) crest settlement, b) crest horizontal displacement.

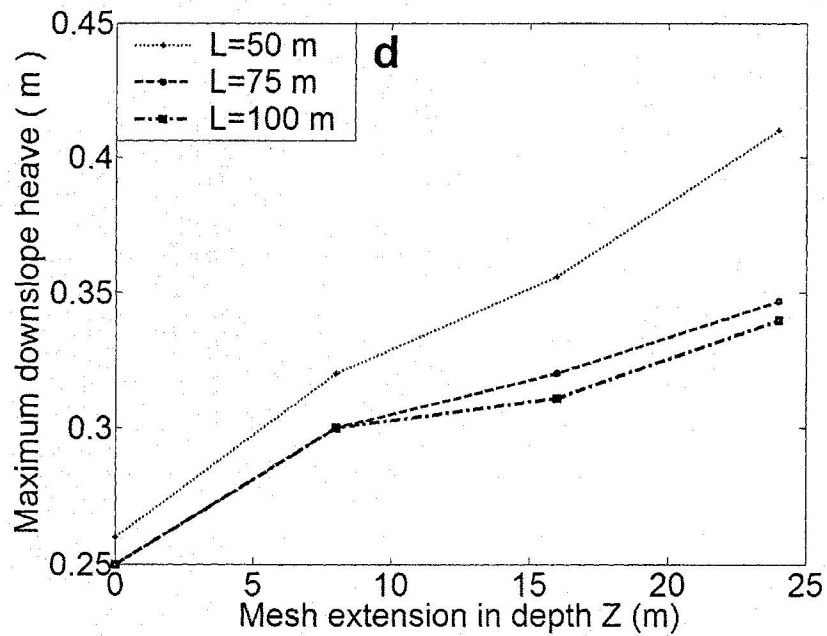
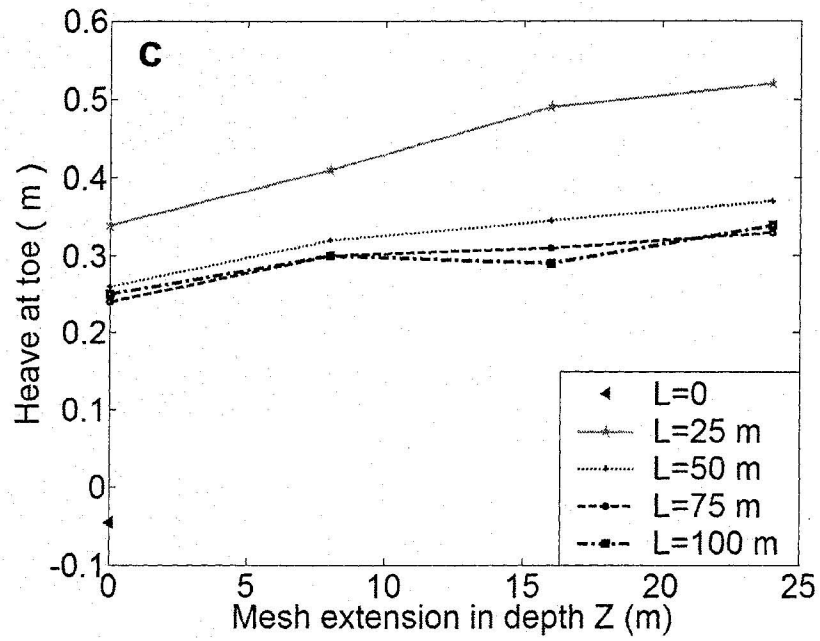


Figure 5.5 (Cont.) c) heave at the toe, d) maximum down-slope heave (anywhere on the line TF in Figure 5.1b).

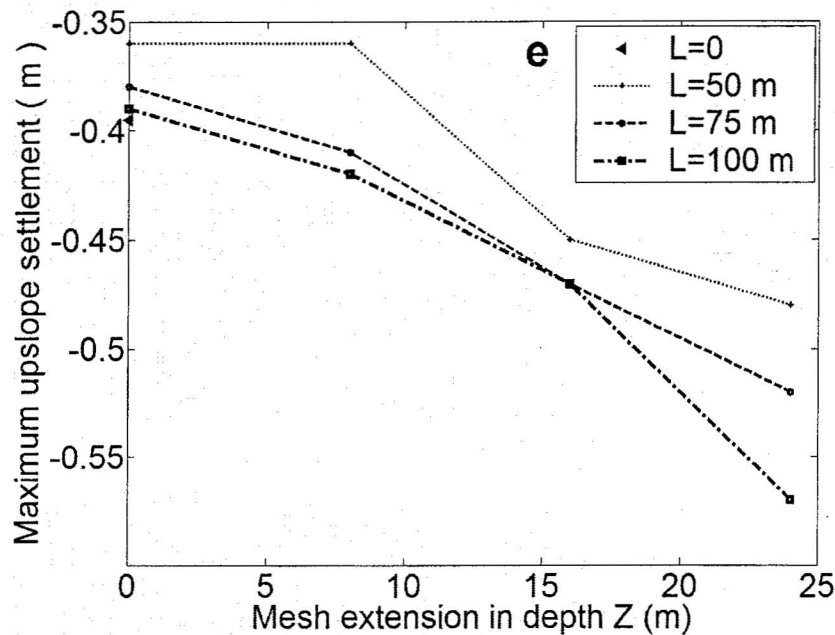


Figure 5.5 (Cont.) e) maximum upslope settlement (anywhere on the line BE in Figure 5.1b).

In Equation (5-1), I is the Arias intensity of an earthquake, g is the gravitational acceleration, $a_g(t)$ is the ground acceleration at instant t , and T_e is the total earthquake duration. Numerical simulations of the slope corresponding to a lateral FE domain extension represented by $L = 75\text{m}$ (Figure 5.1b) were performed for different values of Z using the target base input motion in test CT7, i.e., $2 \times A2475$. Based on the obtained results, the computed values of Arias intensities at point A (near the base of the rigid container as shown in Figure 5.1) were 3.40m/s , 3.66m/s , 4.40m/s , and 4.68m/s corresponding to $Z = 0$, $Z = 8\text{m}$, $Z = 16\text{m}$, and $Z = 24\text{m}$, respectively. As these values show, for the same base input acceleration ($2 \times A2475$) the Arias intensity at point A increases as the depth of the FE domain extension in dense sand increases. As explained in Section 5.2.2, this is mainly due to the amplification of shear waves passing through

the dense layer. In fact, a seismic motion can be either attenuated or amplified when passing through soil layers, depending on many factors, such as stiffness of the soil, stiffness contrast between rock and soil layers and intensity of the seismic motion. As stated by current seismic guidelines (e.g., NBCC 2005), the attenuation coefficients may be larger than one (i.e., amplification), especially for denser/stiffer soils, as is the case of the dense soil layer considered here. Therefore, to obtain the same Arias intensities at point A for different values of Z the target base input acceleration time history should be scaled. It is mentioned that the correction factors (scaling factors) are applied here uniformly over the entire frequency range, while the code-recommended correction factors are frequency dependent (e.g., NBCC, 2005).

Equation (5-1) shows that Arias intensity is proportional to the acceleration squared. Consequently, the first guess for scaling the base input motion corresponding to different values of Z can be obtained from the following relationship:

$$f_z = \sqrt{\frac{I_0}{I_z}} \quad (5-2)$$

I_0 and I_z in Equation (5-2) are the computed Arias intensities at point A corresponding to $Z = 0$ and $Z = Z$, respectively, using the target input acceleration (2 x A2475). Based on the computed Arias intensities at point A (e.g., $I_0 = 3.40\text{m/s}$ for $Z = 0$, etc.), Equation (5-2) resulted in scaling factors $f_8 = 0.96$, $f_{16} = 0.88$, and $f_{24} = 0.85$ related to $Z = 8\text{m}$, $Z = 16\text{m}$, and $Z = 24\text{m}$, respectively.

Using the obtained scaling factors for the base input motion, numerical simulations of the slope were performed for different values of Z and the corresponding Arias intensities at point A were computed and compared to its value at $Z = 0$ ($I_0 = 3.40\text{m/s}$). In case of Z

= 8m the calculated factor resulted in a value of Arias intensity at point A equal to 3.43m/s, which is very close to I_0 (with an error less than 1%). However, for cases corresponding to $Z = 16\text{m}$ and $Z = 24\text{m}$ the obtained Arias intensities with scaling factors were about 6% and 9.6% higher than I_0 . Therefore, for these cases trials were continued to find lower scaling factors that reasonably result in similar Arias intensities at point A. After performing a few trials (numerical simulations of the slope), the final computed scaling factors for the target base input motion were $f_8 = 0.96$, $f_{16} = 0.85$ and $f_{24} = 0.80$ leading to $I_8 = 3.43\text{m/s}$, $I_{16} = 3.41\text{ m/s}$ and $I_{24} = 3.38\text{m/s}$ corresponding to $Z = 8\text{m}$, $Z = 16\text{m}$, and $Z = 24\text{m}$, respectively (with errors less than 1% compared to I_0).

The computed displacements at the end of each analysis (obtained from numerical simulations of the slope using the final scaling factors for the base input motion) at key points of the slope vs. parameter Z are shown in Figure 5.6. Regardless of some small discrepancies the obtained curves remain reasonably horizontal as Z increases. This figure also confirms that centrifuge modeling of a waterfront slope underlain by a very dense layer using a container with rigid base (represented by $Z = 0$) reasonably represents the soil seismic behavior.

Moreover, Figure 5.7 shows the computed displacements at key points of the slope at the end of each analysis ($t = 42.6\text{s}$) as functions of L and for $Z = 0$ (i.e., assuming a rigid base with no FE analysis domain extension in depth). The results include the computed crest horizontal displacement, crest settlement, and heave at the slope toe. For $L \geq 75\text{m}$ the computed displacements do not significantly change by increasing L and the computed curves remain reasonably horizontal. The computed curve corresponding to the

crest horizontal displacement shows an unexpected trend in which the computed displacement in case of $L = 0$ is lower than the values corresponding to $L = 25\text{m}$ and $L = 50\text{m}$ and higher than the values corresponding to $L = 75\text{m}$ and $L = 100\text{m}$. A possible explanation may be related to a stronger interference of the seismic waves reflected by the lateral boundaries for a particular value of L . As shown in Figure 5.7 this is more pronounced for $L = 25\text{m}$. A similar wave reflection/interference phenomenon was mentioned in a paper by Azizian and Popescu (2006). The computed negative value for heave at the slope toe for $L = 0$ is obviously related to the effects of the centrifuge rigid boundaries.

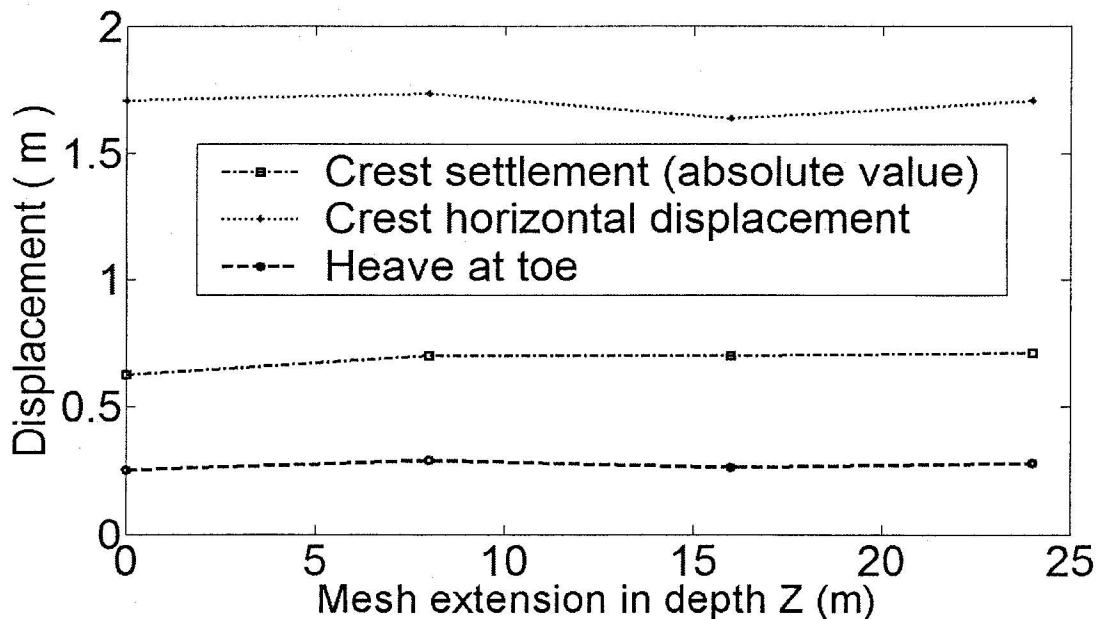


Figure 5.6 Computed displacements at the end of each analysis ($t = 42.6\text{s}$) at key points in the slope as a function of mesh extension in depth with dense sand, Z , using a set of base input accelerations obtained from scaling the event 2 x A2475 by different factors that result in similar Arias intensities at point A shown in Figure 5.1a. The results correspond to a lateral FE analysis domain extension represented by $L = 75\text{m}$ (see Figure 5.1b).

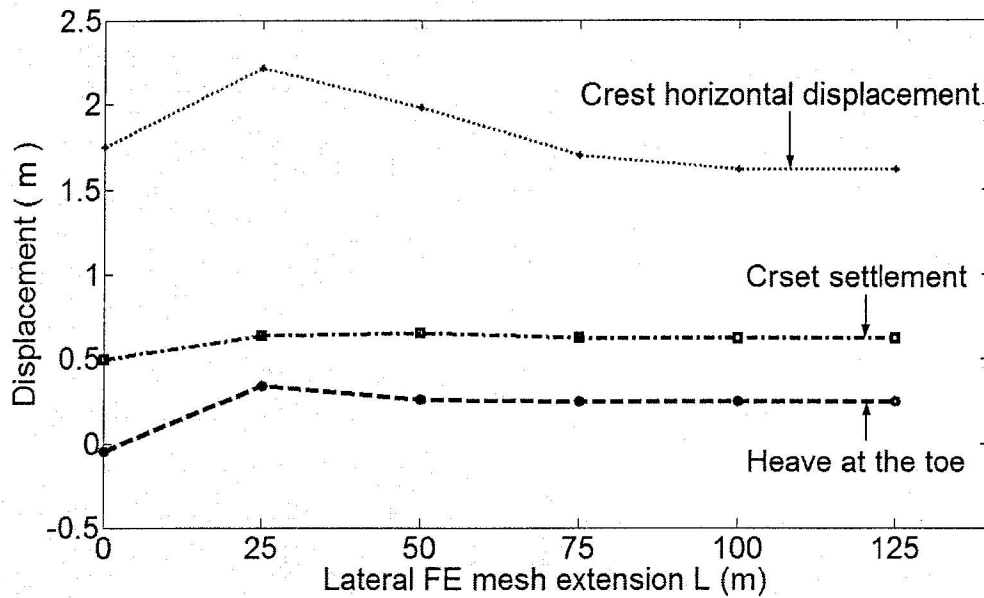


Figure 5.7 Computed displacements at key points of the slope at the end of each analysis ($t = 42.6\text{s}$) versus parameter L in case of $Z = 0$ (i.e., only lateral extension of the FE analysis domain). Event 2 x A2475 was used as the base input acceleration.

The numerical results shown in Figures 5.6 and 5.7 indicate that a lateral FE domain extension on both sides of the rigid box corresponding to $L = 75\text{m}$ (with no FE analysis domain extension in depth, i.e., $Z = 0$) can reasonably diminish the effects of the rigid box on the seismic behavior of the slope; consequently, the extended FE analysis domain corresponding to parameters $L = 75\text{m}$ and $Z = 0$ (see Figure 5.1b) was used in numerical studies on the performance and effectiveness of the waterfront slope liquefaction countermeasures discussed in this chapter.

5.3.2 Performance of the improved slope

The performance of several measures applied to the slope for mitigating soil liquefaction effects is studied and discussed in this section. A descriptive summary of the four remediation measures considered in this study along with the base case with no

mitigation (M0) is presented in Table 5.1. Most of the remediation techniques addressed in this section originate from the ground improvement measures proposed by the LRI industry participants (EIDMSL, 2003). For instance, dykes made of drainage material crossing the inclined silt layer to relieve the excess pore water pressures that build up below this layer during the earthquake were used in tests CT5 and CT8. A large dyke of dense sand for strengthening the upper part of the slope was used as mitigation measure in test CT3. The layout of the mitigation measures considered in this study that include drainage dykes (M1), dense sand dykes (M3) and combinations (M2) is shown in Figure 5.8a (see also Table 5.1). In addition, the performance of a short sheet pile, (mitigation measure labeled as M4 in Table 5.1 and shown in Figure 5.8b) is also investigated. It is mentioned that a series of trials regarding sheet pile location and its length have been done to find the current configuration provided here. While no cost analysis was done, the selected solution (M4) was found to have the best mitigative effects for the slope. As stated in Section 5.3.1, it is assumed that the loose sand slope is underlain by a very dense sand layer at the level of the centrifuge box base and the analysis domain for this study corresponds to $L = 75\text{m}$ and $Z = 0$ (see Figure 5.1b).

Table 5.1 also includes a quantitative comparison of the performances of all mitigation configurations studied here (i.e., measures M1 to M4 along with the unmitigated slope, M0) based on the computed maximum displacements at key points of the slope including maximum crest settlement (C_v), maximum crest horizontal displacement (C_h), and maximum horizontal displacement of the soil wedge above the silt layer relative to the soil below the silt layer (W_h). The latter refers to the difference

between the horizontal displacements of points C and B shown in Figure 5.8. The numerical simulations were performed using the target base input acceleration time history employed in the centrifuge experiments CT5 to CT8, namely 2 x A2475 shown in Figure 4.2b (Chapter 4).

Contours of the maximum shear strain and excess pore water pressure ratio at the end of analyses ($t = 42.6s$) corresponding to measures listed in Table 5.1 are shown in Figures 5.9 and 5.10, respectively.

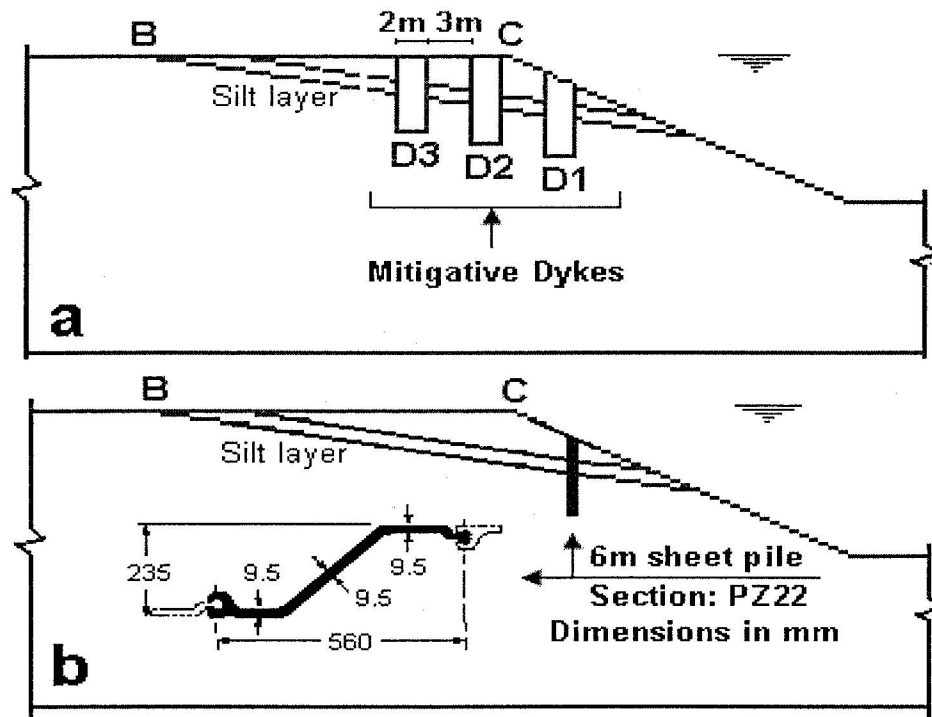


Figure 5.8 Layouts of different mitigation configurations studied a) drainage or dense dykes similar to the measures used in the LRI centrifuge experiments, and b) a 6-m deep sheet pile (sheet pile section from TXI Chaparral Steel, 2003 with modifications).

Table 5.1 Quantitative comparison of the performance of different mitigation measures (C_v , C_h , and W_h are the computed maximum values corresponding to the crest settlement, crest horizontal displacement and horizontal displacement of the soil wedge relative to the soil below the silt layer.).

Mitigation configuration	Description	C_v (m)	C_h (m)	W_h (m)	Reference figure
M0	No soil improvement	0.57	1.57	1.18	5.8a
M1	Three drainage dykes (D1, D2, and D3) as used in LRI CT5 and CT8	0.61	1.27	0.96	5.8a
M2	Two dense dykes (D1 and D2) and one drainage dyke (D3)	0.47	1.24	0.90	5.8a
M3	Mitigated using three dense dykes (D1, D2, and D3)	0.48	1.19	0.83	5.8a
M4	6-m deep sheet pile	0.55	1.26	0.88	5.8b

Regarding the analysis of the sheet pile case (mitigation strategy labeled as M4 in Table 5.1), it is mentioned that two different cases were considered: a model with Coulomb friction contact element (Prevost, 2002) at the pile-soil interface (with an assumed friction angle of 30°) and the perfect stick assumption. The differences between results of the two types of analyses were insignificant (about 2% for the predicted crest settlement and less than 1% for the crest horizontal displacement). Therefore, the perfect stick model was used in this study for comparing the results in Table 5.1 and for building fragility curves as presented in the next section. The sheet pile section was selected to resist the maximum computed bending moment along the pile during the excitation. As shown in Figure 5.8b in this study section PZ22 with a section modulus of 988 cm^3 per unit length (1m) of the pile (TXI Chaparral Steel, 2003) and an allowable stress of 170 MN/m^2 (in accordance with ASTM A328, e.g., Das, 1999) was considered to carry the calculated maximum bending moment of about 150 kN.m per unit length of the sheet

pile. This section due to its optimum distribution of material is one of the most efficient and reliable sheet piling section available for bending strength (TXI Chaparral Steel, 2003).

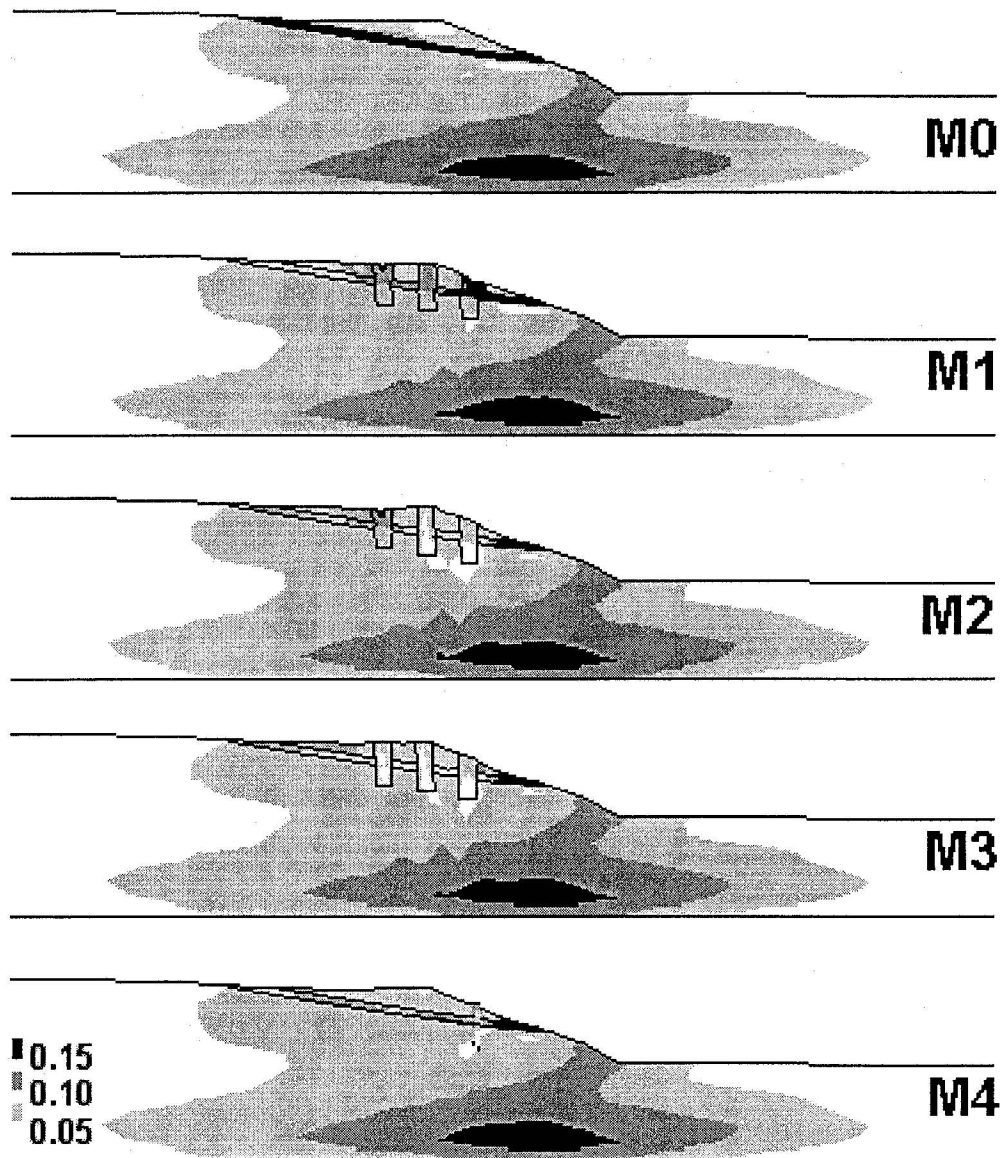


Figure 5.9 Computed contours of the maximum shear strains and deformed shapes (deformation magnification factor = 3) at the end of each analysis ($t = 42.6s$) corresponding to the mitigation measures listed in Table 5.1.

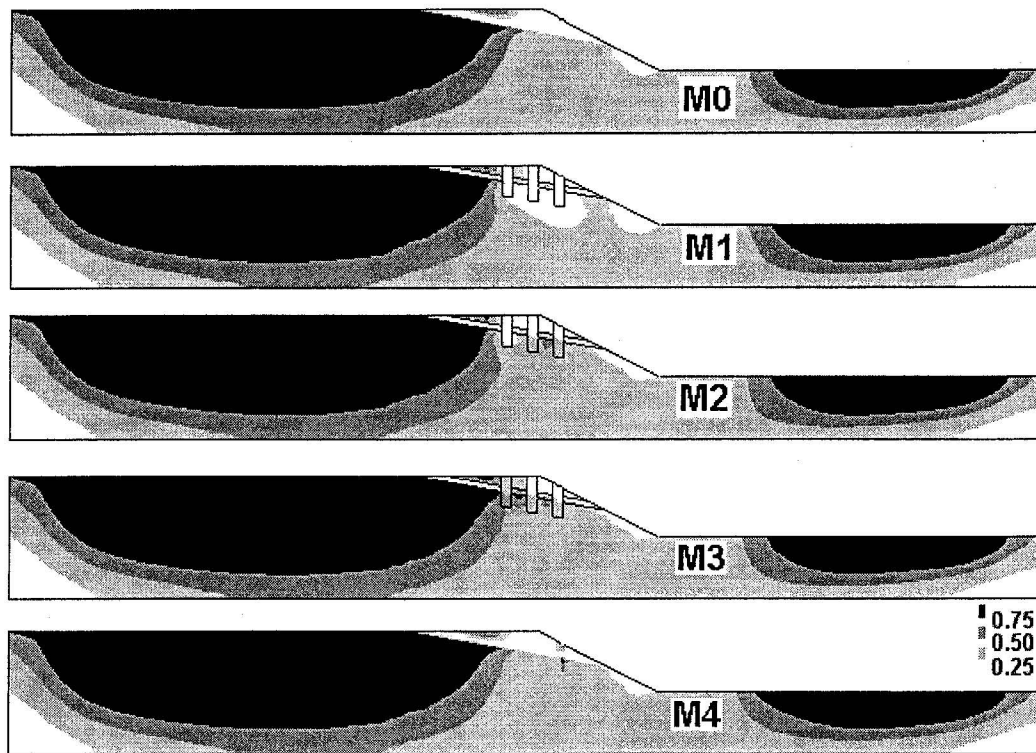


Figure 5.10 Computed contours of the excess pore water pressure ratio at the end of each analysis ($t = 42.6s$) corresponding to the mitigation measures listed in Table 5.1.

First, the results corresponding to dyke type measures, namely M1, M2 and M3 are discussed and compared to the results for the unmitigated slope (M0): M1 (three drainage dykes) was proposed for the LRI centrifuge tests CT5 and CT8. While locally reducing the excess pore water pressure below the silt layer (Figure 5.10) and slightly lowering the crest horizontal displacements, this measure does not reduce the slope crest settlement as compared to M0 (C_v in Table 5.1). This result obtained in numerical simulations was also confirmed by the centrifuge experiments. The explanation is that the drainage dykes reduce excess pore water pressure build up only in their immediate vicinity, and they are not strong enough to sustain large shear stresses developing along the silt layer. In fact, in both centrifuge experiments and numerical simulations it was found that the drainage

dykes are sheared at the level of silt layer (see also the results in case of M1 in Figure 5.9). M2 (two dense dykes and one drainage dyke) seems to be more reliable than M1. In this case (M2) the crest settlement and horizontal displacement were reduced by about 18% and 21%, respectively, as compared to the unmitigated slope (M0). M3 (three dense dykes) shows slightly improved results as compared to M2 in reducing the horizontal movements of the crest and of the soil wedge above the silt layer (i.e., 24% and 30% reduction, respectively, compared to M0); however, the crest settlement was reduced by about 16% as compared to M0, which is slightly lower than the value computed for M2 (i.e., 18%).

In general, the numerical results corresponding to measures M1 to M3 show a better performance of dense dykes in reducing crest displacements than that of drainage dykes. This is mainly due to the increased shear strength of the dense dykes that reduces sliding along the inclined silt layer. At this point it is worth mentioning that actual construction of such dykes dug into submerged loose sand may be very difficult, and such measures may not be economically feasible for mitigating a large waterfront slope.

As listed in Table 5.1, a mitigation method that seems to be as efficient as continuous dykes and easy to build is sheet piling in front of the slope (mitigation using a 6-m deep sheet pile denoted by M4 in Table 5.1 and sketched in Figure 5.8b). Numerical results related to this measure reveal an improved performance compared to M1. Also, the performance of this measure (M4) is comparable to measures M2 and M3 particularly in reducing the general movement of the soil wedge above the silt layer (about 25% reduction compared to the unmitigated case, M0). Sheet piling was found to be not very

effective in reducing the crest settlement as compared to measures M2 and M3. This may be related to the fact that in measures M2 and M3 the slope crest is locally stiffened due to presence of a dense sand dyke (D2 in Figure 5.8a).

As shown in Figure 5.9, all the mitigation measures (M1 to M4) reduce the severity of the local failure along the silt layer as compared to M0. In this respect, the performance of measures M2, M3, and M4 is practically identical; however, dyke D1 in measure M1 is severely sheared as also observed in centrifuge experiments.

5.4 Effectiveness of different mitigation measures

Numerical simulations for the five configurations listed in Table 5.1 (M0 to M4) were performed at different earthquake intensities using a set of 31 simulated earthquake ground accelerations. All these acceleration time histories are compatible with the same response spectrum (namely type 3 design spectrum recommended by the Uniform Building Code, 1994 for soft soil) and have the same duration of the strong ground motion (see also Popescu, 2002). Though having identical frequency and envelope characteristics, each acceleration time history is a sample function of a non-stationary stochastic process, and the differences in the actual realizations of those sample functions reflect the uncertainty in the actual seismic motion arriving at a specific site. The simulated time histories were selected to obtain a range of Arias intensities between 0.5 m/s to 5 m/s, corresponding to a range of peak ground accelerations between 0.17g and 0.53g. The computed Arias intensities for Events A2475 (corresponding to a probability

of 2% in 50 years) and 2 x A2475 are 0.81m/s and 3.24m/s, respectively, which are within the selected range of the Arias intensities considered in this study.

Some of the numerical simulations results are shown in Figure 5.11 in terms of maximum crest settlements (Figure 5.11a), maximum crest horizontal displacements (Figure 5.11b) and maximum relative horizontal displacement of the soil wedge above the silt layer (Figure 5.11c).

As stated in the previous section, the computed crest settlements (Figure 5.11a) show that measure M1 does not have any effect and in all cases the computed crest settlements are higher than those computed for the unmitigated slope (M0). Measures M2 and M3 are effective in this respect for the entire range of Arias intensities considered in this study. M4 was found less effective in reducing crest settlements compared to measures M2 and M3. A possible cause is that for measures M2 and M3 the crest is locally stiffened due to construction of a dense dyke (D2) at the vicinity of slope crest.

Figure 5.11b shows that all mitigation measures are effective in reducing the crest horizontal displacements. Measures M2 and M3 show similar performances.

Significant reduction can be expected for the relative horizontal movement of the soil wedge above the silt layer by applying mitigation measures (Figure 5.11c). This is more noticeable at higher levels of Arias intensities.

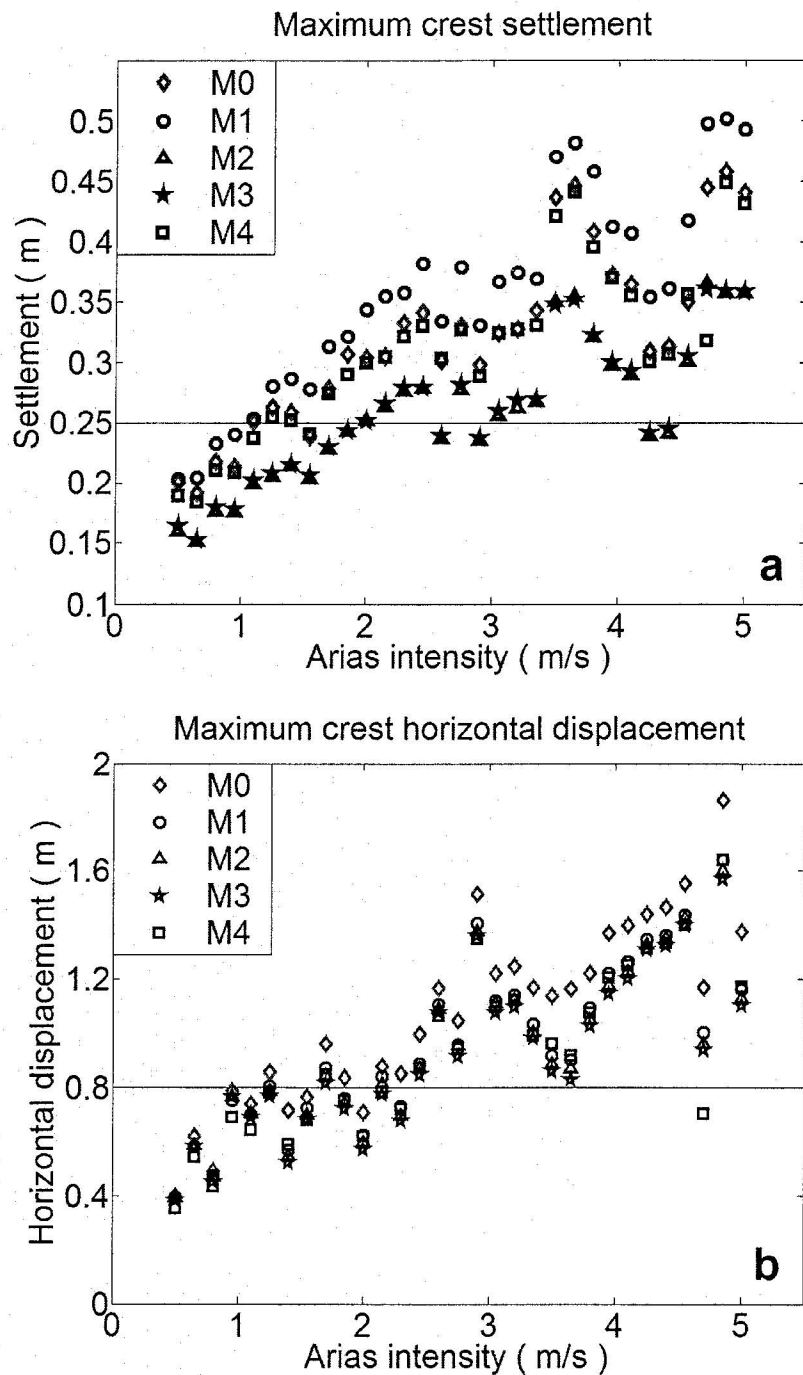


Figure 5.11 Computed maximum displacements for a range of Arias intensities and corresponding to different mitigation measures: a) crest settlement, b) crest horizontal displacement. The horizontal lines on figures represent displacement thresholds used for constructing fragility curves.

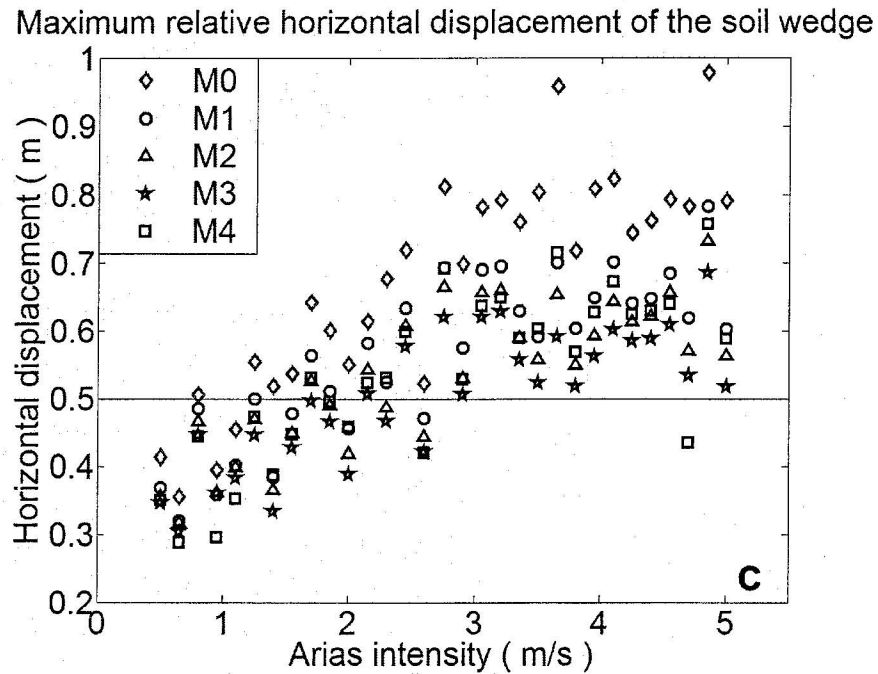


Figure 5.11 (Cont.) c) relative horizontal displacement of the soil wedge.

The horizontal lines shown in Figures 5.11a to 5.11c represent the displacement thresholds used for building fragility curves described hereafter. Fragility curves are an illustrative and practical way of expressing the probability of exceeding a certain degree of structural response as a function of load intensity. Fragility curves have been used extensively in earthquake engineering to describe the seismic vulnerability of structures as a function of the severity of the seismic event (e.g, Shinozuka, et al., 2000; and Popescu et al., 2006). The procedure used here for plotting fragility curves follows that proposed by Shinozuka et al. (2000). Arias intensity is used as a measure of earthquake intensity in this study. After selecting a specific response threshold (e.g., one of the displacement thresholds shown in Figure 5.11), all Arias intensities I for which the response exceeds this threshold are assigned to the unity probability level, while all the

other intensities are assigned to the zero probability level. This is illustrated in Figure 5.12a for the relative horizontal displacements of the soil wedge computed for mitigation type M4. Next, a shifted lognormal distribution function is fitted to those points (zeros and ones) using the maximum likelihood method (Figure 5.12b). A detailed description of the procedure is presented by Shinozuka et al. (2000). Fragility curves can include effects of multiple sources of uncertainty related to material resistance or load characteristics. The curves used in this study reflect only uncertainty in the seismic ground motion.

The thresholds for displacements shown in Figure 5.11 have been arbitrarily selected to represent slope displacements that may cause major damage to waterfront structures. These thresholds should be decided for actual projects on a case by case basis according to the specific utilities at the site. As shown in Figure 5.11, the displacement thresholds considered in this study are 0.25m for crest settlement, 0.8m for crest horizontal displacement, and 0.5m for relative horizontal displacement of the soil wedge above the silt layer.

Fragility curves corresponding to different criteria (crest settlements, crest horizontal displacements and relative displacement of the soil wedge) and different mitigation strategies are shown in Figure 5.13.

In case of crest settlement (Figure 5.13a), the fragility curve related to M1 shows a sudden jump, due to the fact that all crest settlements computed for $I < 1\text{m/s}$ are smaller than the threshold value (here 0.25m) and all crest settlements computed for $I > 1\text{m/s}$ are larger than the assumed threshold (see Figure 5.11a). M2 and M3 resulted in

superimposed fragility curves. It is noted from Figure 5.13a that measures M2 and M3 are very effective in reducing the crest settlements, especially at large seismic intensity. The effectiveness of measures M2, M3, and M4 in reducing the crest settlement at Arias intensities close to the design acceleration time history in Vancouver area (i.e., event A2475 with an Arias intensity of 0.81m/s) are almost identical. It can be inferred from the fragility curves presented in Figure 5.13a that, for M2, M3 and M4, the probability of exceeding crest settlements of 0.25m under an earthquake with $I = 0.81\text{m/s}$ is about 2%, while for the same earthquake, the probability of exceeding crest settlements of 0.25m for an unmitigated slope (M0) is about 11.5% (see Figure 5.13a).

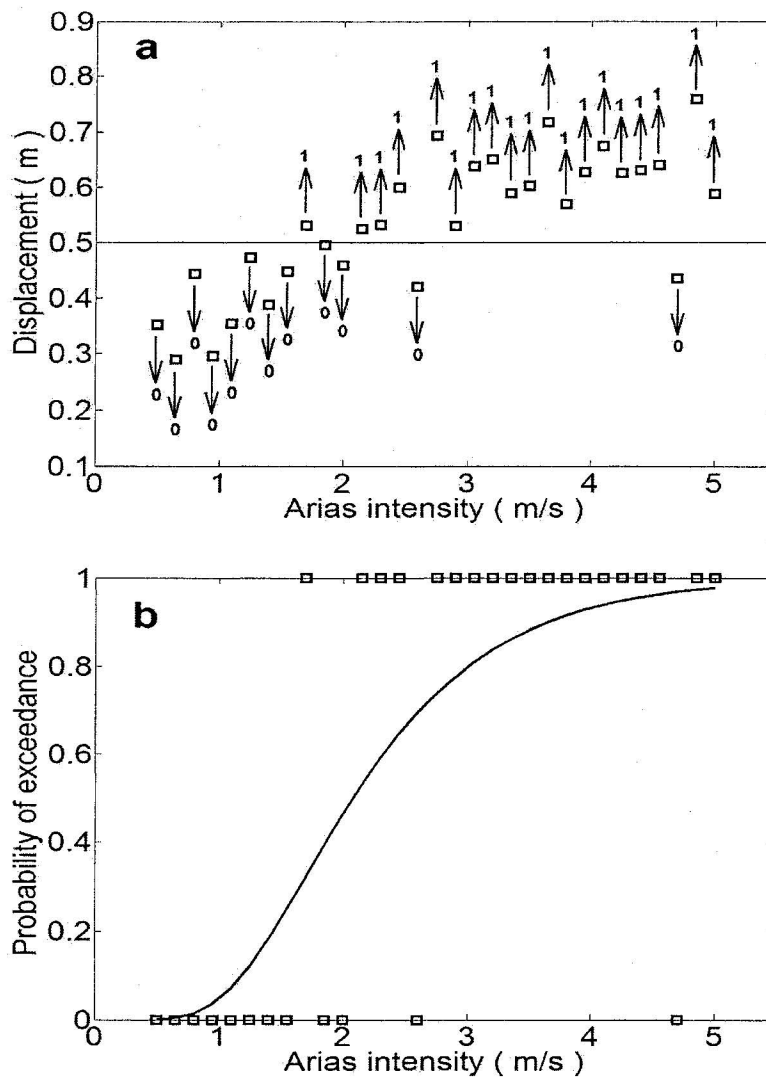


Figure 5.12 An illustrative example regarding the construction of a fragility curve. The data shown in the figure correspond to the relative horizontal displacement of the soil wedge in case of mitigation measure M4, i.e., 6-m deep sheet pile. a) depending upon whether or not the computed displacement exceeds the assumed threshold (0.5m), the corresponding probability level is assigned 1 (in case of exceedance) or 0 (in case of non-exceedance) as shown in the figure, b) fitting a shifted log-normal probability distribution function for the points shown in Figure 5.12a.

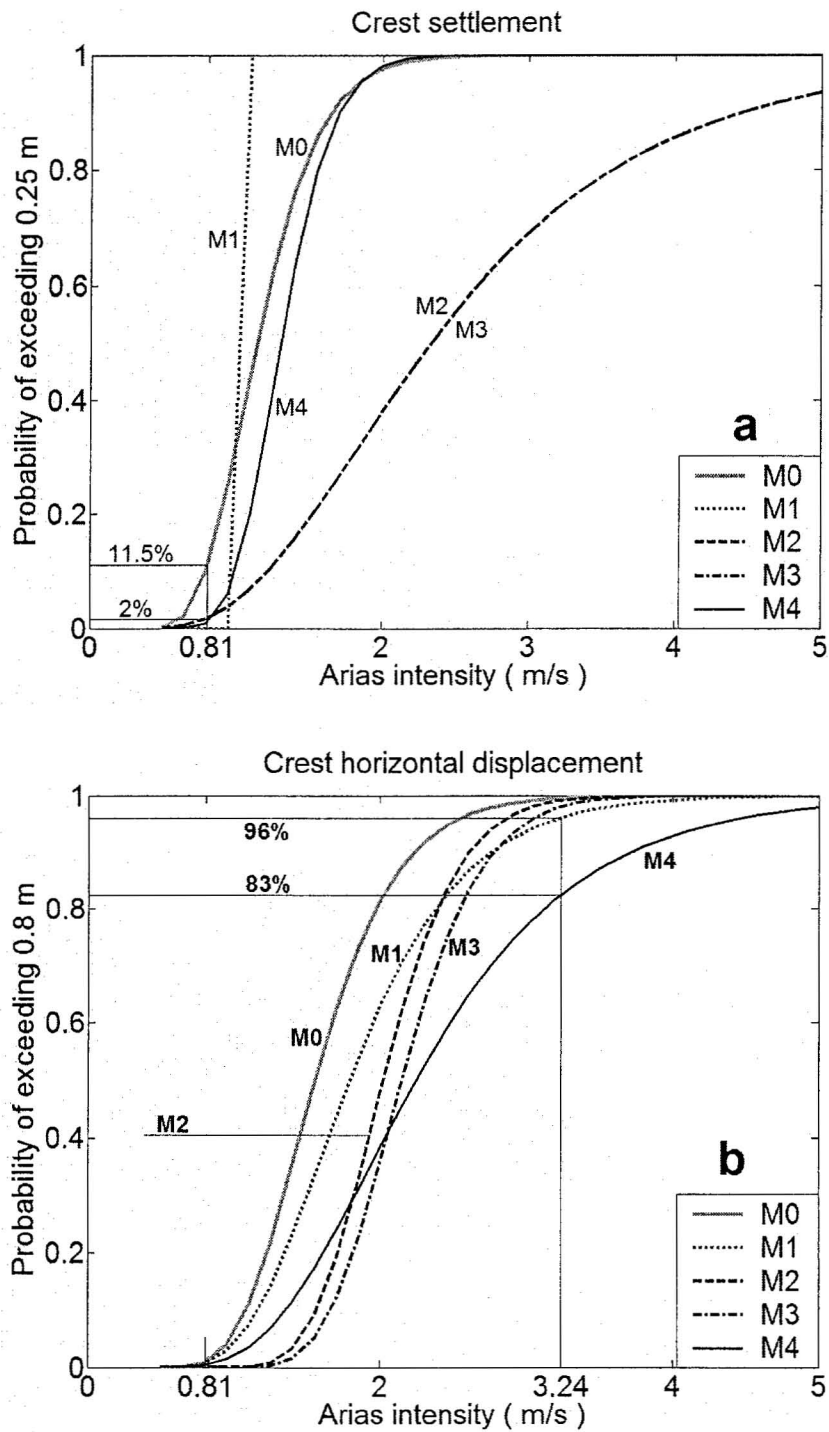


Figure 5.13 Fragility curves illustrating the effectiveness of different mitigation measures expressed at different Arias intensities: a) crest settlement b) crest horizontal displacement).

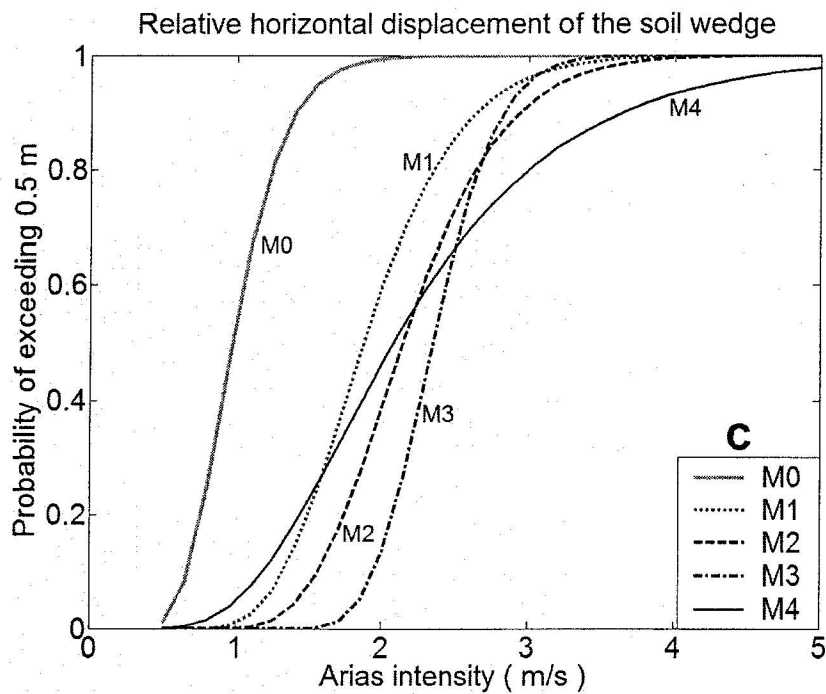


Figure 5.13 (Cont.) c) relative horizontal displacement of the soil wedge.

All four mitigation measures discussed here resulted to be effective in reducing the crest horizontal displacements (Figure 5.13b). Fragility curves corresponding to the crest horizontal displacement reveal that measure M4 (sheet piling) appears to be more effective than the other measures at high levels of Arias intensity (e.g., for $I > 2.5\text{m/s}$), and M2 and M3 work more effectively than the others for lower intensities. For instance, at $I = 0.81\text{ m/s}$ (equal to the Arias intensity of the event A2475) M2 and M3 are slightly more effective than M4 and the probabilities of exceeding the crest horizontal displacement of 0.8m are practically zero for measures M2 and M3 and 0.5% for measure M4 (not shown in Figure 5.13b). On the other hand, at $I = 3.24\text{m/s}$ (similar to the intensity of event 2 x A2475) M4 is more effective than the other measures (M1, M2, and M3). As shown in Figure 5.13b the probability of exceeding the crest horizontal

displacement of 0.8m corresponding to measure M4 is 83%, while for measure M1 this probability is about 96% and for other measures it is higher than 98% (not shown in the figure). Figure 5.13b also shows that the performance of measure M1 at Arias intensities lower than 2m/s is significantly poorer than that of the other remediation techniques.

Fragility curves corresponding to the relative horizontal displacement of the soil wedge above the silt layer (Figure 5.13c) show that all the mitigation measures (M1 to M4) are effective in decreasing the horizontal movement of the soil wedge. Again, M4 is more effective at higher Arias intensities (e.g., for $I > 3\text{m/s}$) than the other measures, while M3 is the most effective measure for Arias intensities lower than 2 m/s.

5.5 Concluding remarks

The performance and effectiveness of various liquefaction countermeasures considered for a waterfront slope within the framework of the NSERC sponsored Liquefaction Remediation Initiative (LRI) centrifuge experiments at different levels of seismic intensity were studied and discussed in this chapter based on numerical simulations. Considerations regarding the effects of centrifuge box rigid boundaries on the seismic behavior of the slope were also assessed and discussed. The rigid centrifuge box was modeled in numerical simulations by applying the same input motion to the lateral boundaries of the mesh as to the base. Any phenomena related to seismic wave reflection at the rigid boundaries were accounted for by the numerical model. It is considered that the numerical model can accurately simulate the effects of a rigid box.

The centrifuge boundary effects were studied for two cases including existence of either a deep loose sand layer or a deep dense sand layer under the level of the centrifuge box base. In case of a deep loose sand layer, it was found that centrifuge modeling using a rigid container does not represent the actual soil seismic behavior, and the results may be misleading and under-conservative. On the other hand, if the slope is underlain by a deep dense sand layer, centrifuge modeling using a rigid base container can reasonably capture the slope seismic behavior. In this case, the results of the numerical simulations with extended finite element domains (both laterally and in depth) showed that a lateral FE analysis domain extension (with no extension in depth) on the both sides of the original model (centrifuge box) equal to 75m is sufficient to reasonably reduce the effects of the centrifuge rigid boundaries.

Study on the performance of dyke type mitigation measures showed that drainage dykes, as suggested in the LRI centrifuge experiments, locally reduce the excess pore water pressure build up, and they are not strong enough to stop the failure along a potential failure surface (along the inclined silt layer in this study). Dense sand dykes exhibit higher shear resistance compared to drainage dykes, and they can prevent failure on a predefined surface.

Due to the difficulties encountered in actual construction of continuous dykes as proposed in the LRI centrifuge experiments, sheet piling in front of the slope crest was suggested to mitigate soil liquefaction effects since it seems to be less expensive and easier to build compared to dykes. It was found that sheet piling has mitigating effects in reducing the horizontal movement of the slope comparable to those of dense dykes;

however, it may not be as effective as dense dykes in reducing the crest settlement. A possible reason may be related to the local stiffening of the crest area in dyke type measures due to construction of a dense dyke at the crest area.

Fragility curves were employed to represent the effectiveness of different liquefaction countermeasures for the slope at different levels of seismic intensities. It was found that the effectiveness of different mitigation measures strongly depends upon the level of seismic intensity. For example, as shown in Figure 13c, sheet piling (M4) is the most effective measure in decreasing the probability of occurrence large relative horizontal movement of the soil wedge above the silt layer (0.5m assumed in this study) at higher Arias intensities (e.g., for $I > 3\text{m/s}$), but it is not as effective as dense dykes at lower Arias intensities (e.g., for $I < 2\text{m/s}$).

Chapter 6 - Conclusions

6.1 Summary and concluding remarks

Post-earthquake observations all over the world indicate that soil liquefaction has been one of the major causes of many disastrous events. Various soil treatment techniques have been employed to battle the effects of soil liquefaction. The Fraser River Delta in British Columbia, Canada, is highly vulnerable to liquefaction hazards, and a large amount of money is annually spent to prevent seismically induced soil liquefaction in this region. In this regard, NSERC sponsored a Liquefaction Remediation Initiative (LRI) to study and optimize some liquefaction mitigation techniques in the Fraser River Delta. LRI included laboratory soil tests, eight centrifuge experiments (CT1 to CT8), and numerical modeling.

This research focused on numerical modeling of seismic liquefaction countermeasures for waterfront slopes in the Fraser River Delta. The numerical model used in this study was the multi-yield plasticity soil constitutive model implemented in the finite element code Dynaflow. The numerical model meets the most important requirements for liquefaction analysis such as solution of coupled field equations, and a kinematic hardening constitutive model with a non-associative flow rule to properly address different soil behavioral features (e.g., material nonlinearity, stress history dependence, shear-induced volumetric dilation/compaction and hysteretic behavior as described in Chapter 3).

The numerical model was calibrated based on the results of laboratory soil tests, information from the literature and back-analyses of the first three LRI centrifuge experiments, and then validated through class A predictions of the other centrifuge tests. Some phenomena that can influence the liquefaction resistance of sands such as effects of incomplete sand saturation and centrifuge model preparation were studied in this research within the process of model calibration. Effects of barrier (silt) layers on the seismic behavior of waterfront slopes were also studied (Chapter 4). After validation, the numerical model was used in this research to study the effects of centrifuge rigid base boundaries and to extend the range of experimental results by analyzing some remediation configurations that were not included in LRI. The model is available at Memorial University for use in further studies on seismic behavior of waterfront slopes in the Fraser River Delta.

From a study on the performance of several liquefaction countermeasures for waterfront slopes it was found that drainage dykes such as those proposed in LRI, locally reduce the excess pore water pressure buildup, but they are too weak to stop the failure. Dense sand dykes exhibit higher shear resistance compared to drainage dykes, and they can prevent failure on a predefined surface (along the silt layer as presented in this study). To address some expected difficulties in construction of continuous dykes such as those proposed in the LRI centrifuge experiments, sheet piling in front of the slope crest was suggested and studied. This measure resulted in having mitigating effects comparable to those of dense sand dykes. Also, a comparative study on the effectiveness of several types of liquefaction countermeasures for waterfront slopes made of Fraser River sand for

a range of earthquake intensities was presented in this thesis. Fragility curves were employed to represent the effectiveness of the soil treatment methods. It was found that the effectiveness of various liquefaction countermeasures is strongly dependent on the level of seismic intensity (Chapter 5).

6.2 Original contributions

The present research provides the following original contributions:

- Calibrating and validating a numerical model for Fraser River sand that was used in this research to study the performance of liquefaction remediation techniques and to extend the scope of the LRI centrifuge experiments. The numerical model can be used in further studies on the seismic behavior of waterfront slopes in the Fraser River Delta.
- Suggesting an original constitutive formulation to account for the effects of incomplete sand saturation on liquefaction as an ingredient of the sand constitutive model used in this study. The main theoretical contribution in this respect is inclusion of the transient air dissolution phenomenon for liquefaction analysis of nearly saturated soils, which has not been done before. This part of the thesis and the theoretical approach provided in the thesis for inclusion of the transient air dissolution in water is entirely original, and it was based on the author's original work.

- Assessing the boundary effects of a rigid box in centrifuge modeling of waterfront slopes.
- Presenting a comparative study on the performance and effectiveness of various liquefaction countermeasures for waterfront slopes in the Fraser River Delta within the framework of the LRI project and proposing a feasible mitigation solution for such slopes.

6.3 Suggestions for future studies

The areas suggested for future research can be built based on the outcomes of the current study to further enhance insight and understanding of the liquefaction phenomenon, dynamic centrifuge experiments, and behavior of mitigation measures against soil liquefaction. Therefore, the following areas are recommended for future studies:

- **Use of the numerical model in further studies on mitigation measures:**
This refers to the use of the calibrated numerical model in simulating the behavior of a wide range of waterfront slopes in the Fraser River Delta with different geometries and various mitigation configurations. This requires performing a few centrifuge experiments to confirm the findings of numerical simulations and extending the scope of the experimental results based on finite element analyses. For instance, study of the performance of gravel berms constructed in front of waterfront slopes is suggested. Also, the performance of a particular mitigation technique can be studied for a wider

range of slope geometries (e.g., study of the effects of milder or steeper slopes compared to the ones studied in LRI as well as effects of position and slope of the barrier layer).

- **Future contributions to centrifuge modeling:** Numerical simulations and centrifuge modeling can benefit from each other. In this respect, the calibrated numerical model can be used as a mathematical tool for designing future dynamic centrifuge experiments on geotechnical structures made of Fraser River sand to 1) identify regions influenced by the boundary effects caused by centrifuge containers for different model geometries and various types of centrifuge boxes (e.g., rigid, ESB, or laminar) that can result in minimizing errors in centrifuge modeling, and 2) efficiently design the centrifuge instrumentation layouts (e.g., quantities and locations of transducers).
- **Solving some limitations of the numerical model:** There is still a need for research on developing constitutive models and numerical procedures used for liquefaction analysis. For instance, the numerical model calibrated here predicted more dilative behavior for the soil below the slope (regions with initial static shear stress) than recorded in the centrifuge experiments.

The topics described in this section indicate that there is still room for further development of the numerical and experimental tools for studying the liquefaction phenomenon and designing remediation techniques.

References

- Adalier, K., and Aydingun, O. 2003. Numerical analysis of seismically induced liquefaction in earth embankment foundations. Part II: Application of remedial measures. *Canadian Geotechnical Journal*, 40: 766-779.
- Adalier, K., and Sharp, M.K. 2004. Embankment Dam on Liquefiable Foundation-Dynamic Behavior and Densification Remediation. *Journal of Geotechnical and Geoenvironmental Engineering*, 130(11): 1214-1224.
- Adalier, K., Elgamal, A.W., and Martin, G.R. 1998. Foundation Liquefaction Countermeasures for Earth Embankments. *Journal of Geotechnical and Geoenvironmental Engineering*, 124(6): 500-517.
- Amini, F. and Chakravarty, A. 2004. Liquefaction testing of layered sand-gravel composites. *Geotechnical Testing Journal*, ASTM, 27(1): 1-19.
- Amini, F., and Duan, Z. 2002. Centrifuge and numerical modeling of soil liquefaction at very large depths. 15th ASCE Eng. Mech. Conf., Columbia University, New York, NY.
- Andrus, R.D., and Stokoe, K.H. II. 2000. Liquefaction resistance of soils from shear-wave velocity. *Journal of Geotechnical and Geoenvironmental Engineering*, 126(11): 1015-1025.
- Arias, A. 1970. A measure of earthquake intensity. In *Seismic design for nuclear power plants*. Edited by R.J. Hansen. MIT Press. Cambridge, Massachusetts: 438- 483.
- Arulanandan, K., and Scott, R.F., editors. 1993. *Proceedings of the international conference on the verification of numerical procedures for the analysis of soil liquefaction problems. 1*, Balkema, Rotterdam.
- Arulanandan, K., and Scott, R.F., editors. 1994. *Proceedings of the international conference on the verification of numerical procedures for the analysis of soil liquefaction problems. 2*, Balkema, Rotterdam.
- Atigh, E., and Byrne, P.M. 2003. Flow liquefaction failure of submarine slopes due to monotonic loadings – an effective stress approach. *Proceedings of the First International Symposium on Submarine Mass Movements and Their Consequences*, Editors, Locat, J., and Mienert, J., Technical editor, Boisvert, held in Nice, Franc, Kluwer Academic Publishers.

- Aydingun, O., and Adalier, K. 2003. Numerical analysis of seismically induced liquefaction in earth embankment foundations. Part I: Benchmark model. *Canadian Geotechnical Journal*, 40: 753–765.
- Azizian, A. 2004. Seismic Analysis of Submarine Slopes: Retrogressive and Three-Dimensional Effects. Ph.D. dissertation, Memorial University of Newfoundland, St. John's, NL, Canada.
- Azizian, A., and Popescu, R. 2006. Three-dimensional seismic analysis of submarine slopes. *Soil Dynamics and Earthquake Engineering*, 26: 870-887.
- Barden, L., and Sides, G.R. 1967. The diffusion of air through the pore water of soils. *Proceedings of the 3rd. Asian Regional Conference on Soil Mechanics and Foundation Engineering*, 1:135-138.
- Bardet, J.P. 1986. Bounding Surface Plasticity Model for Sands. *Journal of Engineering Mechanics*, 112(11): 1198-1217.
- Bardet, J.P., Idriss, I.M., O'Rourke, T.D., Adachi, N., Hamada, M., and Ishihara, K. 1997. North America-Japan Workshop on the Geotechnical Aspects of the Kobe, Loma Prieta, and Northridge Earthquakes. Osaka, Japan 22-24 January 1996. A Report to National Science Foundation, Air Force Office of Scientific Research, and Japanese Geotechnical Society.
- Bathe, K.J. 1982. *Finite element procedures in engineering analysis*. Prentice-Hall, Englewood Cliffs.
- Bathe, K.J., and Wilson, E.L. 1976. *Numerical Methods in Finite Element Analysis*. Englewood Cliffs, New Jersey, Prentice Hall.
- Been, K., and Jefferies, M.G. 1985. A state parameter for sands. *Geotechnique*, 35(2): 99-112.
- Bell, F.G. 1993. *Engineering treatment of soils*. E and FN SPON, London.
- Bell, L. 2000. Seismic mitigation program guidelines for existing buildings funded or managed by the BC government. Sandwell Engineering Services Ltd. British Columbia.
- Bellotti, R., Ghionna, V., Jamiolkowski, M., Lancellotta, R., and Manfredini, G. 1986. Deformation characteristics of cohesionless soils from in-situ tests. In S.P. Clemence, editor, *Use of In-Situ Tests in Geotechnical Engineering*, ASCE, New York: 47-73.

- Biot, M.A. 1962. Mechanics of deformation and acoustic propagation in porous media. *Journal of Applied Physics*, 33(4): 1482-1498.
- Boulanger, R.W. 2002. Evaluating liquefaction resistance at high overburden stress. 3 rd. U.S.-Japan workshop on advanced Research on Earthquake Engineering for Dams. San Diego, CA.
- Brennan, A.J. and Madabhushi, S.P.G., 2002. Effectiveness of vertical drains in mitigation of liquefaction. *Soil Dynamics and Earthquake Engineering*, 22:1059-1065.
- Byrne, P.M., and Park, S.S. 2003. Numerical modeling of Fraser River sand and RPI centrifuge tests. A presentation available at: <http://www.civil.ubc.ca/liquefaction/>.
- Byrne, P.M., Park, S.S., Beaty, M., Sharp, M., Gonzalez, L., and Abdoun, T. 2004a. Numerical modeling of liquefaction and comparison with centrifuge tests. *Canadian Geotechnical Journal*, 41: 193-211.
- Byrne, P. M., Park, S.S., Beaty, M., Sharp, M., Gonzalez, L., and Abdoun, T. 2004b. Numerical modeling of dynamic centrifuge tests. Proc. 13th World Conference on Earthquake Engineering, Vancouver, B.C, Canada. Paper 3387.
- Castro, G. 1975. Liquefaction and cyclic mobility of saturated sands. *Journal of the Geotechnical Engineering Division, ASCE*, 101, GT6: 551-569.
- C-CORE. 2004. Earthquake Induced Damage Mitigation from Soil Liquefaction. Data report- Centrifuge Test CT4. Contract Report Prepared for University of British Columbia. C-CORE Report R-04-030-145.
- C-CORE. 2005. COSTA-C Centrifuge Test Data Report. C-CORE Report R-04-082-075.
- Chakraborty, P., Jafari-Mehrabadi, A., and Popescu, R. 2004. Effects of low-permeability soil layers on the stability of submarine slopes. Proc. 57th Canadian Geotechnical Conference, Quebec city, Canada, (on CD-ROM).
- Chan, A.H.C. 1993. User manual for DIANA-SWANDYNE II. School of Civil Engineering, University of Birmingham, Birmingham, U.K.
- Committee on Modeling Techniques in Geomechanics. 1999. Modeling Techniques in Geomechanics. A millennium paper prepared by Members of the TRB Committee on Modeling Techniques in Geomechanics.
- Cook, R.D., Malkus, D.S., and Plesha, M.E. 1989. Concepts and applications of finite element analysis. 3rd Edition, John-Wiley and Sons Inc., New York, USA.

- Cooke, H.G. 2000. Ground improvement for liquefaction mitigation at existing highway bridges. Ph.D dissertation, Virginia Polytechnic Institute and State University, Blacksburg, VA.
- Coulter, S.E., and Phillips, R. 2003. Simulating submarine slope instability initiation using centrifuge model testing. Proceedings, First International Symposium on Submarine Mass Movements and Their Consequences, eds., Locat, J., and Mienert, J., Nice, Franc.
- Crank, J. 1975. The mathematics of diffusion. Oxford University Press: Oxford.
- Creager, W.P., Justin, J.D., and Hinds, J. 1945. Engineering for Dams. John Wiley and sons, New York.
- Crouch, S.L., and Starfield, A.M. 1983. Boundary element methods in solid mechanics. Allen and Unwin, London.
- Cubrinovski, M. and Ishihara, K. 1998. Modelling of sand behaviour based on state concept, Soils and Foundations, 38(3): 115-127.
- Dafalias, Y.F. and Herrmann, L.R. 1980. A bounding surface soil plasticity model. International Symposium on Soils under Cyclic and Transient Loading, Swansea: 335-345.
- Dafalias, Y.F. and Popov, E.P. 1975. A Model of Nonlinearly Hardening Materials for Complex Loading. Acta Mech., 23: 173-192.
- Das, B.M. 1983. Fundamentals of soil dynamics. Elsevier.
- Das, B.M. 1999. Principles of Foundation Engineering, Fourth ed., Brooks/Cole Publishing company.
- De Nevers, N. 2002. Physical and chemical equilibrium for chemical engineers. John Wiley & Sons, Inc.
- Desai, C.S., and Siriwardane, H.J. 1984. Constitutive laws for engineering materials with emphasis on geologic materials. Prentice-Hall Inc., Englewood Cliff, NJ.
- Dunhum, J.W. 1954. Pile foundations for buildings. Proceedings of the ASCE, Journal. SMF Division, 80, SM.1, paper 385: 1-21.
- EIDMSL. 2003. Earthquake Induced Damage Mitigation from Soil Liquefaction. Available at: <http://www.civil.ubc.ca/liquefaction/>.

- Elgamal, A., Parra, E., Yang, Z., and Adalier, K. 2002a. Numerical analysis of embankment foundation liquefaction countermeasures. *Journal of Earthquake Engineering*, 6(4): 447-471.
- Elgamal, A., Yang, Z., and Parra, E. 2002b. Computational modeling of cyclic mobility and post-liquefaction site response. *Journal of Soil Dynamics and Earthquake Engineering*, 22, Issue 4: 259-271.
- Ferritto, J.M. 1997. Seismic design criteria for soil liquefaction. Naval Facilities Engineering Service Center, Technical report TR-2077-SHR, Port Hueneme, California.
- Ferritto, J.M., Dickenson, S., Priestley, N., Werner, S., Taylor, C., Burke, D., Seelig, W., and Kelly, S. 1999. Seismic criteria for California marine oil terminals. Naval Facilities Engineering Center, Shore Facilities Department, Structures Division, Port Hueneme, California.
- Fredlund, D.G., and Rahardjo, H. 1993. *Soil mechanics for unsaturated soils*. John Wiley & Sons, Inc., New York, N. Y.
- Fredlund, M.D, Fredlund, D.G, and Wilson, G.W. 1997. Prediction of the soil-water characteristic curve from grain-size distribution and volume-mass properties. 3rd Brazilian Symposium on Unsaturated Soils, Rio de Janeiro, Brazil.
- Gallagher, R.H. 1975. *Finite element analysis - Fundamentals*. Prentice-Hall, Englewood Cliffs.
- Gao, X.W., and Davies, T.G. 2002. *Boundary element programming in mechanics*. Cambridge University Press.
- GEOSIM. 2001. Numerical Modeling in Geomechanics at Memorial University of Newfoundland. Available at: <http://geosim.engr.mun.ca/lri/>.
- Griffiths, D.V., and Prevost, J.H. 1990. Stress strain curve generation from simple triaxial parameters. *International Journal for Numerical and Analytical Methods in Geomechanics*, 14: 587-594.
- Grozic, J.L.H. 2003. Liquefaction potential of gassy marine sands. Proceedings of the First International Symposium on Submarine Mass Movements and Their Consequences, Editors, Locat, J., and Mienert, J., Technical editor, Boisvert, held in Nice, Franc, Kluwer Academic Publishers.

- Grozic, J.L.H., Robertson, P.K., and Morgenstern, N.R. 1999. The behavior of loose gassy sand. *Canadian Geotechnical Journal*, 36: 482-492.
- Grozic, J.L.H., Robertson, P.K., and Morgenstern, N.R. 2000. Cyclic liquefaction of loose gassy sand. *Canadian Geotechnical Journal*, 37: 843-856.
- Grozic, J.L.H., Imam, S.M.R., Robertson, P.K., Morgenstern, N.R. 2005. Constitutive modeling of gassy sand behaviour. *Canadian Geotechnical Journal*, 42:812-829.
- Harder, L.F., and Boulanger, R.W. 1997. Application of K-alpha and K-sigma correction factors. Proceedings of the NCEER Workshop on Evaluation of Liquefaction Resistance of Soils, T. L. Youd and I. M. Idriss, Eds., Technical Report NCEER-97-0022, National Center for Earthquake Engineering Research, SUNY, Buffalo, 167-190.
- Hardin, B.O., and Drnevich, V.P. 1972. Shear modulus and damping in soils: Design equations and curves. *Journal of the Soil Mechanics and Foundations Division, ASCE*, 98(7): 667-692.
- Hardin, B.O., and Richart, F.E. 1963. Elastic wave velocities in granular soils. *Journal of the Soil Mechanics and Foundations Division, ASCE*, 89(SM1): 33-65.
- Hausmann, M.R. 1990. Engineering principles of ground modifications. McGraw-Hill, New York.
- Hazen, A. 1930. Water Supply, American Civil Engineers Handbook. JohnWiley & Sons, New York: 1444-1518.
- Hilf, J.W. 1948. Estimating construction pore pressures in rolled earth dams. Proceedings of the 2nd International Conference on Soil Mechanics and Foundation Engineering, Rotterdam, The Netherlands, 3: 234 -240.
- Huang, S., Barbour S.L., and Fredlund D.G. 1998. Development and verification of a coefficient of permeability function for a deformable unsaturated soil. *Canadian Geotechnical Journal*, 35(3): 411-425.
- Hughes, T.J.R. and Liu, W.K. 1978a. Implicit-Explicit Finite Elements in Nonlinear Transient Analysis. *Computer Methods in Applied Mechanics and Engineering, ASME*, 45: 371-374.
- Hughes, T.J.R. and Liu, W.K. 1978b. Implicit-Explicit Finite Elements in Nonlinear Transient Analysis: Implementation and Numerical Examples, *Journal of Applied Mechanics, ASME*, 45: 395-398.

- Ishibashi, I., and Zhang, X. 1993. Unified dynamic shear moduli and damping ratios of sand and clay. *Soils and Foundations*, 33(1): 182-191.
- Ishihara, K. 1984. Post earthquake failure of a tailings dam due to liquefaction of the pond deposit. *Proc., Intl. Conf. on Case Histories in Geotechnical Engineering*, Univ. of Missouri-Rolla, St. Louis, MO, 3: 1129-1143.
- Ishihara, K. 1993. Liquefaction and flow failure during earthquakes. *Geotechnique*, 43(3): 351-415.
- Ishihara, K., Tsuchiya, H., Huang, Y., and Kamada, K. 2001. Recent studies on liquefaction resistance of sand: Effect of saturation. *4th Intl. Conf. on Recent Advances in Geotechnical Earthquake Engineering and Soil Dynamics*, San Diego, CA.
- Itasca Consulting Group Inc. 2000. *FLAC*, version 4.0. Itasca Consulting Group Inc., Minneapolis, Minn.
- Iveson, S. M. 2003. Correction to the gas pressure term in the continuum model for partially saturated granular media presented by Pietruszczak and co-workers. *International Journal for Numerical and Analytical Methods in Geomechanics*, 27: 627-632.
- Iwan, W.D. 1967. On a Class of Models for the Yielding Behavior of Continuous and Composite Systems. *Journal of Applied Mechanics*, ASME, 34: 612-617.
- Iwasaki, T. and Tatsuoka, F. 1977. Effects of grain size and grading on dynamic shear moduli of sands. *Soils and Foundations*, 17(3): 19-35.
- Jafari-Mehrabadi, A., and Popescu, R. 2004a. Solutions for mitigating soil liquefaction effects: A numerical study. *Proc. 13th World Conference on Earthquake Engineering*, Vancouver, B.C, Canada, Paper 3016.
- Jafari-Mehrabadi, A., and Popescu, R. 2004b. Effects of partial saturation on liquefaction. *Proc. 57th Canadian Geotechnical Conference*, Quebec city, Canada, Session 2E: 14-19.
- Jaky, J. 1948. Pressures in silos. *Proc. 2nd Int. Conf. Soil Mechanics*, 1:103-107. Rotterdam.
- Japanese Geotechnical Society. 1998. CD-ROM Library on Geotechnical Centrifuge. Available at: <http://www.geotech.cv.titech.ac.jp/~cen-98/Library/MAIN.HTM>.

- Kammerer, A.M., Wu, J., Riemer, M., Pestana, M., and Seed, R.B. 2001. Use of cyclic simple shear testing in evaluation of the deformation potential of liquefiable soils. Proc. 4th Int. Conf. on Recent Advances in Geotechnical Earthquake Engineering and Soil Dynamics and Symposium in Honor of Professor W.D. Liam Finn, San Diego California.
- Kardestuncer, H., and Norrie, D. 1987. Finite element handbook. Mc. Graw-Hill Company.
- Keanne, C.M., and Prevost J.H. 1989. An analysis of earthquake data observed at the Wildlife Liquefaction Array Site, Imperial County, California. Proceedings 2nd US Japan Workshop on Liquefaction, Large Ground Deformations and Effects on Lifelines, New York, NY: 39-53.
- Kleiber, M. and Borkowski, A. 1998. Handbook of computational solid mechanics: survey and comparison of contemporary methods. Springer.
- Koerner, R.M. 1970. Effect of particle characteristics on soil strength. Journal of the Soil Mechanics and Foundation Division., ASCE, 96(SM4): 1221-1234.
- Kokusho, T. 1999. Water film in liquefied sand and its effect on lateral spread. Journal of Geotechnical and Geoenvironmental Engineering, 125(10): 817-826.
- Koning, H.L. 1963. Some observations on the modulus of compressibility of water. Proceedings of the European conference on SMFE, 1: 33-36.
- Kramer, S.L. 1996. Geotechnical earthquake engineering. Prentice-Hall.
- Kulhawy, F.H. and Mayne, P.W. 1990. Manual on estimating soil properties for foundation design. Final Report 1493-6, EL-6800, Electric Power Research Institute, Palo Alto, CA.
- Kumar, S. 2001. Reducing liquefaction potential using dynamic compaction and construction of stone columns. Journal of Geotechnical and Geological Engineering, 19:169-182.
- Lee, D.H., Juang, C.H., and Ku, C.H. 2001. Liquefaction performance of soils at the site of a partially completed ground improvement project during the 1999 Chi-Chi earthquake in Taiwan. Canadian Geotechnical Journal, 38: 1241-1253.
- Li, X.S. and Dafalias, Y.F. 2000. Dilatancy for cohesionless soils. Geotechnique, 50(4): 449-460.

- Locat, J., Bornhold, B., Byrne, P., Hart, B., Clarke, J.H., Konrad, J.M., Lee, H., Leroueil, S., Long, B., Mosher, D., Piper, D., Phillips, R., Popescu, R., Thomson, R. 2001. COSTA-Canada, a Canadian contribution to the study of continental slope stability: an overview. 2001 An Earth Odyssey: 730-737.
- Manzari, M.T. and Dafalias, Y.F. 1997. A critical-state two-surface plasticity model for sands. *Geotechnique*, 47:255-272.
- Marcuson, W.F. 1978. Definition of terms related to liquefaction. *Journal of Geotechnical Engineering, ASCE*, 104(9): 1197-1200.
- Martin, J.R., Olgun, C.G., Mitchell, J.K., Hon, M., and Durgunoglu, H.T. 2004. High-Modulus Columns for Liquefaction Mitigation. *Journal of Geotechnical and Geoenvironmental Engineering*, 130 (6): 561-571.
- Miller, E.A., and Roycroft, G.A. 2004. Compaction Grouting Test Program for Liquefaction Control. *Journal of Geotechnical and Geoenvironmental Engineering*, 130(4): 355-361.
- Ming, H.Y., and Li, X.S. 2003. Fully Coupled Analysis of failure and remediation of Lower San Fernando Dam. *Journal of Geotechnical and Geoenvironmental Engineering*, 129 (4): 336-349.
- Mroz, Z. 1967. On the Description of Anisotropic Workhardening. *Journal of the Mechanics and Physics of Solids*, 15: 163-175.
- Naylor, D.J., Pande, G.N., Simpson, B., and Tabb, R. 1981. Finite elements in geotechnical engineering. Pineridge Press, Swansea, U.K.
- NBCC. 2005. National Building Code of Canada. National Research council of Canada, Ottawa, Ontario.
- Ochiai, H. 1977. The estimated equation of the coefficient of earth pressure at rest K_0 for sand by using N value. *Report JSSMFE*, 17(3): 93-101.
- Okamura, M., Ishihara, M. and Tamura, K. 2004. Liquefaction resistances and degree of saturation of sand improved with sand compaction piles. 13th World Conference on Earthquake Engineering. Paper 3484, Vancouver, B.C., Canada.
- Owen, D. R.J. and Hinton, E. 1980. Finite Elements in Plasticity: Theory and Practice. Pineridge Press, Swansea.
- Park, S.S., and Byrne, P.M. 2004a. Class A prediction of centrifuge tests at C-CORE (Satge1: Predictions of CT1 and CT2). Available at: <http://www.civil.ubc.ca/liquefaction>.

- Park, S.S., and Byrne, P.M. 2004b. Stress densification and its evaluation. *Canadian Geotechnical Journal*, 41: 181-186.
- Park, S.S., Sharp, M.K., and Byrne, P.M. 2004. The influence of stress densification and centrifuge model preparation method for soil liquefaction. Proc. 57th Canadian Geotechnical Conference, Quebec city, Canada, Session 2E: 20-27.
- Peng, J., Lu, J., LAW, K.H., Elgamal, A. 2004. PARCYCLIC: Finite element modeling of earthquake liquefaction response on parallel computers. *International Journal for Numerical and Analytical methods in Geomechanics*, 28(12): 1207-1232.
- Perry, R.H, and Green, D.W. 1997. Perry's chemical Engineers' Handbook. 7th Edition, McGraw-Hill.
- Pietruszczak, S., and Pande, G. N. 1991. On the mechanics of partially saturated soils. *Computers & Geotechnics*, 12(1): 55-71.
- Pietruszczak, S., and Pande, G. N. 1996. Constitutive relations for partially saturated soils containing gas inclusions. *Journal of Geotechnical Engineering* 1996, 122 (1): 50-59.
- Pietruszczak, S., Pande, G. N., and Oulapour, M. 2003. A hypothesis for mitigation of risk of liquefaction. *Geotechnique*; 53(9): 833-838.
- Phillips, R., Coulter, S.E., and Tu, M. 2004. Earthquake simulator development for the C-CORE geotechnical centrifuge. Proc. 57th Canadian Geotechnical Conference, Quebec city, Canada.
- Popescu, R. 1995. Stochastic variability of soil properties: Data Analysis, Digital Simulation, Effects on System Behavior. Ph.D. dissertation, Princeton University, Princeton, NJ.
- Popescu, R. 2002. Finite element assessment of the effects of seismic loading rate on soil liquefaction. *Canadian Geotechnical Journal*, 39: 331-344.
- Popescu, R., and Prevost, J.H. 1993. Centrifuge validation of a numerical model for dynamic soil liquefaction. *Soil Dynamics and Earthquake Engineering*, 12: 73-90.
- Popescu, R., and Prevost, J.H. 1995. Comparison between VELACS numerical " class A" predictions and centrifuge experimental soil test results. *Soil Dynamics and Earthquake Engineering*, 14: 79-92.

- Popescu, R., Prevost, J.H., Deodatis, G., and Chakraborty, P. 2006. Dynamics of nonlinear porous media with applications to soil liquefaction. *Soil Dynamics and Earthquake Engineering*, 26(6-7): 648-665.
- Pradhan, T.B.S., and Tatsuoka, F. 1989. On stress-dilatancy equations of sand subjected to cyclic loading. *Soils and Foundations*, 29 (1): 65-81.
- Pradhan, T.B.S., Tatsuoka, F., and Sato, Y. 1989. Experimental stress-dilatancy relations of sand subjected to cyclic loading. *Soils and Foundations*, 29(1): 45-64.
- Prevost, J.H. 1977. Mathematical modeling of monotonic and cyclic undrained clay behavior. *Int. J. Num. Analyt. Meth. Geomech.* 1: 195-216.
- Prevost, J.H. 1978. Plasticity theory for soil stress-strain behavior. *J. Eng. Mech. Div, ASCE*, 104(EM5): 1177-1194.
- Prevost, J.H. 1980. Mechanics of Continuous Porous Media. *International Journal of Engineering Science*, 18 (5): 787-800.
- Prevost, J.H. 1982a. Two-surface vs. multi-surface plasticity theories. *International journal for Numerical and Analytical Methods in Geomechanics*, 6:323-338.
- Prevost, J.H. 1982b. Nonlinear Transient Phenomena in Saturated Porous Media. *Computer Methods in Applied Mechanics and Engineering*, 30: 3-18.
- Prevost, J.H. 1985a. A simple plasticity theory for frictional cohesionless soils. *Soil Dynamics and Earthquake Engineering*, 4(1): 9-17.
- Prevost, J.H. 1985b. Wave Propagation in Fluid-Saturated Porous Media: An Efficient Finite Element Procedure. *Soil Dynamics and Earthquake Engineering*, (4):183-202.
- Prevost, J.H. 1989. DYNA1D, a computer program for nonlinear seismic site response analysis. Technical report NCEER-89-0025. National Center for Earthquake Engineering research. State University of New York at Buffalo.
- Prevost, J.H. 1990. Modeling the Behavior of Geomaterials. Princeton Univ. Press.
- Prevost, J.H. 2002. DYNAFLOW - Version 02, Release 01 A. User's manual. Princeton University, Princeton, NJ.
- Prevost, J.H., and Keane, C.M. 1989. Shear stress-strain curve generation from simple material parameters. *Journal of Geotechnical Engineering, ASCE*, 116(8): 1255-1263.

- Prevost, J.H., and Popescu, R. 1996. Constitutive relations for soil materials. *Electronic Journal of Geotechnical Engineering*, ASCE, <http://www.ejge.com/1996/+Ppr9609/Ppr9609>.
- Richart, F.E., Hall, J.R., and Woods, R.D. 1970. *Vibration of soils and foundations*. Prentice Hall, Englewood Cliffs.
- Riemer, M.F., Lok, T.M., and Mitchell, J.K. 1996. Evaluating Effectiveness of Liquefaction Remediation Measures for Bridges Proc., 6th Japan-U.S. Workshop on Earthquake Resistant Design of Lifeline Facilities and Countermeasures for Soil Liquefaction, Technical Report NCEER-96-0006, NCEER, Buffalo, NY, 441-455.
- Robertson, P. and Campanella, R. 1983. Interpretation of Cone Penetration Tests - Part I: Sand. *Canadian Geotechnical Journal*. 20(45): 718-733.
- Robertson, P.K., and Wride, C.E. 1998. Evaluating cyclic liquefaction potential using the cone penetration test. *Canadian Geotechnical Journal*, 35(3): 442-459.
- Schmertmann, J.H. 1975. Measurement of in-situ shear strength. Keynote lecture, Proceedings of the conference on in-situ measurement of soil properties, June 1-4, 1975, Volume II, American Society of Civil Engineers.
- Schofield, A.N. 1980. Cambridge geotechnical centrifuge operations. *Geotechnique*, London, U.K., 30(3): 227-268.
- Schuurman, I. E. 1966. The compressibility of an air/water mixture and a theoretical relation between the air and water pressures. *Geotechnique*, 16(4): 269-281.
- Seed, H.B. 1976. Evaluation of soil liquefaction effects on level ground during earthquakes. *Liquefaction Problems in Geotechnical Engineering*, ASCE annual convention and exposition, Philadelphia, PA, pre-print 2752:1-104.
- Seed, R.B., and Harder, L.F. 1990. SPT-based analysis of cyclic pore pressure generation and undrained residual strength, H. Bolton Seed Memorial Symposium, Volume 2, BiTech Publishers, Vancouver: 351-376.
- Seed, H.B., and Idriss, I.M. 1971. Simplified procedure for evaluating soil liquefaction potential. *Journal of Geotechnical Engineering*, ASCE, 97(9): 1249-1273.
- Seed, H.B., and Idriss, I.M. 1982. *Ground Motions and Soil Liquefaction During Earthquakes*. Earthquake Engineering Research Institute Monograph.
- Seed, H.B., Tokimatsu, K., Harder, L.F., and Chung, R.M. 1985. The influence of SPT procedures in soil liquefaction resistance evaluations. *Journal of Geotechnical Engineering*, ASCE, 111(12): 1425-1445.

- Seed, R.B., Cetin, K.O., Moss, R.E.S., Kammerer, A.M., Wu, J., Pestana, J.M., Riemer, M.F., Sancio, R.B., Bray, J.D., Kayen, R.E., and Faris, A. 2003. Recent advances in soil liquefaction engineering: A unified and consistent framework. 26th Annual ASCE Los Angeles Geotechnical Spring Seminar, Keynote Presentation, H.M.S. Queen Mary, Long Beach, California.
- Segerlind, L.J. 1976. Applied finite element analysis. John Wiley and Sons Inc. New York.
- Seid-Karbasi, M. 2003. Time Histories of Input Motions Selected for Physical and Numerical Modeling. Report No. 2003/02, Civil Engineering Department of University of British Columbia. Available from <http://www.civil.ubc.ca/liquefaction/>.
- Shahabi, A.A., Das, B.M., and Tarquin, A.J. 1984. An empirical relation for coefficient of permeability of sands. Fourth Australia-New Zealand Conference on Geomechanics, 1: 54-57.
- Sharp, M.K., Dorby, R., and Ledbetter, R.H. 2000. Centrifuge research of liquefaction phenomenon. 12th world conference on earthquake engineering. Auckland, New Zealand.
- Sherif, M. A., Tsuchiya, C., and Ishibashi, I. 1977. Saturation effect on initial soil liquefaction. Journal of the Geotechnical Engineering, ASCE, 103(8): 914-917.
- Shinozuka, M., Feng, M.Q., Lee, J., and Naganuma, T. 2000. Statistical Analysis of Fragility Curves. Journal of Engineering Mechanics, 126(12): 1224-1231.
- Simo, J.C., and Ortiz, M. 1985. A unified approach to finite deformation elastoplastic analysis based on the use of hyperelastic constitutive equations. Computer Methods in Applied Mechanics and Engineering, 49(2): 221-245.
- Skempton, A.W. 1954. The pore pressure coefficients A and B. Geotechnique, 4(4): 143-147.
- Smith, I.M. 1982. Programming the finite element method with application to geomechanics. John Wiley and Sons Inc. New York.
- Sy, A., and Campanella, R.G. 1994. Becker and standard penetration tests (BPT-SPT) correlations with consideration of casing friction. Canadian Geotechnical Journal, Ottawa, 31: 343-356.
- Sy, A., Campanella, R.G., and Stewart, R.A. 1995. BPT-SPT correlations for evaluation of liquefaction resistance in gravelly soils. Proc., Spec. Session on Dyn. Properties of Gravelly Soil, ASCE, New York.

- Tamura, S., Tokimatsu, k., Abe A., and Sato, M. 2002. Effects of air bubbles on B-value and P-wave velocity of a partially saturated sand. *Soils and Foundations*, 42(1): 121-129.
- Tatsuoka, F., Ochi, K., Fujii, S., and Okamoto, M. 1986a. Cyclic undrained triaxial and torsional shear strength of sand for different sample preparation methods. *Soils and Foundations*, 26(3): 23-41.
- Tatsuoka, F., Toki, S., Miura, S., Kato, H., Okamoto, M., Yamada, S., Yasuda, S., and Tanizawa, F. 1986b. Some factors affecting cyclic undrained triaxial strength of sand. *Soils and Foundations*, 26(3): 99-116.
- Taylor, R.N. 1995. *Geotechnical centrifuge technology*. Blackie Academic & Professional, London, New York.
- Terzaghi, K., and Peck, R.B. 1967. *Soil Mechanics in Engineering Practice*. 2nd edition, John Wiley and Sons, New York.
- Tsukamoto, Y., Ishihara, K., Nakazawa, Kamada, K., and Huang, Y. 2002. Resistance of partially saturated sand to liquefaction with reference to longitudinal and shear wave velocities. *Soils and Foundations*, 42(6): 93-104.
- Tu, M. 2003. Preliminary research proposal for Ph.D. degree at Memorial University of Newfoundland, St. John's, Newfoundland, Canada.
- Tu, M. 2005. Personal communication (Email of Feb. 15, 2005).
- TXI Chaparral Steel. 2003. *Structural shapes technical manual (Version 3.0)*.
- Uniform Building Code. 1994. *International Conference of Building Officials, ICBO, Whittier, CA. Volume 2*.
- USACE. 1992. *Bearing capacity of soils*. Report No. E M 1110-1-1905.
- USACE. 1994. *Engineering properties of Wetland soils*. WRP Technical Note SG-RS-1.2.
- USACE. 1995. *Geotechnical analysis by the finite element method*. Pub. No. 1110-2-544.
- Vaid, Y.P., and Eliadorani, A. 2000. Undrained and drained (?) stress-strain response. *Canadian Geotechnical Journal*. 37: 1126-1130.
- Vaid, Y.P., and Negussey, D. 1988. Preparation of reconstituted sand specimens. *Advanced Triaxial Testing of Soils and Rock*. ASTM, STP 977: 405-417.

- Vaid, Y.P., and Sivathayalan, S. 1996. Static and cyclic liquefaction potential of Fraser Delta sand in simple shear and triaxial tests. *Canadian Geotechnical Journal*, 33: 281-289.
- Vaid, Y.P., and Sivathayalan, S. 2000. Fundamental factors affecting liquefaction susceptibility of sands. *Canadian Geotechnical Journal*, 37: 592-606.
- Vaid, Y.P., Sivathayalan, S. and Stedman, D. 1999. Influence of specimen-reconstituting method on the undrained response of sand, *Geotechnical Testing Journal*, 22(3): 187-195.
- Vaid, Y.P., Stedman, J.D., and Sivathayalan, S. 2001. Confining stress and static shear effects in cyclic liquefaction. *Canadian Geotechnical Journal*, 38: 580-591.
- Wang, C.T. 1953. *Applied elasticity*. McGraw-Hill, New York.
- Wijewickreme, D., Sriskandakumar, S., Byrne, P. 2005. Cyclic loading response of loose air-pluviated Fraser River sand for validation of numerical models simulating centrifuge tests. *Canadian Geotechnical Journal*. 42: 550-561.
- Weisstein, E.W. 2006. *Finite Difference*. A Wolfram web resource available from <http://mathworld.wolfram.com/FiniteDifference.html>.
- Xia, H., and Hu, T. 1991. Effects of saturation and back pressure on sand liquefaction. *Journal of Geotechnical Engineering*, 117(9): 1347-1362.
- Yanagihara, S., Takeuchi, M., and Ishihara, K. 1991. Dynamic Behavior of Embankment on Locally Compacted Sand Deposits. In *Proc. Fifth International Conference on Soil Dynamics and Earthquake Engineering*. Computational Mechanics Publication, Boston, and Elsevier Applied Science, New York: 365-376.
- Yang, J. 2002. Liquefaction resistance of sand in relation to P-wave velocity. *Geotechnique*, 52(4): 295-298.
- Yang, Z., and Elgamal, A. 2001. Challenges in Computational Modeling of Liquefaction-Induced Ground Deformations. *Proceedings of NSF International Workshop on Earthquake Simulation in Geotechnical Engineering*. Cleveland, Ohio, USA.
- Yang, Z., Elgamal, A., and Parra, E. 2003. Computational model for cyclic mobility and associated shear deformation. *Journal of Geotechnical and Geoenvironmental Engineering*, 129(12): 1119-1127.

- Yang, J., Savidis, S., and Roemer, M. 2004. Evaluating liquefaction strength of partially saturated sand. *Journal of Geotechnical and Geoenvironmental Engineering*, 130(9): 975-979.
- Yoshimi, Y., Tanaka, K., and Tokimatsu, K. 1989. Liquefaction resistance of a partially saturated sand. *Soils and Foundations*, 29: 157-162.
- Youd, T.L., Idriss, I.M., Andrus, R.D., Arango, A., Castro, G., Christian, J.T., Dorby, R., Finn, L.F., Harder, L.F., Hynes, M.E., Ishihara, K., Koester, J.P., Liao, S.S.C., Marcuson, W.F., Martin, G.R., Mitchell, J.K., Moriwaki, Y., Power, M.S., Robertson, P.K., Seed, R.B, and Stokoe, K.H. 2001. Liquefaction resistance of soils: Summary report from the 1996 NCEER and 1998 NCEER/NSF workshops on evaluation of liquefaction resistance of soils. *Journal of Geotechnical and Geoenvironmental Engineering*, 127(10): 817-833.
- Zeng, X. 2001. Benefits of Collaboration between Centrifuge Modeling and Numerical Modeling. *Proceedings of NSF International Workshop on Earthquake Simulation in Geotechnical Engineering*, Case Western Reserve University.
- Zienkiewicz, O.C., and Taylor R.L. 1989. *The finite element method. Volume 1: Basic formulations and linear problems.* McGraw-Hill, London, UK.
- Zienkiewicz, O.C., and Taylor R.L. 1991. *The finite element method. Volume 2: Solid and fluid mechanics: dynamics and non-linearity.* McGraw-Hill, London, UK.

Appendix A- FE meshes and boundary conditions

The finite element (FE) meshes used in the thesis for numerical class A and class C predictions of the LRI centrifuge experiments and the boundary conditions considered in this study are presented in this appendix. They are also available online in the class A prediction reports submitted to UBC placed both on the LRI website (EIDMSL, 2003) as well as GEOSIM (2001) website.

Figures A.1 and A.2 show the finite element meshes used in class A and class C predictions of the LRI centrifuge experiments. The FE model used for numerical predictions of tests CT1 to CT4 (Figure A.1) consisted of 958 nodes and 890 finite elements and the FE model used for numerical predictions of tests CT5 to CT8 (Figure A.2) consisted of 588 nodes and 542 finite elements. The finite elements used in this research are 4-node linear elements with 4 degrees of freedom at each node, two for solid displacements and two for fluid velocities. The FE meshes shown in Figures A.1 and A.2 were selected based on numerical simulations of the slope using some initial trials with coarser FE meshes and subsequent refining to achieve a reasonable convergence in the predicted responses.

The seismic motion was applied in horizontal direction at the base and lateral boundaries of the FE models to simulate the rigid box used in the centrifuge experiments. The base and the lateral boundaries were assumed impervious. It is noted that the input motion is applied to the solid phase. Applying motion to the fluid phase at lateral boundaries causes high numerical noise. To avoid this, and to model impervious

boundary, the horizontal degree of freedom of the fluid phase for nodes at lateral boundaries are slaved to the same degree of freedom of nodes on the next vertical line.

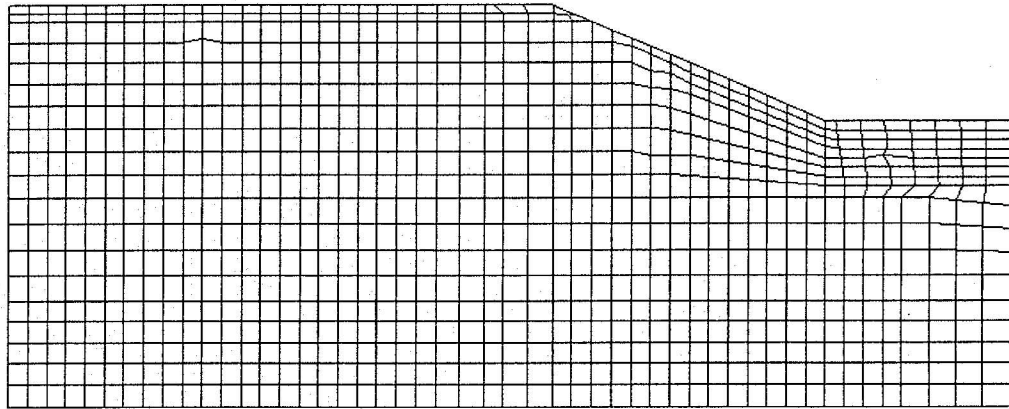


Figure A.1 The finite element mesh used in numerical class A and class C predictions of the LRI centrifuge tests CT1 to CT4.

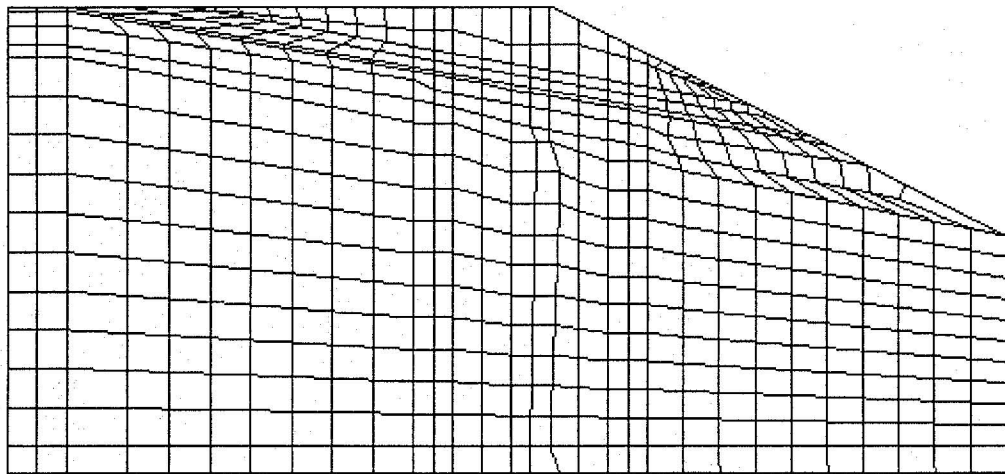


Figure A.2 The finite element mesh used in numerical class A and class C predictions of the LRI centrifuge tests CT5 to CT8.

The time steps used in this research for numerical analyses were selected to accurately reproduce the seismic input motions corresponding to each analysis. It is noted

that for the type of dynamic analysis considered in this research (i.e., time integration using implicit method) the size of time steps does not have significant effects on the results of numerical simulations.

Appendix B- CD ROM including numerical predictions

All the details of numerical class A and class C predictions of the LRI centrifuge experiments and details related to boundary conditions and finite element meshes used in this study as well as comparisons of the numerical predictions with the centrifuge experimental data at all transducer locations are available on a CD ROM as Appendix B of this thesis and also posted on the GEOSIM website administered by MUN Engineering (GEOSIM, 2001).

The CD ROM contains the following reports:

Class A predictions of the LRI centrifuge experiments (these reports were submitted to UBC before the relevant centrifuge experiments were performed) including:

- Class A prediction of test CT1.
- Class A prediction of test CT3.
- Class A prediction of test CT4.
- Class A prediction of test CT5.
- Class A prediction of test CT6.
- Class A prediction of test CT7.
- Class A prediction of test CT8.

Class A predictions of the LRI centrifuge experiments:

- Class C prediction of test CT1.
- Class C prediction of test CT2.
- Class C prediction of test CT3.

- Class C prediction of test CT4.
- Class C prediction of test CT5.
- Class C prediction of test CT6.
- Class C prediction of test CT7.
- Class C prediction of test CT8.

